



THE HONG KONG
POLYTECHNIC UNIVERSITY

香港理工大學

Pao Yue-kong Library

包玉剛圖書館

Copyright Undertaking

This thesis is protected by copyright, with all rights reserved.

By reading and using the thesis, the reader understands and agrees to the following terms:

1. The reader will abide by the rules and legal ordinances governing copyright regarding the use of the thesis.
2. The reader will use the thesis for the purpose of research or private study only and not for distribution or further reproduction or any other purpose.
3. The reader agrees to indemnify and hold the University harmless from and against any loss, damage, cost, liability or expenses arising from copyright infringement or unauthorized usage.

IMPORTANT

If you have reasons to believe that any materials in this thesis are deemed not suitable to be distributed in this form, or a copyright owner having difficulty with the material being included in our database, please contact lbsys@polyu.edu.hk providing details. The Library will look into your claim and consider taking remedial action upon receipt of the written requests.

**INTEGRATED REMOTE SENSING AND MACHINE
LEARNING TECHNIQUES FOR SOLAR FORECASTING
AND RESOURCE ASSESSMENT**

CHEN SHANLIN

PhD

The Hong Kong Polytechnic University

2024

The Hong Kong Polytechnic University

Department of Mechanical Engineering

**Integrated Remote Sensing and Machine Learning Techniques for Solar
Forecasting and Resource Assessment**

CHEN Shanlin

**A thesis submitted in partial fulfillment of the
requirements for the degree of
Doctor of Philosophy**

October 2023

CERTIFICATE OF ORIGINALITY

I hereby declare that this thesis is my own work and that, to the best of my knowledge and belief, it reproduces no material previously published or written, nor material that has been accepted for the award of any other degree or diploma, except where due acknowledgement has been made in the text.

(Signed)

CHEN Shanlin

(Name of student)

Dedication

I would like to dedicate this work to my beloved family, for their unconditional love, support and encouragement.

Abstract

Solar energy is set to be one of the major power sources to enable deep decarbonization owing to its sustainability. However, the integration of solar energy into power systems is still facing challenges due to the variability and intermittency of available solar irradiance. Ground measurements are the most reliable data source for designing solar energy projects, but complete and long-term historical data are scarce. Therefore, it is important to retrieve ground-level solar irradiance from modern geostationary satellites with much improved spatio-temporal resolutions to fill the data gap. Meanwhile, solar forecasting is also a cost-effective method to reduce the negative impacts of solar variability and help with the system integration and management.

Both solar forecasting and resource assessment rely on the clear-sky model, which estimates the clear-sky irradiance under cloudless conditions. To address the difficulty in applying physical clear-sky models and the compromised performance of empirical clear-sky models, an improved turbidity estimation method is proposed for estimating clear-sky irradiance based on common meteorological measurements. It is shown that the clear-sky irradiance from improved turbidity estimation exhibits lower divergences compared with the monthly climatological means. The Ineichen-Perez model based on the improved turbidity estimation is then applied for global horizontal irradiance (GHI) estimation using semi-empirical satellite methods. The results show the GHI estimates have comparable performance to the referenced physical solar model in the national solar radiation database (NSRDB), but with less complexity. To further expand the applicability of the turbidity estimation method, a transferable model is proposed for estimating turbidity and clear-sky irradiance. The results show that clear-sky GHI estimates and day-ahead persistent forecasts are comparable with the physical clear-sky models. Given that the forecasts of meteorological information are much more accurate than solar irradiance forecasts, the transferable turbidity estimation therefore shows valuable potential for solar energy applications.

Since clouds are the major factor attenuating available ground-level solar irradiance, the irradiance estimation under cloudy conditions exhibits huge uncertainties for both semi-empirical and physical models.

To better account for the cloud effect, deep-learning models based on multispectral satellite images are proposed for GHI and direct normal irradiance (DNI) estimations. When compared with NSRDB, deep-learning methods show better overall results for both GHI and DNI estimations. The combination of deep learning and remote sensing shows potential in better extracting cloud information, which can better support solar resource assessment, especially for cloudy conditions. Meanwhile, due to the spatio-temporal nature of solar irradiance, satellite data and satellite-derived products are extensively used in solar forecasting. To investigate the potential benefits of satellite-derived irradiance products and their improvements for solar forecasting, a comparative study for deterministic solar forecasts is performed. The results show that satellite-derived irradiance products generally outperform raw spectral satellite images, and the improved accuracy in satellite-derived irradiance products is likely to produce better forecasts. Similarly, solar forecasting under frequent cloudy conditions is also associated with larger uncertainties. Nevertheless, satellite-derived irradiance with improved accuracy might lead to better forecasts, which is beneficial to a wide range of stakeholders in solar energy.

Publications Arising from the Thesis

Journal papers

S. Chen, C. Li, R. Stull, and M. Li (2023). Improved satellite-based intra-day solar forecasting with a chain of deep learning models. Submitted to *Energy Conversion and Management*.

S. Chen, C. Li, Y. Xie, and M. Li (2023). Global and direct solar irradiance estimation using deep learning and selected spectral satellite images. *Applied Energy*, 352, 121979.

S. Chen, Z. Liang, P. Dong, S. Guo, and M. Li (2023). A transferable turbidity estimation method for estimating clear-sky solar irradiance. *Renewable Energy*, 206, 635-644.

S. Chen, Z. Liang, S. Guo, and M. Li (2022). Estimation of high-resolution solar irradiance data using optimized semi-empirical satellite method and GOES-16 imagery. *Solar Energy*, 241, 404-415.

S. Chen and M. Li (2022). Improved turbidity estimation from local meteorological data for solar resourcing and forecasting applications. *Renewable Energy*, 189, 259-272.

Conference presentations

S. Chen, C. Li, Y. Xie and M. Li, Global and direct solar irradiance estimation using deep learning and selected spectral satellite images. Oral presentation at *APS March meeting 2023*, Las Vegas, Nevada, USA, 5-10 March, 2023.

S. Chen and M. Li, A transferable turbidity estimation method for high fidelity clear-sky solar irradiance computation. Poster presentation at *8th World conference on photovoltaic energy conversion*, Milan, Italy, 26-30 September, 2022.

Acknowledgement

My sincerest thanks go to my supervisor, Dr. Mengying Li, for offering me the opportunity to study in the university and the continuous support on all the research and administrative matters. I would like to express my gratitude to my co-supervisor, Dr. Hui Tang, for the enlightenment on cloud dynamics. Special thanks go to, Dr. Liang An, for serving as the Board of Examiners (BoE) chair, Prof. Zijun Zhang (School of Data Science, City University of Hong Kong) and Dr. Merlinde Kay (School of Photovoltaic and Renewable Energy Engineering, University of New South Wales), for reviewing my thesis and serving as the member of the examination committee.

My gratefulness also goes to my friends in the REALab group as well as in the university, not only for their friendship and kindness, but also for the great teamwork we made on the basketball court. I could not imagine how life in Hong Kong will be without them.

I would also like to thank Prof. Roland Stull for hosting me as a visiting PhD student in the Weather Forecast Research Team (WFRT) at The University of British Columbia, and all the WFRT members, for sharing their expertise on weather forecasting and solar energy.

I wish to acknowledge the financial support from The Hong Kong Polytechnic University and HKSAR Government Scholarship Fund and the support from the general office and technical team in the department.

I am especially grateful to my parents, my sister, my grandfather, and my partner. Knowing that you support me and are with me every step of the way has made this possible. Words cannot describe all that I owe you.

Chapter 2, in full, is a reprint of S. Chen and M. Li (2022). Improved turbidity estimation from local meteorological data for solar resourcing and forecasting applications. *Renewable Energy*, 189, 259-272. The thesis author is the first author of this publication.

Chapter 3, in full, is a reprint of S. Chen, Z. Liang, S. Guo, and M. Li (2022). Estimation of high-resolution solar irradiance data using optimized semi-empirical satellite method and GOES-16 imagery. *Solar Energy*, 241, 404-415. The thesis author is the first author of this paper.

Chapter 4, in full, is a reprint of S. Chen, Z. Liang, P. Dong, S. Guo, and M. Li (2023). A transferable turbidity estimation method for estimating clear-sky solar irradiance. *Renewable Energy*, 206, 635-644. The abstract is accepted as a poster presentation at the *8th World conference on photovoltaic energy conversion*, Milan, Italy, 26-30 September, 2022. A transferable turbidity estimation method for high fidelity clear-sky solar irradiance computation. The thesis author is the first author of this publication.

Chapter 5, in full, is a reprint of S. Chen, C. Li, Y. Xie, and M. Li (2023). Global and direct solar irradiance estimation using deep learning and selected spectral satellite images. *Applied Energy*, 352, 121979. The abstract is accepted as an oral presentation at the *APS March Meeting*, Las Vegas, Nevada, USA, 5-10 March, 2023. The thesis author is the first author of this publication.

Chapter 6, in full, is a reprint of the manuscript submitted to *Energy Conversion and Management*. S. Chen, C. Li, R. Stull, and M. Li (2023). Improved satellite-based intra-day solar forecasting with a chain of deep learning models. The thesis author is the first author of this manuscript.

Contents

Declaration	i
Dedication	ii
Abstract	iii
Publications arising from the thesis	v
Acknowledgement	vi
1 Introduction	1
1.1 Background	1
1.2 Solar radiation	3
1.2.1 Quality control	4
1.2.2 Surface Radiation Budget Network	5
1.3 Clear-sky models	5
1.4 Solar resourcing and forecasting	7
1.4.1 Methods of solar resourcing	7
1.4.2 Methods of solar forecasting	9
1.5 Machine learning in solar irradiance modeling	12
1.6 Research gap and objectives	14
1.7 Dissertation structure	15
2 Improved turbidity estimation from local meteorological data for solar resourcing and forecasting applications	17
2.1 Introduction	17

2.2	Methodology of turbidity estimation	20
2.2.1	Data selection	21
2.2.2	Selection of clear-sky days	22
2.2.3	Derivation of ‘ground truth’ turbidity for model training	23
2.2.4	Turbidity estimation from local meteorological data	27
2.3	Results and discussion	29
2.3.1	Estimations of daily turbidity and 1-minute averaged GHIs in clear-sky days	29
2.3.2	Estimations of daily turbidity and 1-minute averaged GHIs in partially clear days	34
2.3.3	Estimations of daily turbidity and 1-minute averaged DNIs	35
2.3.4	Generic applicability of the proposed method	39
2.4	Conclusions	39
2.5	Acknowledgement	41
3	Estimation of high-resolution solar irradiance data using optimized semi-empirical satellite method and GOES-16 imagery	42
3.1	Introduction	42
3.2	Data and methods	45
3.2.1	Data	46
3.2.2	Semi-empirical models	47
3.2.3	Turbidity estimation	51
3.3	Results and discussion	52
3.3.1	Comparison of ABI bands and derivation methods for CI and CSI	52
3.3.2	Comparison of clear-sky models for GHI estimation	56
3.4	Conclusions	62
3.5	Acknowledgement	63
4	A transferable turbidity estimation method for estimating clear-sky solar irradiance	64
4.1	Introduction	64
4.2	Data and methods	67
4.2.1	Data	67
4.2.2	Clear-sky models	68
4.2.3	Clear-sky detection and turbidity derivation	68
4.2.4	Turbidity estimation model development	69

4.2.5	Turbidity and clear-sky irradiance estimations	70
4.3	Results and discussion	71
4.3.1	Evaluation of turbidity estimation models	71
4.3.2	Comparison of GHICs estimations using different turbidity factors	76
4.3.3	Comparison of GHICs estimations and forecasts with physical models	77
4.4	Conclusions	81
4.5	Acknowledgement	82
4.6	Appendix	82
5	Global and direct solar irradiance estimation using deep learning and selected spectral satellite images	83
5.1	Introduction	83
5.2	Data and methods	86
5.2.1	Data	87
5.2.2	Correlation analysis	89
5.2.3	Deep learning model	91
5.3	Results	94
5.3.1	Comparison of different deep learning networks for irradiance estimations	95
5.3.2	Comparison under clear and cloudy sky conditions	96
5.3.3	Error analysis	99
5.4	Discussion	102
5.5	Conclusions	104
5.6	Acknowledgement	105
5.7	Appendix	106
6	Improved satellite-based intra-day solar forecasting with a chain of deep learning models	110
6.1	Introduction	110
6.2	Data and methods	113
6.2.1	Publicly available data	115
6.2.2	Satellite-derived irradiance from SAT-DL	118
6.2.3	Forecasting method	120
6.2.4	Performance evaluation of forecasts	122
6.3	Results	124

6.3.1	Forecast evaluation in terms of statistical metrics	124
6.3.2	Forecast evaluation in terms of ramp metrics	126
6.3.3	Distribution-oriented forecast evaluation	129
6.4	Discussion	132
6.5	Conclusions	133
6.6	Acknowledgement	134
7	Conclusions and recommendations	135
7.1	Conclusions	135
7.2	Recommendations	138
	Bibliography	139

List of Figures

1.1	Solar PV power potential map from World Bank Group	2
1.2	Global primary energy consumption by source in 2022	2
1.3	GHI is estimated by subtracting cloud attenuation from a clear-sky background (GHI_{cs})	9
1.4	The classification of solar forecasting methods.	10
1.5	The basic structure of MLP with an input layer, a hidden layer, and an output layer.	13
1.6	Some examples of activation functions. (a) ReLU. (b) Sigmoid. (c) Hyperbolic tangent.	13
1.7	The basic structure of CNN with the input, convolution, pooling, fully connected and output layers.	14
2.1	Comparison of measured clear-sky GHI (GHIs) with PVLIB GHIs of the same day in two different years. PVLIB uses the T_L factor from its look-up table, which is based on constant monthly climatology value. The PVLIB GHIs remains the same on the same day of different years, while the measured GHIs are not, indicating T_L factor also varies on a long term (i.e., yearly) basis.	19
2.2	An overview of the method to derive and estimate T_L . The model for estimating the daily, hourly and 5-minute T_L is trained independently, and the input meteorological data is also averaged on the same time basis.	21
2.3	Examples of clear-sky days selection in DRA. Measured GHI data is from SURFRAD, GHIs are computed by both RadFlux and PVLIB. The clear-sky labels are from RadFlux. (a) A detected full clear-sky day. (b) A detected clear-sky day with high solar zenith periods not labeled. (c) A wrongly labeled clear-sky day which is removed by manual check. (d) A typical partly cloudy day.	22

2.4	Derived T_L time series with different averaging modes for a clear-sky day with respect to local standard time (LST). (a) Derived T_L time series on 2020-02-26. The derived T_L shows high variations and unrealistic values in the periods with high solar zenith angles. (b) Averaged T_L on different time basis (5-minute, hourly, and daily) and the irradiance difference between measured GHICs and PVLIB GHICs during the day.	25
2.5	Comparison of GHICs estimation using different T_L averaging modes for the clear-sky days in year 2019 and 2020. (a) Daily RMSE of 1-minute averaged GHICs estimation. (b) Daily MBE of 1-minute averaged GHICs estimation. All the derived T_L regardless of averaging mode produce more accurate GHICs than PVLIB.	26
2.6	Comparison of the derived daily T_L and PVLIB T_L and the performance of applied ML methods. (a) The comparison of derived T_L and PVLIB T_L . The comparison between derived T_L and estimated T_L from different methods (b) Linear Regression (c) Random Forest Regressor and (d) MLP Regressor.	30
2.7	Learning curve of MLP regressor with tenfold cross validation. The dots represent mean values, and the related shadows reflect the standard derivation. Both training and validation errors are decreased with the increased training size. At the end of training, the validation error is slightly larger than training, which indicates a good fit.	31
2.8	Sensitivity analysis and statistical properties of the meteorological inputs for the MLP model. (a) Sensitivity analysis based on the changes of a sole parameter, where the base is the mean value. (b) Box chart of the normalized meteorological measurements. Statistical properties represent the Minimum, Lower Quartile, Median, Upper Quartile, and Maximum.	32
2.9	The comparison of GHICs estimation based on derived and estimated daily T_L factors. (a) Daily RMSE of GHICs estimation. (b) Daily MBE of GHICs estimation. Generally, the estimated T_L performs better than the default PVLIB T_L factor.	33
2.10	Examples of GHI in partially cloudy days during (a) 2019-03-30 (b) 2029-12-27 (c) 2020-03-31 (d) 2020-04-03. The GHICs calculated from the estimated T_L shows a higher accuracy than PVLIB when compared with measured GHI in the clear-sky instants.	34
2.11	The RMSE and MBE of DNICs estimation using the GHICs-based derived and estimated T_L . Both recalculations and estimations have lower overall RMSE and MBE than PVLIB but with some exceptions.	35

2.12	The comparison of DNICs estimation based on derived and estimated daily T_L factors. (a) RMSE of DNICs estimation. (b) MBE of DNICs estimation. Generally, the estimated T_L performs better than the default PVLIB T_L factor in terms of RMSE and MBE.	37
2.13	DNI and GHI time series in partially cloudy days during (a) 2019-03-30 (b) 2029-12-27 (c) 2020-03-31 (d) 2020-04-03. Compared with DNICs estimation in partially cloudy days, GHICs estimated from improved T_L factor has higher accuracy in the clear-sky instants. . . .	38
3.1	The flowchart of GHI estimation using semi-empirical methods with different clear-sky models.	45
3.2	Comparison of the upper bound and lower bound determination using different ABI bands (see Table 3.1) and strategies at DRA (2019-01-01 to 2019-05-31). S1-S4 are the symbols of strategies presented in Table 3.3. The differences between upper and lower bounds are also included for comparison. The lines in the box plots are the median values.	53
3.3	The nRMSE and nMBE of the CSI reference and estimation based on different bands, dynamic range and CI derivation, and empirical regressions between CSI and CI at DRA (2019-01-01 to 2019-05-31). The reference CSI is determined using GHI measurements and REST2 clear-sky model. S1-S4 are the symbols of strategies presented in Table 3.3, and M1-M4 represent the empirical methods described in Table 3.4.	54
3.4	The nRMSE and nMBE between the GHI measurements and estimations based on different bands, dynamic range and CI derivation, and empirical regressions between GHI and CI using REST2 clear-sky model at DRA (2019-01-01 to 2019-05-31). S1-S4 are the symbols of strategies presented in Table 3.3, and M1-M4 represent the empirical methods described in Table 3.4.	55
3.5	The nRMSE and nMBE between the measured and estimated GHI for four clear-sky models in semi-empirical method, seven SURFRAD stations, and four evaluated conditions (all-sky, cloudy days, partially cloudy days, and clear days). GHI estimation from NSRDB is also included for comparison.	58
3.6	The nRMSE and nMBE between the GHI measurements and estimates using semi-empirical method for four clear-sky models, seven SURFRAD stations, and three evaluation conditions (all-sky, cloudy periods, and clear periods).	60

3.7	The nRMSE and nMBE between the GHI measurements and estimates in clear periods for four clear-sky models, and seven SURFRAD stations. ‘ALL’ means all the seven stations are included. ‘Estimated GHI’ means the GHI estimates of semi-empirical model. ‘Clear-sky GHI’ means the GHIs directly calculated from clear-sky models.	61
4.1	The flowchart of transferred T_L estimation model using machine learning and meteorological measurements.	67
4.2	Summary of the seven SURFRAD stations. The information in the brackets is (altitude [m], time difference from UTC [hours], climate classifications), where Köppen climate classifications are: Bsk (arid, steppe, cold), Bwk (arid, desert, cold), Cfa (temperate, without dry season, hot summer), Dfa (continental, without dry season, hot summer), Dfb (continental, without dry season, warm summer).	68
4.3	The comparison of ground truth T_L (T_L derived), PVLIB T_L (T_L default), and T_L estimations from local (T_L local) and transferred methods (T_L transfer) for clear-sky and partially clear days in 2019, at seven SURFRAD stations: (a) DRA, (b) BON, (c) FPK, (d) GWN, (e) PSU, (f) SXF, and (g) TBL. Only the results of 2019 are presented here to show the trends, and the T_L profiles in 2018 and 2020 are similar.	73
4.4	The statistic properties of the meteorological inputs in the year of 2019. (a) Ambient temperature, (b) Relative humidity, (c) Wind speed, and (d) Atmospheric pressure.	74
4.5	The nRMSE and nMBE between the 5-minute averaged GHIs measurements and estimations using different models at SURFRAD stations in 2018-2020. GHIs is estimated by the Ineichen-Perez model with three different T_L inputs, the McClear model, and the REST2 model.	79
4.6	The nRMSE and nMBE between the 5-minute averaged GHIs measurements and day-ahead forecasts using the day persistent method at SURFRAD stations in 2018-2020.	80
5.1	The flowchart of ground-level solar irradiance estimation using deep learning and satellite measurements of GOES-16.	86
5.2	Sample satellite images including all the spectral bands of GOES-16 for Bondville (40.05°, -88.37°) at 2019-01-10 20:45:00 (UTC). The image is in the size of 11×11 pixels, where Bondville is located at the center. All the spectral images are normalized to the range of [0,1] using the Min-Max normalization.	88

5.3	Correlation analysis among measurements of the 16 spectral bands of GOES-16 at (a) BON and (b) All stations of SURFRAD.	90
5.4	The structure of deep learning model for estimating ground solar irradiance using the GOES-16 images of selected bands. The inputs are images of 8 selected bands with size of 11×11 pixels, the output is the clear-sky index. Note that the hyperparameters might vary for different locations, this figure is just to show the structure.	92
5.5	The loss curves of training and validation process for GHI estimation at BON. Both training loss and validation loss decrease with the trained epochs and finally converge with a slightly higher validation loss, which indicates a good fit.	93
5.6	GHI and DNI estimation results on some selected days at BON and DRA. (a) and (d) are on clear days, (b) and (e) are on cloudy days, while (c) and (f) are for partially cloudy days.	98
5.7	The comparison of GHI estimation using deep learning (DNNa8) and physical solar model (NSRDB) under clear, cloudy, all-sky conditions at all SURFRAD stations.	98
5.8	The comparison of DNI estimation using deep learning (DNNa8) and physical solar model (NSRDB) under clear, cloudy, all-sky conditions at all SURFRAD stations.	99
5.9	The comparison of GHI estimation using deep learning (DNNa8) and physical solar model (NSRDB) across clear-sky index intervals at all SURFRAD stations. 'ALL' means all the stations are included.	100
5.10	The comparison of DNI estimation using deep learning (DNNa8) and physical solar model (NSRDB) across clear-sky index intervals at all SURFRAD stations. 'ALL' means all the stations are included.	101
5.11	The cloud enhancement events at the SURFRAD stations. GHI is the actual measurement, GHI_DNN and GHI_NSRDB are the estimations from the deep learning model and physical solar model, respectively. GHI_EX is the extraterrestrial radiation projected on the horizontal surface.	103
A5.1	Joint and marginal distributions for GHI measurements and estimations of DNNa8 and NSRDB at all SURFRAD stations: (a) BON, (b) DRA, (c) FPK, (d) GWN, (e) PSU, (f) SXF, (g) TBL, (h) ALL. 'ALL' means all the stations are included. The colors show 2D kernel densities. GHI estimations of DNNa8 generally show better agreements with GHI observations than NSRDB.	106

A5.2	The error distributions for GHI estimations of DNNa8 and NSRDB at all the SURFRAD stations: (a) BON, (b) DRA, (c) FPK, (d) GWN, (e) PSU, (f) SXF, (g) TBL, (h) ALL. 'ALL' means all the stations are included. The density is a normalized probability density, the error is the difference between DNI estimate and measurement. A gaussian regression is performed for each distribution. The error of DNNa8 shows a narrower profile compared with NSRDB.	107
A5.3	Joint and marginal distributions for DNI measurements and estimations of DNNa8 and NSRDB at all SURFRAD stations: (a) BON, (b) DRA, (c) FPK, (d) GWN, (e) PSU, (f) SXF, (g) TBL, (h) ALL. 'ALL' means all the stations are included. The colors show 2D kernel densities. DNI estimations of DNNa8 generally show better agreements with DNI observations than NSRDB.	108
A5.4	The error distributions for DNI estimations of DNNa8 and NSRDB at all the SURFRAD stations: (a) BON, (b) DRA, (c) FPK, (d) GWN, (e) PSU, (f) SXF, (g) TBL, (h) ALL. 'ALL' means all the stations are included. The density is a normalized probability density, the error is the difference between DNI estimate and measurement. A gaussian regression is performed for each distribution. The error of DNNa8 shows a narrower profile compared with NSRDB.	109
6.1	The methodology flowchart of solar irradiance forecasting employed in this work. The deep learning model chain derives irradiance from satellite data and subsequently generates forecasts. The end-to-end deep learning model only applies satellite data, and the hybrid physical-deep learning model uses physically satellite-derived NSRDB data.	114
6.2	An illustration of solar irradiance forecasting for the Table Mountain (TBL) station using surrounding spatial information. (a) The target and 121 surrounding locations with satellite-derived irradiance, (b) The target with 121 surrounding locations and the domain of used spectral satellite images. A pixel-wise 11×11 shifting window is applied to get the SAT-DL for the 121 surrounding stations.	119
6.3	The structure of the deep learning model for CSI forecasts using spectral satellite images or satellite-derived GHI products. This is a model with multiple CSI forecasts (multiple outputs), where the structures of different inputs are similar, but the hyperparameters are optimized separately using the KerasTuner, as shown in Table 6.3.	121

6.4	Some possible outputs of ramp forecasts. GHI_c denotes the clear-sky irradiance, 10% bounds define the upper and lower bounds on the threshold, FH is the forecast horizon.	123
6.5	Comparison of nRMSE [%] for GHI forecasts up to 180 minutes using different methods/inputs: smart persistent (SP), spectral satellite images (SAT), NSRDB GHI estimates (NS), GHI estimates of SAT-DL (SDL), at all the SURFRAD stations. The colors are to differ the stations, and the symbols are to distinguish the methods.	125
6.6	Same as Fig. 6.5, but for the comparison of nMBE [%] for GHI forecasts.	125
6.7	Comparison of forecast skill for GHI forecasts using different inputs across the forecast horizons up to 180 minutes at all the SURFRAD stations. Larger skill indicates a more accurate forecast.	126
6.8	The selected representative stations of SURFRAD. DRA has the most clear periods, PSU has the most cloudy skies, and SXF is selected as it is in the geographical 'middle' of the rest stations.	127
6.9	The ramp analysis for GHI forecasts across the forecast horizon up to 180 minutes. RDI, FRI and RMI at (a) BON, (b) DRA and (c) PSU. For RDI and RMI, values closer to 100% are better. For FRI, smaller is better.	128
6.10	Joint and marginal distributions of GHI forecasts and measurements, at (a) DRA, (b) PSU, and (c) SXF, for forecast horizons of 30, 60, 120, and 180 minutes (only a subset of forecast horizons is selected to be representatives). GHI forecasts are based on raw satellite data (SAT), satellite-derived GHI estimates of NSRDB (NS) and SAT-DL (SDL).	130
6.11	Same as Fig. 6.10, but for conditional distributions of GHI forecasts, given the measurements.	131

List of Tables

1.1	Summary of the seven SURFRAD stations.	5
2.1	Comparison of 1-minute averaged GHICs recalculations and estimations using derived and estimated T_L for clear-sky days in the year of 2019 and 2020. PVLIB results are presented here for reference.	29
2.2	Training and testing errors of the applied ML algorithms for T_L estimation.	30
2.3	Comparison of DNICs recalculations and estimations using derived and estimated T_L for clear-sky days in the year of 2019 and 2020. Although 5-minute averaged T_L has the lowest RMSE for DNICs recalculations, the 1-minute averaged DNICs estimations based on daily, hourly and 5-minute averaged T_L show little difference.	36
2.4	Results of 1-minute averaged GHICs estimations using estimated T_L for clear-sky and partially clear days in 2019 for all the SURFRAD stations. PVLIB results from default T_L are presented in brackets for reference.	39
3.1	Summary of the blue, red, veggie bands of GOES-16. All the information is obtained from the GOES-R Series Product Definition and User’s Guide (PUG)	46
3.2	Summary of the seven SURFRAD stations.	47
3.3	Summary of the strategies used to derive CI for GHI estimation.	49
3.4	Different methods to calculate GHI via CSI, CI and GHICs. GHICs is estimated from a selected clear-sky model.	49
3.5	Input parameters for the used clear-sky models. The variables are the solar constant I_0 [W m^{-2}], solar zenith angle θ [$^\circ$], altitude h [m], Linke turbidity T_L , surface albedo ρ_g , local pressure P_a [mb], ambient temperature T_a [K], AOD at 550 nm τ_{550} , Ångström exponent α , total ozone amount u_{O_3} [atm-cm], total precipitable water vapor u_{H_2O} [cm], total nitrogen dioxide amount u_{NO_2} [atm-cm], relative humidity ϕ [%], wind speed V [m s^{-1}].	50

3.6	Summary of the ABI band performance in 5-minute GHI estimation using RSET2 clear-sky model, Strategy 4, and Method 3 at DRA (2019-01-01 to 2019-05-31). The GHI estimation from NSRDB is also included as reference.	56
3.7	The overall nRMSE [%] and nMBE [%] between GHI estimations and measurements at seven SURFRAD stations using semi-empirical method with different clear-sky models under four evaluation cases (all-sky, cloudy days, partially cloudy days, and clear days). The GHI estimation from NSRDB is also included for comparison.	57
3.8	The overall nRMSE [%] and nMBE [%] between GHI estimations and measurements at seven SURFRAD stations using semi-empirical method with different clear-sky models under three evaluation cases (all-sky, cloudy periods, and clear periods). The GHI estimation from NSRDB is also included.	59
4.1	The RMSE and MBE between derived T_L and T_L estimations from interpolation, local and transferred models at seven SURFRAD stations for both clear-sky and partially clear days in 2019.	72
4.2	The comparison of T_L and GHICs estimations at TBL in 2018-2020, including the T_L estimation models developed with and without atmospheric pressure (P_a).	75
4.3	The nRMSE [%] and nMBE [%] of 1-minute averaged GHICs estimations using different T_L factors at SURFRAD stations in 2018-2020. The used T_L coefficients are default interpolations (T_L default), estimations of the local model (T_L local) and transferred model (T_L transfer).	77
4.4	Overall results of GHICs estimations and day-ahead persistent GHICs forecasts with the time resolution of 5-minute at SURFRAD stations excluding TBL in 2018-2020. Used models are the Ineichen-Perez model with three T_L inputs, the McClear model, and the REST2 model.	78
5.1	The detailed information of the ABI spectral bands of GOES-16.	87
5.2	Detailed information of the seven SURFRAD stations. The climate is based on Köppen classifications. The elevation angle and azimuth angle are from the station to GOES-16, and the azimuth angle starts from the North (0°).	89
5.3	The RMSE and MBE in [W m^{-2}], and nRMSE and nMBE in [%], of GHI estimation using different deep learning models at SURFRAD stations. The GHI estimation error of NSRDB is included as the benchmark.	95

5.4	The RMSE and nMBE, in [W m^{-2}], nRMSE and nMBE in [%], of DNI estimation using different deep learning models at SURFRAD stations. The DNI estimation error of NSRDB is included as the benchmark.	96
5.5	The comparison of GHI estimation results under clear and cloudy periods at all SURFRAD stations using deep learning (DNNa8) and physical solar model (NSRDB).	97
5.6	The comparison of DNI estimation results under clear and cloudy periods at all SURFRAD stations using deep learning (DNNa8) and physical solar model (NSRDB).	97
6.1	A summary of the publicly available data used in this work.	115
6.2	The detailed information of the selected ABI spectral bands of GOES-16	117
6.3	Hyperparameters shown in Fig. 6.3 for Bayesian optimization using the KerasTuner.	121
6.4	The amount of clear and cloudy periods (in percentage) in 2020 at all the SURFRAD stations. The clear and cloudy conditions are grouped based on 1-minute QC data and Bright-Sun clear-sky detection model	127

Chapter 1

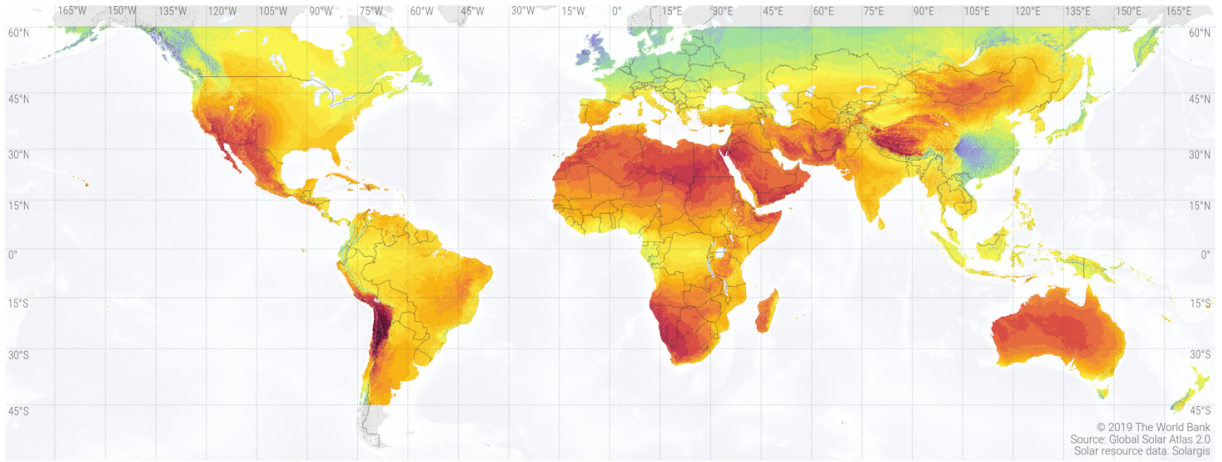
Introduction

1.1 Background

Factors such as energy crisis and global warming have increased the usage of renewable sources of energy in the last few decades, owing to their properties of being sustainable and low carbon emissions. According to the International Energy Agency (IEA) Outlook reports [1, 2, 3], several countries have introduced their targets to achieve net-zero emissions by 2050 (NZE2050), and many countries are either in discussion or in legislation phases regarding greenhouse gas (GHG) emissions reduction targets by 2050. It is estimated that CO₂ emissions from the power sector will decrease by nearly 60% between 2019 and 2030. The importance of renewable energy sources (RES) e.g., solar and wind, is obvious as the global electricity supplied by renewables will go from 27% in 2019 to 60% in 2030.

Among the renewable sources of energy, solar energy has gained the utmost popularity because it is inexhaustible and considered to be one of the most promising renewable energy resources for power generation even on large scales [4]. Solar energy, as an attractive power source, not only can be used for the electricity and heat generation but also has minimal environmental and social impacts. It is reported that solar thermal technologies provided about 480 TWh energy in 2019, which saves an energy equivalent of 43 million tons of oil and 130 million tons of CO₂ emission [5]. Meanwhile, as one of the major technologies used for converting solar energy into electricity, photovoltaic (PV) power potential is sufficient for most regions in the world (as illustrated in Fig. 1.1). The total annual solar PV additions in NZE2050 is expected to expand from 110 GW in 2019 to nearly 500 GW in 2030 [1]. However, fossil fuels are still the dominant part in the global energy mix at current stage, based on the statistics of global primary energy consumption in 2022 (see Fig. 1.2), just around 14% of the energy consumption was supplied by renewable sources (except nuclear), and the amount of solar energy was only 2.07% [6].

SOLAR RESOURCE MAP
PHOTOVOLTAIC POWER POTENTIAL



	2.0	2.4	2.8	3.2	3.6	4.0	4.4	4.8	5.2	5.6	6.0	6.4
Daily totals:												
Yearly totals:	730	876	1022	1168	1314	1461	1607	1753	1899	2045	2191	2337

kWh/kWp

This map is published by the World Bank Group, funded by ESMAP, and prepared by Solargis. For more information and terms of use, please visit <http://globalsolaratlas.info>.

Figure 1.1: Solar PV power potential map from World Bank Group [7]

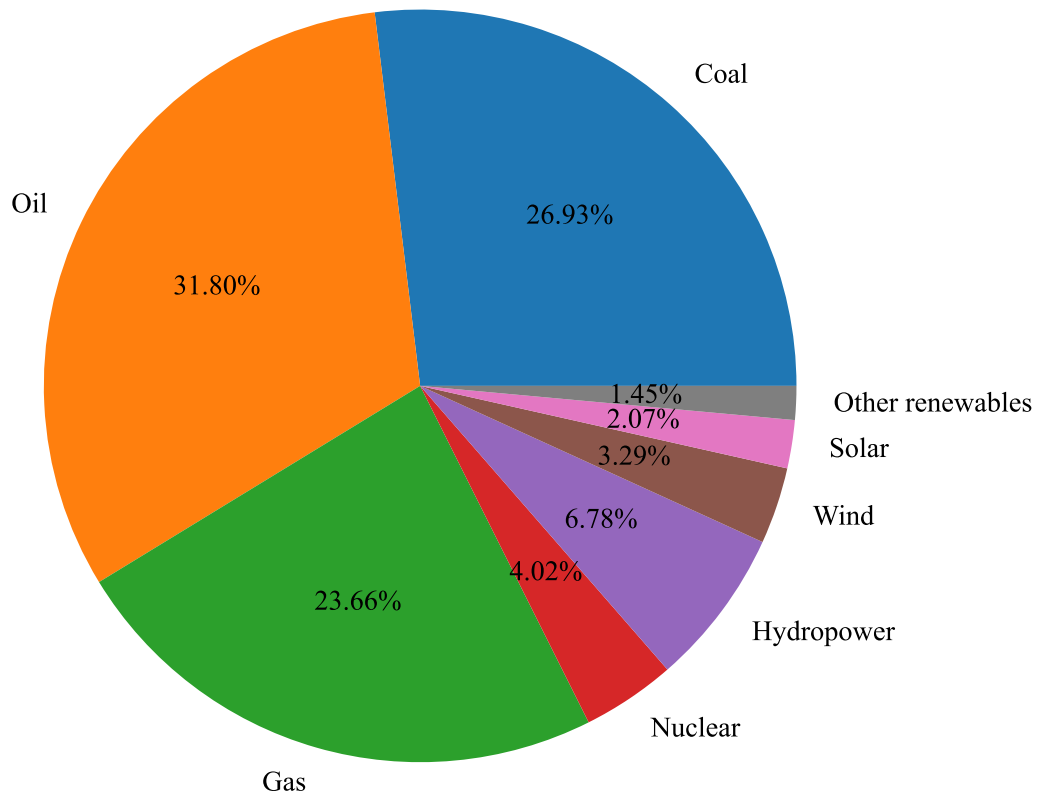


Figure 1.2: Global primary energy consumption by source in 2022 [6]

Despite the advantages of solar energy on the issues of global warming, air pollution, and health concerns, its integration into electricity grids has several challenges due to the intermittency and variability in the source availability caused by the high dependence on local atmospheric conditions [8, 9, 10, 11]. Therefore, long-term and accurate historical solar irradiance data is of great importance for designing the solar energy projects and related feasibility studies [8]. However, long-term and high-quality solar irradiance measurements are scarce at most of the locations due to the technical and financial issues [12], for instance, the equipment measuring solar irradiance is costly, the maintenance routine and data quality control (QC) are associated with difficulties. It is necessary to employ the recent advancements in geostationary satellite for ground-level solar irradiance estimation and reanalysis [13]. This could provide support for the feasibility study, optimal system design, and the modeling of solar irradiance [8, 12]. Meanwhile, the irradiance variability also has an influence on the operational stage of solar projects, which could cause a mismatch between the energy demand and power supply sides, generating issues on stability, safety, reliability and frequency response of the electricity grids [9, 14].

To overcome issues related to the intermittency of solar energy, potential solutions involve the implementation of energy storage, demand response, and solar irradiance or power forecasting [15, 16, 17]. At current stage, many storage technologies are still costly and somewhat inefficient, because only 70–85% of the stored energy is recoverable [18], and demand response programs typically have significant implementation costs [18]. On the other hand, solar forecasting, i.e., solar irradiance forecasting or solar power output forecasting, is one of the cost-effective solutions of efficiently integrating solar power [19, 20], particularly at higher penetration levels. By forecasting future solar irradiance and power productions, the grid operators can have more information to reliably and efficiently balance generation and demand in real-time and perform power scheduling [21, 14]. The study in [22] has shown that a 25% improvement in PV power output forecast's accuracy can lead to a net reduction of 1.56% (US\$ 46.5 million) in the generation cost. Moreover, for optimal usages of energy storage and demand response systems, the forecasting of solar irradiance and power is also necessary [23, 24].

1.2 Solar radiation

The Sun's surface has a temperature about 5800 K that can be approximated as a blackbody [25]. Solar radiation reaching the Earth's top-of-atmosphere (TOA) is nearly fixed even the Sun-Earth distance varies slightly across the year. Solar constant quantifies the energy received on a unit area of TOA surface perpendicular to the radiation propagation per unit time from the Sun at the mean Sun-Earth distance. Various

values of the solar constant have been reported in the range of 1353 - 1374 W m², and a value of 1367 W m² is adopted by the World radiation center (WRC) with an uncertainty of 1% [25].

Due to the complex interactions between solar radiation and the Earth's atmosphere, the available solar irradiance at the ground surface exhibits both temporal and spatial variations [26]. Therefore, three fundamental components are used to quantify the solar radiation for solar forecasting and resource assessment [8]:

- Direct normal irradiance (DNI): solar beam radiation from the Sun received by a surface normal to the solar rays, which can be measured by a pyrliometer.
- Diffuse horizontal irradiance (DHI): solar radiation excluding DNI from the sky dome received by a horizontal surface, which is scattered by clouds, aerosols, and other atmospheric compositions, as measured by a shaded pyranometer.
- Global horizontal irradiance (GHI): total solar radiation received on a horizontal surface that includes both direct and diffuse components, which is measured by an unshaded pyranometer.

The three components are related, on any surface that is perpendicular to the solar rays, the global irradiance is the sum of direct and diffuse irradiance. For a horizontal surface, GHI can be expressed by:

$$GHI = DNI \cdot \cos(\theta) + DHI \quad (1.1)$$

where θ [°] is the solar zenith angle.

1.2.1 Quality control

Several procedures are required in QC of solar irradiance, including the extremely rare limit test and the three-component closure test [27]. Three parts are involved in the extremely rare limit test for solar irradiance:

$$-2 \leq GHI \leq 1.2 \cdot E_{0n} \cdot \cos^{1.2}(\theta) + 50 \quad (1.2)$$

$$-2 \leq DHI \leq 0.75 \cdot E_{0n} \cdot \cos^{1.2}(\theta) + 30 \quad (1.3)$$

$$-2 \leq DNI \leq 0.95 \cdot E_{0n} \cdot \cos^{0.2}(\theta) + 10 \quad (1.4)$$

whereas two parts are in the three-component closure test:

$$abs(closr) \leq 8\% \text{ for } \theta \leq 75^\circ \text{ and } GHI > 50 \quad (1.5)$$

$$abs(closr) \leq 15\% \text{ for } 75^\circ < \theta < 93^\circ \text{ and } GHI > 50 \quad (1.6)$$

where GHI [W m^{-2}], DHI [W m^{-2}], and DNI [W m^{-2}] are the three solar irradiance components, θ [$^\circ$] is the solar zenith angle, E_{0n} [W m^{-2}] is the extraterrestrial irradiance, $closr = GHI / (DNI \cdot \cos(\theta) + DHI) - 1$, which defines the closure relationship of the three solar irradiance components. These QC steps are based on the theoretical aspects detailed by Long and Shi [28].

1.2.2 Surface Radiation Budget Network

The Surface Radiation Budget Network (SURFRAD) [29] is a network consisting of seven weather monitoring stations in different climatological zones across the contiguous United States. Since its establishment in 1995, SURFRAD has focused on measuring data of solar radiation and atmospheric conditions. SURFRAD collects a variety of meteorological and solar data with research quality, which is widely used in climate research and applications related to renewable energy, atmospheric science, and weather studies. SURFRAD data including GHI, DNI, DHI, and meteorological measurements plays a vital role in this thesis for both method development and validation. The detailed description of SURFRAD is presented in Table 1.1.

Table 1.1: Summary of the seven SURFRAD stations.

Station	Full name	Latitude ($^\circ$)	Longitude ($^\circ$)	Altitude (m)	Timezone
BON	Bondville	40.05	-88.37	230	UTC-6
DRA	Desert Rock	36.62	-116.02	1007	UTC-8
FPK	Fort Peck	48.31	-105.10	634	UTC-7
GWN	Goodwin Creek	34.25	-89.87	98	UTC-6
PSU	Pennsylvania State University	40.72	-77.93	376	UTC-5
SXF	Sioux Falls	43.73	-96.62	473	UTC-6
TBL	Table Mountain	40.12	-105.24	1689	UTC-7

1.3 Clear-sky models

Solar radiation reaching the ground is scattered, transmitted or absorbed by the atmosphere based on the types and amounts of intervening constituents and their radiative (or optical) properties [8, 26]. Clouds are known as the major factor affecting the solar irradiance available at the ground level. Even cloudless skies

produce complicated interactions between solar radiation and the variable atmospheric compositions [8, 26], where the amount of aerosol, total precipitable water, ozone, and other gaseous constituents are the modulators. The aerosol optical depth (AOD) is used to describe the aerosol property, and Linke turbidity (T_L) is used to define the transparency of the atmosphere [30]. Although the atmospheric compositions under cloudless sky are temporally and spatially variable, their attenuation effect of solar irradiance is well documented in the clear-sky models [31, 32, 33]. As summarized in [34, 35], clear-sky models, that aims to estimate solar irradiance under clear-sky conditions, can be broadly classified into two groups: physical models and empirical models. Physical clear-sky models, for example, REST2 [33] and McClear [32], perform detailed radiative simulations of the atmospheric attenuation processes with generally higher performance [34, 36]. While empirical models, such as Ineichen-Perez model [31], are based on simplified parameterizations of the radiation attenuating effect [35].

Clear-sky models are a key component in both solar resourcing and forecasting applications [9]. The ground solar irradiance, e.g., GHI, can be retrieved using satellite-based methods based on a clear-sky model [37, 38]. Meanwhile, the clear-sky model is suggested to remove the variations of solar irradiance by introducing the clear-sky index (CSI) in the development of solar forecasting models [21]. The clear-sky models used in this work includes the Ineichen-Perez model [31], the McClear model [32], and the REST2 model [33], which are selected as the representatives of average, good and best clear-sky models to keep the generality [36].

The Ineichen-Perez model is based on the T_L factor, which is defined as the number of dry and clean atmospheres producing that equivalent attenuation to the real atmosphere [30]. Due to the simplicity, Ineichen-Perez model (documented in PVLIB [39]) is extensively used in solar forecasting [36]. However, the clear-sky irradiance estimation of Ineichen-Perez is unsatisfying because of the invariant T_L factor based on the SoDa monthly climatology means [40]. The divergences of T_L modeled and measured clear-sky irradiance are observed in [41, 42]. The McClear model and the REST2 model are physical clear-sky models, which are much more complicated than empirical clear-sky models [36]. The complexity of physical clear-sky models, e.g., prevailing the detailed atmospheric conditions, generally leads to higher performance [36]. The input parameters of McClear include solar constant (I_0 [W m^{-2}]), solar zenith angle (θ [$^\circ$]), local altitude (h [m]), surface albedo (ρ_g), atmospheric pressure (P_a [mb]), ambient temperature (T_a [K]), AOD at 550 nm (τ_{550}), Ångström exponent (α), total ozone amount (u_{O_3} [atm-cm]), and total precipitable water vapor (u_{H_2O} [cm]) [32]. McClear adopts a lookup table and libRadtran [43] to speed up the calculations of radiative transfer models (RTMs). Both the inputs and the clear-sky irradiance of McClear are available from the Copernicus Atmosphere Monitoring Service (CAMS) [44]. The REST2 model has been repeatedly

validated as the one of the clear-sky models with high performance [34, 35]. The essential inputs of REST2 are I_0 [W m^{-2}], θ [$^\circ$], ρ_g , P_a [mb], τ_{550} , α , u_{O_3} [atm-cm], u_{H_2O} [cm], and total nitrogen dioxide amount u_{NO_2} [atm-cm] [33]. These atmospheric information can be obtained via satellites and reanalyzes products, for instance, the Modern-Era Retrospective Analysis for Research and Applications, Version 2 (MERRA-2) [45] or Moderate Resolution Imaging Spectroradiometer (MODIS) [46].

1.4 Solar resourcing and forecasting

With the rapid expansion of solar energy projects in recent years, the availability of reliable and accurate ground surface solar irradiance data is of great importance [12]. Historical data is essential for the feasibility and optimal system design phases of a solar power conversion project, which can reduce the risk and provide support for the project location selection and appropriate design of the solar energy conversion technology [8].

Ground-based irradiance measurements are the most reliable data source for solar energy applications but generally with limited availability [12]. Therefore, solar irradiance estimation and reanalysis from the measurements of geostationary satellite can provide information for evaluating and designing the solar energy projects [47], especially for the locations with limited on-site instrumentation. As an essential part for monitoring and modeling solar irradiance, geostationary satellites are widely used for solar resource assessment and forecasting as they continuously observe the same part of the Earth's surface, which can generate site specific data with high time resolution for solar energy applications [8]. The advancement in modern remote sensing technique brings data in finer temporal and spatial resolutions as well as new insights in solar irradiance modeling [13].

1.4.1 Methods of solar resourcing

Satellite-based solar irradiance derivation models can be broadly classified as physical, empirical, and semi-empirical [8]. Physical methods typically apply RTMs through various different layers to simulate the interactions between solar radiation and compositions in the atmosphere, which requires accurate and detailed information of the atmospheric constituents, such as cloud optical properties (COD), AOD, and water vapor content [8]. Pure empirical models attempt to simulate the regression between the satellite measurements and ground based records [8], which is straightforward and easy to implement. While semi-empirical models are a combination of physical and empirical methods, which employ a simple RTM and regression approach to fit the observations [8, 48].

Many studies have been conducted to retrieve ground-level GHI from geostationary satellites' images [49, 50, 51]. GHI can then be separated into DNI and DHI by various separation models [21] for different applications. Both physical and semi-empirical satellite models are widely used in estimating GHI as simple empirical methods typically have inferior performance due to the lack of generality [51, 52]. Physical models usually have better performance than semi-empirical satellite methods [51], since they technically need the detailed atmospheric information. For example, the national solar radiation database (NSRDB) [49], as a widely accessed and publicly available data source over most parts of the Americas with high quality, provides satellite-derived irradiance components as well as other auxiliary variables. NSRDB is produced using the physical solar model (PSM) and products from several other associations [49], including the Geostationary Operational Environmental Satellite (GOES), the Interactive Multisensor Snow and Ice Mapping System (IMS), MODIS, and MERRA-2. The Heliosat-4 method [50] is also a fully physical model that uses a fast and approximated radiative simulation approach with high performance. Heliosat-4 method consists of two separate steps based on the libRadtran method [43] and a look-up table: the first step relies on McClear model [32] for clear-sky solar irradiance under cloud free conditions, and the second step is to apply McCloud for irradiance attenuation caused by clouds. The cloud and other atmospheric properties are obtained from CAMS [44]. However, although the physical models generally have better accuracy, the complexity in models' implementation, high demand of computing resources, and the difficulties and uncertainties [8, 53] in retrieving the essential atmospheric inputs greatly hinder the applications [36, 54].

On the other hand, semi-empirical satellite methods are much easier to implement and generally have comparable performance, which are widely used in solar forecasting and resource assessment [48, 55, 56]. There are mainly two steps in semi-empirical satellite method for GHI estimation, which deal with the irradiance attenuation caused by atmospheric compositions (e.g., aerosol, water vapor, and ozone) and the cloud's effect separately [48]. As presented in Fig. 1.3, The first step is to estimate the clear-sky irradiance using a clear-sky model, and the second step is to determine the cloud index (CI) from a set of satellite images in a defined period to account for the cloud attenuation effect [8, 48]. Heliosat method series [38, 57, 58] are examples of semi-empirical satellite models with a long history that offers easy and fast implementation and operation [51], which can be traced back to the contribution of Cano et al. [59]. As an essential component in semi-empirical satellite method, various clear-sky models have been used for clear-sky GHI estimation, for instance, the Ineichen-Perez model [31] in the operational SUNY model [37], the McClear model in the work of Jia et al. [60], and the REST2 [33] model in Solcast [61]. There are also different methods and strategies proposed to determine the GHI based on clear-sky index (CSI) and CI in the literature [37, 48, 62]. As mentioned, the recent advancements in modern geostationary satellites provide much better data in both

temporal and spatial resolutions, which provides new insights for solar resource assessment. However, the empirical regression relationship and CI derivation strategies might not be suitable for modern satellites as the spectral bands and temporospatial resolutions are much improved.

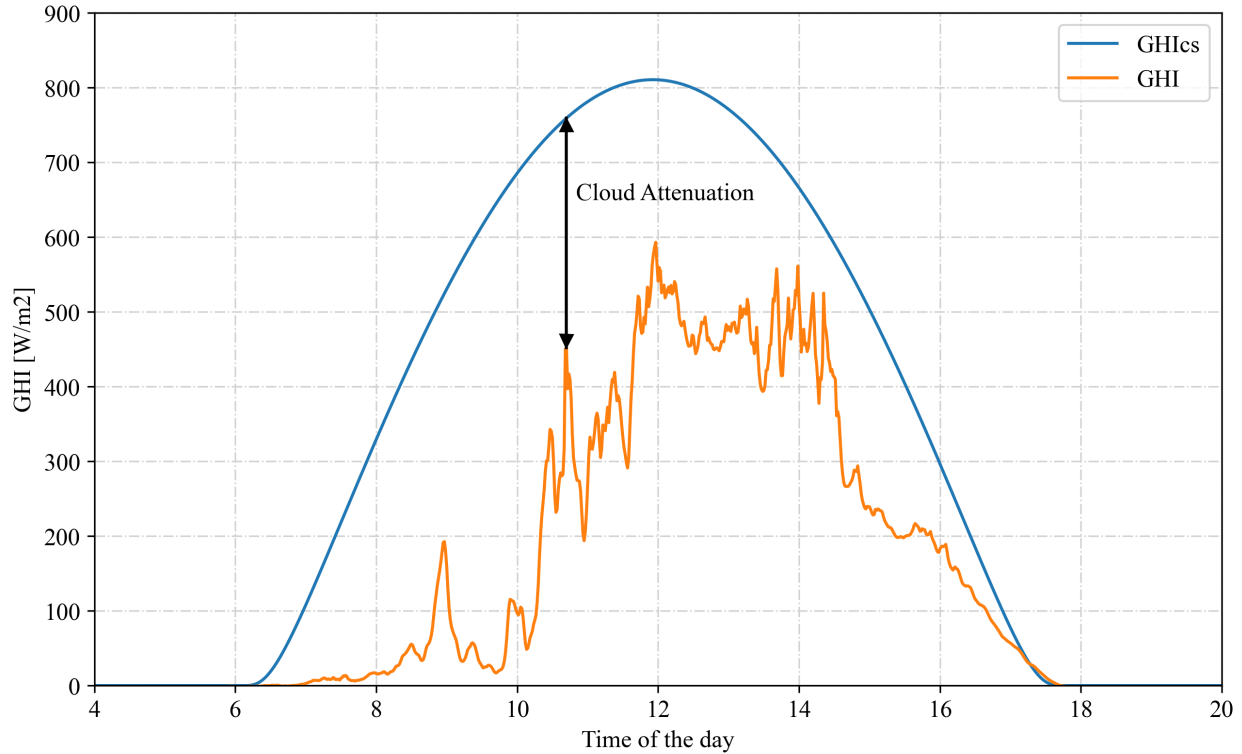


Figure 1.3: GHI is estimated by subtracting cloud attenuation from a clear-sky background (GHI_{cs}) [8].

1.4.2 Methods of solar forecasting

Solar forecasting aims to predict the solar irradiance or power output in a future time, which can support the system management and power scheduling [21]. The spatial and temporal resolution of different solar forecasting methods are shown in Fig. 1.4 [21]. Based on the forecasting time horizons, solar forecasting methods can be classified as intra-hour, intra-day, and day-ahead forecasting [21]. Intra-hour forecasting is in the time scale of minutes (usually less than one hour), which mainly relies on the local sensed parameters, e.g., solar irradiance, meteorological data, and sky images [14]. Intra-day forecasting focuses on the time horizon of hours, which is usually in the same day. Forecasting methods based on the satellite are typically suitable for intra-day forecasting [21], since modern satellite with better remotely sensed data brings new insights. Numerical weather prediction (NWP) can also give intra-day forecasts but with inferior performance [14]. Day-ahead forecasting usually provides predictions for day or even days ahead, where

the NPW is likely to yield better results [21]. Data driven methods are more based on historical observations [63, 64, 65], therefore, a huge amount of data is needed. While hybrid methods are combinations of two or more independent methods, which might also require a lot of historical data [14]. Both data-driven and hybrid methods can be applied for intra-hour, intra-day, and day-ahead forecasting as long as there are data available with required temporal resolutions.

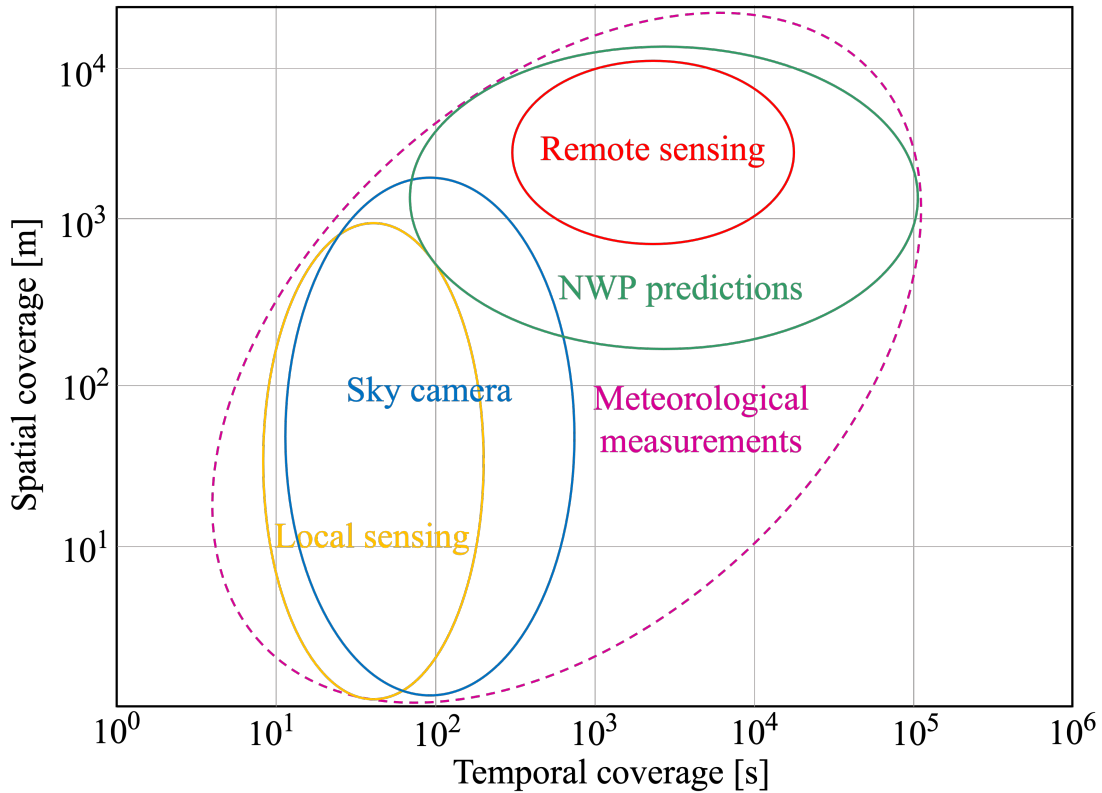


Figure 1.4: The classification of solar forecasting methods, modified based on Fig.3 in [21].

Since long-term and complete solar irradiance data is rarely available [12], the applications of data-driven and local sensed forecasting methods are greatly restricted. However, data and products from geostationary satellites are available worldwide which is an essential part in solar forecasting over a large area. In semi-empirical satellite forecasting models, the visible Earth radiance seen by the satellite is approximately proportional to cloud opacity and cosine of the solar-zenith angle [8], the GHI is derived based on the clear-sky irradiance and cloud attenuation (see Fig. 1.3), where clear-sky irradiance is based on the clear-sky model and cloud attenuation is determined by the satellite information referred as CI [66, 67]. The satellite count is used to define the dynamic range (upper and lower bounds) for each pixel at a given location, period, and CI, then the GHI is calculated based on CI. Therefore, the key part in forecasting is to estimate the CI

in a future time [55].

Cloud motion analysis based on sequential satellite images is widely used to generate cloud motion vectors (CMVs) that can be used to predict future cloud locations and then estimate the cloud cover [68, 69]. Currently, the used methods for cloud motion analysis include phase correlation, block matching, and optical flow [70]. These methods are originally used in computer vision, and tailored in cloud motion analysis based on several assumptions, for instance, the pixel intensities in both images are constant, the wind fields are smooth at the cloud height, and the formation or dissipation of clouds are not considered [8]. Phase correlation is first introduced by Kuglin et al. [71], which is to find the transition between two images based on the Fourier shift theorem. Block matching compares the neighbouring rectangular areas to detect the advection patterns of cloud between the two subsequent images by minimizing the mean squared pixel differences [8]. Optical flow is a general image processing to detect the object motions with vectors showing the movements of points, it uses image gradients and assumes the neighbouring points have similar motions [72].

Due to the complicated dynamics in the atmosphere since clouds not only move, but also change the shape, form and even disappear, it is difficult to model the cloud movements. Therefore, there are many assumptions and simplifications made in cloud motion analysis and forecast, e.g., the cloud height is assumed constant, the velocity field of clouds is persistent in the forecast of next image. Actually, the CMVs are a two-dimensional (x, y) vectors with the z axis neglected, which implicitly assumes that the clouds are at a plane with same altitude. This assumption provides the baselines for the cloud motion analysis algorithms without considering the vertical cloud motions and complex convection processes [70]. Despite these assumptions and simplifications, cloud motion analysis and forecast based on consecutive satellite images have been proved to be a solution for intra-day (1-5 h ahead) solar irradiance forecasting [70]. However, in most of the cloud advection forecast models, cloud patterns and wind fields are assumed persistent over the forecast horizon [70]. Therefore, the changes in wind speed and direction are not considered and thus can lead to large uncertainties in a longer forecast timescale. It would be of interest to consider the change of the velocity field of clouds in the forecast of next image, which could improve the forecasting accuracy.

In physical-based forecast models, radiative transfer simulation is applied through different layers in the atmosphere by taking the advantage of modern satellite remote sensing [73, 74, 75]. Essential parameters like cloud types and heights, AOD, and water vapor can be derived from the satellite measurements. Once the properties of cloud, aerosol, water vapor as well as other minor atmospheric compositions are determined, the RTM is applied to estimate the ground-level solar radiation. NWP is the ultimate physical-based forecasting tool, all the physical processes along with their evolution are interpreted by physical models [21]. NWP models could simulate the atmosphere with high-accuracy given correct initial state information and

adequate computational resources. However, errors in satellite observations, insufficient information for initial conditions and the complexity of the RTMs make the accuracy of physical-based methods unsatisfactory [8]. On the other hand, the forecasts of meteorological parameters, such as ambient temperature and humidity, are much more accurate [21], it would be beneficial to develop solar forecasting models using NWP products that have relatively higher accuracy.

1.5 Machine learning in solar irradiance modeling

Machine learning has been widely applied in solar resource assessment and forecasting. This section is to provide some fundamentals of the machine learning methods used in this study. Linear regression (LR), random forest (RF), and multiple layer perception (MLP) are applied as the representatives of classical machine learning algorithms.

LR is one of the fundamental statistical methods in machine learning that models the relationship between input and output variables by linear functions. The mathematical expression of LR is:

$$y = w \cdot X + w_0 + e \quad (1.7)$$

where y is the output variable, X is the input vector, w is the weight vector, w_0 is the intercept term, and e is the error term. The parameters of w and w_0 can be optimized by minimizing a loss function. Although LR is easy to implement, it might not be applicable for complex problems [76].

RF is in the category of ensemble learning methods that combines multiple decision trees to solve a particular task. RF can reduce overfitting in decision trees and help to improve the accuracy by capturing complex nonlinear relationships between input features and the output [77]. The final prediction is the average result of all the individual decision trees:

$$y = \frac{1}{M} \sum_m^M f_m(X) \quad (1.8)$$

where y is the target, X is the input vector, M is the total number of trees in the ensemble, f_m is the function of the m^{th} decision tree. Although RF has some advantages over a single decision tree, it requires more computational resources and time in training.

MLP is a type of artificial neural networks that consists of at least three layers (an input layer, a hidden layer, and an output layer as shown in Fig. 1.5). The node in the hidden and output layers is called neuron that employs a nonlinear activation functions, such as ReLU, Sigmoid, and Hyperbolic tangent functions as shown in Fig. 1.6. Neurons in MLP are interconnected by wights and biases that are updated in the learning

process by minimizing the difference between the predicted output and observations. Backpropagation and gradient descent are the techniques used to optimize the weights of neurons [76].

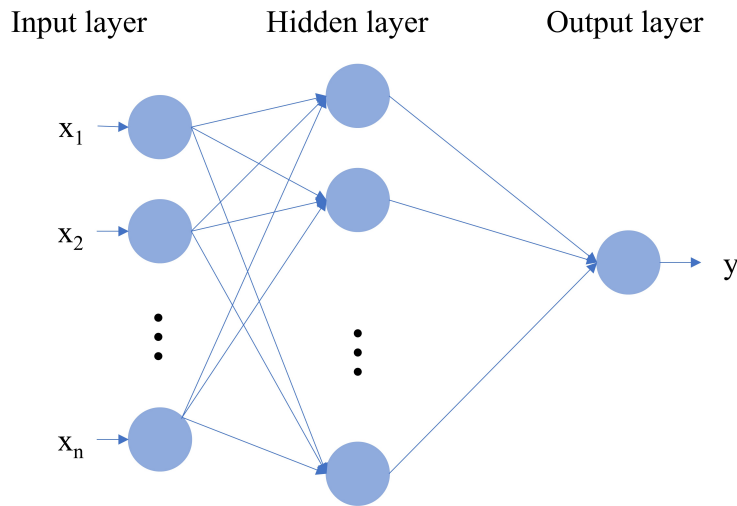


Figure 1.5: The basic structure of MLP with an input layer, a hidden layer, and an output layer.

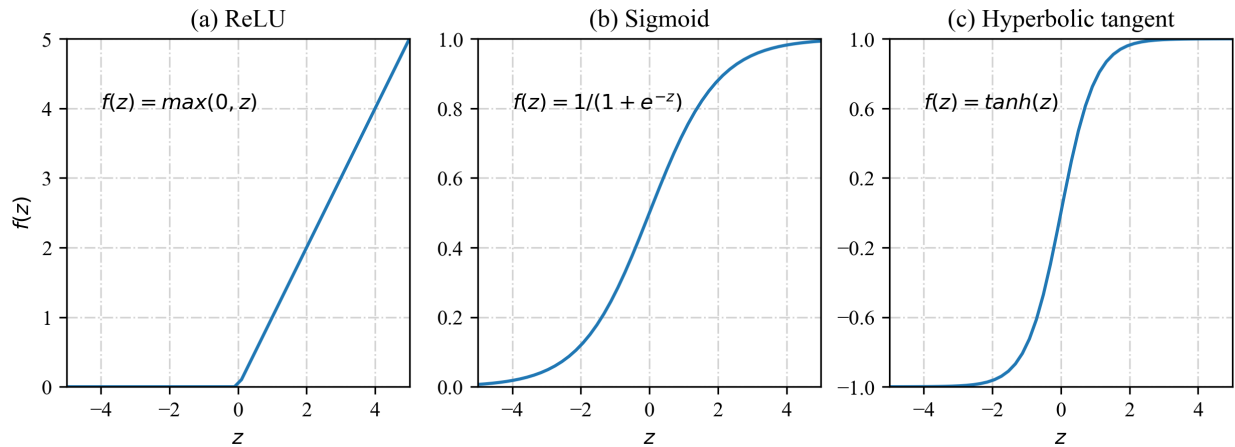


Figure 1.6: Some examples of activation functions. (a) ReLU. (b) Sigmoid. (c) Hyperbolic tangent.

Since the information from geostationary satellite is in a 2-dimensional form, some deep learning algorithms such as convolutional neural networks (CNNs) are also applied to extract features from satellite images. CNNs are feed-forward neural networks that can efficiently capture the features with reduced amount of parameters by extracting properties of input images. A typical CNN has three types of layers: the convolutional layer, the pooling layer and the fully connected layer as shown in Fig. 1.7. As the main block of a CNN, convolutional layer applies numerous filters to extract features of input images such as edges, corners, and complex shapes [78]. An activation function (e.g., ReLU in Fig. 1.6) is usually applied

to introduce non-linearity on the output feature maps. The pooling layer provides a form of down-sampling to reduce the spatial size gradually and help to control overfitting [78]. While the fully connected layer is applied to learn the representations between the extracted input features and outputs.

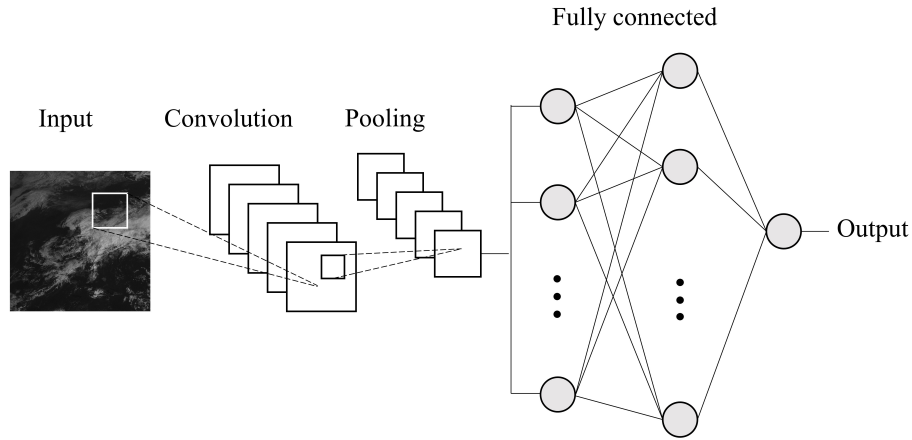


Figure 1.7: The basic structure of CNN with the input, convolution, pooling, fully connected and output layers.

1.6 Research gap and objectives

Considering the aggressive development of solar energy projects, the variability and intermittence of solar irradiance, and the limited availability of ground-level irradiance data, it is necessary to develop solar irradiance modeling and forecasting methods to facilitate the integration of solar energy systems. Although there are many advanced clear-sky models, databases providing solar irradiance under clear-sky and satellite-derived irradiance components, and various solar forecasting models developed in the solar community, there are still some challenges in supporting the design and operation of solar energy projects.

As mentioned, ground-based solar irradiance measurements are the most reliable data source for solar energy applications, but complete and long-term historical irradiance data is not available at most locations due to the technical and financial constraints [12], the geostationary satellites can therefore provide support in solar resource assessment. Meanwhile, it has been proved that satellite-derived irradiance data can be used for the development of solar forecasting models [12]. Since the new-generation geostationary satellites show much improvement in remote sensing, it is expected to have better reanalyses atmospheric products [13] for solar resourcing and forecasting applications. Furthermore, satellite based solar forecasting is usually classified as methods for intra-day irradiance forecasts. With the temporal resolution improved to 5-minute,

geostationary satellite may also be capable of supporting the intra-hour solar forecasting applications. In this regard, the present project aims to help with the design and operation of solar energy projects by providing more accurate irradiance estimations and forecasts with remote sensing and machine learning methods.

The objectives of this thesis are to 1) develop methods for improved spatio-temporal solar resource assessment with easy and fast implementation using the recent advancements of geostationary satellites for supporting solar energy projects; 2) develop more accurate solar irradiance forecasting models using remote sensing and deep learning techniques to support the operation of solar energy systems.

1.7 Dissertation structure

In Chapter 2, an improved method is proposed for turbidity estimation using common meteorological measurements. The improved method to estimate turbidity shows comparable performance with physical models in estimating clear-sky irradiance but with less complexity. Since the clear-sky model is an indispensable component in solar resource assessment and forecasting, this paves the way in obtaining improved clear-sky irradiance estimation.

As mentioned, the clear-sky model is an essential part in solar irradiance modeling, Chapter 3 evaluates and compares four different clear-sky models (two physical, one empirical models, and the improved empirical one proposed in Chapter 2) in solar irradiance estimation using a semi-empirical satellite method. The improved method can provide irradiance estimations that have a comparable performance with the physical model. Moreover, its applicability can be expanded to other locations covered by geostationary satellites for solar energy projects.

The method for turbidity and clear-sky irradiance estimation proposed in Chapter 2 shows potential in supporting solar resourcing and forecasting applications. However, one limitation that hinders the wider applicability is the need of on-site irradiance measurements. To address this limitation, a transferable turbidity estimation method for estimating clear-sky irradiance is proposed in Chapter 4. The transferred method shows a comparable performance with physical models but with less complexity, which provides an alternative in estimating clear-sky solar irradiance.

It is found in Chapter 2 that both semi-empirical and physical methods show large uncertainties in irradiance estimation under cloudy conditions. To better account for the cloud effect on ground-level solar radiation, Chapter 5 presents the application of deep learning and remote sensing in solar resource assessment. Multiple selected spectral satellite images are used to extract the cloud information and estimate global and direct solar irradiance by deep learning. The improved performance over the physical method in

solar irradiance estimation can provide more accurate information for designing solar energy projects.

Based on the improved performance in solar resource assessment presented in Chapter 5, an solar forecasting model using satellite-derived spatiotemporal irradiance with improved accuracy is proposed in Chapter 6. The proposed method can provide more accurate irradiance forecasts, which is beneficial to the operation and management of solar energy projects.

Chapter 7 briefly summarizes this thesis and provides recommendations for future studies.

Chapter 2

Improved turbidity estimation from local meteorological data for solar resourcing and forecasting applications

2.1 Introduction

Solar radiation reaching the Earth surface is either absorbed or scattered by the atmosphere based on the types and concentrations of the participating constituents and their radiative optical properties [8]. For solar energy conversion systems such as photovoltaics (PV) and concentrating solar power (CSP), ground level irradiance assessment and forecasting are crucial for their design and operation [11, 14, 79, 80]. The attenuation of ground level solar irradiance is mainly caused by clouds, aerosols, water vapor, carbon dioxide and ozone [26], where clouds are the major modulator followed by aerosols and water vapor. However, the high temporal and spatial variations of the three major modulators as well as sensing difficulties of their concentrations [81] have posed considerable challenges for solar resourcing and forecasting applications. Therefore, a variety of clear-sky models have been developed over the years to estimate time varying ground level global horizontal irradiance (GHI), direct normal irradiance (DNI) and diffuse horizontal irradiance (DHI) if there were no clouds in the sky. The clear-sky models have been used extensively to quantify the effects of local aerosols and water vapor, as well as to facilitate cloud identification and analysis for forecasting applications [8, 9, 10, 35].

As summarized in [35, 82], clear-sky models with different complexity and performance can be broadly classified into two main groups: physical models and empirical models. Physical models apply radiative

transfer models (RTMs) to estimate the irradiance attenuation effect of atmospheric constituents, and the ground level solar irradiance can be obtained through integration of the attenuation caused by different atmospheric components [35]. Empirical models are based on simplified parameterizations of the attenuation processes [35], which estimate the clear-sky irradiance using some atmospheric parameters, such as the aerosol optical depth (AOD) and precipitable water in simplified Solis model [83], and the Linke turbidity (T_L) in Ineichen-Perez model [31].

Physical models perform detailed analysis of the atmospheric attenuation processes, which generally lead to higher accuracy [36, 82]. However, they require many inputs about local atmospheric conditions, some of them are not widely available. For instance, the REST2 model [33] has been verified as one of the most accurate clear-sky models [36, 82], but the required information about the atmospheric constituents, such as AOD at 550 nm, column amount of ozone, nitrogen dioxide and precipitable water are difficult to obtain for most locations [36, 54]. Yang [36] discussed the choice of clear-sky models in solar forecasting applications from the perspectives of accessibility, forecast performance and statistical properties. It is found that high-fidelity physical models like REST2 are not frequently used for solar forecasting due to its complexity, and no evidence suggests that physical models can lead to more accurate forecast results when compared with empirical models [36].

As a member of the empirical model family, the Ineichen-Perez model is extensively used in solar forecasting due to its simplicity [36]. The main input of the Ineichen-Perez model is the T_L factor, which is defined as the number of clean and dry atmospheres that produce the same attenuation equivalent to the real atmosphere [30]. The T_L factor quantifies the attenuation of aerosols and water vapor [84], which typically varies between 1 and 10 [35]. The T_L factor is available worldwide as monthly climatology value from the SoDa database [40]. In PVLIB [39], linear interpolations of the monthly values are applied to build daily T_L time series for each location when using the Ineichen-Perez clear-sky model.

The T_L factor is also directly used in other clear-sky models [35, 42]. However, the invariant T_L factor based on the monthly climatology value and its linear interpolation cannot account for the short-term [41] and long-term variations [85] of atmospheric aerosols and water vapor concentrations, resulting in unsatisfying estimation of clear-sky irradiance [34]. The discrepancy of clear-sky irradiance obtained from T_L based clear-sky models and from measurements are observed in the studies by Moldovan et al. [42] and Polo et al. [41], and also noticeable when comparing the clear-sky solar irradiance measurements from Dessert Rock, Nevada (DRA) with PVLIB clear-sky model output (see Fig. 2.1).

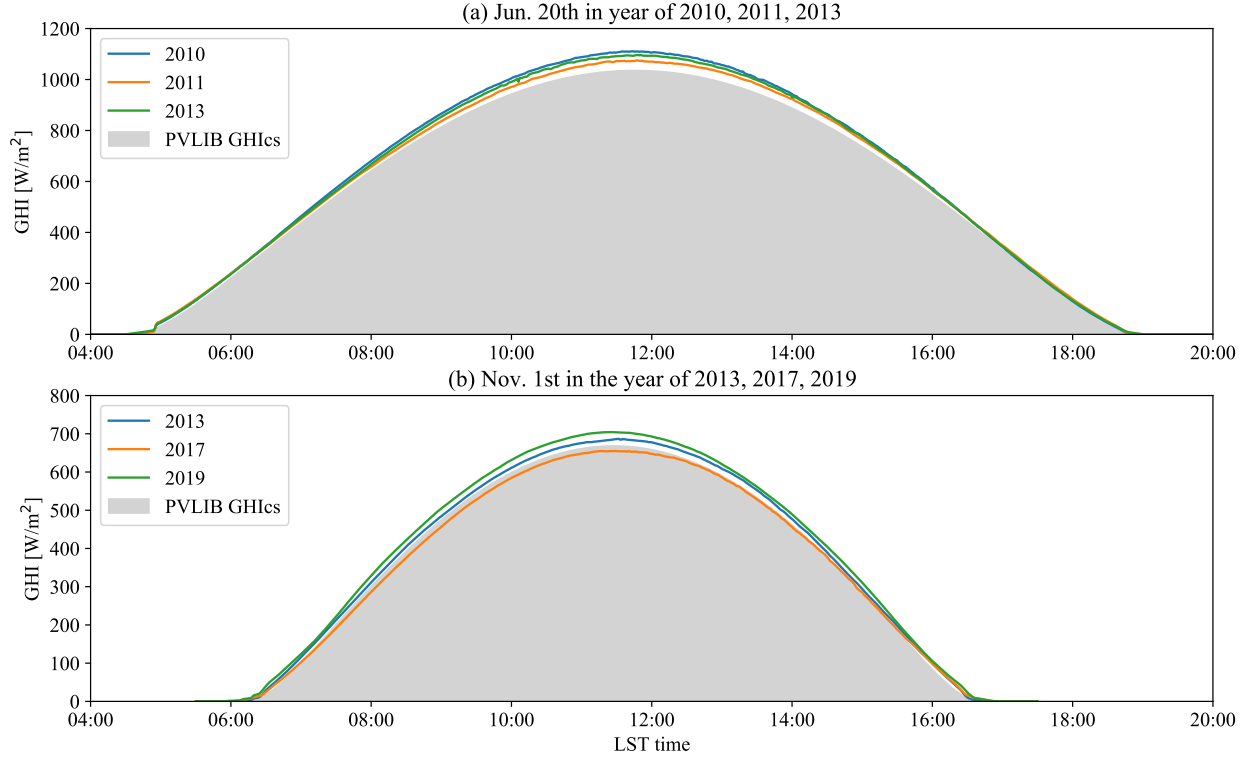


Figure 2.1: Comparison of measured clear-sky GHI (GHIs) with PVLIB GHIs of the same day in two different years. PVLIB uses the T_L factor from its look-up table, which is based on constant monthly climatology value. The PVLIB GHIs remains the same on the same day of different years, while the measured GHIs are not, indicating T_L factor also varies on a long term (i.e., yearly) basis.

Therefore, some studies were conducted to estimate T_L factor by different means with the aim to investigate its variations or to improve the estimation accuracy. Chaâbane et al. [81] adopted pyrheliometric measurements for the calculation of T_L factor in Tunisia during three summer months, where diurnal and monthly variations of T_L factor are observed. Polo et al. [41] estimated the daily T_L factor for clear days by using global irradiance measurements at solar noon and monthly mean T_L values. Using the estimated T_L to recalculate clear-sky solar irradiance results in a reduced root mean squared deviation (RMSD) when compared with using monthly mean values. The relative RMSD (rRMSD) decreases from 17.1% to 14.2% for the dataset of Baseline Surface Radiation Network (BSRN). For the dataset from Spanish Meteorological Agency (AEMet), the rRMSD reduces from 24.4% to 16.8%. Hove and Manyumbu [86] calculated the T_L factor based on daily GHIs and ESRA clear-sky model [87], which typically has a lower value than the monthly mean. Inman et al. [88] reported a method for daily average T_L estimation using broadband DNI measurements under cloudless skies, and then applied the estimated T_L in DNI forecasting during cloud-

free periods under the assumption of a persistence of daily averaged T_L within the forecasting horizon. The relative RMSE (rRMSE) and relative mean bias error (rMBE) are smaller than 5% for both historical and forecasted values, which are much smaller than the error range (10-20%) of SoDa monthly means. Behar et al. [89] used ambient temperature and relative humidity to estimate T_L and solar irradiance via the estimated optical thickness of clean-dry atmosphere, water vapor and aerosol. The T_L estimation has a rRMSE of 10.22% and a rMBE of 1.31%, the rRMSE and rMBE of corresponding DNI estimate are 5.21% and 0.91%, respectively. Moldovan et al. [42] applied time dependent interpolation polynomials instead of a constant daily T_L factor to improve the clear-sky model. Two different interpolation polynomials are obtained for the T_L factor in warm and cold seasons, respectively. The result shows that the relative error is reduced from 8.12% to 4% in the warm season and from 5.02% to 4.15% in the cold season.

The derivation of T_L based on irradiance and meteorological measurements offers a simpler way to estimate T_L without the detailed information about aerosol and water vapor contents. However, the methods summarized above still have some shortcomings to overcome. For example, the clear-sky irradiance measurements are not available in a cloudy day, and only using the GHIs at the solar noon presented by Polo et al. [41] may lead to errors in estimating the clear-sky irradiance in other periods such as solar mornings, evenings and cloudy days. The method also cannot be used for locations without irradiance measurements. For the method presented by Behar et al. [89], using ambient temperature and relative humidity to estimate perceptible water and AOD may result in error accumulations in estimating T_L . For the study by Modlovan et al. [42], the T_L interpolation polynomials for warm and cold seasons are not capable of accounting for year-to-year T_L variation as shown in Fig. 2.1.

Therefore, we propose a new T_L estimation method to estimate high-fidelity T_L with the consideration of its short-term and long-term variations, and without the data dependence on local real-time irradiance measurements. The T_L factor is proposed to be estimated using local meteorological data by machine learning (ML) algorithms. In the following sections, data processing and proposed methodology are presented in Section 2.2. Section 2.3 presents the results and discussions of T_L and corresponding clear-sky irradiance estimations. The key findings and recommendations are summarized in Section 2.4.

2.2 Methodology of turbidity estimation

This section presents the data and methods used for T_L derivation and estimation. The T_L derivation is performed by applying Ineichen-Perez clear-sky model (PVLIB) reversely, i.e., taking the 1-minute averaged GHIs as the input to compute the ‘ground truth’ T_L . Then the derived minute-wise T_L time series is

further averaged on the basis of daily, hourly and 5-minute as the ML model training targets. The input meteorological data is also averaged with the same time basis for model training, tuning and testing. Finally, the trained model is applied to estimate the T_L for GHICs estimation. The flowchart of the method for estimating the T_L and clear-sky irradiance is shown in Fig. 2.2. The T_L derivation and estimation can also be applied to clear-sky DNI (DNICs), which will be discussed in Section 2.3.3.

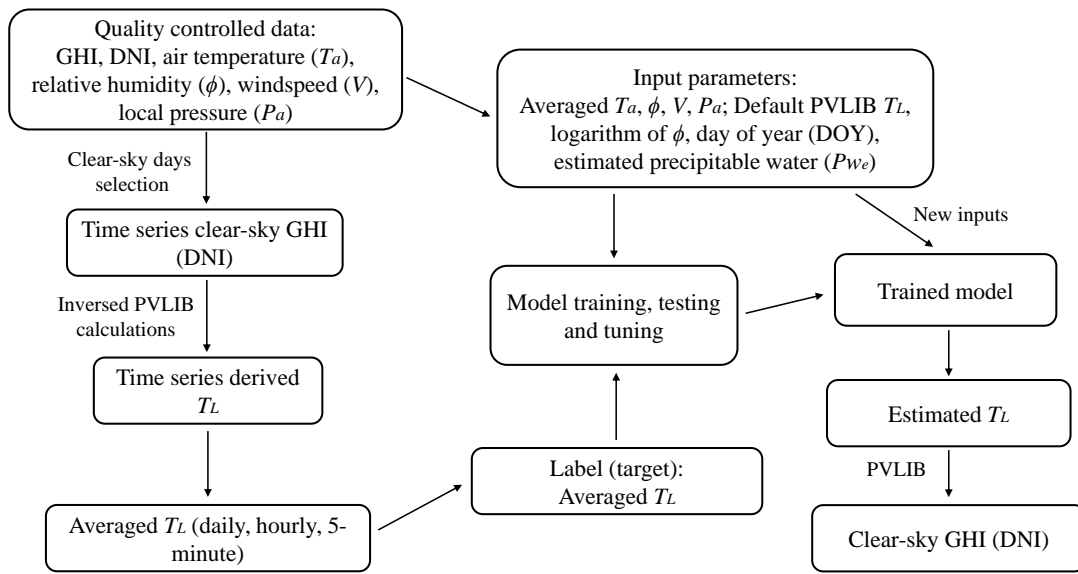


Figure 2.2: An overview of the method to derive and estimate T_L . The model for estimating the daily, hourly and 5-minute T_L is trained independently, and the input meteorological data is also averaged on the same time basis.

2.2.1 Data selection

The data used in this work is from DRA, one of the Surface Radiation Budget Network (SURFRAD) stations [29]. DRA has a latitude of 36.62373°N, a longitude of 116.01947°W, an elevation of 1007 m, and a time zone of UTC-8 (8 hours difference than coordinated universal time (UTC)). High resolution solar irradiance and meteorological data collected from year 2000 to 2020 are used in this work. Among the diverse variables in the comprehensive dataset, measurements of the downwelling global solar irradiance (GHI), direct normal irradiance (DNI), ambient air temperature (T_a), relative humidity (ϕ), wind speed (V) and local atmospheric pressure (P_a) are selected to build and test the proposed T_L estimation model. The selected data has high temporal resolutions (3-minute averaged from year 2001 to 2008, and 1-minute averaged from year 2009 to 2020) and its quality is carefully controlled.

DRA is chosen among the seven SURFRAD stations due to its high occurrence of cloudless days, which

could provide adequate learning samples for the development and validation of the proposed T_L estimation model. The same methodology can be applied to other locations if sufficient data is given.

2.2.2 Selection of clear-sky days

The clear-sky irradiance is defined as the incident radiation at the Earth’s surface under the conditions that would occur under a perfect “cloudless sky” [90]. The presence of clouds in the sky, especially when clouds obscure the Sun disc, will greatly affect the surface solar radiation, resulting in irradiance fluctuations. Since T_L is a factor that quantifies the attenuation of solar irradiance by atmospheric constituents (especially water vapor and aerosols) under cloud-free conditions, we only select clear-sky days for model development and validation.

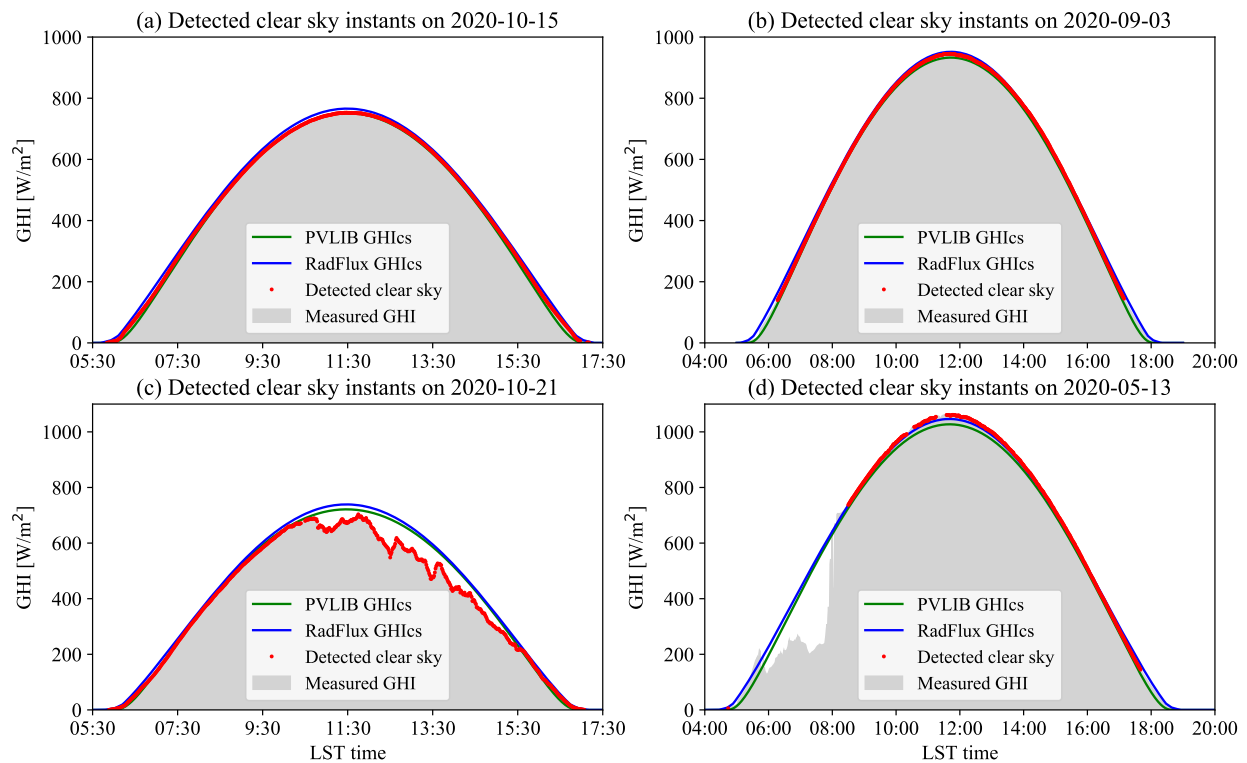


Figure 2.3: Examples of clear-sky days selection in DRA. Measured GHI data is from SURFRAD, GHIs are computed by both RadFlux and PVLIB. The clear-sky labels are from RadFlux. (a) A detected full clear-sky day. (b) A detected clear-sky day with high solar zenith periods not labeled. (c) A wrongly labeled clear-sky day which is removed by manual check. (d) A typical partly cloudy day.

The clear-sky days are selected following the approach developed by Long and his collaborators [91, 92, 93], and the clear-sky labels provided by RadFlux algorithm [91, 93] are publicly available on the

website of SURFRAD network. Specifically, the days will be labelled as "clear-sky day" if most of the time instants within the day are "clear" as detected by solar shortwave irradiance measurements ($\lambda < 4\mu m$), or detected by atmospheric longwave irradiance measurements ($\lambda > 4\mu m$). The shortwave clear-sky detection algorithm has a 160° field of view, so the clear-sky instants with high solar zenith angles could not be detected [92]. During the daytime, the presence of clouds is more noticeable in the shortwave spectrum when compared with the longwave spectrum [93]. Therefore, most of the clear-sky instants detected by the longwave RadFlux algorithm [93] are in the nighttime. To verify the RadFlux clear-sky labels, we performed an additional manual check by comparing the measured GHI, clear-sky GHI estimated by RadFlux [94] and Ineichen–Perez clear-sky model from PVLIB [39]. Then, clear-sky detection for periods with high solar zenith angles are performed, and wrongly labeled clear-sky days are removed, as demonstrated in Fig. 2.3. Our training and testing datasets only contain the clear-sky days that pass both the RadFlux and manual checks (examples are presented in Fig. 2.3).

2.2.3 Derivation of ‘ground truth’ turbidity for model training

We adapt the methodology documented in PVLIB [39] to derive ‘ground truth’ T_L factor for model development. At each clear-sky time instance, the ‘ground truth’ T_L factor is derived from measured GHIs values by inverting the following equation provided in PVLIB (proposed in [31]),

$$\text{GHI}_{\text{cs}} = c_1 \cdot I_0 \cdot \cos(\theta) \cdot \exp(-c_2 \cdot AM \cdot (f_1 + f_2 \cdot (T_L - 1))) \quad (2.1)$$

Then the derived T_L based on GHIs measurement is,

$$T_L = \left[\ln \left(\frac{\text{GHI}_{\text{cs}}}{c_1 \cdot I_0 \cdot \cos(\theta)} \right) / (-c_2 \cdot AM) - f_1 \right] / f_2 + 1 \quad (2.2)$$

T_L could also be derived from DNIs by inverting the following equations from PVLIB,

$$B_1 = I_0 \cdot b \cdot \exp(-0.09 \cdot AM \cdot (T_L - 1)) \quad (2.3)$$

$$B_2 = \text{GHI}_{\text{cs}} \cdot \left[\left(1 - \frac{(0.1 - 0.2 \cdot \exp(-T_L))}{(0.1 + 0.882/f_1)} \right) / \cos(\theta) \right] \quad (2.4)$$

$$\text{DNI}_{\text{cs}} = \text{Minimum}(B_1, B_2) \quad (2.5)$$

Then the derived T_L based on DNIs measurements is,

$$T_L = \ln \left(\frac{\text{DNI}_{\text{cs}}}{I_0 \cdot b} \right) / (-0.09 \cdot AM) + 1, (\text{when } B_1 < B_2) \quad (2.6)$$

$$T_L = -\ln \left[\left(0.1 - \left(1 - \frac{\text{DNI}_{\text{cs}}}{\text{GHI}_{\text{cs}}} \cdot \cos(\theta) \right) \cdot (0.1 + 0.882/f_1) \right) / 0.2 \right], (\text{when } B_1 > B_2) \quad (2.7)$$

with:

$$AM = \left(\frac{1}{\cos(\theta) + 0.50572 \cdot (6.07995 + (90 - \theta)^{-1.6364})} \right) \cdot \frac{P_a}{101325} \quad (2.8)$$

$$c_1 = 5.09 \cdot 10^{-5} \cdot h + 0.868 \quad (2.9)$$

$$c_2 = 3.92 \cdot 10^{-5} \cdot h + 0.0387 \quad (2.10)$$

$$f_1 = \exp(-h/8000) \quad (2.11)$$

$$f_2 = \exp(-h/1250) \quad (2.12)$$

$$b = 0.664 + 0.163/f_1 \quad (2.13)$$

where GHI_{cs} [W m^{-2}] is the measured clear-sky GHI. DNI_{cs} [W m^{-2}] is the measured clear-sky DNI. B_1 [W m^{-2}] is the normal beam clear-sky radiation (B_2 is the empirical correction for low T_L conditions). c_1 , c_2 , f_1 , f_2 , b are altitude-dependant coefficients, I_0 [W m^{-2}] is the solar constant, θ [$^\circ$] represents the solar zenith angle, AM is the absolute airmass, T_L is the Linke Turbidity factor, P_a [Pa] is the local atmospheric pressure, and h [m] is local altitude.

Fig. 2.4 (a) illustrates the GHICs-derived T_L in a randomly selected clear-sky day (one can find similar results in any other clear-sky days). Unlike the T_L factor used in PVLIB default calculations, the derived T_L factor is not a constant but varies during the day. Note that for periods with large solar zenith angle (greater than 85°), the derived T_L has large variations and unrealistic values (less than 1.0 and even negative), which are resulted from the applicable limitations of Eq. (2.2). Therefore, in the following sections when derived T_L time series are temporally averaged, the instances from the period when the solar zenith is greater than 85° are not included. Fig. 2.4 (b) shows the T_L time series averaged on different time basis, where the daily averaged T_L is much lower than the value used in PVLIB. The asymmetry of estimated T_L with respect to the zenith angle is observed in Fig. 2.4 (b), especially during morning and evening periods. This is possibly due to the high airmass effect, where the small difference in measured clear-sky irradiance will result in large discrepancy in the derived T_L values. In addition, the profile of clear-sky irradiance is not perfectly symmetric as shown in Fig. 2.4 (b) that the measured GHICs in the morning (e.g., 6:00-8:00) is smaller than the ones near the evening (e.g., 16:00-18:00). Meanwhile, the water vapor content in the atmosphere is usually higher in the morning, which results in higher T_L values and thus lower GHICs.

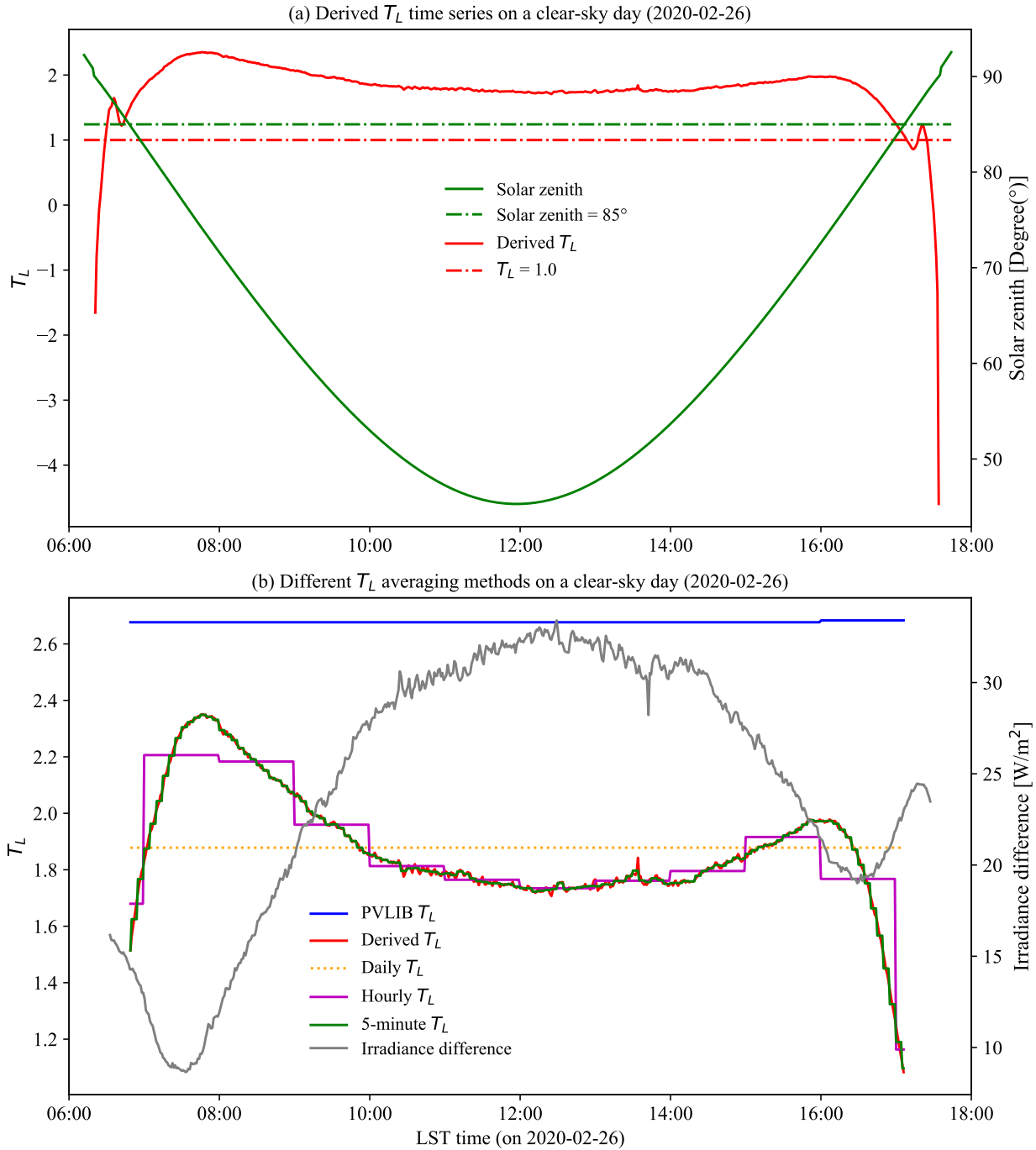


Figure 2.4: Derived T_L time series with different averaging modes for a clear-sky day with respect to local standard time (LST). (a) Derived T_L time series on 2020-02-26. The derived T_L shows high variations and unrealistic values in the periods with high solar zenith angles. (b) Averaged T_L on different time basis (5-minute, hourly, and daily) and the irradiance difference between measured GHICs and PVLIB GHICs during the day.

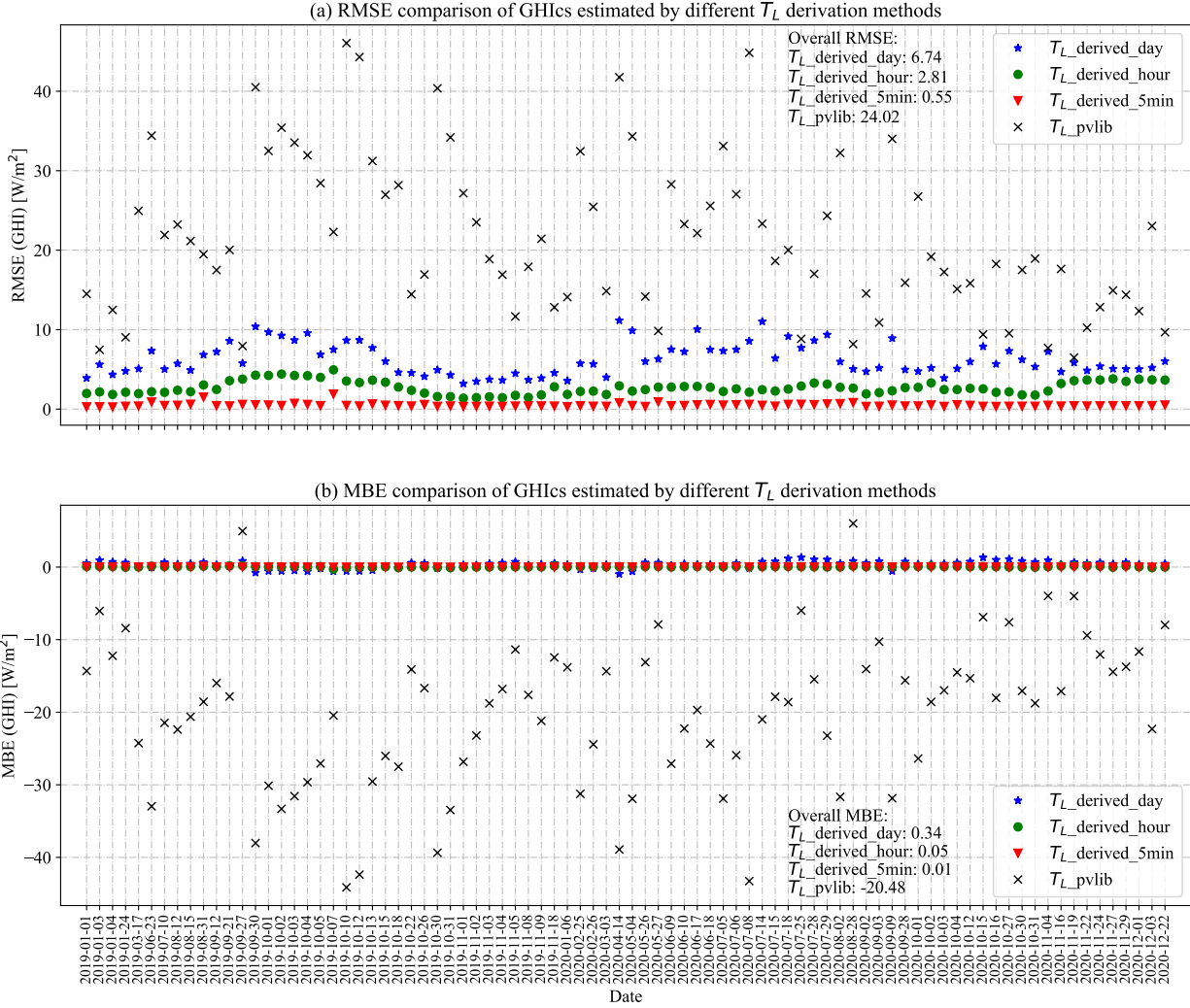


Figure 2.5: Comparison of GHICs estimation using different T_L averaging modes for the clear-sky days in year 2019 and 2020. (a) Daily RMSE of 1-minute averaged GHICs estimation. (b) Daily MBE of 1-minute averaged GHICs estimation. All the derived T_L regardless of averaging mode produce more accurate GHICs than PVLIB.

The averaged T_L derivations are then used to recalculate the 1-minute averaged GHICs using PVLIB, which shows noticeable improvement in estimating GHICs, as shown in Fig. 2.5. In the clear-sky days of 2019 and 2020 (a total of 84 days are identified as clear), using PVLIB T_L generally underestimates the GHICs with a mean bias error (MBE) of -20.48 W m^{-2} and a root mean square error (RMSE) of 24.02 W m^{-2} , when computed using 1-minute averaged data when solar zenith angle is smaller than 85° . Using derived daily mean T_L yields a GHICs estimation with overall MBE of 0.34 W m^{-2} and RMSE of 6.74 W m^{-2} , a 98.3% reduction in MBE and 71.9% decrease in RMSE. As the time resolution increases, the

recalculated results become better as expected. Hourly mean T_L produces a RMSE of 2.81 W m^{-2} and a MBE of 0.05 W m^{-2} for GHIs estimation. The 5-minute averaged T_L gives an estimation of GHIs with the lowest MBE of 0.01 W m^{-2} and lowest RMSE of 0.55 W m^{-2} . In general, using daily mean T_L can successfully correct the bias in estimating GHIs and reduce RMSE by 71.9%. Using temporally finer hourly and 5-minute averaged T_L can further reduce the RMSE in GHIs estimations, but they also substantially increased the size of training data in the following ML based T_L estimation models.

2.2.4 Turbidity estimation from local meteorological data

The previous section demonstrates that improving T_L estimations could substantially improve the accuracy of GHIs estimations. However, the T_L is derived from GHIs measurements, which is not known as a priori in real-time applications. Therefore, we propose to use ML methods with widely available meteorological measurements to estimate local T_L .

We use three independent ML models for daily, hourly and 5-minute averaged T_L factors. The label (target) is the averaged T_L derivations from Section 2.2.3, and the input parameters are: the default PVLIB T_L , ambient air temperature T_a , relative humidity ϕ (and its logarithm), wind speed V , atmospheric pressure P_a , day of year (DOY), and estimated precipitable water Pw_e . The meteorological time series (i.e., air temperature, relative humidity, wind speed, pressure) are averaged on the same time basis as the T_L . The PVLIB T_L is adapted to the corresponding time resolution as well. The logarithm of relative humidity is based on its averaged value, and the estimated precipitable water is calculated from the averaged temperature and the averaged relative humidity using the empirical model proposed by Gueymard [95, 96] with the following equations:

$$Pw_e = 0.1 \cdot H_v \cdot \rho_v \quad (2.14)$$

$$H_v = 0.4976 + \frac{1.5265 \cdot T_a}{273.15} + \exp\left(\frac{13.6897 \cdot T_a}{273.15} - 14.9188 \cdot \left(\frac{T_a}{273.15}\right)^3\right) \quad (2.15)$$

$$\rho_v = 216.7 \cdot \phi \cdot e_s / T_a \quad (2.16)$$

$$e_s = \exp\left(22.330 - 49.140 \cdot \frac{100}{T_a} - 10.922 \cdot \left(\frac{100}{T_a}\right)^2 - 0.39015 \frac{T_a}{100}\right) \quad (2.17)$$

where Pw_e [cm] is the estimated precipitable water. H_v [km] is the apparent water vapor scale height. ρ_v [g, m^{-3}] is the surface water vapor density. ϕ [%] is the relative humidity. e_s [millibar] is the saturation water vapor pressure. T_a [°C] is the ambient air temperature.

ML technique is a powerful tool in regression modelling, which can model the relations between input features and target especially when the representation is complicated. ML algorithms have been widely used in classification, prediction and pattern recognition applications [76]. Here, we apply and compare Linear Regression (LR), Random Forest (RF), and Multilayer Perceptron (MLP) for T_L estimation, which are three commonly available and extensively used methods in real applications.

LR involves a linear combination of the input variables, which may have significant limitations for pattern recognition, particularly for problems with high dimensionality [76]. Therefore, linear model is extended by considering linear combinations of fixed nonlinear functions (basis function) of the input variables. Polynomial (powers of input variables) regression is one example of the extended linear models [76]. Although linear models are considered relatively simple and might not be suitable for high-dimensional problems, they have good analytical properties and form the fundamental for more advanced models [76]. Here we apply LR as a reference method in estimating T_L .

RF regressor is an ensemble method that combines several randomized regression decision trees to achieve a better performance [77]. RF is a bagging technique, all the involved decision trees are built in parallel and depend on the random vectors sampled from the training dataset. The predictions are averaged using bootstrap aggregation, which is one of the most computational-efficient methods to improve stability of the estimates [77]. RF models have been demonstrated to be robust predictors for both small sample sizes and data with high dimensionality [77].

MLP is also known as feed-forward neural network, which consists of an input layer, one or more hidden layers and one output layer [76]. MLP networks have high flexibility in approximation and can easily extend the structure by adding more hidden layers. MLP networks are trained and the parameters are obtained by back propagation [76]. There are different nonlinear activation functions of hidden layer(s), which could differ for different applications.

Data from 2000-2018 is used as the training set (20% of which is for validation) and data from 2019-2020 is used for testing. The model hyperparameters are tuned by using tenfold cross-validation method. The error evaluation metrics are MBE, RMSE and their normalized counterparts. All the above-mentioned ML models are adapted from Scikit-learn [97] and PyCaret [98], where more details regarding the applied algorithms can be found.

2.3 Results and discussion

The best ML model is selected separately for daily, hourly and 5-minute averaged T_L estimation, and the overall corresponding 1-minute averaged GHICs estimation results for clear-sky days in year 2019 and 2020 are presented in Table 2.1. Compared with the GHICs recalculation, GHICs based on the estimated T_L yields slightly larger MBE and RMSE. Although 5-minute averaged T_L has the best performance for GHICs recalculations, but the fine temporal resolution does not show much superior results in GHICs estimation. Estimating hourly averaged T_L results to better GHICs estimation with an MBE of 1.45 W m^{-2} and a RMSE of 9.62 W m^{-2} . Using daily averaged T_L achieves a comparable result with slightly larger MBE of 2.09 W m^{-2} and RMSE of 9.94 W m^{-2} . Given that less complexity and computational resource are required for using daily averaged T_L , the subsequent results and discussion are based on the daily averaged T_L and the associated model.

Table 2.1: Comparison of 1-minute averaged GHICs recalculations and estimations using derived and estimated T_L for clear-sky days in the year of 2019 and 2020. PVLIB results are presented here for reference.

T_L	GHICs recalculations ¹		GHICs estimations ²	
	RMSE [W m^{-2}]	MBE [W m^{-2}]	RMSE [W m^{-2}]	MBE [W m^{-2}]
Daily mean	6.74	0.34	9.94	2.09
Hourly mean	2.81	0.05	9.62	1.45
5-minute mean	0.55	0.01	10.28	-0.01
PVLIB ³	24.02	-20.48	24.02	-20.48

¹ GHICs recalculations are based on the averaged T_L factors derived from GHICs.

² GHICs estimations are based on the estimated T_L factors from the ML (MLP) models with meteorological parameters as input.

³ PVLIB uses the daily interpolated T_L based on the monthly climatological T_L map.

2.3.1 Estimations of daily turbidity and 1-minute averaged GHICs in clear-sky days

When compared with the monthly climatology mean of T_L , the derived daily T_L generally has a lower value and has a much higher fluctuation (see Fig. 2.6 (a)). The T_L values of 2020 is different from the year of 2019, which indicates the T_L also has a yearly variation. This long-term fluctuation of T_L is possibly caused by pollution [85] and the dynamics of aerosols and water vapor in the atmosphere [41]. Among the applied

ML algorithms, MLP regressor gives the best results as shown in Table 2.2 and Fig. 2.6, with comparatively lower testing RMSE and MBE values. The normalized RMSE (nRMSE) of T_L estimation from all the ML models are around 10%. The learning curve of MLP regressor is shown in Fig. 2.7.

Table 2.2: Training and testing errors of the applied ML algorithms for T_L estimation.

ML algorithm	Training		Testing	
	RMSE	MBE	RMSE	MBE
LR	0.2452	0.0000	0.2104	-0.0644
RF	0.2127	-0.0004	0.2098	-0.0591
MLP	0.2339	0.0044	0.2066	-0.0520

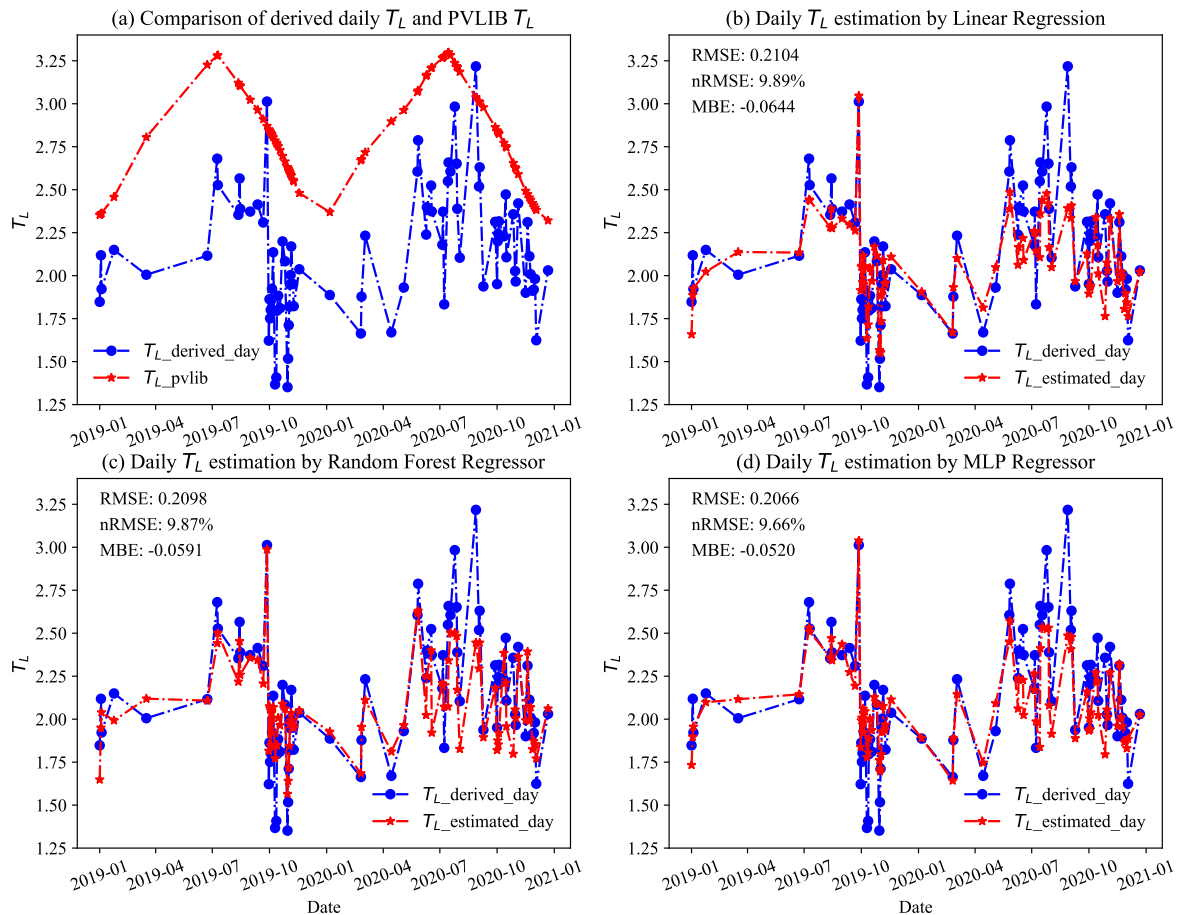


Figure 2.6: Comparison of the derived daily T_L and PVLIB T_L and the performance of applied ML methods. (a) The comparison of derived T_L and PVLIB T_L . The comparison between derived T_L and estimated T_L from different methods (b) Linear Regression (c) Random Forest Regressor and (d) MLP Regressor.

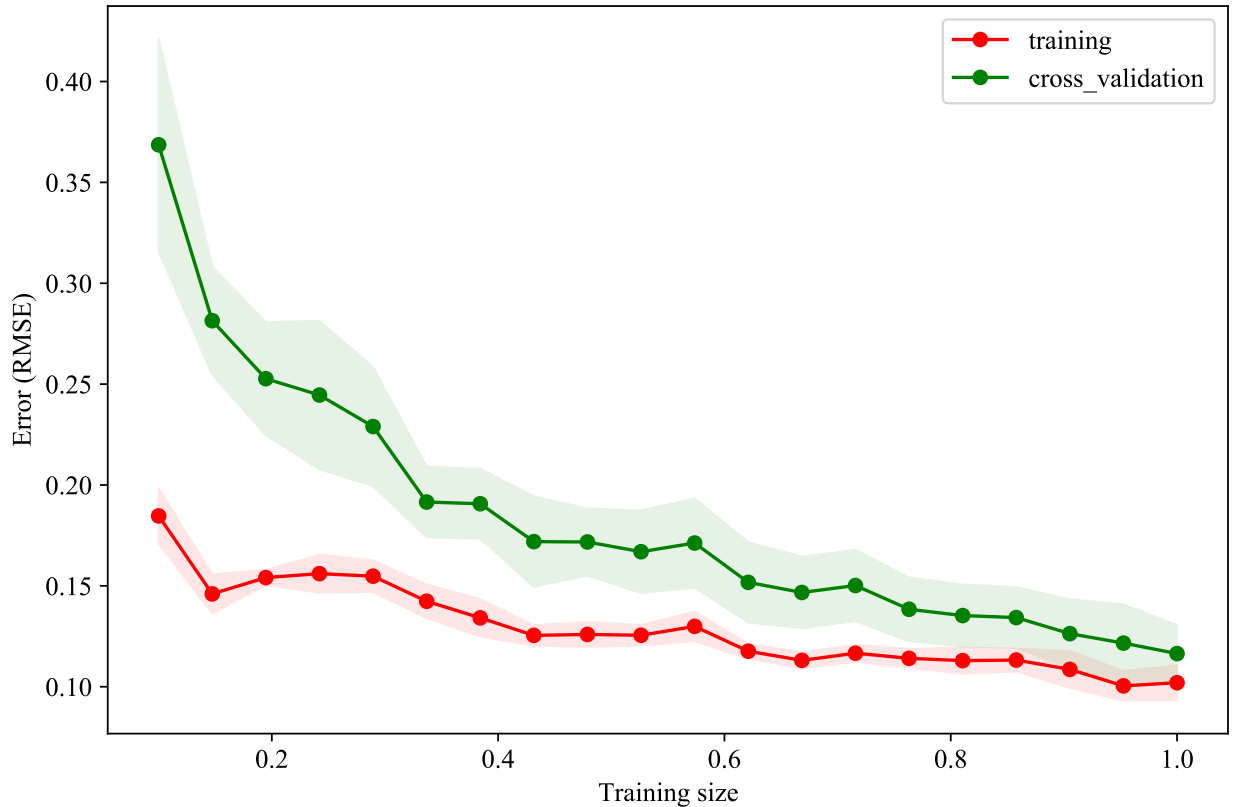


Figure 2.7: Learning curve of MLP regressor with tenfold cross validation. The dots represent mean values, and the related shadows reflect the standard derivation. Both training and validation errors are decreased with the increased training size. At the end of training, the validation error is slightly larger than training, which indicates a good fit.

Fig. 2.8 (a) presents the sensitivity analysis of the meteorological inputs for the MLP model. The estimated T_L increases when the temperature and relative humidity become higher, while the increases in wind speed and pressure lead to a drop in the T_L estimation. Wind speed is the least sensitive parameter, so its impact on the T_L estimation is limited. Relative humidity and temperature have comparatively larger influence than wind speed, and temperature is a more crucial input for T_L estimation compared with relative humidity. Regards to local pressure, it does not have large variance as shown in Fig. 2.8 (b), so either increase or decrease pressure by 10% would lead it to be out of its min-max range. Since the MLP model is trained based on data samples with a small range of pressure variation, the out-of-range pressure will produce unrealistic T_L estimation. This is why the pressure shows the relatively larger sensitivity. In practical applications, the pressure of a certain place has limited variation, so its influence on T_L estimation also remains limited.

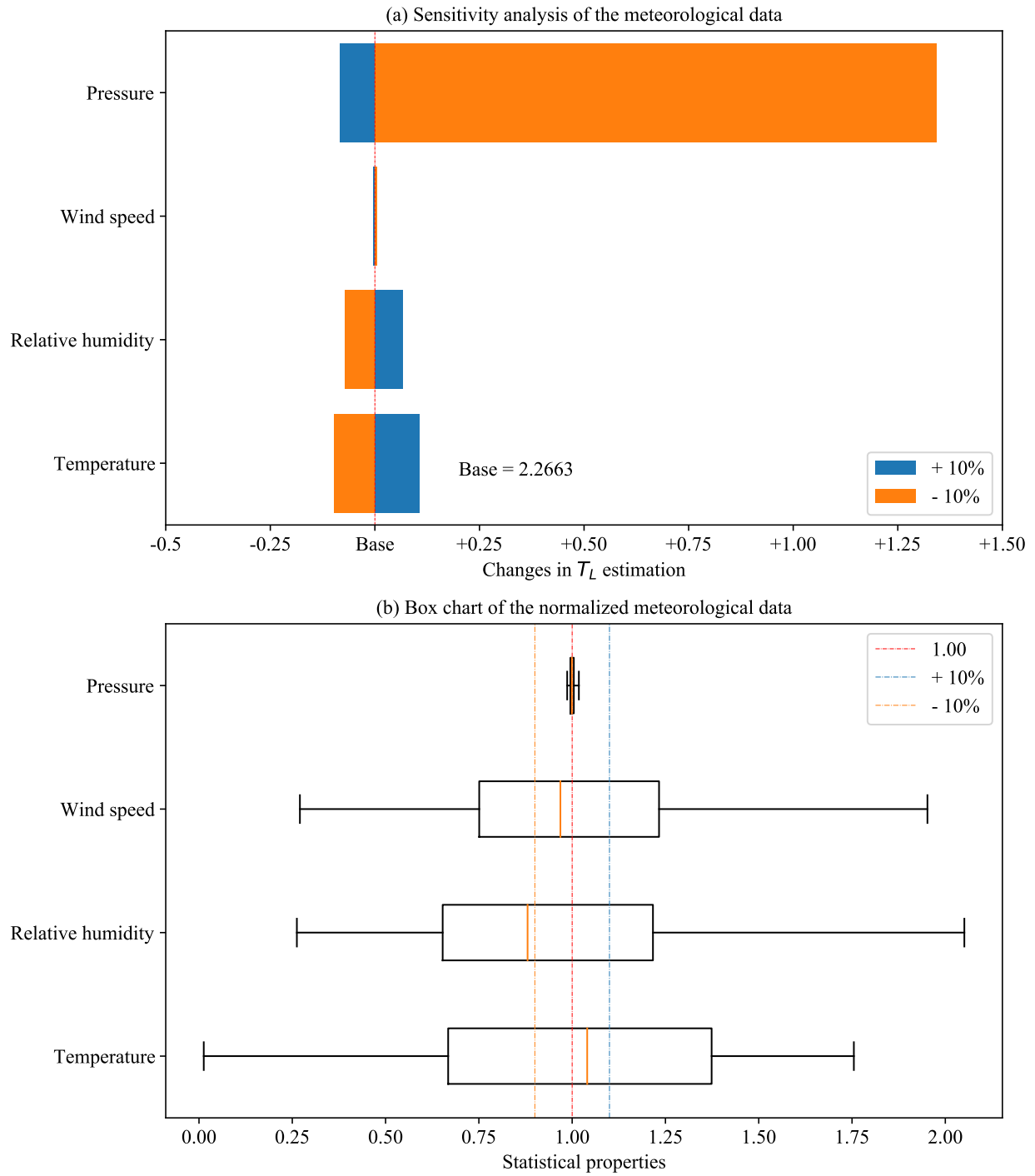


Figure 2.8: Sensitivity analysis and statistical properties of the meteorological inputs for the MLP model. (a) Sensitivity analysis based on the changes of a sole parameter, where the base is the mean value. (b) Box chart of the normalized meteorological measurements. Statistical properties represent the Minimum, Lower Quartile, Median, Upper Quartile, and Maximum.

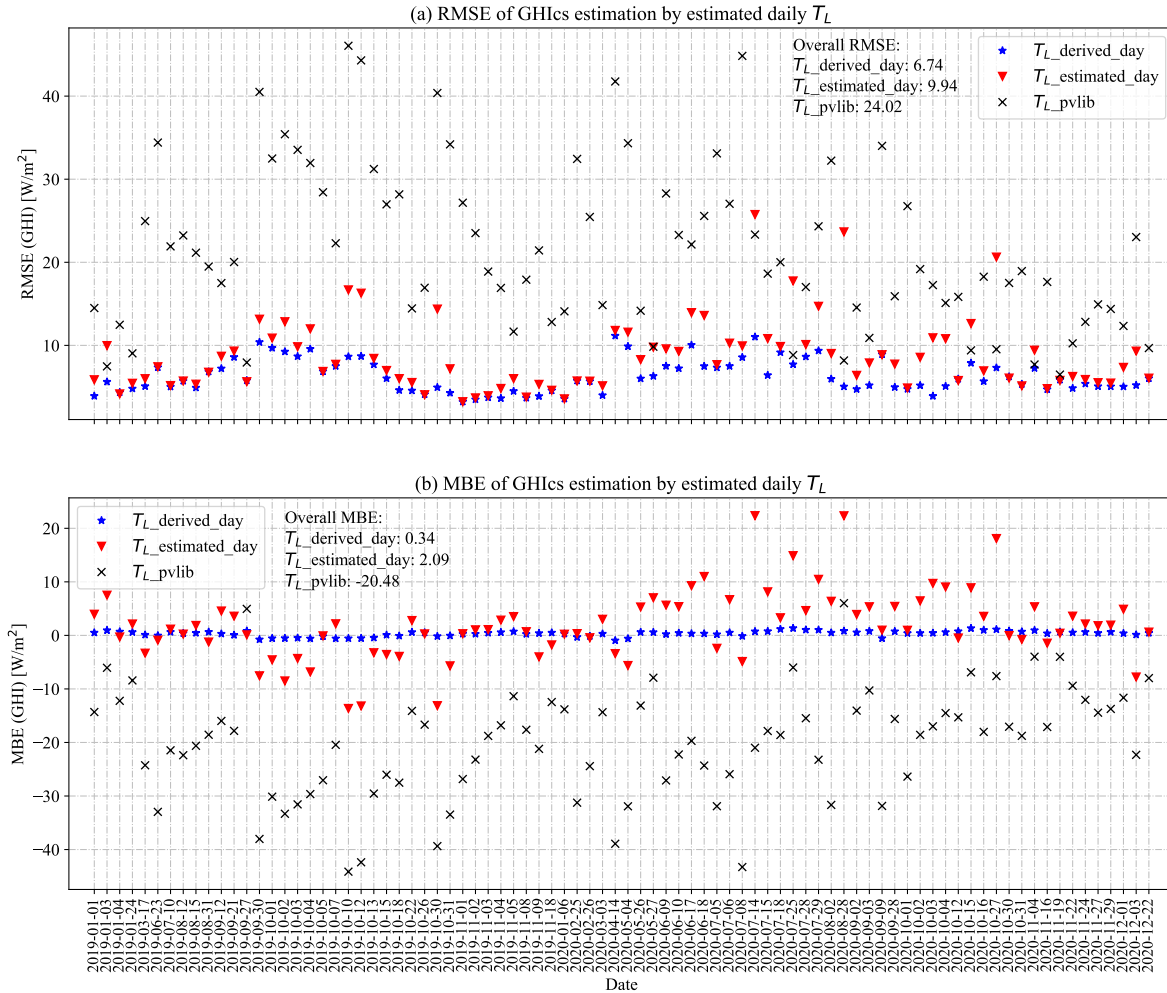


Figure 2.9: The comparison of GHICs estimation based on derived and estimated daily T_L factors. (a) Daily RMSE of GHICs estimation. (b) Daily MBE of GHICs estimation. Generally, the estimated T_L performs better than the default PVLIB T_L factor.

When using the estimated daily T_L from the MLP model to estimate 1-minute averaged GHICs, most of the tested clear-sky days in the year of 2019 and 2020 show noticeable improvements when compared with the PVLIB GHICs in terms of RMSE and MBE (see Fig. 2.9). The overall RMSE of GHICs estimation using the MLP-estimated T_L in 2019 and 2020 is 9.94 W m^{-2} , which is slightly higher than the RMSE (6.74 W m^{-2}) of GHICs recalculation from the derived T_L , but much lower than the RMSE of 24.02 W m^{-2} from PVLIB. Note that there are some cases of model underperformance, which are likely due to that PVLIB T_L is already close to the derived T_L . Nevertheless, the GHICs estimation using the estimated T_L factor has an overall better performance compared with PVLIB, which uses unmodified T_L based on the monthly climatology values, especially when the PVLIB GHICs and measured GHICs have large discrepancy.

2.3.2 Estimations of daily turbidity and 1-minute averaged GHIs in partially clear days

Furthermore, we test our T_L estimation model in partially cloudy days when not all periods are cloudless throughout the day. As shown in Fig. 2.10, the model is also applicable to estimate T_L in this case and the corresponding 1-minute averaged GHIs estimation shows better agreement when compared with PVLIB for the clear-sky instants during the day.

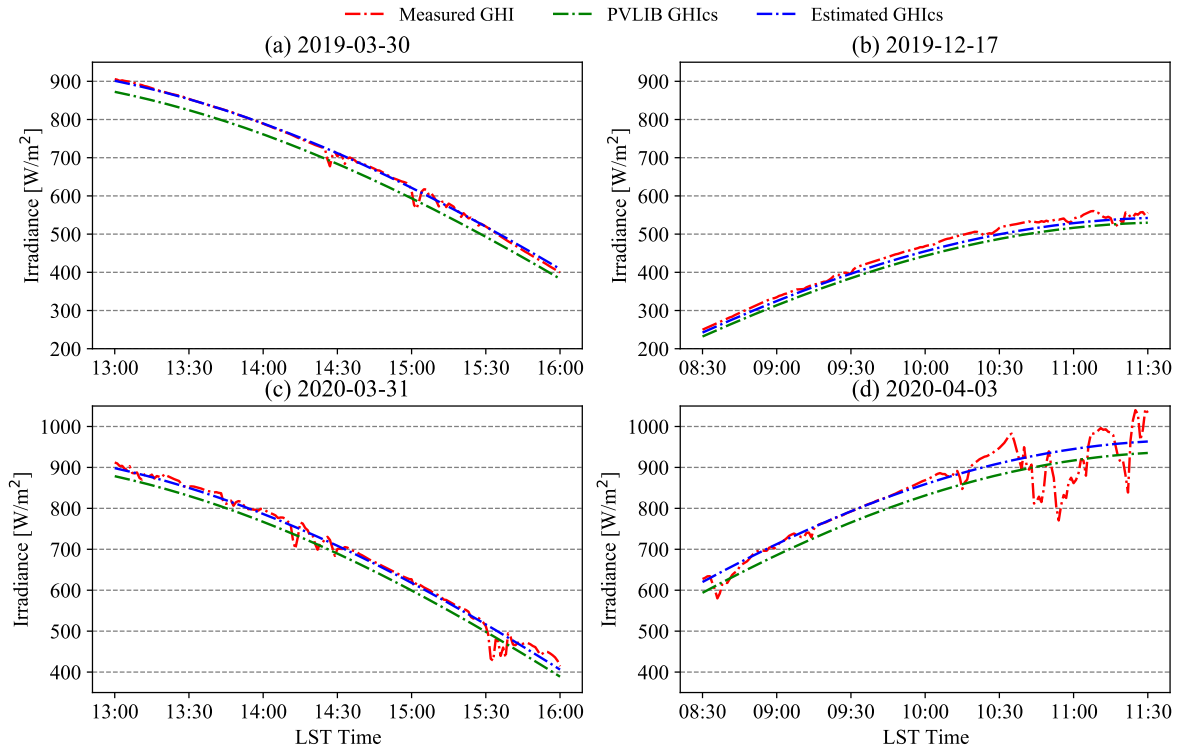


Figure 2.10: Examples of GHI in partially cloudy days during (a) 2019-03-30 (b) 2019-12-17 (c) 2020-03-31 (d) 2020-04-03. The GHIs calculated from the estimated T_L shows a higher accuracy than PVLIB when compared with measured GHI in the clear-sky instants.

The potential explanation to this phenomenon is that the presence of clouds in partially clear days has limited effect on local meteorological parameters as well as ground level aerosols and water vapor concentrations. Accordingly, using local meteorological measurements (e.g., temperature, relative humidity) to estimate GHI with the presence of clouds may not be effective. Note that the phenomenon could be different in fully overcast days as the meteorological parameters might be affected, which needs further investigation. Nevertheless, the trained model works for the partially cloudy days, which would provide more accurate clear-sky irradiance during those periods for solar resourcing and forecasting applications. In addition, since the ML model can estimate T_L in both clear-sky and partially cloudy days, the derived T_L

from the clear-sky instants in the partially cloudy days as well as corresponding meteorological variables can be included in the dataset for model development and testing. Which in turn can provide more data for ML model training and could potentially improve the model accuracy.

2.3.3 Estimations of daily turbidity and 1-minute averaged DNICs

The same method is applied to estimate 1-minute averaged DNICs using the improved T_L estimations. Since PVLIB uses the same T_L value for calculating GHICs and DNICs, we use the GHICs-estimated T_L to estimate DNICs, as shown in Fig. 2.11.

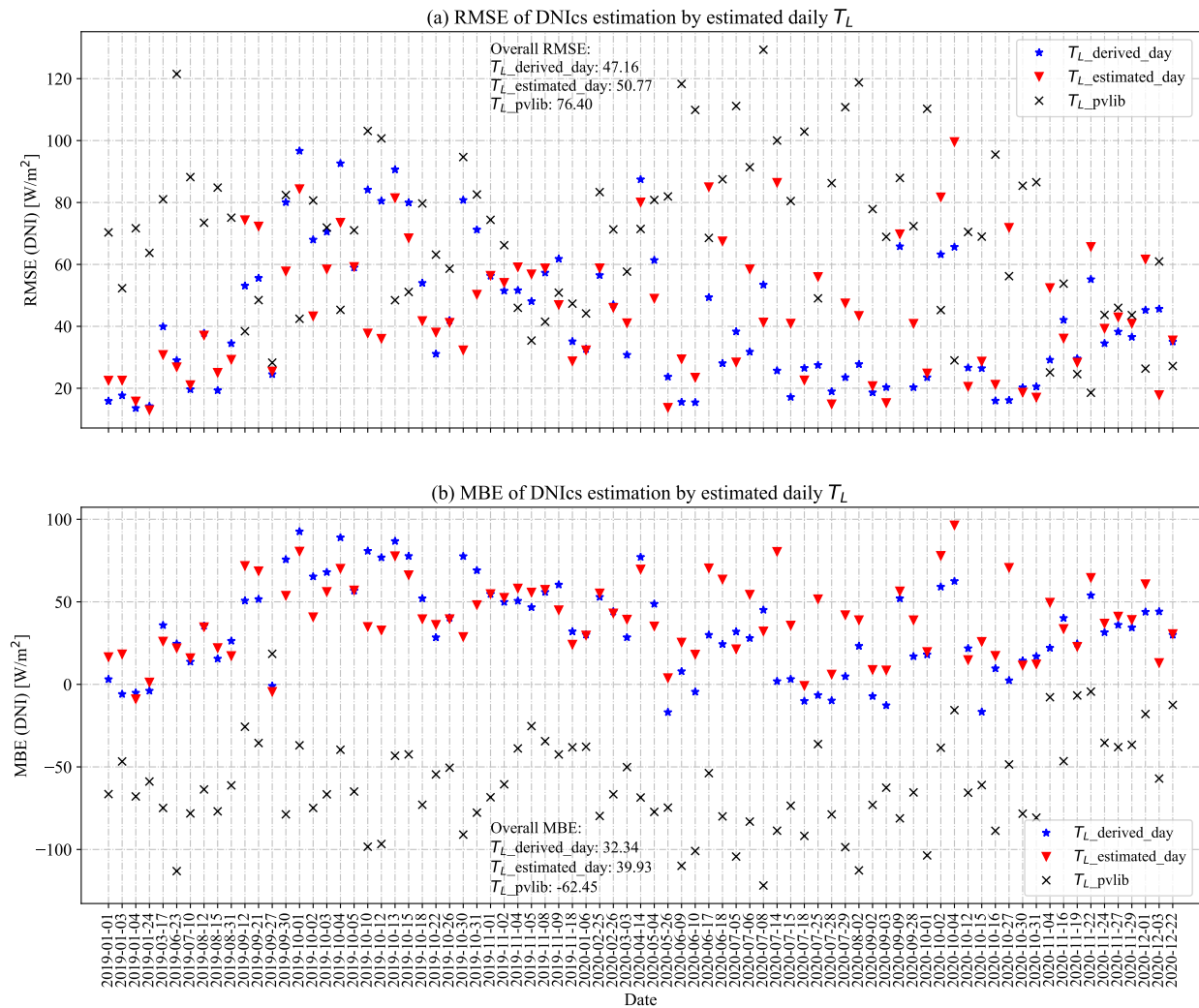


Figure 2.11: The RMSE and MBE of DNICs estimation using the GHICs-based derived and estimated T_L . Both recalculations and estimations have lower overall RMSE and MBE than PVLIB but with some exceptions.

Both the recalculations and estimations have better overall performance than PVLIB, the RMSE is reduced from 76.40 W m^{-2} to 47.16 W m^{-2} and 50.77 W m^{-2} , respectively. The MBE is decreased from -62.45 W m^{-2} to 32.34 W m^{-2} for recalculations, and to 39.93 W m^{-2} for estimations. However, the error reduction is not as effective as GHICs estimation, as it is noticed that the derived T_L from GHICs could not always lead to better DNICs estimations than PVLIB. Consequently, the estimated T_L could potentially lead to large errors by accumulating uncertainties in T_L estimation, as shown in Fig. 2.11.

To further improve the accuracy of DNICs estimations, we derive T_L from DNICs and develop separate ML models for T_L estimation following the similar strategy as described in Section 2.2. T_L is derived using Eq. (2.6) and (2.7) from measured clear-sky DNI. A comparison among different T_L modelling methods for DNICs estimation is shown in Table 2.3.

Table 2.3: Comparison of DNICs recalculations and estimations using derived and estimated T_L for clear-sky days in the year of 2019 and 2020. Although 5-minute averaged T_L has the lowest RMSE for DNICs recalculations, the 1-minute averaged DNICs estimations based on daily, hourly and 5-minute averaged T_L show little difference.

T_L	DNICs recalculations ¹		DNICs estimations ²	
	RMSE [W m^{-2}]	MBE [W m^{-2}]	RMSE [W m^{-2}]	MBE [W m^{-2}]
Daily mean	18.93	-1.75	29.96	2.68
Hourly mean	8.96	-1.46	30.75	-0.04
5-minute mean	5.74	-1.36	31.96	-1.24
PVLIB ³	76.40	-62.45	76.40	-62.45

¹ DNICs recalculations are based on the averaged T_L factors derived from DNICs.

² DNICs estimations are based on the estimated T_L factors from the ML (MLP) model developed from the derived T_L .

³ PVLIB uses the daily interpolated T_L based on the monthly climatological T_L map.

All the improved T_L factors for DNICs recalculations and estimations have superior results than default PVLIB. The 5-min averaged T_L gives the lowest RMSE of 5.74 W m^{-2} and a MBE of -1.36 W m^{-2} for recalculating DNICs, while daily mean T_L generates a RMSE of 18.93 W m^{-2} and a MBE of 1.75 W m^{-2} . However, the developed MLP models for daily, hourly and 5-minute T_L estimation yield comparable results for estimating DNICs, which means averaging T_L on smaller time basis has limited potential to improve the DNICs estimation accuracy. Since using daily mean T_L can generate comparable DNICs estimations with

less complexity, a detailed comparison of DNICs estimation by using estimated daily T_L and default PVLIB T_L is shown in Fig. 2.12.

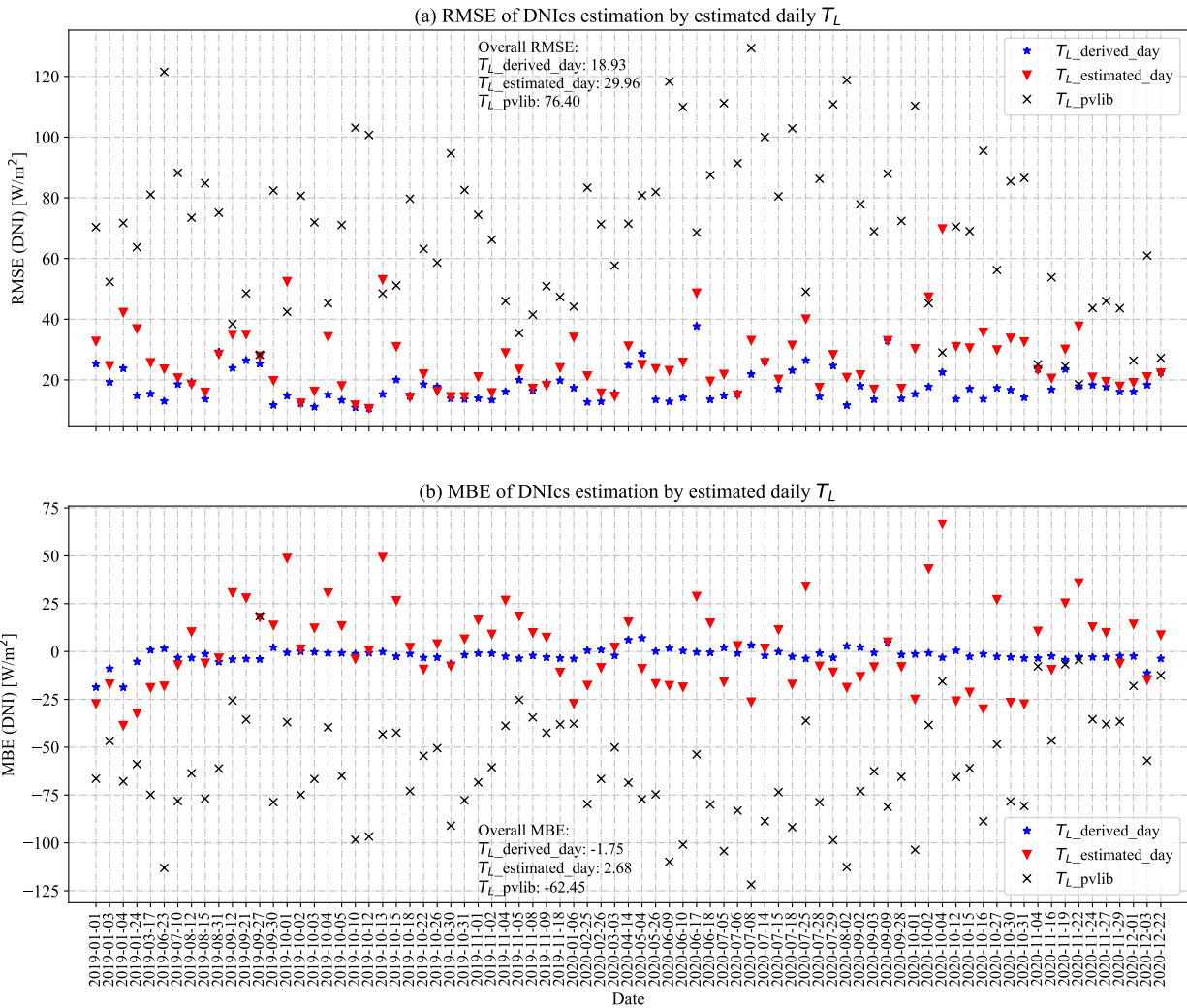


Figure 2.12: The comparison of DNICs estimation based on derived and estimated daily T_L factors. (a) RMSE of DNICs estimation. (b) MBE of DNICs estimation. Generally, the estimated T_L performs better than the default PVLIB T_L factor in terms of RMSE and MBE.

From the perspective of atmospheric radiative transfer, DNI is comparatively more sensitive than GHI to the variations of atmospheric constituents and cloud dynamics, as GHI is the sum of DHI and the horizontal projection of DNI ($GHI = DNI \cdot \cos(\theta) + DHI$, where θ [°] is the solar zenith angle). The rapidly changing DNICs in the solar morning and evening also makes the DNICs estimation more challenging than GHICs. As demonstrated by our results, the default PVLIB T_L yields a RMSE of 76.40 W m^{-2} and a MBE of -62.45 W m^{-2} for DNICs estimation, which is about three times of the RMSE (24.02 W m^{-2}) and MBE (-20.48

W m^{-2}) for estimating GHICs.

Compared with GHICs estimation from derived and estimated T_L factors, DNICs estimation generally has comparatively larger errors of RMSE and MBE (see Table 2.1 and Table 2.3). Using the 5-minute averaged T_L factor almost produce a "perfect" GHICs recalculation with the RMSE of 0.55 W m^{-2} and MBE of 0.01 W m^{-2} , while the RMSE is 5.74 W m^{-2} and MBE is -1.36 W m^{-2} for DNICs recalculation. When it comes to estimation, the ML model (MLP is chosen) estimated daily T_L for DNICs estimation has a RMSE of 29.96 W m^{-2} , which is nearly three times of the RMSE (9.94 W m^{-2}) of estimating GHICs. For partially cloudy days, the proposed DNICs estimating method also outperforms PVLIB, but the degree of error reduction is smaller than those of GHICs estimation, as demonstrated by Fig. 2.13. In sum, DNICs estimation is more challenging than GHICs and often has larger discrepancies, the applications that rely heavily on accurate DNICs estimation is recommended to adopt the methods to improved DNICs estimation (such as the one presented in this work).

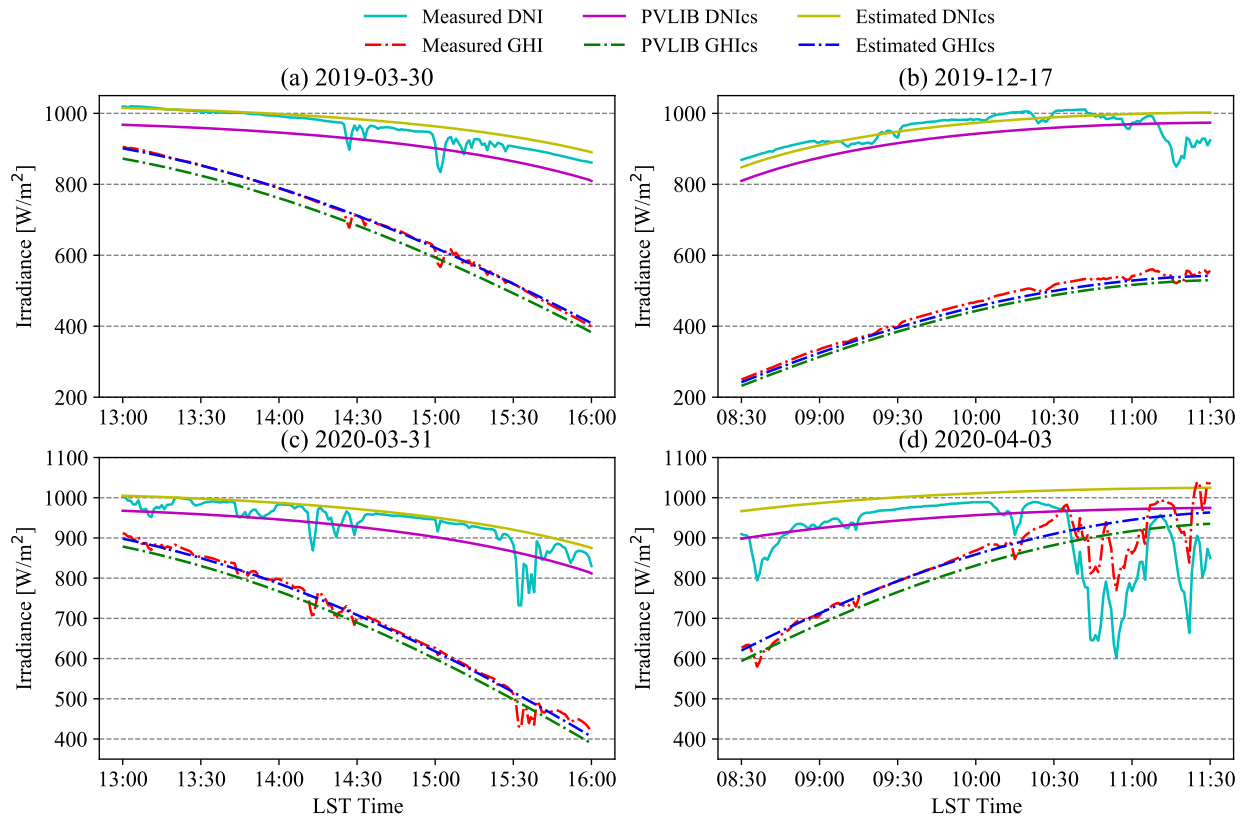


Figure 2.13: DNI and GHI time series in partially cloudy days during (a) 2019-03-30 (b) 2019-12-17 (c) 2020-03-31 (d) 2020-04-03. Compared with DNICs estimation in partially cloudy days, GHICs estimated from improved T_L factor has higher accuracy in the clear-sky instants.

2.3.4 Generic applicability of the proposed method

Here we apply the proposed methodology at other SURFRAD stations with limited occurrences of clear-sky days to demonstrate the generic applicability of the proposed method. The results of 1-minute averaged GHIs estimation for all the SURFRAD stations using the T_L estimation models developed using both clear-sky and partially clear days are presented in Table 2.4. Compared with the default PVLIB calculations, the proposed method generally produces better GHIs estimations for all SURFRAD stations.

Table 2.4: Results of 1-minute averaged GHIs estimations using estimated T_L for clear-sky and partially clear days in 2019 for all the SURFRAD stations. PVLIB results from default T_L are presented in brackets for reference.

Stations	Clear-sky days		Partially clear days		Clear-sky and partially clear days	
	nRMSE[%]	nMBE[%]	nRMSE[%]	nMBE[%]	nRMSE[%]	nMBE[%]
BON	3.81(10.68)	-1.90(-9.08)	3.16(9.24)	-0.96(-7.80)	3.38(9.16)	-0.37(-7.58)
DRA	1.42(4.09)	-0.20(-3.33)	1.48(3.79)	-0.17(-3.02)	1.52(3.80)	-0.13(-2.99)
FPK	2.90(7.03)	-1.91(-4.83)	2.53(5.32)	-0.78(-2.97)	2.62(5.09)	-0.48(-2.59)
GWN	3.10(8.52)	-1.19(-7.52)	3.12(7.06)	-0.64(-5.27)	3.24(7.00)	-0.44(-4.97)
PSU	1.73(8.47)	-0.28(-7.81)	2.29(7.01)	-0.25(-6.07)	2.62(7.11)	-0.35(-6.04)
SXF	1.69(7.24)	-0.09(-6.66)	2.85(6.13)	-0.03(-5.01)	3.05(6.29)	-0.16(-5.14)
TBL	2.50(2.73)	1.15(-0.75)	2.37(2.45)	1.40(-0.47)	2.63(2.66)	1.39(-0.24)

2.4 Conclusions

In this chapter, we present a new method to estimate turbidity factor T_L using common meteorological data by ML algorithms. The model inputs are: the default PVLIB T_L , ambient air temperature, relative humidity (and its logarithm), wind speed, atmospheric pressure, day of year (DOY), and estimated precipitable water. The model output is estimated T_L , which has the same temporal resolution as the input parameters. The training target of the ML algorithms is the T_L derived from measured clear-sky GHI or DNI. When tested using data from Desert Rock, Nevada, the new method successfully captures both the short-term and the long-term temporal variations of T_L by inferring from the local meteorological measurements, thus leading to substantial accuracy improvement in estimating clear-sky irradiance. The major findings and recommendations are:

- We perform T_L estimation on the averaging basis of a day, an hour and every 5-minute. Although 5-minute averaged T_L can better represents its temporal variation, using daily or hourly averaged T_L to estimate GHICs or DNICs has no significant reduction in accuracy. Therefore, we recommend using the improved daily-averaging T_L (with less complexity and less computational resource requirement) for GHICs or DNICs estimations.
- Although the default Ineichen-Perez clear-sky model uses the same turbidity factor for GHICs and DNICs estimations, we found that using the same values would deteriorate DNICs estimation. Therefore, we recommend using two separately trained ML models to generate different T_L values, one for GHICs estimation and one for DNICs estimation.
- During clear days, when compared with the default PVLIB T_L , the RMSE of GHICs estimation based on the improved daily T_L decreased from 24.02 W m^{-2} to 9.94 W m^{-2} , a 58.6% reduction of error. The RMSE of DNICs estimation is reduced from 76.40 W m^{-2} to 29.96 W m^{-2} , a 60.8% reduction of error. The default PVLIB generally underestimates the GHICs and DNICs with an MBE of -20.48 W m^{-2} and -62.45 W m^{-2} , respectively. The bias are corrected when using the improved daily T_L , yielding an MBE of 2.09 W m^{-2} for estimating GHICs, and 2.68 W m^{-2} for estimating DNICs, respectively.
- The daily T_L estimation method is also tested in partially cloudy days (with partial clear periods and partial cloudy periods). It is observed that the corresponding GHICs and DNICs estimations show better agreement with clear-sky irradiance measurements during cloudless time instances, when compared with default PVLIB results. The results indicate that the presence of clouds does not significantly change local air temperature and relative humidity, as well as water vapor and aerosol concentrations. Furthermore, the results demonstrate the potential of the proposed method in assisting solar irradiance modelling and forecasting in partially cloudy conditions, especially for cloud identification applications.

In sum, our proposed method offers a simpler way for T_L estimation without priori knowledge of aerosol and water vapor content in the atmosphere. The estimated T_L can substantially improve the accuracy of clear-sky GHI and DNI estimations when used in an empirical clear-sky model. Our results also imply that local meteorological data such as air temperature and relative humidity can represent column water vapor and aerosol concentrations with high accuracy during both clear and partially cloudy days. Solar resourcing and forecasting applications are expected to be improved when the proposed method is used to estimate clear-sky irradiance with higher accuracy.

2.5 Acknowledgement

This chapter, in full, is a reprint of S. Chen and M. Li (2022). Improved turbidity estimation from local meteorological data for solar resourcing and forecasting applications. *Renewable Energy*, 189, 259-272.

The thesis author is the first author of this publication.

Chapter 3

Estimation of high-resolution solar irradiance data using optimized semi-empirical satellite method and GOES-16 imagery

3.1 Introduction

Solar radiation is a significant source of renewable energy systems, which can be directly captured to produce heat and electricity. It is reported that solar thermal technologies produced 479 TWh energy in 2019, which is an equivalent energy savings of 43 million tons of oil and 130 million tons emissions of CO₂ [5]. Meanwhile, solar photovoltaic (PV) has also been one of the most promising renewable energy technologies in recent years with an estimated average yearly growth of 15% between 2019 and 2030 [99]. However, the power output of a solar energy system is highly variable due to the intermittent and uncertainty of local irradiance conditions [9, 10, 11, 14]. The variability in power production also introduces difficulties in system operation [100]. Considering the rapid expansion of solar energy conversion applications, it is important to have reliable and accurate ground solar irradiance data at the location of interest. Historical data is essential for the feasibility and optimal system design phases of a solar power conversion project to support decision making and reduce the risk [8].

Ground-based measurement is the most reliable irradiance data source for solar energy applications. However, due to difficulties in routine calibration, data quality control, as well as the high cost associated

with the instrumentation, complete and long-term ground-based measurements are scarce [12]. Therefore, solar irradiance estimation and reanalysis from satellite offer an alternative to the ground measurements for evaluating and designing the solar energy projects [47]. Despite the general belief that solar irradiance data based on satellite observation and model reanalysis is less accurate than ground-based measurements, satellite-derived solar irradiance data can help with model development [12].

As an essential part for solar irradiance modelling, geostationary satellites are widely used for resource monitoring and assessment as they observe continuously the same part of the Earth [8]. The advancement in modern remote sensing technique brings data in finer temporal and spatial resolutions as well as new insights in solar irradiance modelling. Satellite-based solar irradiance models can be broadly classified as physical, empirical, and semi-empirical methods [8]. Physical methods usually apply radiative transfer models (RTMs) through different layers in the atmosphere, which requires detailed and accurate information of the atmospheric constituents, such as cloud optical properties, aerosol optical depth (AOD), and water vapor content [8]. Pure empirical models attempt to simulate the regression between the satellite measurements and ground based records [8]. While semi-empirical models are a combination of physical and empirical method, which apply a simple RTM and regression approach to fit the observations [8].

Many studies have been conducted to estimate the global horizontal irradiance (GHI) from geostationary satellites images [48, 49, 50, 51]. Both physical and semi-empirical models are extensively used in estimating GHI while simple empirical methods are barely applied due to their inferior performance caused by the lack of generality [51, 52]. Physical models usually have better performance than semi-empirical methods [51], as they technically need the details of atmospheric compositions. For instance, the national solar radiation database (NSRDB) [49], as a widely accessed and publicly available data source, provides broadband irradiance and other auxiliary variables. NSRDB is produced using the physical solar model (PSM) and products from a number of associations [49]. The Heliosat-4 method [50] is also a fully physical model using a fast, approximated, but still accurate RTM approach. Heliosat-4 consists of two models based on libRadtran [43] and look-up tables: the McClear [32] for solar irradiance under cloud free conditions and the McCloud for irradiance attenuation due to clouds. However, apart from the complexity and high computing resource requirement, the essential inputs of physical models, such as water vapor, AOD, and cloud properties are difficult to obtain and generally associated with uncertainties [8, 54, 80].

On the other hand, semi-empirical methods typically deal with the irradiance attenuation of atmospheric constituents and cloud extinction separately, with a clear-sky model for clear-sky irradiance and a cloud index (CI) derived from satellite image to account for cloud attenuation [8, 48]. Heliosat method series [38, 57, 58] are examples of semi-empirical models, which offer easy implementation, fast calculation

and operation [51]. Many clear-sky models have been used in semi-empirical models for GHI estimation, such as the Ineichen-Perez model [31] in the operational model (SUNY model) developed by Perez et al. [37], the McClear model in the work of Jia et al. [60], and the REST2 [33] model in Solcast [61]. There are also different methods proposed to calculate the GHI based on clear-sky index (CSI) and CI in the literature [37, 48, 62].

Given that a variety of clear-sky models are available for estimating GHI in semi-empirical satellite models with different regressions between CSI and CI, there has been a dearth of study to compare the performance of different clear-sky models and empirical relationships for GHI estimation. Some related studies from the literature are summarized as follows, Rigollier and Wald [101] compared several clear-sky models developed at the early stages and selected the ESRA [87] model for the HelioClim project [102], which was later replaced by McClear for improvements [56]. Laguarda et al. [52] applied the ESRA and McClear model in hourly GHI estimation over the Pampa Húmeda with different locally adjusted CI methods. McClear model performs better than ESRA model under clear-sky conditions, and both ESRA and McClear models have small negative biases of -1.1% for all-sky GHI estimates while McClear yields a slightly lower relative root mean square deviation (rRMSD, 12.5% versus 12.1%). Garniwa et al. [51] analyzed the performance of different semi-empirical models for hourly GHI estimation in Korea and found the Hammer model presented in [48] has a better result. Meanwhile, a hybrid model was also proposed with smaller root mean square error (RMSE) than the Hammer model (97.08 W m^{-2} versus 103.92 W m^{-2}). However, limited studies have been conducted to compare and evaluate the performance of different clear-sky models, CI and CSI derivation methods in solar resourcing. Considering the advanced clear-sky models have been developed with high performance and much finer resolution of the data (e.g., 5-minute images) provided by modern satellites, it would be of interest to compare and evaluate the methods and clear-sky models used in semi-empirical model for GHI estimation with a fine spatiotemporal resolution (i.e., 5-minute and 1 km).

This chapter aims to optimize the semi-empirical satellite model for 5-minute GHI estimation via comparing and evaluating the performance of different clear-sky models, CI and CSI derivation methods, and satellite bands. Ineichen-Perez, McClear, and REST2 are compared as the representatives of average, good and best clear-sky models to keep the generality [36]. The main contributions of this chapter are summarized as follows:

- Evaluates the performance of 5-minute all-sky GHI estimate based on different bands of GOES-16 and different empirical relationships between CSI and CI.
- Compares different methods to derive the CI based on GOES-16 data for 5-minute GHI estimation, in

particular, the time window, the upper and lower bounds used in semi-empirical methods.

- Introduces the modified Ineichen-Perez clear-sky model based on estimated turbidity from local meteorological measurements [103] in all-sky GHI estimation.
- Compares and evaluates the four aforementioned clear-sky models for estimating 5-minute GHI using semi-empirical methods under different sky conditions.

The remainder of this chapter is structured as follows: Section 3.2 describes the used data, semi-empirical GHI estimation method, and the details of the compared clear-sky models. The performance of different CI, CSI calculation methods, and different clear-sky models for GHI estimation and discussions are presented in Section 3.3. Finally, the key findings of this chapter and recommendations are summarized in Section 3.4.

3.2 Data and methods

This section describes the used data and the semi-empirical satellite method for GHI estimation. The satellite data will first undergo a radiance conversion to eliminate the negative points, then the CI and CSI are determined using different strategies and methods that are described in Section 3.2.2. Finally, the GHI is calculated via the CSI and clear-sky GHI (GHIcs) from the clear-sky model as shown in Fig.3.1. Four clear-sky models are compared, the GHIcs of REST2 and McClear are publicly available, Ineichen-Perez documented in PVLIB [39] adopts the default calculations, while Ineichen-Perez TL model uses the estimated turbidity based on local meteorological measurements [103]. The detailed method for estimating turbidity is presented in Section 3.2.3.

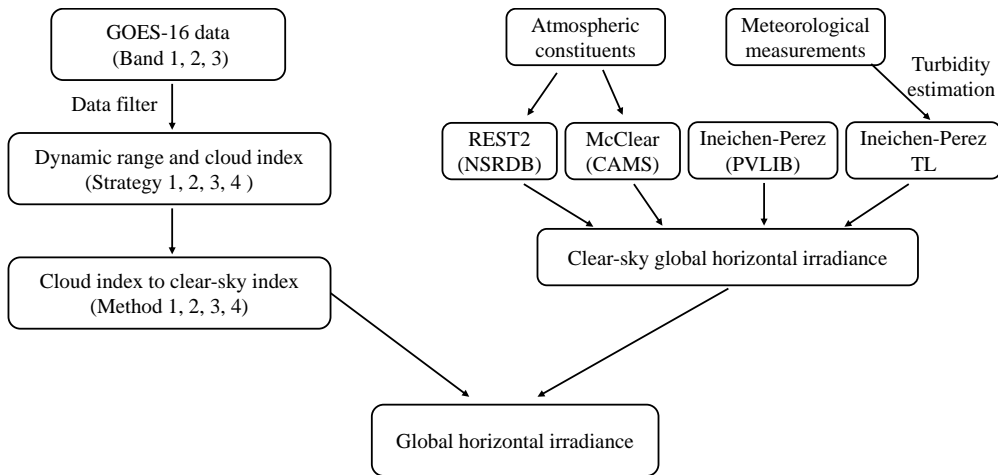


Figure 3.1: The flowchart of GHI estimation using semi-empirical methods with different clear-sky models.

3.2.1 Data

The satellite data used in this chapter is from GOES-16, operated by National Oceanic and Atmospheric Administration (NOAA). GOES-16 has 16 spectral bands, the Advanced Baseline Imager (ABI) provides data with temporal resolution of 5 - 15 minutes, and spatial resolution of 0.5 - 2 km at the sub-satellite point [13]. In this chapter, the data from two visible bands (blue, red) and one near-infrared band (veggie) in the year of 2019 are retrieved from publicly available sources and then georeferenced to the ground location of interest, the detailed information about the aforementioned bands is presented in Table 3.1. There are three UTC (Universal Time Coordinated) timestamps referring the time of file creation, start and end of the scan. To be compatible with ground measurements and real-time applications, the end timestamp is applied to index the data after rounded to the next nearest 5-minute interval.

Table 3.1: Summary of the blue, red, veggie bands of GOES-16. All the information is obtained from the GOES-R Series Product Definition and User’s Guide (PUG) [104].

Band No.	Type	Center wavelength (Range) [μm]	Resolution [km]	Valid range*	Scale factor	Add offset
1 (Blue)	Visible	0.47 (0.450-0.490)	1.0	0-1022	0.8121	-25.9366
2 (Red)	Visible	0.64 (0.590-0.690)	0.5	0-4094	0.1586	-20.2899
3 (Veggie)	Near-Infrared	0.87 (0.846-0.885)	1.0	0-1022	0.3769	-12.0376

* Valid range is in packed and scaled integer form. Scale factor and add offset are used to convert scaled integer to physical quantity, which is radiance [$\text{W m}^{-2} \text{sr}^{-1} \mu\text{m}^{-1}$] in this case.

The corresponding ground irradiance measurements are from the stations in Surface Radiation Budget Network (SURFRAD) [29]. Detailed information of the seven stations are summarized in Table 3.2. The initial dataset includes a variety of 1-minute averaged solar irradiance as well as meteorological information. Ambient air temperature, relative humidity, wind speed and atmospheric pressure are averaged on a daily basis (when solar zenith angle is less than 85°) for turbidity estimation, and GHI is averaged on a basis of 5-minute. The quality control (QC) for meteorological recordings is available in the original dataset, any data point that does not meet the QC is excluded when calculating the daily average. The QC procedure for GHI follows the steps detailed in [105], any 1-minute data points that do not pass the QC are discarded when aggregating the GHI to 5-minute resolution in the round way (i.e., data points from 13:58, 13:59, 14:00, 14:01, 14:02 are aggregated and indexed as 14:00).

Table 3.2: Summary of the seven SURFRAD stations.

Station	Latitude (°)	Longitude (°)	Altitude (m)	Timezone	Snow-free period
BON	40.05	-88.37	230	UTC-6	2019-04-01 - 2019-10-31
DRA	36.62	-116.02	1007	UTC-8	2019-01-01 - 2019-12-31
FPK	48.31	-105.10	634	UTC-7	2019-05-03 - 2019-09-30
GWN	34.25	-89.87	98	UTC-6	2019-01-01 - 2019-12-31
PSU	40.72	-77.93	376	UTC-5	2019-04-01 - 2019-10-31
SXF	43.73	-96.62	473	UTC-6	2019-05-01 - 2019-09-30
TBL	40.12	-105.24	1689	UTC-7	2019-05-02 - 2019-09-30

The 5-minute satellite-derived GHI at the SURFRAD stations in the year of 2019, provided by NSRDB [49], is also used in this chapter for comparison. NRSDB is produced using the PSM and REST2 [33] clear-sky model (the GHIcs estimation from REST2 is also available in NRSDB), the spatiotemporal resolution is improved to 5-minute and 2 km.

Without extra algorithm for cloud and snow detection, semi-empirical models (e.g., Heliosat method) could not account for the significant changes in the ground surface albedo due to the snow cover, which may introduce large uncertainty and unreliability in deriving surface solar irradiance [55]. Therefore, the GHI estimation and comparison are performed in the snow-free periods for all the SURFRAD stations. The information of snow depth is available from the dataset of National Aeronautics and Space Administration (NASA) National Snow and Ice Data Center (NSIDC) [106, 107]. We use data in full months, however, a month having only a few days detected with snow cover at the beginning (or ending) is also included after removing the snow-present days. The detailed information of snow-free periods at all SURFRAD stations could be found in Table 3.2.

3.2.2 Semi-empirical models

Semi-empirical models are typically developed to exploit data recorded by the visible channel of a geostationary satellite [8], which can be traced from the contribution of Cano et al. [59]. Compared with physical methods, semi-empirical models use a simplified radiative-transfer approach [8], which are extensively used in solar resourcing [108, 109, 110] and forecasting [55, 66, 67] applications.

The underlying idea of semi-empirical method is to estimate the global surface solar irradiance from satellite measurements considering atmospheric and cloud attenuation separately [48]. In the first step the

clear-sky irradiance is derived for a given location and time via a clear-sky model. In the second step the cloud attenuation is determined from the visible radiance by introducing CI, which is then correlated to CSI. Finally, the global surface solar irradiance is calculated from the clear-sky irradiance and CSI [48].

The CI for the SURFRAD stations are calculated following the methods presented in [37]. First, the pixel value is normalized:

$$\text{norpix} = \text{pix} \cdot \text{AM} \cdot \text{soldist} \quad (3.1)$$

where pix is the satellite pixel intensity, AM is the absolute airmass, and soldist [AU] is the Sun-Earth distance. In the original proposed method in [37], the raw data such as digital number (digital count) is used as the pixel intensity. In this chapter, we first convert the digital number (scaled integer) to the radiance via the scale factor and add offset as shown in Table 3.1, and eliminate the negative data points considering the radiance measured by the ABI sensor should not be negative. Note that this step does not show much difference with the original method but discarding some data points, as the raw pixels are proportional to the Earth's radiance observed by the satellite [37] and the linear transformation does not introduce any non-linearity.

To account for high airmass effect, the normalized pixels considered for dynamic range maintenance are subjected to a secondary normalization:

$$\text{npix} = \text{norpix} / (2.283h^{-0.26} \cdot \exp(0.004h)) \quad (3.2)$$

where h [°] is the solar elevation, which is in the range of 1.5° to 65° and the value is set to be 65° when the solar elevation is greater than 65°. Note that although solar elevations of low and medium airmass are included, they have different normalization extents, where the high airmass effects could be accounted for.

Then the CI value is determined by:

$$\text{CI} = \frac{\text{npix} - \text{low}}{\text{high} - \text{low}} \quad (3.3)$$

where high is equal to the mean of the 10 highest npix values in a month to estimate the upper dynamic range, while low is calculated as the mean of the second to the fifth lowest values for that time of the day in a month, the lowest value is excluded due to its variation and the undetected defects in the original image [58, 108]. Our method for determining the upper and lower bond is different from the methods presented in [31, 67, 109], the time window is one month to better account for the seasonal variations of the ground reflectance [48, 111]. Meanwhile, the low is calculated every 5 min for time in the day (when the solar zenith angle is less than 80°) taking advantage of the improved time resolution of GOES-16. Four strategies for CI derivation are compared in this chapter, where Table 3.3 details the time window used, the determinations of upper and lower bounds in each strategy.

Table 3.3: Summary of the strategies used to derive CI for GHI estimation.

Strategy	Time window*	Upper bound	Lower bound	Reference
1	90 days (moving)	mean of 20 highest values	mean of 40 lowest values	Perez et al. [37]
2	60 days (moving)	mean of 20 highest values	mean of 40 lowest values	Harty et al. [67]
3	30 days (moving)	mean of 10 highest values	mean of 2nd to 5th lowest values	
4	1 month (fixed)	mean of 10 highest values	mean of 2nd to 5th lowest values	

* Time window is used to determine the dynamic range, a moving time window means it moves with the time of interest, so the upper and lower bound will change. While the monthly fixed time window means it is fixed in the month of interest, so the upper and lower bounds remain constant in the month.

Table 3.4: Different methods to calculate GHI via CSI, CI and GHICs. GHICs is estimated from a selected clear-sky model.

Method	GHI calculation	Reference
1	$\text{GHI} = \text{GHICs} \cdot \text{CSI}$ $\text{CSI} = 0.02 + 0.98 \cdot (1 - \text{CI})$	Perez et al. [37]
2	$\text{GHI} = \text{CSI} \cdot \text{GHICs} \cdot (0.0001 \cdot \text{CSI} + 0.9)$ $\text{CSI} = 2.36 \cdot \text{CI}^5 - 6.3 \cdot \text{CI}^4 + 6.22 \cdot \text{CI}^3 - 2.63 \cdot \text{CI}^2 - 0.58 \cdot \text{CI} + 1$	Perez et al. [37]
3	$\text{GHI} = \text{GHICs} \cdot \text{CSI}$ $\text{CSI} = 1.2, \text{CI} \leq -0.2;$ $\text{CSI} = 1.0 - \text{CI}, -0.2 < \text{CI} \leq 0.8;$ $\text{CSI} = 2.0667 - 3.6667 \cdot \text{CI} + 1.6667 \cdot \text{CI}^2, 0.8 < \text{CI} \leq 1.1;$ $\text{CSI} = 0.05, 1.1 < \text{CI}.$	Hammer et al. [48]
4	$\text{GHI} = \text{GHICs} \cdot \text{CSI}$ $\text{CSI} = 1.2, \text{CI} \leq -0.2;$ $\text{CSI} = 1.0 - \text{CI}, -0.2 < \text{CI} \leq 0.8;$ $\text{CSI} = 1.1661 - 1.781 \cdot \text{CI} + 0.73 \cdot \text{CI}^2, 0.8 < \text{CI} \leq 1.05;$ $\text{CSI} = 0.09, 1.05 < \text{CI}.$	Mueller et al. [62]

After the derivation of CI, the next step is the conversion from CI to CSI and then to GHI. Similarly,

there are also different methods proposed as shown in Table 3.4. In general, CI is first converted to CSI via an empirical method, GHI is then calculated based on CSI and GHICs, where GHICs [W m^{-2}] is the clear-sky GHI estimated from the chosen clear-sky model. In the development of the CI-to-CSI methods, Perez et al. [37] compares the old method (Method 1) and newly-developed method (Method 2) using GOES-8 and GOES-10 satellites, and the involved ground stations are Albany (New York), Burlington (Kansas), Eugene, Gladstone, and Hermiston (Oregon). Method 3 presented in Hammer et al. [48] and Method 4 proposed in Mueller et al. [62] are developed using Meteosat series of satellites and ground stations in Europe. Therefore, the use of SURFRAD stations in the comparison of the CI-to-CSI methods is acceptable since they are not involved in the methods development.

Table 3.5: Input parameters for the used clear-sky models. The variables are the solar constant I_0 [W m^{-2}], solar zenith angle θ [$^\circ$], altitude h [m], Linke turbidity T_L , surface albedo ρ_g , local pressure P_a [mb], ambient temperature T_a [K], AOD at 550 nm τ_{550} , Ångström exponent α , total ozone amount u_{O_3} [atm-cm], total precipitable water vapor u_{H_2O} [cm], total nitrogen dioxide amount u_{NO_2} [atm-cm], relative humidity ϕ [%], wind speed V [m s^{-1}].

Clear-sky model	Input parameters	Data source	Reference
Ineichen-Perez	I_0, θ, h, T_L	SoDa database [40]	Ineichen and Perez [37]
McClear	$I_0, \theta, h, \rho_g, P_a, T_a, \tau_{550}, \alpha, u_{O_3}, u_{H_2O}$	CAMS [44]	Lefèvre et al. [32]
REST2	$I_0, \theta, \rho_g, P_a, \tau_{550}, \alpha, u_{O_3}, u_{NO_2}, u_{H_2O}$	NSRDB [49]	Gueymard [33]
Ineichen-Perez TL*	$I_0, \theta, h, P_a, T_a, \phi, V$	Local measurements	Chen and Li [103]

* Ineichen-Perez TL model is also based on T_L . Instead of using the SoDa database, the T_L is estimated from local meteorological measurements (P_a, T_a, ϕ, V) [103].

In this chapter, we apply and compare four clear sky models, namely, the Ineichen-Perez model [37] documented in PVLIB [39] using default turbidity interpolated from SoDa monthly climatology mean database [40], the McClear model [32], the REST2 model [33], and the Ineichen-Perez model using turbidity estimated from the local meteorological measurements [103] (hereafter referred as Ineichen-Perez TL model). Table 3.5 summarizes the input parameters for the aforementioned clear-sky models. The detailed method of estimating the turbidity is introduced in the following subsection. McClear model and REST2 model are physical models, which might be generally superior to those models taking reduced forms or using approximations [36]. However, the physical models are of much more complexity due to their prevailing atmospheric conditions on the attenuation constituents and the application of RTMs. For instance, the REST2 model has repeatedly been validated as one of the models with high-performance [36], but it

requires at least nine input parameters, and some of them such as aerosol optical depth (AOD) at 550 nm, amount of ozone, and precipitable water are difficult to obtain [36, 54]. The clear-sky irradiance of REST2 used in this chapter is from the database of NSRDB. The McClear is also a fully physical model requiring input parameters regarding the optical property of the atmosphere, e.g., the amount of ozone, precipitable water, and AOD at 550 nm [32]. McClear applies a lookup table to speed up the calculation of RTMs, and the clear-sky irradiance is available from the Copernicus Atmosphere Monitoring Service (CAMS) [44]. The time resolution is from 1 minute to 1 month in the time range of 2004-01-01 up to two days ago.

3.2.3 Turbidity estimation

The original method of estimating turbidity via local meteorological measurements is presented in [103]. Although the original model is trained based on the data samples focused on clear-sky days, the results show that the method can also be applied to estimate the turbidity in partially clear days. In this chapter, the data samples from partially clear days are also included in the model training following the same methodology described in [103]. The data used in turbidity estimation for SURFRAD stations are in the year range of 2010 to 2018. The clear-sky instants are detected by the Bright-Sun method described in [112], and the solar zenith angle is set to be less than 85° as the turbidity exhibits high variations during sunrise and sunset [103]. To better represent the GHICs-derived turbidity on a daily basis, only a day with more than one third clear-sky instants detected of the daytime are included (e.g., if the daytime of a day is 8 hours, only when the detected clear-sky instants are more than 2.4 hours, the day will be included in the dataset). It is also necessary to mention that the turbidity typically varies between 1 and 10 [35], so any derived turbidity with the value less than 1 (or extremely high) should be excluded. The turbidity estimation model for each station is trained and validated separately. However, it is possible to build a more universal model by involving more locations using the same methodology. The estimated turbidity is then used as the input to calculate the GHICs using PVLIB.

Since semi-empirical model (e.g., Heliosat-2 method) can be adapted to geostationary satellite in the visible band (0.4 - 1.1 μm) [113], the GOES-16 blue band (visible, 0.47 μm), red band (visible, 0.64 μm), and veggie band (near-infrared, 0.87 μm) are applied and compared for 5-minute GHI estimation in this chapter. Apart from different strategies described in Table 3.3 for determining CI, there are also different methods proposed to calculate the GHI (see Table 3.4). The detailed comparisons of the reported strategies, the proposed methods, as well as the applied clear-sky models for GHI estimation are presented in the following section. The performance evaluation metrics are RMSE, mean bias error (MBE), and their normalized counterparts nRMSE and nMBE defined by the following equations:

$$\text{RMSE} = \sqrt{\frac{1}{N} \sum (e_i - o_i)^2} \quad (3.4)$$

$$\text{nRMSE} = \frac{\sqrt{\frac{1}{N} \sum (e_i - o_i)^2}}{\frac{1}{N} \sum o_i} \quad (3.5)$$

$$\text{MBE} = \frac{1}{N} \sum (e_i - o_i) \quad (3.6)$$

$$\text{nMBE} = \frac{\sum (e_i - o_i)}{\sum o_i} \quad (3.7)$$

where e_i and o_i are the pair of GHI estimation and ground observation, N is the total number of compared data points.

3.3 Results and discussion

Despite difficulties associated in acquiring the input parameters, the REST2 model has been proved as the one of the best clear-sky models for estimating clear-sky irradiance [34]. Given that the clear-sky irradiance of REST2 is available in the dataset of NSRDB and the fact that a better clear-sky model (i.e., McClear) can lead to better GHI estimation results [56], we use the REST2 GHICs in the comparison of the GHI estimation performance based on different ABI bands, empirical regressions between CSI and CI, and methods to determine the CI. The information of used ABI bands is presented in Table 3.1, Table 3.3 details the strategies used for deriving CI, and the methods for GHI calculation via GHICs, CSI, and CI are listed in Table 3.4. The comparison of different clear-sky models used in GHI estimation with semi-empirical method is then based on the combined approach (i.e., the ABI band, CI derivation, and GHI calculation) that is likely to obtain superior GHI estimation results.

3.3.1 Comparison of ABI bands and derivation methods for CI and CSI

Since the GOES-16 ABI bands have different spatial resolution, Band 2 (red) is re-scaled to the same resolution as Band 1 and Band 3. The comparison of upper and lower bounds determination based on different ABI bands and strategies at DRA is presented in Fig. 3.2. The upper bound from Band 1 has higher values than Bands 2 and 3, while Band 3 results in relatively lower upper bounds no matter what strategy is applied. Similarly, lower bound based on Band 1 turns to be higher, followed by Band 2 and Band 3 has the comparatively lower value. Unlike upper bounds that do not show many fluctuations, lower bounds have relatively larger variations. Compared with Strategies 1 and 2, Strategies 3 and 4 generally leads to larger upper bound and smaller lower bound. The reason could be the shorter periods and less points used for

determining upper and lower bounds as shown in Table 3.3. This also results in wider dynamic ranges, i.e., the differences between upper and lower bounds, which exhibit similar trends with the upper bound, Band 1 leads to higher value than Bands 2 and 3, while Band 3 has the lowest value.

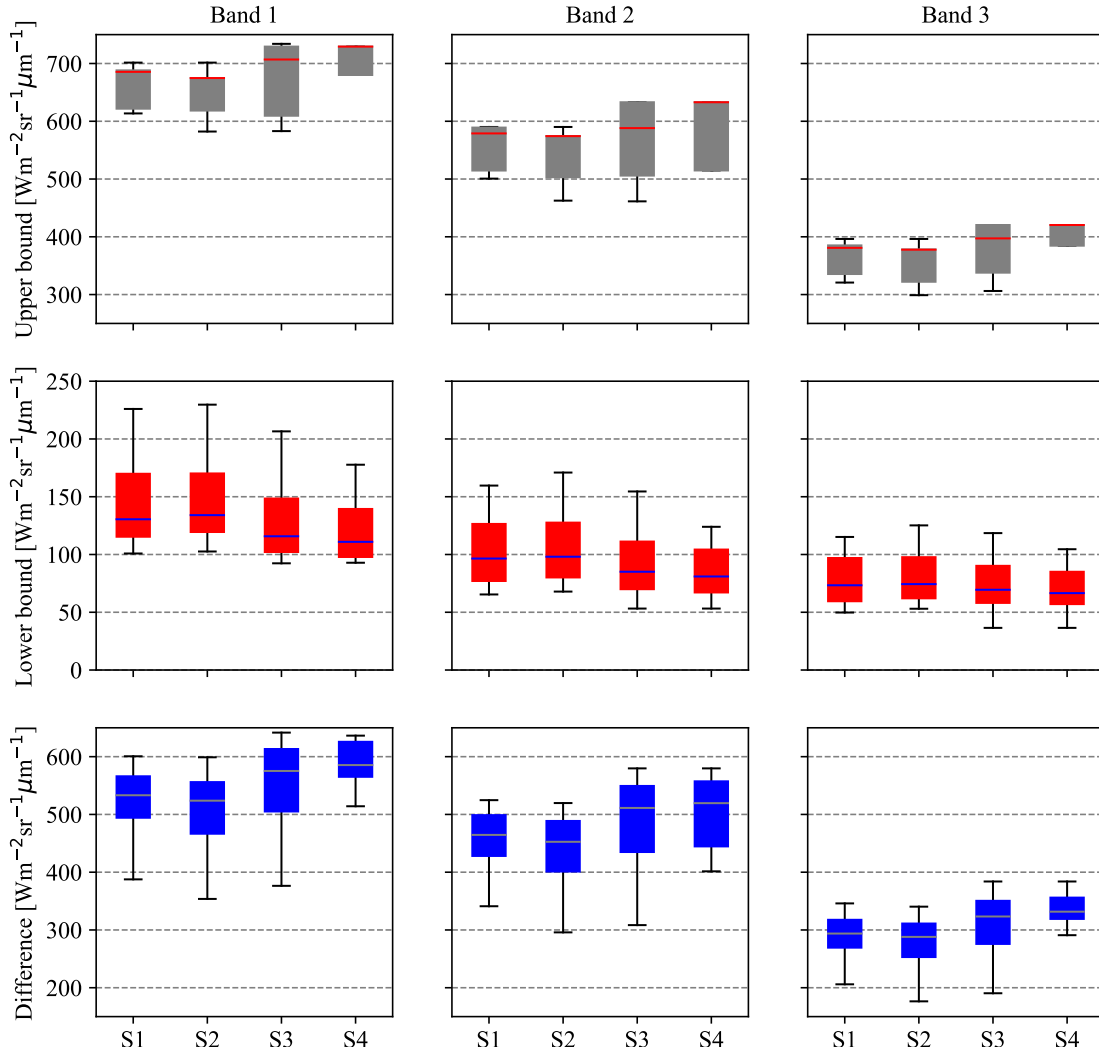


Figure 3.2: Comparison of the upper bound and lower bound determination using different ABI bands (see Table 3.1) and strategies at DRA (2019-01-01 to 2019-05-31). S1-S4 are the symbols of strategies presented in Table 3.3. The differences between upper and lower bounds are also included for comparison. The lines in the box plots are the median values.

Upper and lower bounds are used to determine CI, CSI is then calculated from CI using empirical regressions (see Table 3.4). Fig. 3.3 shows the comparison of CSI calculations from different bands, CI derivation strategies, and CI-to-CSI methods, where the CSI reference is the ratio between GHI measurement and GHICs from REST2 clear-sky model. Generally, the CSI derived from Band 1 has smaller divergences

in terms of nRMSE and nMBE with the referenced CSI compared with the other two bands, while Band 3 shows relatively larger differences no matter what CI derivation strategy and CI-to-CSI method are applied. Among the used CI derivation strategies, they have comparable results in terms of nRMSE, while Strategies 3 and 4 produce lower biases compared with Strategies 1 and 2. Similarly, there is no huge difference when comparing the CI-to-CSI methods regarding nRMSE. However, Methods 3 and 4 are more likely to yield lower nMBE values. It is worthwhile to mention that the combination of Band 1, Strategy 4, and Method 3 (or Method 4) outperforms other combinations with comparatively smaller nRMSE and nMBE.

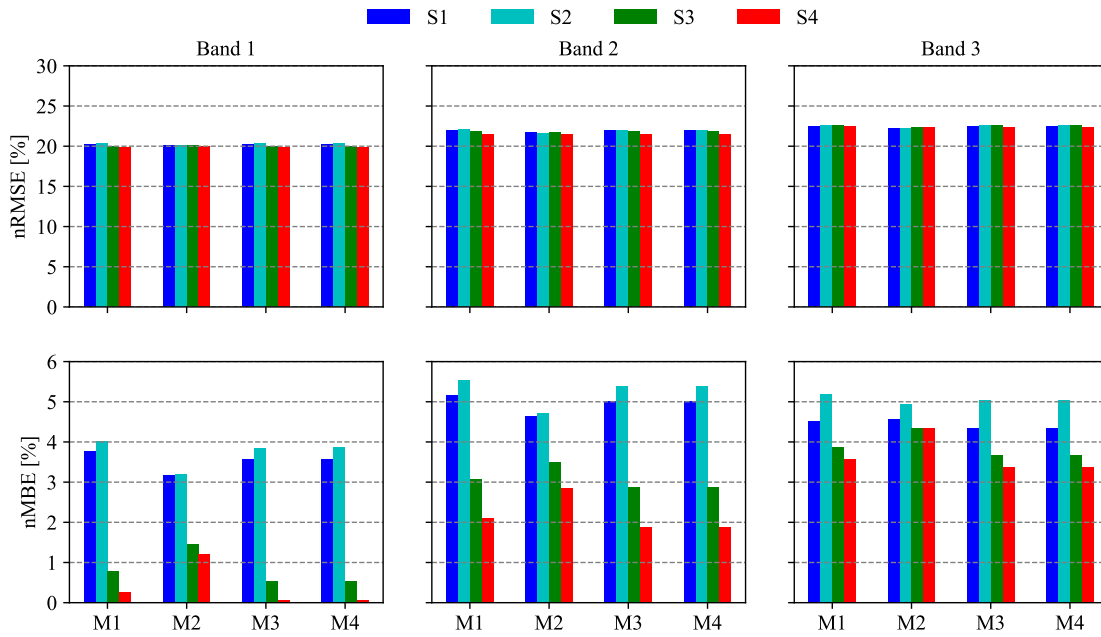


Figure 3.3: The nRMSE and nMBE of the CSI reference and estimation based on different bands, dynamic range and CI derivation, and empirical regressions between CSI and CI at DRA (2019-01-01 to 2019-05-31). The reference CSI is determined using GHI measurements and REST2 clear-sky model. S1-S4 are the symbols of strategies presented in Table 3.3, and M1-M4 represent the empirical methods described in Table 3.4.

A detailed comparison of different bands and methods used to estimate GHI is illustrated in Fig. 3.4. Using Method 2 generally yields GHI estimation with larger nRMSE and nMBE values, while the rest of the three methods have comparable GHI estimation results with similar nRMSE. Method 1 leads to slightly higher nMBE values than Methods 3 and 4. When it comes to the dynamic range and CI determination, all the strategies generate GHI estimation with nRMSE greater than 20% no matter which method is used, while Strategies 1 and 2 have slightly larger values. Moreover, Strategies 1 and 2 show comparatively larger

discrepancies in nMBE than Strategies 3 and 4, while Strategy 4 produces the lowest nMBE. There is no significant difference (i.e., nRMSE and nMBE) in Methods 3 and 4 to calculate GHI via the relationship between CSI and CI regardless of which strategy is applied to derive the dynamic range and CI. The combination of Strategy 4 and Method 3 (or Method 4) is likely to generate GHI estimations with lower nRMSE and nMBE. Strategies 1 and 2 are proposed for GHI estimation at a rough time resolution (e.g., hourly), which might be inappropriate when the time resolution is much improved to 5-minute. Therefore, the subsequent results and discussion are based on the combination of Strategy 4 and Method 3 in 5-minute GHI estimation.

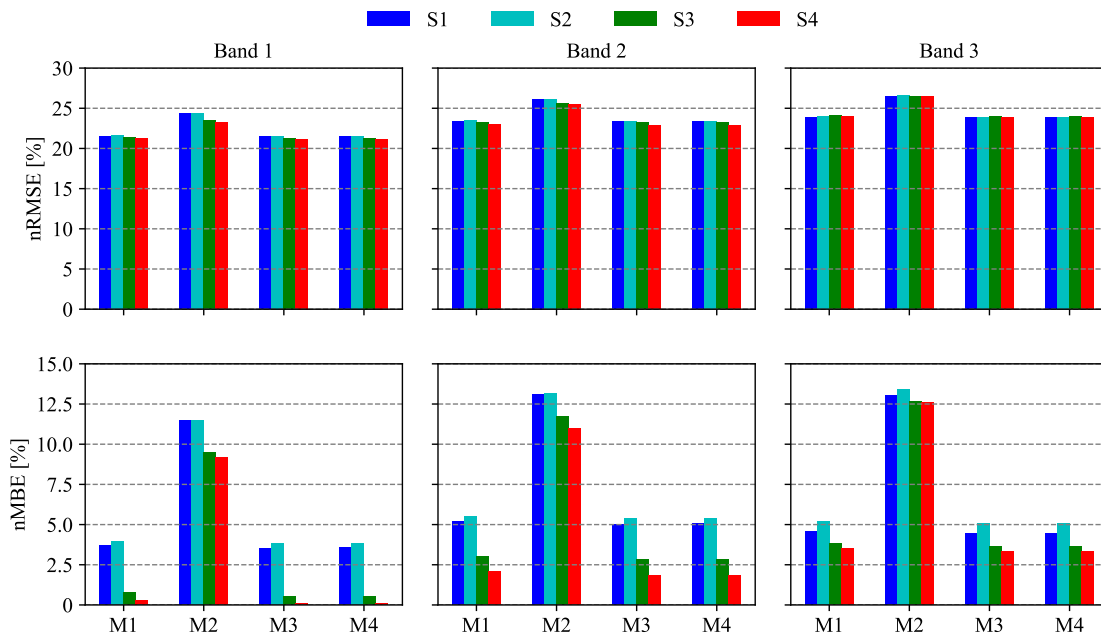


Figure 3.4: The nRMSE and nMBE between the GHI measurements and estimations based on different bands, dynamic range and CI derivation, and empirical regressions between GHI and CI using REST2 clear-sky model at DRA (2019-01-01 to 2019-05-31). S1-S4 are the symbols of strategies presented in Table 3.3, and M1-M4 represent the empirical methods described in Table 3.4.

It is shown in Fig. 3.4 that Band 1 generally produces lower nRMSE and nMBE values than Bands 2 and 3 no matter which combination of method and strategy is applied in estimating GHI. The possible explanation could be that Band 1 results in higher upper and lower bounds as well as wider dynamic ranges (see Fig. 3.2), which are less sensitive to the uncertainties in sensor’s measurements when determining the dynamic range for CI derivation. Therefore, the estimated CSI from Band 1 show comparatively lower discrepancies than Bands 2 and 3 (see Fig. 3.3) and thus better GHI estimations. To further evaluate the

performance of GHI estimation using different ABI bands, it is necessary to ensure that the used methods, data points, and time periods are the same. Therefore, the REST2 clear-sky model, Strategy 4, and Method 3 are set as the preconditions for comparing the ABI bands used in semi-empirical model for GHI estimation.

Table 3.6: Summary of the ABI band performance in 5-minute GHI estimation using RSET2 clear-sky model, Strategy 4, and Method 3 at DRA (2019-01-01 to 2019-05-31). The GHI estimation from NSRDB is also included as reference.

Band	RMSE [W m^{-2}]	nRMSE [%]	MBE [W m^{-2}]	nMBE [%]
1	109.37	21.47	7.18	1.41
2	117.73	23.11	15.21	2.99
3	124.05	24.35	22.75	4.46
NSRDB	110.79	21.74	-13.44	-2.64

Table 3.6 details the performance of different ABI bands used for GHI estimation. Band 1 generates the lowest divergence with a nRMSE of 21.47% and a nMBE of 1.41%, while Band 3 produces the largest nRMSE of 24.35% and nMBE of 4.46%. The reflective spectral radiance measured by the ABI sensor used in GHI estimation with semi-empirical models leads to decreased performance when using bands with larger wavelength. It is worthwhile to mention that the GHI estimates based on Band 1 using semi-empirical model have slightly lower errors of nRMSE and nMBE than the results from NSRDB, which means the semi-empirical model may produce comparable results with physical models but with less complexity.

3.3.2 Comparison of clear-sky models for GHI estimation

Based on the results from the previous subsections, a better GHI estimation is achieved using the measurements of ABI Band 1, the Strategy 4 for dynamic range and CI determination, and the Method 3 for CI to GHI conversion. At this stage, the prerequisites for evaluating the performance of different clear-sky models in GHI estimation using semi-empirical model have been settled. The following sections present the comparisons between different clear-sky models applied in semi-empirical method under different sky conditions. We use two types of methods for classifying sky conditions here: one is based on days, in which the days are classified as cloudy, partially cloudy, and clear days [114]; The other one is based on periods, where the instants are grouped as cloudy and clear periods [80]. In specific, clear and cloudy instants are detected using the Bright-Sun method with ground irradiance measurements [112] and then clustered as clear/cloudy/partially cloudy days and clear/cloudy periods.

3.3.2.1 Comparison under cloudy, partially cloudy and clear days

The overall performance of GHI estimation using semi-empirical method with different clear-sky models is shown in Table 3.7. There is no significant discrepancy between clear-sky models in GHI estimation under conditions of all-sky, cloudy, and partially cloudy. REST2 is likely to generate slightly lower nRMSE in all-sky and partially cloudy conditions, while Ineichen-Perez yields the lowest nRMSE when only cloudy days are considered. Compared with the physical model based GHI estimation results in NSRDB, using semi-empirical model produces GHI estimates with similar or slightly larger nRMSE no matter which clear-sky model is applied. However, there are comparatively larger biases (i.e., nMBE) in semi-empirical methods under most conditions.

Table 3.7: The overall nRMSE [%] and nMBE [%] between GHI estimations and measurements at seven SURFRAD stations using semi-empirical method with different clear-sky models under four evaluation cases (all-sky, cloudy days, partially cloudy days, and clear days). The GHI estimation from NSRDB is also included for comparison.

	All-sky ¹		Cloudy days ²		Partially cloudy days ³		Clear days ⁴	
	nRMSE	nMBE	nRMSE	nMBE	nRMSE	nMBE	nRMSE	nMBE
Ineichen-Perez	25.43	2.03	37.60	9.20	19.54	-1.61	5.77	-4.62
McClear	25.38	5.42	38.03	11.87	19.23	1.94	2.55	0.62
REST2	25.19	4.87	37.68	11.32	19.13	1.45	2.53	-0.15
Ineichen-Perez TL	25.53	5.22	38.36	12.80	19.24	1.23	2.53	-1.11
NSRDB	25.25	-0.45	38.37	-1.50	18.75	0.23	2.37	0.45

¹ ‘All-sky’ means the whole time period with cloudy, partially cloudy and clear days.

² ‘Cloudy days’ means the days without clear-sky periods or the detected clear-sky instants are less than one third of the daytime.

³ ‘Partially cloudy days’ includes the days with cloudless periods (more than one third of the daytime).

⁴ ‘Clear days’ only involves the cloudless days.

Semi-empirical methods are more possibly to have overestimated results, especially in the cloudy days. Although Ineichen-Perez produces the lowest nMBE in all-sky and cloudy conditions, it does not mean Ineichen-Perez provides better clear-sky irradiance estimations. The low overall bias of Ineichen-Perez in GHI estimations is a compromise of the overestimation in semi-empirical methods and the underestimation

in Ineichen-Perez’s clear-sky irradiance, since the Ineichen-Perez based GHI estimations in partially cloudy and clear-sky days show negative biases of -1.61% and -4.62%, respectively.

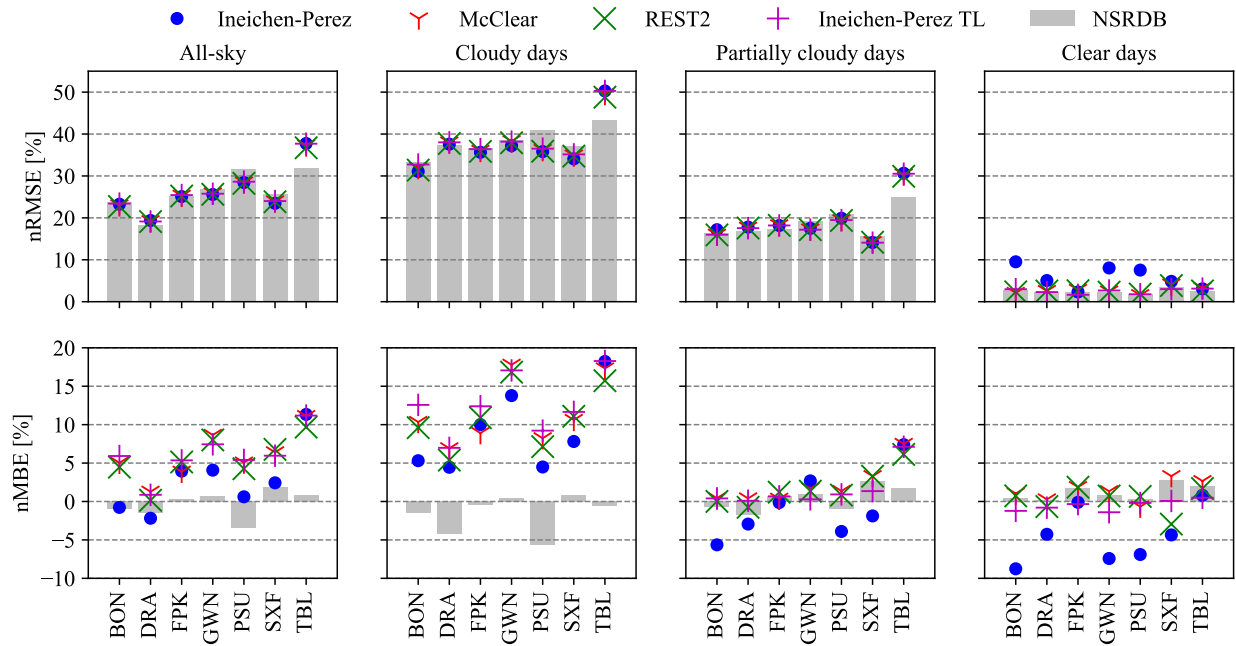


Figure 3.5: The nRMSE and nMBE between the measured and estimated GHI for four clear-sky models in semi-empirical method, seven SURFRAD stations, and four evaluated conditions (all-sky, cloudy days, partially cloudy days, and clear days). GHI estimation from NSRDB is also included for comparison.

Fig. 3.5 presents the detailed comparison of different clear-sky models for GHI estimation using semi-empirical method at seven SURFRAD stations under four sky conditions. The GHI estimations based on four clear-sky models have comparable results in terms of nRMSE under all-sky, cloudy and partially cloudy conditions, while Ineichen-Perez tends to generate larger nRMSE values in clear-sky days. Compared with the physical model based GHI estimation results in NSRDB, using semi-empirical model produces GHI estimates with similar or slightly lower nRMSE at most SURFRAD stations except TBL, where the occurrence of cloudy days is comparatively higher. For each individual station, the GHI estimation under cloudy days is most likely associated with the largest uncertainties of nRMSE and nMBE. The lower biases of Ineichen-Perez based GHI estimations under all-sky and cloudy conditions are shown in some of the stations (i.e., BON, GWN, PSU, and SXF), whose biases are apparently higher in partially cloudy and clear conditions compared with other clear-sky models, proving the overestimation in semi-empirical methods and the underestimation in Ineichen-Perez’s clear-sky irradiance.

The primary uncertainty for GHI estimation is caused by the clouds for both physical and semi-empirical

methods. The nRMSE of GHI estimates in cloudy days are in the range of 37.60%-38.37%, which is approximate two times of the nRMSE in partially cloudy days (18.75%-19.54%). The nRMSE in clear-sky days are around 2.50% besides Ineichen-Perez, which has a larger value of 5.77%. Since clouds are the primary factor affecting the solar irradiance reaching the ground level, it is necessary to improve the method to account the irradiance attenuation caused by clouds for both physical and semi-empirical models. That said, the future research on satellite-based solar resourcing could be the improvements of satellite-derived cloud properties (for physical model) and cloud attenuation determinations (for semi-empirical model).

3.3.2.2 Comparison under cloudy and clear periods

To further evaluate the performance of GHI estimation using semi-empirical model under different conditions, the sky is divided into cloudy and clear based on periods. The overall comparison at seven SURFRAD stations is shown in Table 3.8. Similarly, the GHI estimation in cloudy periods is associated with larger uncertainties (e.g., nRMSE), and semi-empirical model is likely to yield higher bias than the physical model. In cloudless periods, all the clear-sky models except Ineichen-Perez produce comparable results with NSRDB. When using GHICs directly as the GHI estimates, Ineichen-Perez generates the largest errors, and Ineichen-Perez TL yields better results than other three clear-sky models.

Table 3.8: The overall nRMSE [%] and nMBE [%] between GHI estimations and measurements at seven SURFRAD stations using semi-empirical method with different clear-sky models under three evaluation cases (all-sky, cloudy periods, and clear periods). The GHI estimation from NSRDB is also included.

	All-sky ¹		Cloudy periods ²		Clear periods ³		GHICs ⁴	
	nRMSE	nMBE	nRMSE	nMBE	nRMSE	nMBE	nRMSE	nMBE
Ineichen-Perez	25.43	2.03	31.23	5.03	5.37	-3.93	4.86	-3.29
McClear	25.38	5.42	31.36	8.87	2.98	0.56	2.54	1.22
REST2	25.19	4.87	31.12	8.23	2.91	-0.07	2.43	0.52
Ineichen-Perez TL	25.53	5.22	31.54	9.20	2.81	-0.86	2.16	-0.20
NSRDB	25.25	-0.45	31.21	-1.01	2.43	0.52	-	-

¹ ‘All-sky’ means the whole time period with cloudy and clear instants.

² ‘Cloudy periods’ contains the periods are detected as cloudy.

³ ‘Clear periods’ includes all the detected cloudless periods.

⁴ ‘GHICs’ is to use GHICs directly as GHI estimation in clear periods.

The detailed comparison of GHI estimation under cloudy and clear instants for all the SURFRAD stations is presented in Fig. 3.6. Semi-empirical model tends to overestimate GHI with comparatively larger positive biases in cloudy periods, and the highest bias can be about 15% at TBL. In the application of semi-empirical method, Ineichen-Perez generally produces lower bias than the other three clear-sky models under cloudy conditions. However, in cloudless periods, Ineichen-Perez is likely to produce GHI estimation with larger discrepancies. The possible explanation for this is the same as the phenomenon that Ineichen-Perez produces GHI estimation with lower biases in all-sky and cloudy days as discussed in the Section 3.3.2.1.

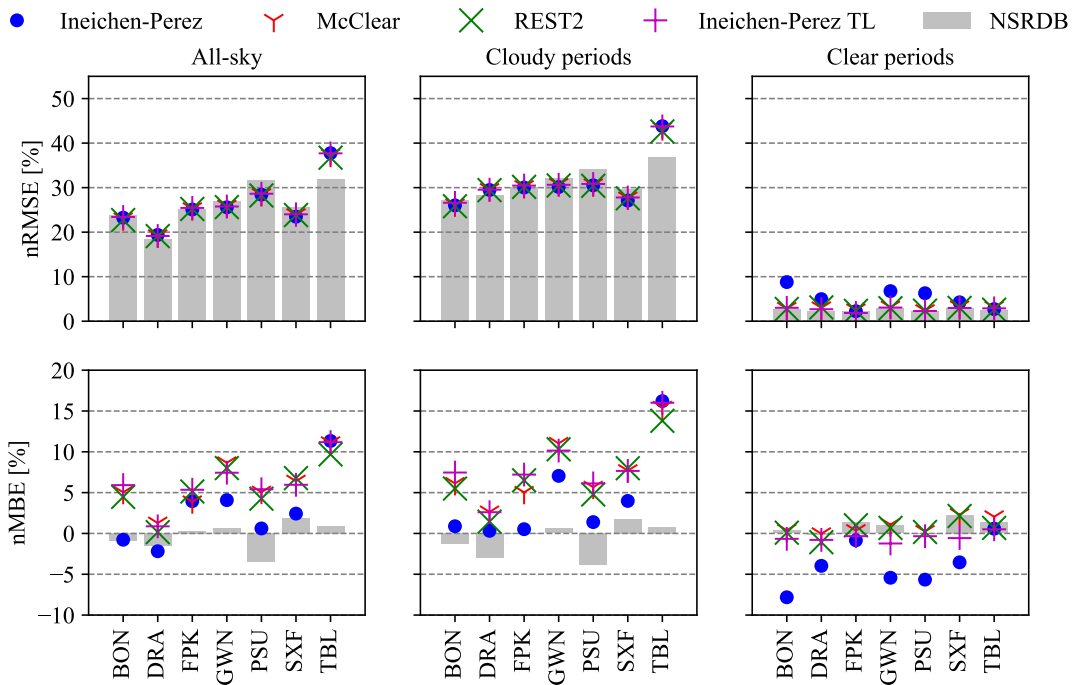


Figure 3.6: The nRMSE and nMBE between the GHI measurements and estimates using semi-empirical method for four clear-sky models, seven SURFRAD stations, and three evaluation conditions (all-sky, cloudy periods, and clear periods).

3.3.2.3 Comparison between physical and semi-empirical methods for GHI estimation

In physical model for GHI estimation, the GHICs is directly used as the GHI estimate when the sky is free from cloud. Where the accuracy of used clear-sky model is crucial for the overall GHI estimation performance. Generally, physical GHI estimation methods apply physical clear-sky model, for instance, REST2 in NSRDB, McClear in Heliosat-4. It might be of interest to compare the performance of GHI estimation using semi-empirical and physical models under clear-sky conditions. As shown in Table 3.8, it

is more likely to generate GHI results with relatively lower nRMSE values using GHICs as GHI estimates (nRMSE ranges from 2.16% to 4.86%) than CI based method (nRMSE varies from 2.81%-5.37%). The situation of nMBE differs, McClear and REST2 produce larger biases, while Ineichen-Perez and Ineichen-Perez TL yield slightly lower nMBE values. It is worthwhile to mention that Ineichen-Perez TL has the lowest nRMSE and nMBE, which means Ineichen-Perez TL has the potential to improve GHI estimation in physical models.

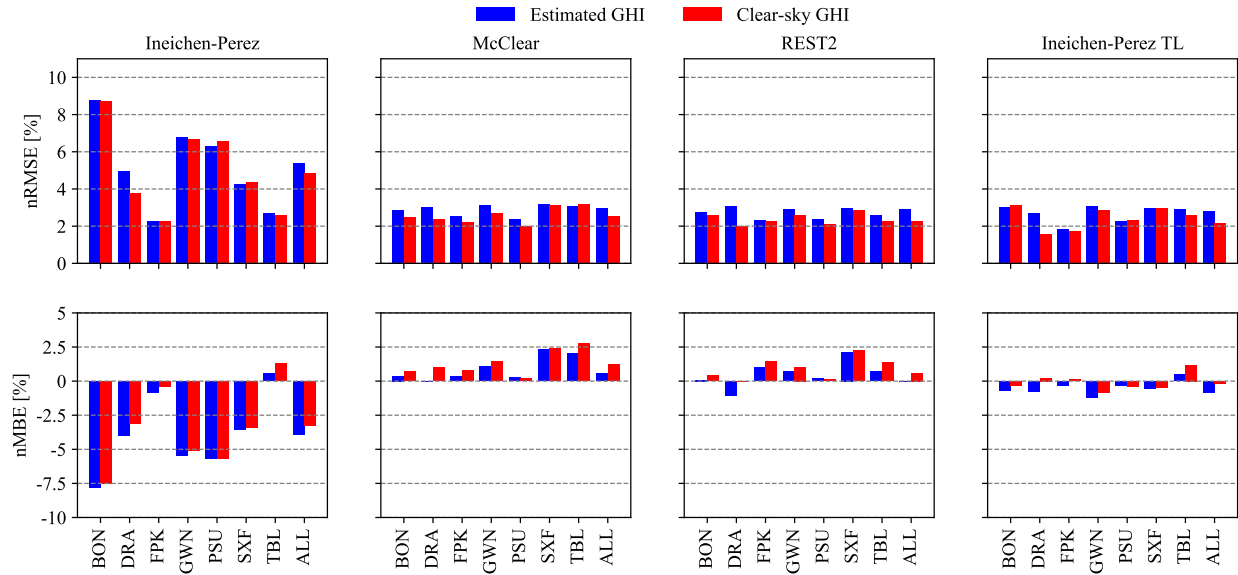


Figure 3.7: The nRMSE and nMBE between the GHI measurements and estimates in clear periods for four clear-sky models, and seven SURFRAD stations. ‘ALL’ means all the seven stations are included. ‘Estimated GHI’ means the GHI estimates of semi-empirical model. ‘Clear-sky GHI’ means the GHICs directly calculated from clear-sky models.

The detailed comparison of GHI estimates using semi-empirical model and GHICs for SURFRAD stations is presented in Fig. 3.7. Generally, both estimated and GHICs of Ineichen-Perez show larger nRMSE and nMBE at most of the stations except FPK. Better clear-sky models, such as McClear and REST2, are likely to produce better GHI estimations with relatively lower nRMSE and nMBE in cloudless periods using both semi-empirical and physical models. Ineichen-Perez tends to yield negative biases in GHI estimations or using GHICs directly due to its underestimation of clear-sky irradiance. Ineichen-Perez TL produces comparable results with McClear and REST2 in terms of nRMSE, while the biases tend to be smaller. For McClear, REST2, and Ineichen-Perez TL, using the semi-empirical model is probably to generate GHI estimation with larger nRMSE and nMBE compared with the direct GHI estimates from GHICs. Which means

another challenge of semi-empirical method is how to improve the CI and CSI derivation considering the variations in clear-sky irradiance caused by the dynamics of aerosol and water vapor in the atmosphere.

All the applied clear-sky models yield comparable overall results of GHI estimations (see Table 3.7 and Table 3.8) using semi-empirical method, REST2 has the lowest nRMSE of 25.19% while Ineichen-Perez TL has the highest nRMSE of 25.53%. Ineichen-Perez performs better than other clear-sky models in terms of nRMSE and nMBE under cloudy conditions, while Ineichen-Perez TL produces the largest nRMSE and nMBE. Although Ineichen-Perez has the lowest biases in GHI estimation under all-sky and cloudy conditions, it does not mean that Ineichen-Perez provides better clear-sky irradiance, as there is a compromise of the overestimation of GHI using semi-empirical model and the underestimation of Ineichen-Perez's GHICs. Ineichen-Perez tends to generate negative biases in clear conditions, with the largest nMBE of -4.62% in clear-sky days and -3.93% in cloudless periods. When comparing the two physical clear-sky models of McClear and REST2 in the application of semi-empirical method, REST2 outperforms McClear in all the sky conditions with slightly lower nRMSE and nMBE. Compared with Ineichen-Perez, Ineichen-Perez TL has lower values of nRMSE and nMBE in partially cloudy days and clear conditions. The GHI estimation in each individual station (see Fig. 3.5 and Fig. 3.6) exhibits similar results as the overall picture but with some site-specific divergences. It is important to note that Ineichen-Perez TL generally performs better than other clear-sky models when using GHICs as the GHI estimations in clear periods with comparatively lower nRMSE and nMBE.

3.4 Conclusions

In this chapter, different strategies for dynamic range and CI determination, methods to calculate GHI via GHICs, CSI and CI are compared in 5-minute averaged GHI estimation using semi-empirical model and GOES-16 images. Then, a comparison of three different ABI bands (i.e., blue, red, veggie) in GHI estimation is performed. Finally, the performance of four clear-sky models in GHI estimation using the same semi-empirical method is evaluated under different sky conditions. The key findings are:

- More accurate 5-minute averaged GHI estimates are achieved using a fixed time window (i.e., Strategy 4), Method 3 (or Method 4) of GHI conversion from CI and CSI, and Band 1 for solar resourcing applications (e.g., GHI assessment). A fixed time window is easy to implement without much computing resource, but it is not suitable for operational applications, such as solar forecasting, where a moving time window is required.

- There is no significant difference in GHI estimation using different clear-sky models, the semi-empirical model yields comparable results compared with the NRSDB, but with comparatively larger biases. Semi-empirical model tends to overestimate the GHI in cloudy conditions, the uncertainties in cloudy periods are noticeably higher than cloud free conditions. Therefore, it is crucial to determine the irradiance attenuation caused by clouds for both physical and semi-empirical models.
- In the application of semi-empirical method, Ineichen-Perez has lower biases under all-sky and cloudy conditions, this does not mean Ineichen-Perez provides better clear-sky irradiance due to the compromise of overestimation in semi-empirical model and Ineichen-Perez's underestimation of clear-sky irradiance. REST2 generally outperforms McClear under all sky conditions.
- Ineichen-Perez TL, as a modified model based on estimated turbidity, provides GHI estimation using semi-empirical method with slightly larger values of nRMSE and nMBE in all-sky and cloudy conditions. The performance of Ineichen-Perez TL under partially cloudy day and clear periods is comparable with McClear and REST2, and comparatively better than Ineichen-Perez. When using clear-sky irradiance as the direct estimation of GHI, Ineichen-Perez TL has a better performance.
- A better clear-sky model (e.g., REST2 versus McClear) can generally lead to better GHI estimation using semi-empirical method. Considering the difficulties associated in obtaining the atmospheric inputs of REST2, and the limited divergences in GHI estimation between these two clear-sky models, McClear is more appropriate due to its global availability. Ineichen-Perez TL provides better clear-sky irradiance for clear-sky conditions, therefore has the potential for the improvements in physical models where clear-sky irradiance is directly used as GHI estimation.

3.5 Acknowledgement

This chapter, in full, is a reprint of S. Chen, Z. Liang, S. Guo, and M. Li (2022). Estimation of high-resolution solar irradiance data using optimized semi-empirical satellite method and GOES-16 imagery. *Solar Energy*, 241, 404-415. The thesis author is the first author of this paper.

Chapter 4

A transferable turbidity estimation method for estimating clear-sky solar irradiance

4.1 Introduction

Clear-sky models, which estimate ground-level solar irradiance under clear-sky (cloudless) conditions, are an important part in solar resourcing and forecasting applications to support solar energy projects [8, 36, 49, 55]. In solar resourcing, the ground solar irradiance, e.g., global horizontal irradiance (GHI), can be retrieved from satellite images using either physical or semi-empirical satellite methods based on a clear-sky model [8]. The retrieved solar irradiance data can help with the project feasibility study and optimal system design when there is no on-site ground irradiance measurement available [8, 12, 47]; Moreover, clear-sky models are also essential in solar forecasting to reduce the negative impact on the system operation caused by the intermittency and variability [8, 14, 36]. The solar forecasts usually rely on the clear-sky index (CSI), which has different definitions depending on the forecasting method. CSI is the ratio of measured GHI and clear-sky GHI (GHIcs) in a time series forecasting [36]. Meanwhile, CSI can also be calculated from the cloud index (CI) based on the satellite images [8, 55], which is particularly applied for locations without sufficient solar irradiance data.

In physical-based solar resourcing methods, radiative transfer simulation is applied through through various layers in the atmosphere taking the advantage of modern satellite remote sensing technologies [49, 50]. Where the physical clear-sky models, e.g., McClear [32] and REST2 [33], are used to quantify the surface solar irradiance when the sky is free from clouds. The essential inputs such as aerosol properties, atmospheric profiles, and surface albedo can be obtained from a number of reanalysis products including the Modern-

Era Retrospective Analysis for Research and Applications, Version 2 (MERRA-2), Moderate Resolution Imaging Spectroradiometer (MODIS), and Copernicus Atmosphere Monitoring Service (CAMS) reanalysis [49, 50]. As a major modulator attenuating the solar irradiance in the atmosphere, the cloud properties can be derived from the geostationary satellites, for example, Geostationary Operational Environmental Satellite (GOES) and Meteosat Second Generation (MSG) satellites. Although physical methods generally have better performance as they technically require more detailed atmospheric inputs [8], the inputs acquisition and model implementation are typically associated with difficulties and uncertainties [36, 54].

In semi-empirical satellite methods for solar resourcing, a clear-sky model is used to determine the clear-sky irradiance, i.e., GHIs, which accounts for the irradiance attenuation of aerosol, water vapor content, and other gaseous atmospheric constituents [8]. While the effect of clouds relies on the CI and CSI derived from a set of satellite images within a period [37, 58]. Semi-empirical satellite methods are much easier and faster to apply, and the combination with a physical clear-sky model can improve the performance [56]. In Chapter 3, we compared four clear-sky models, namely, REST2, McClear, Ineichen-Perez [31], and Ineichen-Perez TL in GHI estimation using optimized semi-empirical satellite method and GOES-16 imagery. The results show the performance of semi-empirical satellite method is comparable with the physical method, i.e., National Solar Radiation Database (NSRDB) [49]. The Ineichen-Perez TL even produces better GHIs estimations than McClear and REST2, therefore, has potential in supporting solar resourcing applications. The Ineichen-Perez TL model is based on the Ineichen-Perez model using Linke turbidity (T_L) estimated from common local meteorological measurements [103].

When it comes to solar forecasting, the clear-sky model is suggested to deseasonalize the variations of solar irradiance using CSI in the development of solar forecasting models [21]. Generally, local sensing is particularly suitable for intra-hour forecasting with adequate on-site instrument [10, 79]; Numeric Weather Prediction (NWP) performs better in day-ahead forecasting, but the computation is demanding and the initial boundary conditions may inherit biases [8]; Satellite-based method is popular for intra-day forecasting where the satellite images are used to identify and forecast the cloud distribution [8, 21]. Yang [36] discussed the choice of clear-sky models in time series solar forecasting, it is reported that a better clear-sky model does not yield better forecasts and McClear model is recommended due to its global availability. However, in practical forecasting applications, the clear-sky irradiance of McClear model is not readily available as an online service that can only be downloaded since 2004-01-01 up to two days ago [44]. Moreover, the required atmospheric inputs of physical clear-sky models (e.g., REST2 and McClear) are difficult to obtain [36, 54], their forecasts are therefore associated with more difficulties. In the development of solar forecasting models, the clear-sky irradiance of the applied clear-sky model (e.g., REST2 or McClear) is

assumed to be available, which may not be known a priori for real-time applications.

The Ineichen-Perez model in PVLIB [39] based on T_L from SoDa database [40] is extensively applied in solar forecasting due to its simplicity in implementation [36]. Recently, a new T_L estimation method is proposed to improve the accuracy of T_L estimation using meteorological measurements [103]. The improved T_L estimation is then used as the input of the Ineichen-Perez model with noticeable accuracy improvement in estimating clear-sky irradiance. Considering that the forecasts of meteorological information such as temperature and humidity are far more accurate than solar irradiance forecasts [21], the Ineichen-Perez TL model based on T_L estimated via meteorological information has broad potential in supporting solar forecasting applications.

Despite the potentials of the aforementioned T_L estimation method, it has one limitation that on-site solar irradiance data is required for model development. However, solar irradiance measurements might not be always available due to technical and financial constraints [12, 115]. To further expand the applicability of the T_L estimation method, in this work, we herein propose a transferable T_L estimation model based on the methodology presented in [103]. Instead of using local solar irradiance measurements for model development, we first train the model involving the locations with sufficient data, and then apply the developed model at the location of interest for T_L estimation and then clear-sky irradiance estimation. The main meteorological inputs are ambient temperature, relative humidity, wind speed, and atmospheric pressure, which are available at most of the weather stations or can be easily obtained using low-cost instrumentation. The major contributions of this chapter are summarized as follows:

- Develops a transferable T_L estimation method using common meteorological measurements.
- Compares and evaluates the performance of the transferable T_L estimation method with SoDa interpolated (the default T_L used in PVLIB) and locally estimated T_L .
- Further compares the performance of GHIs estimation with high-performance physical models including McClear and REST2.
- Evaluates the performance of the transferable T_L estimation model for solar forecasting applications by comparing with physical models.

The remainder of this chapter is structured as follows: Section 4.2 describes the used data, the T_L estimation method, and details of clear-sky models. The performance of the T_L estimation method, and clear-sky models for GHI estimation and discussion are presented in Section 4.3. Finally, the key findings of this chapter and recommendations are summarized in Section 4.4.

4.2 Data and methods

This section describes the used data and the transferred T_L estimation method. As shown in Fig. 4.1, we first develop the T_L estimation model involving stations with sufficient solar irradiance data, and then apply the trained model at locations of interest where solar irradiance measurement is not available. The meteorological inputs are ambient temperature, relative humidity, wind speed, and atmospheric pressure, which are easy to obtain and available at most of the weather stations. There are mainly four steps involved in the T_L estimation, namely, clear-sky detection, T_L derivation, model development, and model transfer for T_L and clear-sky irradiance estimations. The details of the used method for each step are presented in the following subsections.

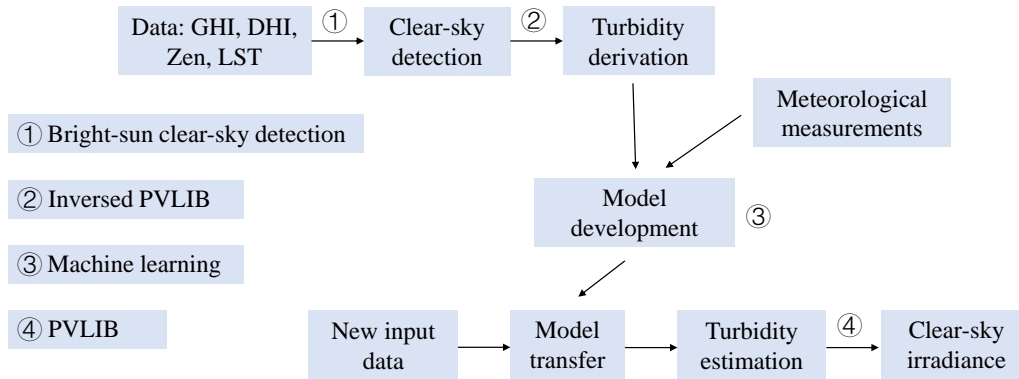


Figure 4.1: The flowchart of transferred T_L estimation model using machine learning and meteorological measurements.

4.2.1 Data

The data used in this chapter is from the Surface Radiation Budget Network (SURFRAD) stations [29], namely, Bondville (BON), Desert Rock (DRA), Fort Peck (FPK), Goodwin Creek (GWN), Pennsylvania State University (PSU), Sioux Falls (SXF), and Table Mountain (TBL). The detailed information of the SURFRAD stations is presented in Fig. 4.2. Data including GHI, diffuse horizontal irradiance (DHI), solar zenith angle, and meteorological measurements over 2010-2020 of all the stations are downloaded and quality controlled. The used meteorological data includes ambient temperature, relative humidity, wind speed, and atmospheric pressure. All the aforementioned measurements are in the time resolution of 1 minute and indexed using coordinated universal time (UTC). Note that the GHI and other data at solar zenith angles over 85° are removed, since the GHI value is very low, and the derived T_L is unrealistic due to the high airmass effect [103].

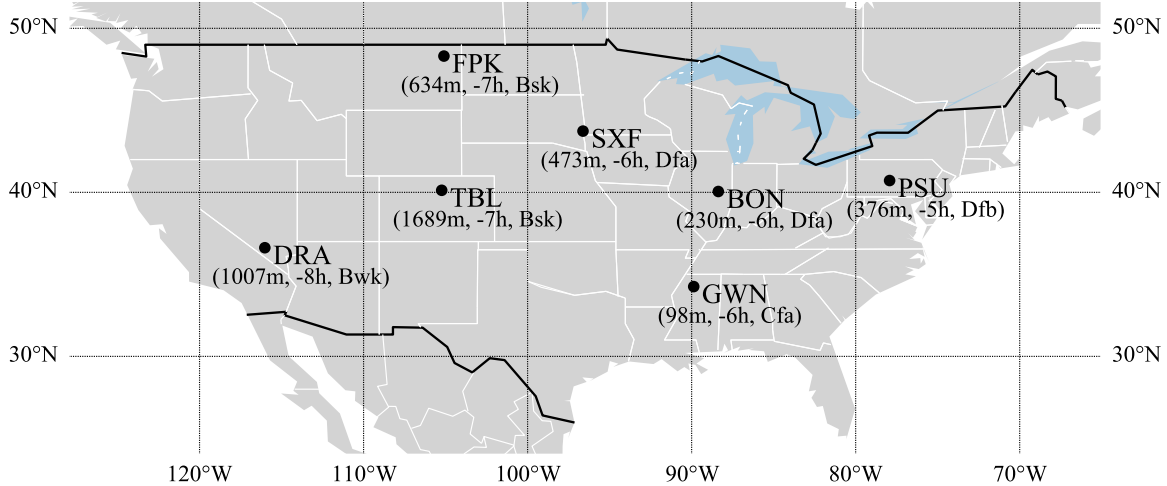


Figure 4.2: Summary of the seven SURFRAD stations. The information in the brackets is (altitude [m], time difference from UTC [hours], climate classifications), where Köppen climate classifications are: Bsk (arid, steppe, cold), Bwk (arid, desert, cold), Cfa (temperate, without dry season, hot summer), Dfa (continental, without dry season, hot summer), Dfb (continental, without dry season, warm summer).

4.2.2 Clear-sky models

The clear-sky models used for comparison in this chapter are REST2 [33], McClear [32], Ineichen-Perez [31] model using default T_L (available in PVLIB [39]). The physical REST2 model has repeatedly been verified as one of the high-performance models [34, 105], and many of the required input parameters, such as aerosol optical depth (AOD) at 550 nm, amount of ozone, and precipitable water need to be locally measured or remotely sensed [33, 36]. The clear-sky irradiance of REST2 used in this chapter is from the NSRDB [49] with a time resolution of 5-minute. The McClear is also a fully physical model requiring atmospheric inputs including AOD at 550 nm, ozone amount, water vapor content, and the aerosol type [32]. McClear applies a lookup table to speed up the RTMs calculations, and the clear-sky irradiance of McClear is available from CAMS [44], with the best time resolution of 1-minute up to two days ago since 2004-01-01. PVLIB [39] estimates clear-sky irradiance based on the interpolated T_L coefficient of SoDa monthly means, and the time resolution used in this chapter is 1-minute.

4.2.3 Clear-sky detection and turbidity derivation

The clear-sky instants for all the SURFRAD stations are detected by the Bright-Sun clear-sky detection algorithm [112], which is a globally applicable and freely available clear-sky detection model. The inputs of Bright-Sun model are GHI [W m^{-2}], GHICs [W m^{-2}], DHI [W m^{-2}], clear-sky DHI (DHICs) [W m^{-2}],

solar zenith angle [$^{\circ}$], horizontal projection of extraterrestrial irradiance [W m^{-2}], and local standard time (LST). Where GHI, DHI, and solar zenith angle are already available, LST is calculated based on UTC and the timezones detailed in Fig. 4.2. GHIs, DHIs, and extraterrestrial irradiance are derived using PVLIB, horizontal projection of extraterrestrial irradiance is then calculated referring the solar zenith angle. The Bright-Sun model consists of three steps, namely, clear-sky irradiance optimization, tri-component analysis of GHI, DHI, and direct normal irradiance (DNI), and duration filter [112]. The optimization of clear-sky irradiance is to remove the excessive dependence on clear-sky models, the tri-component analysis is to identify the 'clear' periods of all the irradiance components (i.e., GHI, DNI, DHI), and the duration filter is to further improve the accuracy of clear-sky detection by removing the cloud ramp events. More details could be reached in [112]. After detecting the clear-sky instants, the ground truth T_L is derived based on measured GHIs using inversed Ineichen-Perez model [31] and PVLIB [39] (see the adopted equations from [103] in the Appendix).

4.2.4 Turbidity estimation model development

In our previous work [103], the results show that the T_L estimation model developed on a daily basis yields comparable GHIs estimations with the models developed on the time basis of hourly and 5-minute, but with much less complexity. The daily T_L estimation model can also be applied in partially clear days [103]. That said, both data samples of clear-sky days and partially clear days can be included in the model development following the same methodology. In specific, to better represent the GHIs-derived T_L on a daily basis, only the days with more than one third detected clear-sky periods of the daytime are involved in the model training (e.g, if the daytime of day with the solar zenith angle less than 85° is 8 hours, only when the detected clear-sky instants are more than 2.4 hours, the day is included). Note that the derived T_L should be averaged in the clear-sky periods to represent the daily T_L value, while the meteorological measurements need to be averaged on the daily basis (when the solar zenith angle is less than 85°).

The daily T_L estimation model can be trained locally if the location has adequate data, especially the solar irradiance measurements. In this chapter, local T_L estimation model is trained, validated, and tested independently for all the SURFRAD stations for comparison. Data in the year range of 2010-2017 is used for training (20% of which is used for validation), data in 2018-2020 is used for testing. The transferable T_L estimation model is firstly trained and validated at stations with sufficient instrumentation, and then the developed model is applied at another location of interest where the common meteorological measurements are available. For instance, the T_L estimation model can be trained and validated using data from BON, DRA, FPK, PSU, SXF, TBL, and then be applied at GWN for estimating T_L and then GHIs estimation.

The transferred T_L model for each SURFRAD station is developed likewise, where the model is first trained and validated with the other six stations (e.g., excluding GWN) and then applied at the target location (e.g., GWN). Data in 2010-2017 at other six stations is used for training (80%) and validation (20%), data in 2018-2020 at the target location is used for testing and comparison.

The used machine learning algorithm in this chapter is multilayer perceptron (MLP). MLP is known as feed-forward neural network consisting of the input layer, output layer, and one or more hidden layers based on the applications [76]. The parameters in MLP networks are obtained through back propagation [76]. MLP has a high flexibility in approximation and is widely applied in real applications. The hyperparameters of MLP are tuned using tenfold cross-validation method. For more details on MLP algorithm and the cross-validation method, the reader is referred to Scikit-learn [97], which is the used tool for the model development in this chapter.

4.2.5 Turbidity and clear-sky irradiance estimations

Two T_L estimation models, namely, local and transferred T_L estimation models are developed for comparison. The daily T_L is then estimated by the local and transferred models, separately. The meteorological inputs are daily averaged ambient temperature, relative humidity, wind speed, and atmospheric pressure. The 1-minute GHICs at all the SURFRAD stations in 2018-2020 are then derived using Ineichen-Perez (PVLIB) model with the estimated T_L factor, for both the local and transferred T_L estimation models. Since the measured GHI at solar zenith over 85° are not included, the corresponding GHICs estimations are also removed.

The comparison of GHICs estimated by different models is in two time resolutions. The GHICs estimated by PVLIB using default T_L (referred as T_L default), T_L estimated by the local model (referred as T_L local), and T_L estimated by the transferred model (referred as T_L transfer) are in the time resolution of 1-minute. Therefore, the comparison of T_L default, T_L local, and T_L transfer is also in 1-minute resolution. Since the clear-sky irradiance of REST2 is in a time resolution of 5-minute, then the comparison involving REST2 should have the same time resolution. Note that the aggregating measured and estimated GHICs to 5-minute resolution should be the round way (i.e., data points from 13:58, 13:59, 14:00, 14:01, 14:02 are aggregated and indexed as 14:00) [105].

The error evaluation metrics are root mean squared error (RMSE), mean bias error (MBE), and their normalized counterparts (nRMSE, nMBE) defined by the following equations:

$$\text{RMSE} = \sqrt{\frac{1}{N} \sum (e_i - o_i)^2} \quad (4.1)$$

$$\text{nRMSE} = \frac{\sqrt{\frac{1}{N} \sum (e_i - o_i)^2}}{\frac{1}{N} \sum o_i} \quad (4.2)$$

$$\text{MBE} = \frac{1}{N} \sum (e_i - o_i) \quad (4.3)$$

$$\text{nMBE} = \frac{\sum (e_i - o_i)}{\sum o_i} \quad (4.4)$$

where e_i and o_i are the pair of GHI estimation and ground observation, N is the total number of compared data points.

4.3 Results and discussion

In this section, we evaluate the local and transferable T_L estimation models described above through the comparison of default T_L , derived T_L , and estimated T_L in Section 4.3.1, the performance of GHICs estimation using different T_L factors is presented in Section 4.3.2. We then quantitatively compare the local and transferable T_L estimation models for estimating and forecasting GHICs with physical clear-sky models of REST2 and McClear in Section 4.3.3, as physical models are generally considered as most accurate models. Where the comparison of GHICs estimation is presented in Section 4.3.3.1, and the result of GHICs forecasting is elaborated in Section 4.3.3.2.

4.3.1 Evaluation of turbidity estimation models

The invariant T_L interpolations based SoDa monthly climatology means cannot account for the short-term and long-term variations of the aerosols and water vapor content in the atmosphere. As shown in Fig. 4.3, the derived and estimated T_L factors generally exhibit high fluctuations during the year of 2019, while the default T_L has a comparatively smoother profile. Meanwhile, all the T_L curves show a similar trend that the T_L tends to increase from the beginning of year to some peak point around the middle of the year, then follows a drop till the year end. Apart from higher variations, the derived and estimated T_L coefficients at most stations are generally lower than SoDa interpolations with some exceptions that are likely to happen around the third quarter of the year. The diurnal and monthly variations of T_L factor were also observed in the study of Chaâbane et al. [81], and the typically higher T_L value of the monthly climatology means than the derivations was confirmed by Hove and Manyumbu [86].

The detailed comparison between the derived T_L and T_L estimations is presented in Table 4.1. It is shown that the default T_L based on interpolations generally shows larger discrepancy in terms of RMSE and MBE than the T_L estimations regardless of local or transferred method is applied (excluding TBL, the possible

reason is explained later on). For instance, at BON, default T_L shows a RMSE of 1.02 and a MBE of 0.85, the RMSE of T_L estimation from the local method is 0.34 and the corresponding MBE is -0.06, while T_L estimation of the transferred method also has smaller RMSE and MBE values of 0.34 and 0.01, respectively (see Table 4.1).

Table 4.1: The RMSE and MBE between derived T_L and T_L estimations from interpolation, local and transferred models at seven SURFRAD stations for both clear-sky and partially clear days in 2019.

	T_L default ^a		T_L local ^b		T_L transfer ^c	
	RMSE	MBE	RMSE	MBE	RMSE	MBE
BON	1.02	0.85	0.34	-0.06	0.34	0.01
DRA	0.62	0.37	0.35	-0.17	0.32	-0.04
FPK	0.69	0.46	0.33	-0.02	0.33	-0.12
GWN	0.75	0.57	0.41	-0.18	0.43	-0.20
PSU	0.91	0.77	0.27	-0.06	0.28	-0.03
SXF	0.92	0.73	0.44	-0.17	0.44	-0.05
TBL	0.73	0.05	0.64	-0.32	0.95	-0.67

^a ' T_L default' means the T_L interpolation of SoDa monthly means, which is used in the default PVLIB calculations.

^b ' T_L local' means the T_L estimated by the local model.

^c ' T_L transfer' means the T_L estimated by the transferred model.

When comparing the derived T_L with T_L estimations, both local and transferred T_L estimations can follow the fluctuations of the derived T_L along the year with different discrepancies (see Fig. 4.3), which means the local and transferred T_L estimation methods can account for the variations of the aerosol and water vapor concentration in the atmosphere. Generally, the transferred method tends to produce T_L estimation with larger values of RMSE and MBE since the local T_L estimation method is developed based on the on-site sensed data, which is more likely to generate better results. For example, at GWN, the locally estimated T_L has a RMSE of 0.41 and a MBE of -0.18, while the T_L estimation of the transferred method yields a result with comparatively larger RMSE and MBE of 0.43 and -0.20, respectively. Note that the transferred method sometimes may also yield comparable or even better T_L estimations (see the results of DRA in Table 4.1). Although the transferred T_L estimation method may lead to larger uncertainties when compared

with local estimation, it is a potential way to provide more accurate T_L coefficient than the default PVLIB interpolations.

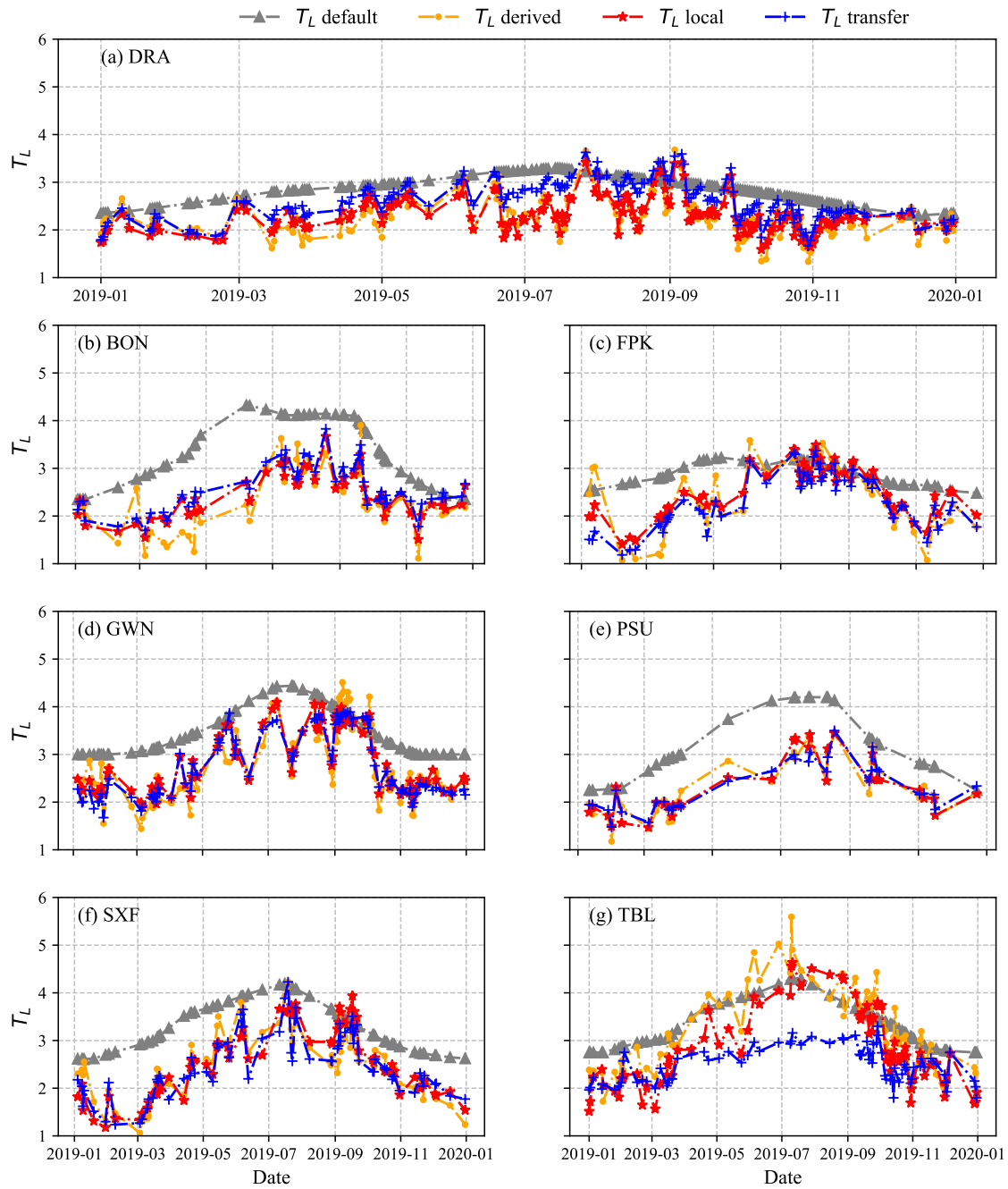


Figure 4.3: The comparison of ground truth T_L (T_L derived), PVLIB T_L (T_L default), and T_L estimations from local (T_L local) and transferred methods (T_L transfer) for clear-sky and partially clear days in 2019, at seven SURFRAD stations: (a) DRA, (b) BON, (c) FPK, (d) GWN, (e) PSU, (f) SXF, and (g) TBL. Only the results of 2019 are presented here to show the trends, and the T_L profiles in 2018 and 2020 are similar.

The generally higher T_L estimations based on the SoDa monthly means, the variations of derived T_L followed by the T_L estimations, and the comparable T_L estimation results of local and transferred models are observed at most of the SURFRAD stations in Fig. 4.3 and Table 4.1. However, when it comes to TBL, the observations change noticeably. The default T_L shows relatively lower errors with a RMSE of 0.73 and a MBE of 0.05 when compared with most of the other stations. As illustrated in Fig. 4.3(g), the derived T_L is more likely to be higher than the default interpolations of SoDa monthly means during the year. The locally estimated T_L exhibits a similar profile with the T_L derivation, but the overall result is inferior to the the results at other stations, and the improvement of the T_L estimation performance is also limited. The transferred T_L estimation model even fails to estimate the T_L during some periods, where a clear underestimation is observed and thus the intra-year T_L variations are also not accounted for. It is most likely that the unique climate condition at TBL leads to the under-performance of the transferred T_L estimation model.

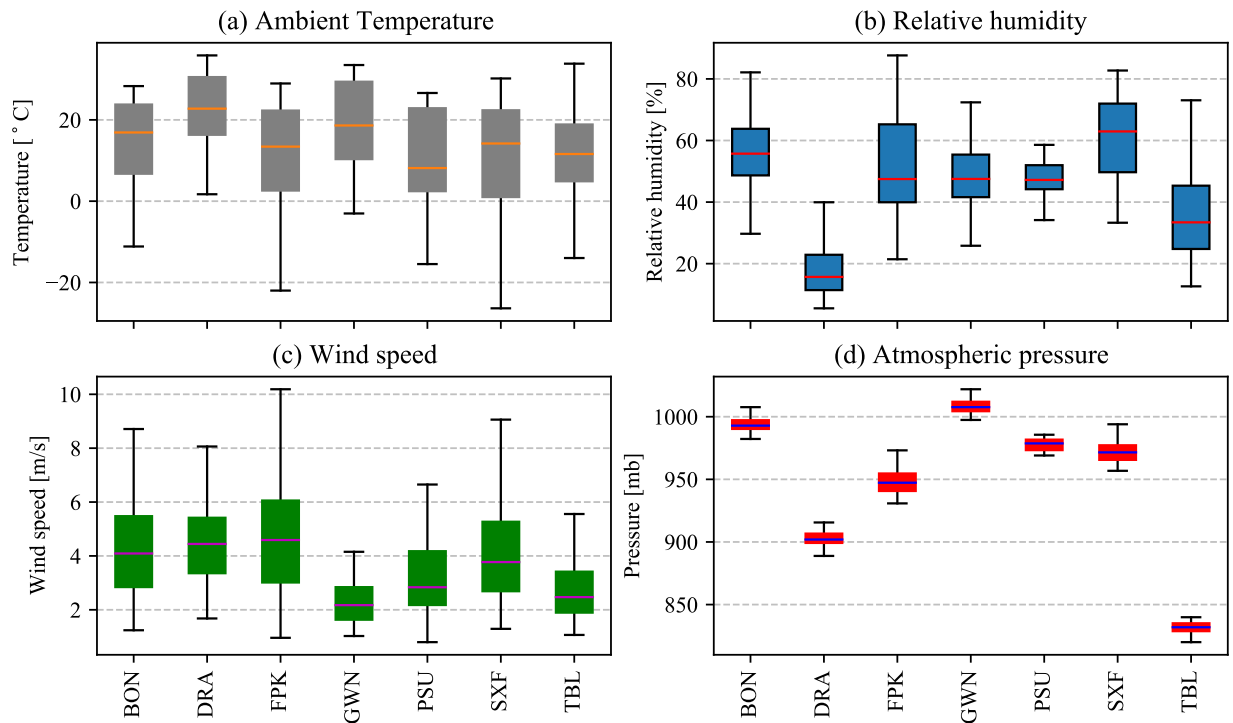


Figure 4.4: The statistic properties of the meteorological inputs in the year of 2019. (a) Ambient temperature, (b) Relative humidity, (c) Wind speed, and (d) Atmospheric pressure.

As presented in Fig. 4.4, the meteorological measurements show different statistic properties, such as the maximum, the minimum, and the mean, at each station. Therefore, a better T_L estimation model could be developed when local climate features are accounted for. When there is no sufficient on-site data for

local model development, the transferred model could be an option. Recall that the transferred T_L estimation model is first trained and validated at stations with adequate information, and then applied at the location of interest. The transferred T_L estimation method can generally work for most locations but TBL. The possible reason could be the lower atmospheric pressure than the other stations as shown in Fig. 4.4(d). When developing the transferable T_L estimation model for TBL using data from other six stations, the atmospheric pressure, unlike ambient temperature, relative humidity, and wind speed, stays far away from the range of used inputs. The use of out-of-range local pressure as an input for the transferred T_L estimation method might produce a result with large discrepancy, this is why the transferable T_L estimation model underperforms. That said, it is suggested to use data from the locations with similar climate characteristics when developing the transferable T_L estimation model for practical applications.

The sensitivity analysis in the study of Chen and Li [103] shows that ambient temperature and relative humidity have comparatively larger influence on the T_L estimation than wind speed. The estimated T_L goes up with the increases in ambient temperature and relative humidity, while the increases in wind speed and atmospheric pressure result in a drop of T_L estimation. Wind speed has the least importance in T_L estimation. As for pressure, the sensitivity analysis presents relatively larger variations when changing the pressure by 10%. However, this has limited implications as the piratical atmospheric pressure for a certain place does not have high variations compared with other meteorological parameters. Since the transferred T_L estimation follows the same methodology of the local methods, the sensitivity analysis of the transferred T_L estimation model should have similar results.

Table 4.2: The comparison of T_L and GHICs estimations at TBL in 2018-2020, including the T_L estimation models developed with and without atmospheric pressure (P_a).

	T_L estimation		GHICs estimation	
	RMSE	MBE	nRMSE [%]	nMBE [%]
T_L local with P_a	0.64	-0.32	3.23	1.55
T_L local without P_a	0.70	-0.46	3.40	1.84
T_L transfer with P_a	0.95	-0.67	4.43	2.84
T_L transfer without P_a	1.48	-1.20	6.70	5.23

To further investigate the influence of atmospheric pressure in the T_L estimation models, new local and transferred T_L estimation models for TBL are developed without using atmospheric pressure. The results of T_L and related GHICs estimations are presented in Table 4.2. When the atmospheric pressure is excluded

in the development of T_L estimation models, both local and transferred models produce T_L estimations with larger errors of RMSE and MBE as shown in Table 4.2. Similarly, the GHICs estimations based on T_L estimated by models without using atmospheric pressure also have comparatively larger discrepancies of nRMSE and nMBE. Therefore, it is suggested to use the atmospheric pressure as an input parameter in the development of T_L estimation models.

4.3.2 Comparison of GHICs estimations using different turbidity factors

Since the default T_L interpolations generally have larger RMSE and MBE values and do not show many variations along the year (see Table 4.1 and Fig. 4.3), the related GHICs estimations are then also associated with higher discrepancies of nRMSE and nMBE as shown in Table 4.3. It tends to underestimate the GHICs using default PVLIB as the interpolated T_L from SoDa monthly means are typically higher than the T_L derivations. When compared with default T_L interpolations, the estimated T_L from both local and transferred methods are more likely to yield better GHICs estimations (see Table 4.3).

As discussed in Section 4.3.1, the local T_L estimation models tends to generate better T_L estimations via the direct inferring to the on-site meteorological features. Therefore, the GHICs estimation using the locally estimated T_L might also have smaller divergences in terms of nRMSE and nMBE. Since the transferred models are developed using data from other locations, there could be more uncertainties associated in the related T_L estimations. This also introduces comparatively larger discrepancies in the GHICs estimations using T_L estimated by the transferable models. However, there is no significant difference between the local and transferred T_L estimation methods regarding the GHICs estimations. Consequently, the transferred T_L estimation model at TBL shows inferior performance in T_L estimations, which also leads to larger errors in estimating GHICs.

The overall performance of GHICs estimation at SURFRAD stations (TBL is not included due to the under-performance) is also presented in Table 4.3. Using the default T_L to generate GHICs estimation has comparatively larger errors with an nRMSE of 5.24% and an nMBE of -3.41%, while using the estimated T_L from local and transferred methods show noticeable improvements. The nRMSE of GHICs estimation based on estimated T_L is reduce to 2.75% and 2.80% for the local and transferred methods, respectively. The nMBE is improved to 0.45% for the local method, and to 0.84% for the transferred method. Although the overall performance of locally estimated T_L is slightly better than the transferred T_L estimations, the transferable model is still viable to estimate the T_L and GHICs for locations without sufficient data.

Table 4.3: The nRMSE [%] and nMBE [%] of 1-minute averaged GHICs estimations using different T_L factors at SURFRAD stations in 2018-2020. The used T_L coefficients are default interpolations (T_L default), estimations of the local model (T_L local) and transferred model (T_L transfer) .

Station	T_L default		T_L local		T_L transfer	
	nRMSE [%]	nMBE [%]	nRMSE [%]	nMBE [%]	nRMSE [%]	nMBE [%]
BON	8.04	-6.32	3.25	0.39	3.31	-0.18
DRA	3.40	-1.96	2.15	0.89	1.97	0.14
FPK	4.88	-2.78	2.56	0.24	2.54	0.80
GWN	5.91	-3.83	3.58	1.32	3.67	1.37
PSU	6.71	-5.29	2.86	0.25	2.78	0.36
SXF	6.76	-4.88	3.69	1.48	3.68	0.67
TBL	3.55	-0.23	3.23	1.55	4.43	2.84
ALL*	5.24	-3.41	2.75	0.45	2.80	0.84

* TBL is not included due to the under-performance of the transferred T_L estimation model.

4.3.3 Comparison of GHICs estimations and forecasts with physical models

To further evaluate the results of GHICs estimation using improved T_L estimations, we herein compare the performance with physical models, namely, the McClear model and the REST2 model. The comparison is in two folds: one is the real-time GHICs estimation and the other one is persistent day-ahead GHICs forecasts.

4.3.3.1 Comparison of GHICs estimations with physical models

Table 4.4 details the overall performance of 5-minute GHICs estimations and forecasts using T_L based model and physical at SURFRAD stations, TBL is not included due to the under-performance in T_L estimations using the transferred method. The default T_L produces a GHICs estimation with the largest nRMSE of 4.99% and the nMBE is -3.37%, while the local T_L estimation generates the best GHICs estimation with the nRMSE of 2.38% and the nMBE of 0.16%. As expected, the transferred T_L estimation yields a result with relatively larger discrepancies compared with the locally estimated T_L , the nRMSE and nMBE are 2.44% and 0.57%, respectively. Note that the transferred T_L estimation even produces better results than the McClear model and the REST2 model in terms of nRMSE and nMBE (see Table 4.4), while the REST2 model

outperforms McClear with the nRMSE of 2.55% and nMBE of 1.30%. However, there is no significant difference between estimations from the transferred model and the physical models. The detailed comparison of GHICs estimations at each SURFRAD station is presented in Fig. 4.5. Physical models are more likely to produce over-estimations, and the local and transferred T_L estimations also tend to overestimate GHICs but with smaller bias.

The possible reason why the empirical model based on improved T_L estimation yields comparable results with physical clear-sky models could be the avoidance of uncertainty accumulation. Physical models require detailed atmospheric inputs such as aerosol, water vapor and ozone, these inputs are usually based on reanalysis products such as MERRA-2. The MERRA-2 reanalysis products are derived from satellite measurements and therefore are associated with uncertainties [116]. This means the use of reanalysis products for clear-sky irradiance estimation in physical models would have accumulated uncertainties. However, the T_L derivation is a one-step-through process based on quality-controlled irradiance data, which includes embedded T_L information. Therefore, it is more likely to avoid the accumulation of multi-step uncertainties. Although physical clear-sky models are proved to have higher accuracy in GHICs estimation, the comparable results with less complexity of the transferred T_L estimation model demonstrates its potential usage for locations without sufficient on-site information.

Table 4.4: Overall results of GHICs estimations and day-ahead persistent GHICs forecasts with the time resolution of 5-minute at SURFRAD stations excluding TBL in 2018-2020. Used models are the Ineichen-Perez model with three T_L inputs, the McClear model, and the REST2 model.

Model	GHICs estimation		GHICs forecasts*	
	nRMSE [%]	nMBE [%]	nRMSE [%]	nMBE [%]
T_L default	4.99	-3.37	4.64	-3.02
T_L local	2.38	0.16	2.85	0.32
T_L transfer	2.44	0.57	2.99	0.74
McCclear	3.32	2.10	4.11	1.55
REST2	2.55	1.30	3.51	0.79

* The forecast is based on a day persistent method, where the day-ahead GHICs is assumed as the same as the present day.

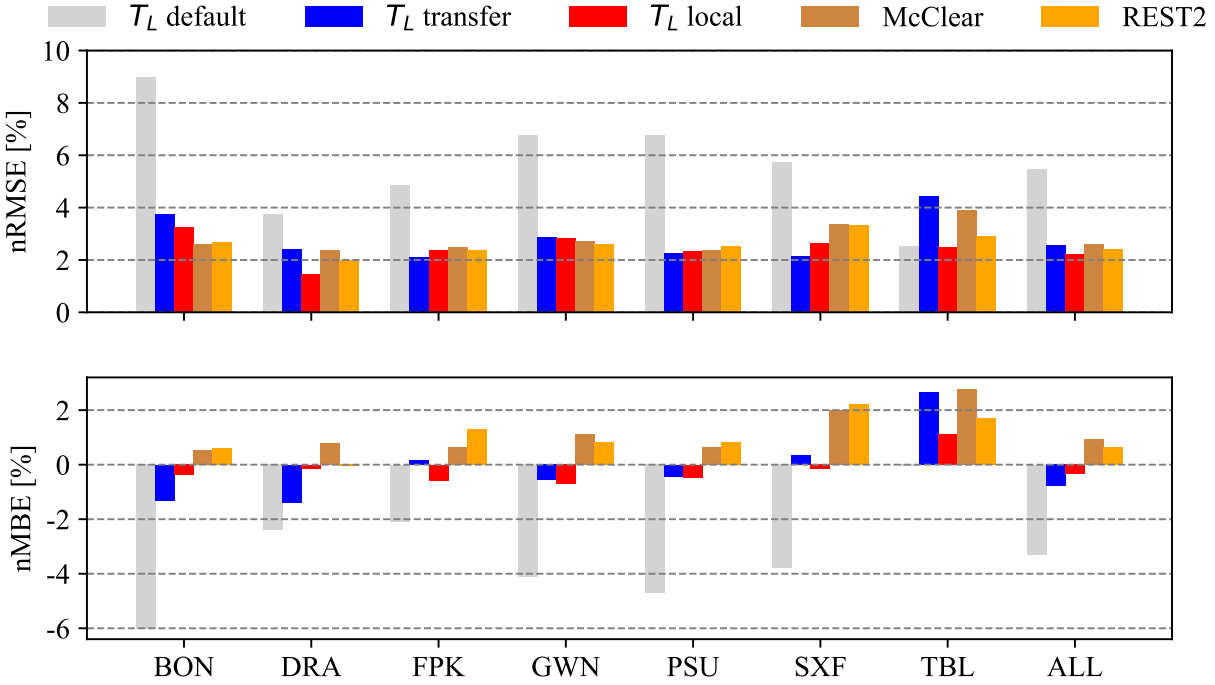


Figure 4.5: The nRMSE and nMBE between the 5-minute averaged GHICs measurements and estimations using different models at SURFRAD stations in 2018-2020. GHICs is estimated by the Ineichen-Perez model with three different T_L inputs, the McClear model, and the REST2 model.

4.3.3.2 Comparison of GHICs forecasts with physical models

Since clear-sky irradiance (clear-sky model) is also essential in solar forecasting, we also evaluate and compare the performance of T_L based forecasts with the McClear model and the REST2 model. Considering that McClear and REST2 are physical models requiring detailed atmospheric inputs, which are difficult to obtain and forecast, we therefore apply a day persistent method to predict the GHICs in the coming day. In specific, the profile of GHICs for the coming day is assumed as the same as the present day [117, 118]. Note that McClear is available as a web service from 2004-01-01 up to two days ago, and is recommended for solar forecasting applications in [36]. However, in real time forecasting applications, e.g., the present day and the coming day, the clear-sky irradiance of McClear is not available. This means the atmospheric inputs for both McClear and REST2 should be obtained at present day, which introduces even more difficulties in retrieving and measuring the atmospheric optical properties. To perform a fair comparison, we assume the clear-sky irradiance (i.e., GHICs) of REST2 and McClear could be obtained for the present day, and the meteorological measurements are available.

The overall result of GHICs forecasts using the day persistent method is presented in Table 4.4. The largest nRMSE (4.64%) and nMBE (-3.02%) are generated using the default T_L , while the other two T_L based GHICs predictions show lower nRMSE than the physical models. The local and transferred T_L estimations yield GHICs forecasts with the nRMSE of 2.85% and 2.99%, respectively. The nRMSE of McClear based forecasts is 4.11%, while REST2 produces a result with the nRMSE of 3.51%. GHICs forecasts based on estimated T_L also have smaller biases, the transferred method generates a comparatively larger nMBE of 0.74%, while the local model produces a result with the nMBE of 0.32%. The physical models are likely to produce relatively larger over-estimations in forecasting GHICs, where the McClear shows an nMBE of 1.55 and the REST2 has an nMBE of 0.79%. Compared with GHICs estimations (except the default T_L method), GHICs forecasts are generally associated with larger uncertainties of nRMSE as shown in Table 4.4. The comparison of day-ahead GHICs forecasts at each SURFRAD station is illustrated in Fig. 4.6. The results of local and transferred T_L estimations produce comparable day-ahead GHICs forecasts with physical models in terms of nRMSE and nMBE. Similarly, considering the comparable results for day-ahead GHICs forecasts with less complexity, the uncertainty and time lag in obtaining atmospheric inputs for physical models, the methods of improved T_L estimations show potential in supporting solar forecasting applications.

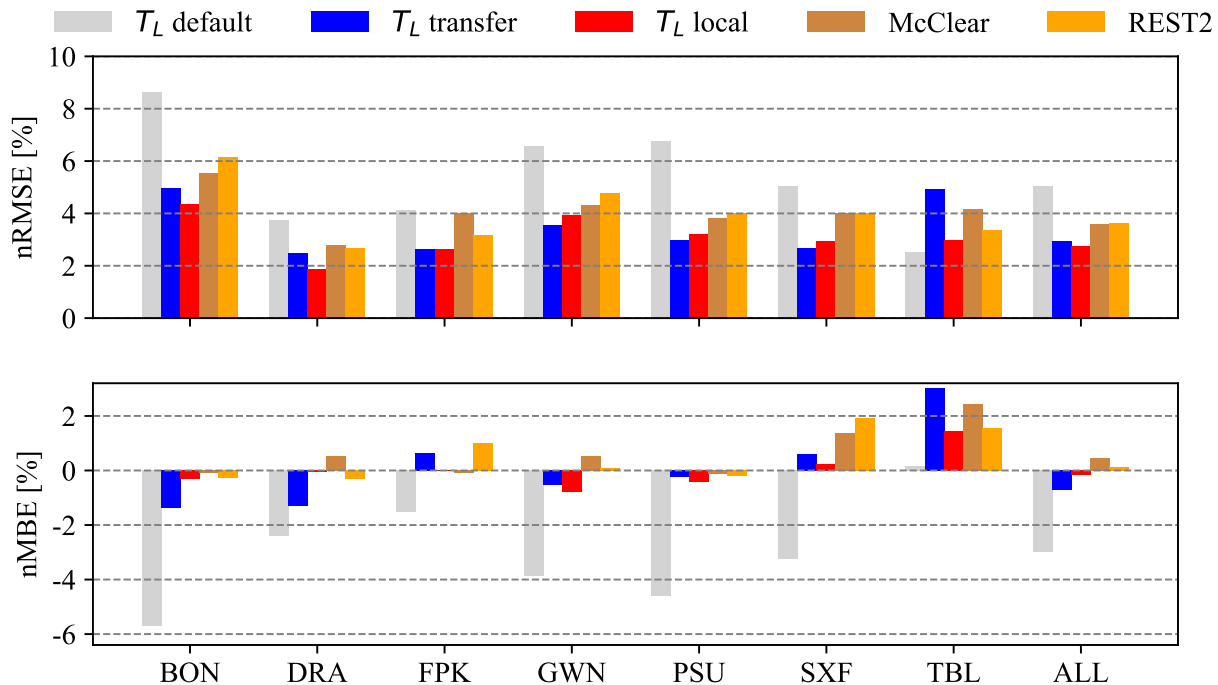


Figure 4.6: The nRMSE and nMBE between the 5-minute averaged GHICs measurements and day-ahead forecasts using the day persistent method at SURFRAD stations in 2018-2020.

4.4 Conclusions

In this chapter, we propose a transferable T_L estimation method for estimating GHICs. The transferred T_L estimation model follows a similar methodology with the local T_L estimation model presented in [103]. Instead of using on-site solar irradiance data for model development in the local model, the transferable model is first trained and validated involving stations with sufficient data, and then applied at the location of interest for T_L estimation and thus the clear-sky irradiance. The main meteorological inputs of the T_L estimation model are ambient temperature, relative humidity, wind speed, and local atmospheric pressure. As common meteorological information, they are easy to obtain and available at most of the weather stations. Both local and transferred T_L estimation models are applied at the SURFRAD stations, the performance of GHICs estimation is evaluated with the on-site measurements and also compared with physical McClear and REST2 models.

The local T_L estimation method shows a high performance in GHICs estimation with the nRMSE of 2.38% and the nMBE of 0.16%, the nRMSE and nMBE of GHICs forecasts are 2.85% and 0.32%, respectively. The transferred T_L estimation model yields results with slightly larger divergences for both GHICs estimations and forecasts. When applying the method at all the SURFRAD stations (excluding TBL), the overall nRMSE of GHICs estimation is reduced from 4.99% to 2.44%, and the overall nMBE is decreased from -3.37% to 0.57% compared with the default PVLIB calculations. The result of GHICs estimation based on the estimated T_L is also comparable with the physical clear-sky models, where the McClear yields an overall nRMSE of 3.32% and the nMBE is 2.10%, while the REST2 produces the overall result with an nRMSE of 2.55% and an nMBE of 1.30%. Considering the difficulties and uncertainties in forecasting the atmospheric inputs and meteorological data, we further compare the aforementioned methods for estimating the day-ahead GHICs using a persistent way, where the day-ahead GHICs is assumed as the same as the present day. The results show that the local T_L estimation has an overall forecasting with the nRMSE of 2.85% and nMBE of 0.32%, the transferred method for T_L estimation generates the GHICs forecasts with an overall nRMSE of 2.99% and an nMBE of 0.74%, the McClear produces an nRMSE of 4.11% and an nMBE of 1.55%, while the REST2 yields a result with the nRMSE of 3.51% and the nMBE of 0.79%.

The transferred T_L estimation model does not yield similar results at TBL due to its unique climate features, so one recommendation for developing the transferable T_L estimation model is to use data from locations with similar climate conditions. Considering the improved GHICs estimations and day-ahead forecasts, the comparable results with physical clear-sky models, and the complexity and difficulty in obtaining atmospheric inputs, both the local and transferred T_L estimation methods show a potential to support the

solar resourcing and forecasting applications. The local T_L estimation method is suggested for stations with sufficient data, and the transferred T_L estimation model is therefore recommended for locations without adequate information.

4.5 Acknowledgement

This chapter, in full, is a reprint of S. Chen, Z. Liang, P. Dong, S. Guo and M. Li (2023). A transferable turbidity estimation method for estimating clear-sky solar irradiance. *Renewable Energy*, 206, 635-644. The thesis author is the first author of this publication. The abstract is presented as a poster presentation at the *8th World conference on photovoltaic energy conversion*, Milan, Italy, 2022. A transferable turbidity estimation method for high fidelity clear-sky solar irradiance computation.

4.6 Appendix

The equations used to derive ground truth T_L are adopted from [103].

$$T_L = \left[\ln \left(\frac{\text{GHI}_{\text{cs}}}{c_1 \cdot I_0 \cdot \cos(\theta)} \right) / (-c_2 \cdot AM) - f_1 \right] / f_2 + 1$$

with:

$$AM = \left(\frac{1}{\cos(\theta) + 0.50572 \cdot (6.07995 + (90 - \theta)^{-1.6364})} \right) \cdot \frac{P_a}{101325}$$

$$c_1 = 5.09 \cdot 10^{-5} \cdot h + 0.868$$

$$c_2 = 3.92 \cdot 10^{-5} \cdot h + 0.0387$$

$$f_1 = \exp(-h/8000)$$

$$f_2 = \exp(-h/1250)$$

where T_L is the Linke turbidity, GHI_{cs} [W m^{-2}] is the measured GHIs. c_1 , c_2 , f_1 , f_2 are altitude-dependant coefficients, I_0 [W m^{-2}] is the solar constant, θ [$^\circ$] represents the solar zenith angle, AM is the absolute airmass, T_L is the Linke Turbidity factor, P_a [Pa] is the local atmospheric pressure, and h [m] is local altitude.

Chapter 5

Global and direct solar irradiance estimation using deep learning and selected spectral satellite images

5.1 Introduction

Climate change, carbon neutrality and net zero emissions have drawn unprecedented attention worldwide among the energy-related industry and academia over the past decade [119]. Many countries have introduced their national energy policies and plans to reach the global climate goals [21]. Under such a blueprint, the rapid expansion and integration of renewable energy sources into current power systems in a near future could be foreseen [119]. It is predicted that the global electricity capacity of renewables will rise more than 60% between 2020 and 2026 [120]. Solar energy, as a promising candidate with worldwide potential, is set to be one of the primary power sources to enable the deep decarbonization in the energy sector. Despite the variability and intermittency, both solar photovoltaic (PV) and concentrated solar power (CSP) are important components on the pathway towards net zero emissions [121, 122]. The power production of solar PV or CSP is heavily related to the available solar irradiance, i.e., global horizontal irradiance (GHI) and direct normal irradiance (DNI), at the location of interest [8]. That said, as long as solar energy is involved in the roadmap to carbon neutrality, the need for solar resource assessment and forecasting is essential in supporting solar energy projects [21, 14].

The uncertainty and intermittency of local irradiance leads to high variability in the power output of solar energy projects, which also introduces challenges in the system operation [10, 11, 123]. Solar resource

assessment aims to support the feasibility study and optimal design of solar energy projects by projecting power demand and supply potentials, analyzing techno-economic viability and minimizing the long-term risks [8, 21, 20]. Ground irradiance measurements with careful calibrations are the most accurate data source in solar resource assessment. However, complete and long-term on-site measurements are not available at most locations due to associated technical and financial issues [12, 115]. Even though ground irradiance measurements are invaluable, their limited data availability greatly hinders the wider application [124]. On the other hand, the irradiance estimation and retrievals via remote sensing provide an alternative in the evaluation and design of solar energy projects [12, 125].

Satellite-to-irradiance algorithms can be broadly grouped as physical methods that based on radiative transfer and statistical methods [20, 126]. The physical solar model used in the National Solar Radiation Database (NSRDB) [49] and Heliosat-4 method [50] are the representatives of physical models, where the detailed interactions between solar radiation and atmospheric compositions are simulated using radiative transfer models (RTMs). The essential atmospheric inputs such as cloud properties, aerosol optical depth (AOD), and water vapor content can be obtained from geostationary satellites [49, 50], for instance, Geostationary Operational Environmental Satellite (GOES) and Meteosat Second Generation (MSG) satellites. Of statistical models, the pure empirical methods are of limited applications due to the inferior performance and lack of generality [20]; Semi-empirical methods rely on separate attenuation processes of cloud and other constituents in the atmosphere. Physical models are generally have better performance with more complexity, while semi-empirical models are easier to implement with a compromised performance. Both physical and semi-empirical methods show large uncertainties in estimating solar irradiance under cloudy conditions [127].

As the ground-truth in validating solar irradiance models, on-site measurements are of great importance [117]. Moreover, the local qualified observations in just a short period could be used in the processes to get long-term modeled data, for instance, site adaptation [128], and machine learning based models [129, 130, 131]. Given the high temporal and spatial information provided by the new generation satellites and the advancements in machine learning algorithms, the combination of machine learning (especially deep learning) and remote sensing, as an optimized statistical method, brings new insights in reducing the uncertainties of solar irradiance modeling [125, 132, 133, 134]. Lu et al. [135] applied all the bands of Multi-functional Transport Satellite (MTSAT) for daily GHI estimation with the aim to fully exploit the information of visible and infared channels. Jiang et al. [132] proposed a deep learning algorithm based on convolutional neural network (CNN) and multilayer perception (MLP) for hourly GHI estimation using images from visible channel of MTSAT, in an attempt to reduce the spatial effects related to the approxima-

tion of an independent pixel. Verma and Patil [136] presented a machine learning method for solar radiation assessment using pixels of multispectral Meteosat satellite images for the target location. Similarly, the iterative random forest model was adopted for estimating half-hourly global, direct, and diffuse components of solar irradiance using GOES-16 data and some viewing geometrical parameters [137, 138]. Rocha and Santos [139] reported a deep learning network based on CNN and long short-term memory (LSTM) network for GHI and DNI estimation using GOES-16 imagery of all channels. However, the developed model could not produce better GHI estimation than NSRDB, while the improvement of DNI estimation remains limited.

To further exploit the application of new-generation geostationary satellite with much finer spatiotemporal resolution (i.e., 2-km and 5-min) in solar resource assessment, this work proposes a deep learning model with attention layer for high-resolution (5-min) GHI and DNI estimations. It is expected that the data with high spatiotemporal resolution and high accuracy can provide better resource information for designing solar energy projects, as it better captures the variability of solar irradiance [105]. Instead of using all spectral satellite bands, a correlation analysis is performed to select representative bands, which can improve the modeling efficiency and thus be beneficial for large-scale applications. To address the spatial effects such as nonlocal cloud shadows, multispectral images are applied as the input rather than single pixels. The major contributions of this work are summarized as follows:

- A correlation analysis is applied to select the representative satellite spectral bands, which can reduce the modeling complexity for satellite-to-irradiance mapping. This method is also beneficial for large-scale applications that involve long time periods and/or large areas of interest.
- The application of attention mechanism [140] and spectral satellite images around the target location aims to better account for the nonlocal cloud effect, which can improve the accuracy of irradiance estimations by deep learning.
- The estimates of 5-min GHI and DNI are benchmarked with NSRDB and show improved overall accuracy. Considering that NSRDB represents the state-of-the-art in satellite-to-irradiance methods, the improvements in irradiance estimations might bring more benefits to the solar community.
- Further evaluations and error analysis of irradiance estimations are performed to identify the sources of error and potential ways for future improvements.

The remainder of this chapter is structured as follows: Section 5.2 describes the data and the methods for solar irradiance estimations. The performance of the proposed model for solar irradiance estimation and

the comparisons with other models are presented in Section 5.3. Section 5.4 details the explanation and implication of the results. Finally, key findings are summarized in Section 5.5.

5.2 Data and methods

This section describes the used data and the deep learning method for estimating ground-level solar irradiance (i.e., GHI or DNI). As shown in the flowchart (see Fig. 5.1), the GOES-16 data of all bands are extracted from publicly available source. Then the cropped images for a location centered in the region of 11×11 pixels are pre-processed to be consistent in temporal and spatial resolutions. Images of selected bands from the correlation analysis are the inputs of the deep learning model, while the labels are clear-sky indexes obtained from irradiance measurements and Ineichen-Perez clear-sky model [31, 39]. The trained model is applied for estimating clear-sky index via new input data of GOES-16, and the solar irradiance estimation is obtained using the estimated clear-sky index and Ineichen-Perez clear-sky irradiance. Note that the methodologies for estimating GHI and DNI are the same, but deep learning models should be developed separately. The detailed descriptions of the used data and method are presented in the following subsections.

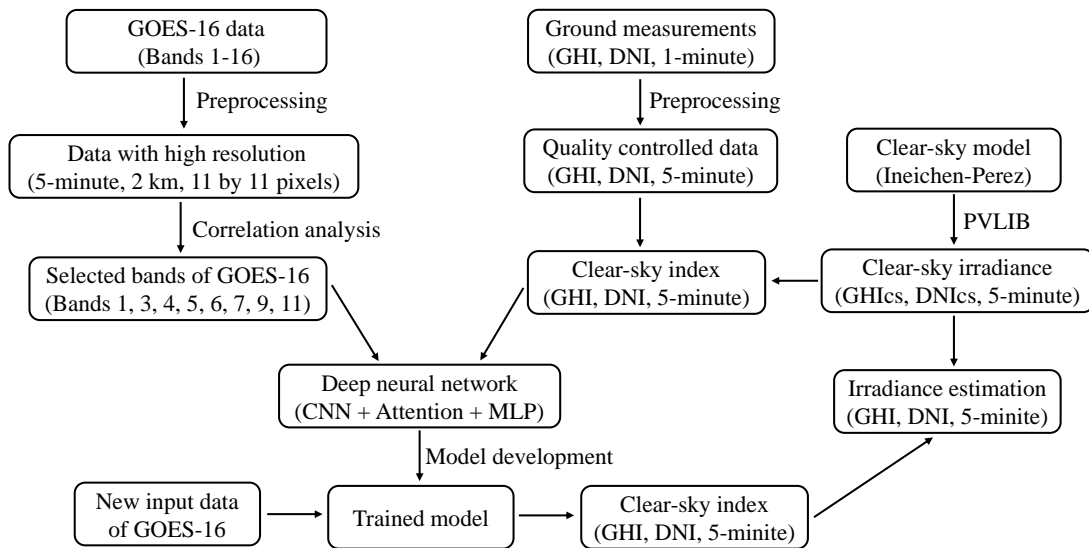


Figure 5.1: The flowchart of ground-level solar irradiance estimation using deep learning and satellite measurements of GOES-16.

5.2.1 Data

The data used in this work mainly includes spectral satellite images of GOES-16 and ground-level irradiance measurements from the Surface Radiation Budget Network (SURFRAD) stations [29]. GOES-16 (75.2° West), as one of the GOES-R series, is operated by National Oceanic and Atmospheric Association (NOAA). The Advanced Baseline Imager (ABI) has 16 spectral bands, which provide data with much finer temporal and spatial resolutions compared to the previous generations. The detailed information of each spectral band is presented in Table 5.1. 5-min spectral satellite measurements of all the 16 spectral bands in the year of 2019 are downloaded, which are then extracted as images and georeferenced to the target ground locations.

Table 5.1: The detailed information of the ABI spectral bands of GOES-16.

Band	λ [μm]	Center λ [μm]	Resolution [km]	Nickname	Type
1	0.45-0.49	0.47	1	Blue	Visible
2	0.59-0.69	0.64	0.5	Red	Visible
3	0.846-0.885	0.865	1	Veggie	Near-Infrared
4	1.371-1.386	1.378	2	Cirrus	Near-Infrared
5	1.58-1.64	1.61	1	Snow/Ice	Near-Infrared
6	2.225-2.275	2.25	2	Cloud particle size	Near-Infrared
7	3.80-4.00	3.90	2	Shortwave window	Infrared
8	5.77-6.60	6.19	2	Upper-level water vapor	Infrared
9	6.75-7.15	6.95	2	Mid-level water vapor	Infrared
10	7.24-7.44	7.34	2	Lower-level water vapor	Infrared
11	8.30-8.70	8.50	2	Cloud-top phase	Infrared
12	9.42-9.80	9.61	2	Ozone	Infrared
13	10.10-10.60	10.35	2	”Clean” longwave window	Infrared
14	10.80-11.60	11.20	2	Longwave window	Infrared
15	11.80-12.80	12.30	2	”Dirty” longwave window	Infrared
16	13.00-13.30	1.378	2	CO ₂ longwave	Infrared

The spectral satellite images are in the size of 11×11 pixels, and the target ground station locates at the center. Note that the spectral bands have different spatial resolutions as shown in Table 5.1. The spatial

resolution is in the range of 0.5 - 2-km at the sub-satellite point, and spectral bands with better resolutions are therefore re-scaled to 2-km. The end timestamp of each scan in Coordinated Universal Time (UTC) is used to index the images after rounded to the next nearest 5-min interval. This is for the compatibility with ground irradiance measurements and real-time applications. Sample spectral images for one of the target locations are presented in Fig. 5.2, where the images have a size of 11×11 pixels and a spatial resolution of 2-km.

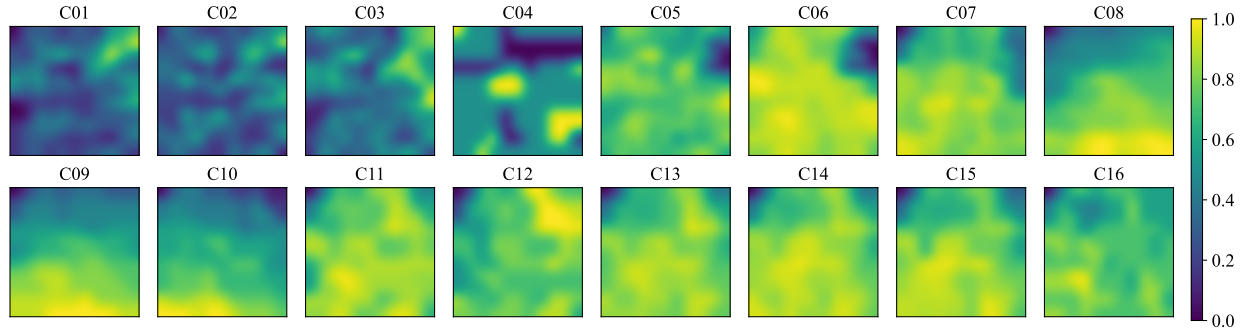


Figure 5.2: Sample satellite images including all the spectral bands of GOES-16 for Bondville (40.05° , -88.37°) at 2019-01-10 20:45:00 (UTC). The image is in the size of 11×11 pixels, where Bondville is located at the center. All the spectral images are normalized to the range of $[0,1]$ using the Min-Max normalization.

The ground-level irradiance measurements are from SURFRAD stations, namely, Bondville (BON), Desert Rock (DRA), Fort Peck (FPK), Goodwin Creek (GWN), Pennsylvania State University (PSU), Sioux Falls (SXF), and Table Mountain (TBL) as summarized in Table 5.2. Measurements including GHI, DNI, diffuse horizontal irradiance (DHI), solar zenith angle in 2019 at all the seven stations are obtained after quality control. Note that DHI is not of interest in this work, however, it is required in the classification of cloudy and clear periods [112] for the performance evaluation. All the measurements are in the 1-min temporal resolution and indexed in UTC time. Due to the high airmass effect, all the irradiance measurements over the solar zenith angle of 85° are eliminated. Note that the satellite images are in the time resolution of 5-min, GHI and DNI are therefore aggregated into the same temporal resolution.

The satellite-derived GHI and DNI provided by NSRDB [141] are used for comparison to evaluate the performance of the applied deep learning algorithms. Both GHI and DNI estimations of NSRDB for all the SURFRAD stations in 2019 are downloaded, with the spatiotemporal resolution of 2-km and 5-min. As a publicly available data source that is extensively accessed for solar energy applications, NSRDB is based on the physical solar model and the reanalysis products from many other associations [49]. Broadband irradiance including GHI, DNI, and other auxiliary variables such as cloud type, are available in NSRDB.

Since 2018, the spatiotemporal resolution of NSRDB has been improved to 2-km and 5-min. Meanwhile, NSRDB represents the state-of-the-art in the satellite-based estimation of solar irradiance. Considering that other deep learning satellite-to-irradiance models usually have different locations of interest and various spatiotemporal resolutions, NSRDB is selected as the benchmark and its accuracy is validated against ground measurements [105].

Table 5.2: Detailed information of the seven SURFRAD stations. The climate is based on Köppen classifications. The elevation angle and azimuth angle are from the station to GOES-16, and the azimuth angle starts from the North (0°).

Station	Latitude (°)	Longitude (°)	Altitude (m)	Climate*	Elevation (°)	Azimuth (°)
BON	40.05	-88.37	230	Dfa	41.7	160.0
DRA	36.62	-116.02	1007	Bwk	29.9	124.6
FPK	48.31	-105.10	634	Bsk	47.2	155.0
GWN	34.25	-89.87	98	Cfa	27.5	142.4
PSU	40.72	-77.93	376	Dfb	42.8	175.8
SXF	43.73	-96.62	473	Dfa	35.2	150.4
TBL	40.12	-105.24	1689	Bsk	34.3	138.1

* Köppen climate classifications are: Bsk (arid, steppe, cold), Bwk (arid, desert, cold), Cfa (temperate, without dry season, hot summer), Dfa (continental, without dry season, hot summer), Dfb (continental, without dry season, warm summer).

5.2.2 Correlation analysis

In machine learning applications, feature selection is extensively applied to decrease the dimensionality by eliminating redundant and irrelevant features [142]. Feature selection has been proved to be helpful in understanding data, reducing the complexity, and improving the learning efficiency as well as predictive performance of machine learning tasks [142, 143]. Typically, feature selection methods can be grouped as filter and wrapper methods [142]. A filter method usually assesses the general characteristics of the dataset before the application of any machine learning algorithms. While a wrapper method requires a predefined learning algorithm in the process of feature selection, the features are selected based on the performance of the predetermined algorithm. Therefore, the wrapper method is more computationally expensive than the filter method [143].

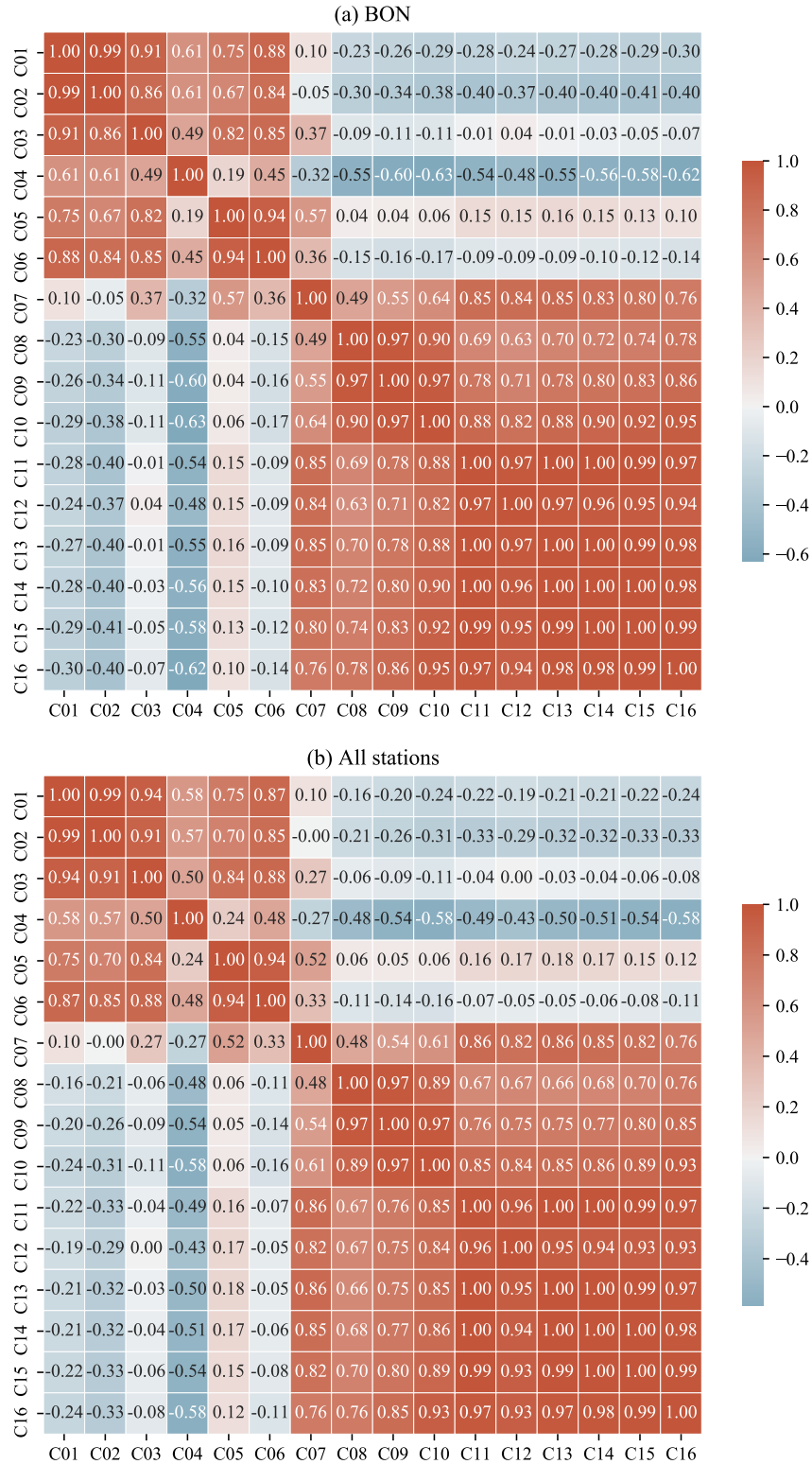


Figure 5.3: Correlation analysis among measurements of the 16 spectral bands of GOES-16 at (a) BON and (b) All stations of SURFRAD.

In general, a good feature is relevant to the target but is not redundant to any other input features [144]. Feature correlation is usually applied to describe the similarity and redundancy among the features [144, 145]. A feature is defined to be redundant if it is highly correlated with one or more other features [144]. Therefore, a correlation analysis is performed among the measurements of 16 spectral bands of GOES-16 to reduce the input size. This can improve the modeling efficiency, especially for large-regional applications.

One commonly used measure of similarity between two variables (X, Y) is the correlation coefficient $r(X, Y)$, which is defined as

$$r(X, Y) = \frac{\sum(x_i - \bar{x})(y_i - \bar{y})}{\sqrt{\sum(x_i - \bar{x})^2} \sqrt{\sum(y_i - \bar{y})^2}} \quad (5.1)$$

where (x_i, y_i) are the paired data of (X, Y) , \bar{x} and \bar{y} are the means of X and Y , respectively. The value of $r(X, Y)$ is inclusively between -1 and 1, with the value of 1 (shows an increase in both) or -1 (shows an increase in one but a decrease in the other) indicating X and Y are totally correlated. When X and Y are completely independent, the value of $r(X, Y)$ is 0.

The correlation analysis result for 16 spectral bands of GOES-16 is shown in Fig. 5.3. Fig. 5.3(a) presents the correlation coefficients of the 16 spectral bands at BON. There are some bands highly correlated, for instance, the coefficient of C12 and C13 is 1.00. Correlation analysis of GOES-16 bands at other SURFRAD stations have similar results, the overall coefficients involving all SURFRAD stations are shown in Fig. 5.3(b). Note that the correlation analysis is based on the satellite measurements at the target location with the pixel size of 1x1. When using more pixels, for example, 3x3 or 5x5, there are limited differences using averaged satellite measurements. It is shown in Fig. 5.3 that $r(X, Y) = r(Y, X)$ and $r(X, X) = 1.00$. A threshold of 0.95 is predefined to select the representative bands. In specific, if the coefficient of two channels is greater than 0.95, one of them is selected to represent the other. It is necessary to mention the selection of representative band for C08, C09, and C10. Since $r(C08, C09)$ and $r(C09, C10)$ are above the threshold, while $r(C08, C10)$ is below it, C09 is selected to represent both C08 and C10. As a result, the selected bands are C01, C03, C04, C05, C06, C07, C09, and C11.

5.2.3 Deep learning model

With the improvement of computational ability and the advancement of learning algorithms, deep learning has attracted increasing attention in solar resource assessment and forecasting in the past decade [132, 146]. Deep learning introduces simpler but more efficient representations that provide capabilities to build complex concepts in representation learning. Meanwhile, the depth of deep neural network (DNN) enables the multistep sequential instructions, which offer great power and flexibility in modeling complicated problems [78]. Different DNN structures have been proposed for solar irradiance modeling referring satellite

and sky images [132, 147, 148].

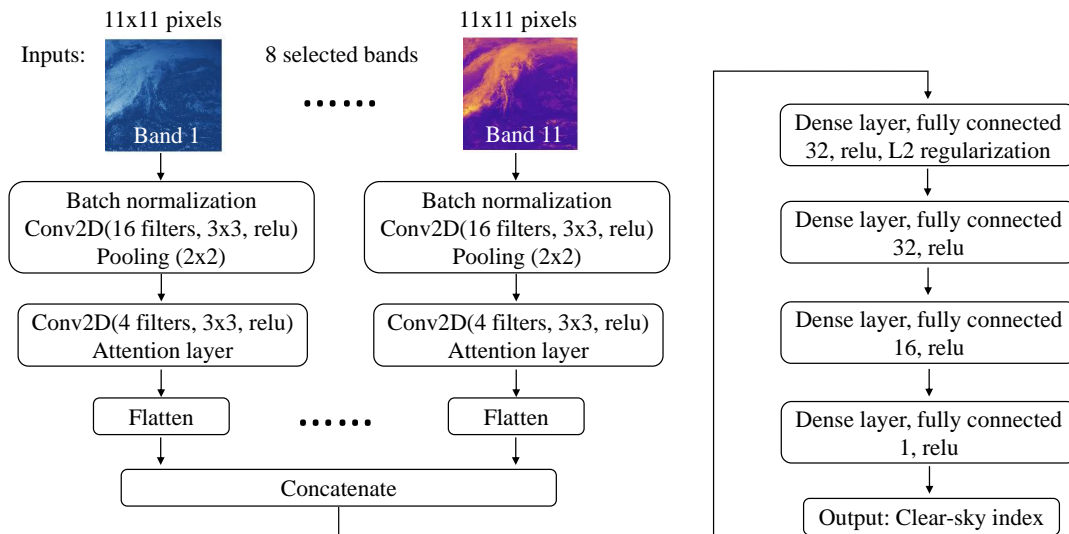


Figure 5.4: The structure of deep learning model for estimating ground solar irradiance using the GOES-16 images of selected bands. The inputs are images of 8 selected bands with size of 11×11 pixels, the output is the clear-sky index. Note that the hyperparameters might vary for different locations, this figure is just to show the structure.

The deep learning model proposed in this study employs convolutional, attention, and four fully connected dense layers as shown in Fig. 5.4. In specific, CNNs provide specialized neural networks to deal with data with a grid-structured topology such as images. Compared with fully connected networks, CNNs are more computationally efficient and easier in implementation and hyperparameters tuning [78]. As feed-forward neural networks, CNNs are powerful in extracting properties of input images, which can capture the features efficiently and reduce the amount of parameters. Convolutional layer is the core block of CNNs to discover local relationships via sparse connectivity, parameter sharing and equivariant representations [78]. An activation function (e.g., ReLU) is usually applied on the linear convolution results to introduce non-linearity on the output feature maps. While the pooling layer is to extract representative characteristics over local regions and reduce the dimension gradually [78]. The attention layer is based on attention mechanism [140] that has been extensively adopted in different applications such as image analysis including satellite images [149]. The attention mechanism can process perceptual information efficiently and accurately, by focusing on the target area and suppressing other useless content [150]. Similarly, the attention mechanism in deep learning is to enable the model focus on the features that are more important to the cur-

rent output [146], which can improve the performance of the model. While the dense layers are employed to learn the representations between the extracted input features and the targets.

The cropped satellite images of 8 selected GOES-16 bands are the inputs for the deep learning model based on Tensorflow [151]. As shown in Fig. 5.4, 8 images are processed parallelly via normalization, convolutional and attention layers. The extracted features of each image are then flattened and concatenated as the input vector of the four fully connected dense layers. The ReLU activation is applied in convolutional and dense layers, and the L2 regularization is to avoid over-fitting and improve the performance. The output is the clear-sky index, which is defined as the ratio between measured GHI and clear-sky GHI estimate. Clear-sky index is used to normalize the irradiance time series and reduce the seasonal and diurnal variations. Note that the clear-sky index is defined based on GHI. However, when developing the deep learning model for DNI estimation, the concept of clear-sky index is also adopted for DNI measurements and clear-sky DNI. Clear-sky GHI and clear-sky DNI are estimated by the Ineichen-Perez model [31] due to the simplicity. Although the Ineichen-Perez model has compromised performance in estimating clear-sky irradiance [103, 152], the impact on the final irradiance estimation remains limited as the estimated clear-sky index is converted back to irradiance components (i.e., GHI and DNI) by multiplying the clear-sky irradiance [36].

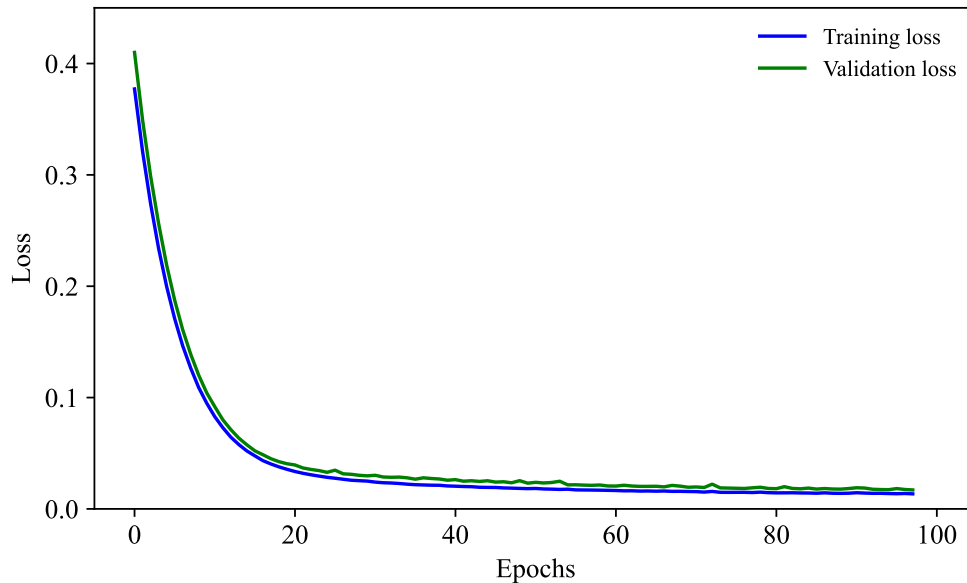


Figure 5.5: The loss curves of training and validation process for GHI estimation at BON. Both training loss and validation loss decrease with the trained epochs and finally converge with a slightly higher validation loss, which indicates a good fit.

To better represent the yearly variations, data in March, June, September, and December are used for testing, while the data in the remaining months in 2019 are used as training and validation sets (in which 20% of the data is used for validation). Adam is the applied optimizer and the Huber loss function is used to update the network parameters. The numbers of layers and units, the numbers of filters and kernel size, and other hyperparameters such as learning rate and regularization factor are optimally selected by grid search. In training the deep learning model, the Xavier initialization method [153] is employed. After obtaining the optimal hyperparameters, many independent trainings are conducted with data shuffling. In the end, the model with the best performance on the validation data is selected. Fig. 5.5 presents one of the loss curves during the training and validation process for GHI estimation at BON.

The error evaluation metrics are root mean squared error (RMSE), mean bias error (MBE), and their normalized counterparts (nRMSE, nMBE) defined by the following equations:

$$\text{RMSE} = \sqrt{\frac{1}{N} \sum (e_i - o_i)^2} \quad (5.2)$$

$$\text{nRMSE} = \frac{\sqrt{\frac{1}{N} \sum (e_i - o_i)^2}}{\frac{1}{N} \sum o_i} \quad (5.3)$$

$$\text{MBE} = \frac{1}{N} \sum (e_i - o_i) \quad (5.4)$$

$$\text{nMBE} = \frac{\sum (e_i - o_i)}{\sum o_i} \quad (5.5)$$

where e_i and o_i are the pair of irradiance estimation and ground observation (i.e., GHI or DNI), N is the total number of compared data points.

5.3 Results

To evaluate the effectiveness of satellite bands selection from correlation analysis, we compare the performance of GHI and DNI estimations based on the proposed deep learning network (without the attention layer) using satellite images of 16 bands (referred as DNN16 model) and 8 selected bands (referred as DNN8 model). Similarly, to assess the application of attention mechanism in processing satellite images, the results of deep learning model with attention layer (referred as DNNa8 model) are also included in the comparisons in Section 5.3.1, where the reference is the irradiance estimations from NSRDB. As clouds are the dominant factor affecting the available solar irradiance on the ground level, the comparisons of irradiance estimations of the deep learning model and NSRDB are detailed in clear and cloudy periods in Section 5.3.2. While

a further error analysis of irradiance estimation within different clear-sky index intervals is presented in Section 5.3.3.

5.3.1 Comparison of different deep learning networks for irradiance estimations

The irradiance estimation results at SURFRAD stations are presented in Table 5.3 (for GHI) and Table 5.4 (for DNI). It is shown in Table 5.3 that deep learning models for GHI estimations using 16 satellite bands (DNN16) and 8 selected bands (DNN8) have comparable overall performance. DNN16 generates GHI estimations at all the SURFRAD stations with the nRMSE of 20.62% and nMBE of 0.72%, while DNN8 yields a result with slightly larger discrepancies, the nRMSE is 21.17% and the nMBE is -1.97%. When it comes to DNI estimation (see Table 5.4), the overall results of DNN16 and DNN8 also have limited differences. In specific, the result of DNN16 for DNI estimation has an nRMSE of 24.43% and an nMBE of 0.53%, while DNN8 produces a slightly better result with the nRMSE of 24.36% and the nMBE of 0.44%.

The integration of attention mechanism generally can improve the irradiance estimations. As shown in Tables 5.3 and 5.4, the overall GHI estimation of DNNa8 has a lower nRMSE value of 20.57% than DNN8 (nRMSE of 21.17%), while the nMBE is almost the same (-2.04% vs -1.97%); The DNNa8 model also yields better DNI estimations compared with DNN8, the overall nRMSE is improved from 24.36% to 23.63%, and the nMBE is reduced from 0.44% to 0.36%.

Table 5.3: The RMSE and MBE in $[W m^{-2}]$, and nRMSE and nMBE in [%], of GHI estimation using different deep learning models at SURFRAD stations. The GHI estimation error of NSRDB is included as the benchmark.

	DNN16 ^a		DNN8 ^b		DNNa8 ^c		NSRDB	
	RMSE (nRMSE)	MBE (nMBE)	RMSE (nRMSE)	MBE (nMBE)	RMSE (nRMSE)	MBE (nMBE)	RMSE (nRMSE)	MBE (nMBE)
BON	89.34 (23.65)	7.53 (1.99)	91.66 (24.26)	8.20 (2.17)	89.13 (23.59)	-9.27 (-2.45)	97.81 (25.89)	-1.28 (-0.34)
DRA	64.64 (12.65)	-5.19 (-1.02)	64.80 (12.68)	-4.62 (-0.90)	66.67 (13.04)	2.83 (0.55)	86.02 (16.83)	-5.05 (-0.99)
FPK	84.44 (22.40)	6.04 (1.60)	87.55 (23.23)	-9.43 (-2.50)	88.65 (23.52)	0.50 (0.13)	105.05 (27.87)	-1.10 (-0.29)
GWN	85.60 (19.30)	9.78 (2.21)	87.88 (19.82)	-14.42 (-3.25)	88.76 (20.02)	-27.58 (-6.22)	107.08 (24.15)	0.18 (0.04)
PSU	97.00 (25.73)	18.97 (5.03)	97.18 (25.78)	-7.35 (-1.95)	91.13 (24.17)	-10.47 (-2.78)	123.42 (32.73)	6.45 (1.71)
SXF	79.57 (20.75)	-15.71 (-4.10)	84.72 (22.09)	-22.12 (-5.77)	80.33 (20.95)	-13.16 (-3.43)	103.12 (26.89)	19.59 (5.11)
TBL	95.84 (22.53)	-0.66 (-0.15)	98.81 (23.22)	-8.75 (-2.06)	92.33 (21.70)	-1.91 (-0.45)	121.47 (28.55)	-0.56 (-0.13)
ALL	85.78 (20.62)	2.98 (0.72)	88.05 (21.17)	-8.18 (-1.97)	85.55 (20.57)	-8.50 (-2.04)	106.96 (25.72)	2.43 (0.58)

^a 'DNN16' means DNN with inputs of all the 16 channels.

^b 'DNN8' means DNN with inputs of the 8 selected channels.

^c 'DNNa8' means DNN with attention layer using the 8 selected channels.

Compared with the GHI and DNI estimations from NSRDB, deep learning based models show substantial improvements as shown in Tables 5.3 and 5.4. GHI estimation using DNNa8 reduces the nRMSE by 5.15% from 25.72% to 20.57%, while the bias turns to be enlarged from 0.58% to -2.04%. While for DNI estimation, deep learning models show more aggressive improvements. The nRMSE is reduced from 37.40% to 23.63% (a 13.77% reduction) using the DNNa8 model, and the bias decreases from 6.25% to 0.36%.

Table 5.4: The RMSE and nMBE, in $[W m^{-2}]$, nRMSE and nMBE in [%], of DNI estimation using different deep learning models at SURFRAD stations. The DNI estimation error of NSRDB is included as the benchmark.

	DNN16 ^a		DNN8 ^b		DNNa8 ^c		NSRDB	
	RMSE (nRMSE)	MBE (nMBE)	RMSE (nRMSE)	MBE (nMBE)	RMSE (nRMSE)	MBE (nMBE)	RMSE (nRMSE)	MBE (nMBE)
BON	148.26 (26.25)	33.30 (5.90)	143.01 (25.32)	22.45 (3.98)	143.70 (25.44)	-1.07 (-0.19)	214.61 (38.00)	40.72 (7.21)
DRA	124.35 (17.05)	22.69 (3.11)	122.89 (16.85)	19.05 (2.61)	119.28 (16.36)	24.66 (3.38)	185.50 (25.44)	1.75 (0.24)
FPK	178.43 (29.13)	-2.18 (-0.36)	174.16 (28.43)	29.10 (5.64)	165.76 (27.07)	-13.32 (-2.18)	256.06 (41.81)	40.53 (6.62)
GWN	129.80 (22.40)	-23.11 (-3.99)	133.64 (23.06)	-27.88 (-4.81)	123.81 (21.37)	3.88 (0.67)	200.48 (34.60)	40.12 (6.92)
PSU	163.44 (29.90)	-28.28 (-5.17)	165.87 (30.34)	-30.22 (-5.53)	161.80 (29.60)	5.09 (0.93)	245.39 (44.89)	50.07 (9.16)
SXF	147.58 (25.68)	21.84 (3.80)	149.16 (25.95)	19.43 (3.38)	143.46 (24.96)	-6.33 (-1.10)	253.93 (44.18)	73.79 (12.84)
TBL	156.15 (25.90)	-6.82 (-1.13)	156.45 (25.95)	-11.80 (-1.96)	154.95 (25.70)	-7.36 (-1.22)	247.34 (41.02)	37.57 (6.23)
ALL	148.69 (24.43)	3.24 (0.53)	148.26 (24.36)	2.66 (0.44)	143.84 (23.63)	2.20 (0.36)	227.61 (37.40)	38.04 (6.25)

^a 'DNN16' means DNN with inputs of all the 16 channels.

^b 'DNN8' means DNN with inputs of the 8 selected channels.

^c 'DNNa8' means DNN with attention layer using the 8 selected channels.

5.3.2 Comparison under clear and cloudy sky conditions

Since the cloud is the primary atmospheric constitute affecting the available solar irradiance on the ground level, solar resource assessment under cloudy sky conditions is generally associated with larger uncertainties in both semi-empirical and physical satellite-based methods [127]. Therefore, it might be of interest to evaluate the performance of deep learning based model for solar irradiance (i.e., GHI and DNI) estimation under cloudy and clear sky conditions that are based on Bright-Sun clear-sky detection algorithm [112].

The overall performance of GHI and DNI estimations using deep learning model (DNNa8) and physical solar model (NSRDB) are presented in Tables 5.5 and 5.6. As shown in Table 5.5, GHI estimation of DNNa8 has larger discrepancies than NSRDB in clear sky periods. In specific, DNNa8 has a RMSE of

39.88 W m² and a MBE of -9.78 W m², while the RMSE and MBE of NSRDB are 27.09 W m² and 2.15 W m², respectively. In cloudy sky periods, GHI estimates of DNNa8 show better performance than NSRDB in terms of nRMSE with the reduction of 6.92% from 32.48% to 25.56%, while the bias becomes larger from 0.68% to -2.22%. As for DNI estimation (see Table 5.6), DNNa8 typically shows better results than NSRDB with the exception of a larger bias in clear sky periods. Compared with NSRDB for estimating DNI in clear skies, DNNa8 reduces the RMSE from 85.43 W m² to 73.55 W m², while the MBE is enlarged from -12.28 W m² to -20.23 W m². When the sky is cloudy, the DNI estimation of NSRDB has a RMSE of 263.85 W m² and the MBE is 58.17 W m². DNNa8 yields an estimation with the errors of RMSE and MBE decreased to 163.73 W m² and 11.18 W m², respectively. The results of GHI and DNI estimation on some selected days are presented in Fig. 5.6 for clear, cloudy, and partially cloudy days. It is shown that both GHI and DNI of DNNa8 have lower divergences compared with NSRDB in cloudy periods.

Table 5.5: The comparison of GHI estimation results under clear and cloudy periods at all SURFRAD stations using deep learning (DNNa8) and physical solar model (NSRDB).

	DNNa8				NSRDB			
	RMSE [W m ⁻²]	nRMSE [%]	MBE [W m ⁻²]	nMBE [%]	RMSE [W m ⁻²]	nRMSE [%]	MBE [W m ⁻²]	nMBE [%]
Clear periods	39.88	6.65	-9.78	-1.63	27.09	4.52	2.15	0.36
Cloudy periods	93.94	25.56	-8.16	-2.22	119.40	32.48	2.50	0.68
All periods	85.55	20.57	-8.18	-2.04	106.96	25.72	2.43	0.58

Table 5.6: The comparison of DNI estimation results under clear and cloudy periods at all SURFRAD stations using deep learning (DNNa8) and physical solar model (NSRDB).

	DNNa8				NSRDB			
	RMSE [W m ⁻²]	nRMSE [%]	MBE [W m ⁻²]	nMBE [%]	RMSE [W m ⁻²]	nRMSE [%]	MBE [W m ⁻²]	nMBE [%]
Clear periods	73.55	8.40	-20.23	-2.31	85.43	9.76	-12.28	-1.40
Cloudy periods	163.73	32.62	11.18	-2.22	263.85	52.59	58.17	11.59
All periods	143.84	23.63	2.20	0.36	227.61	37.40	38.04	6.25

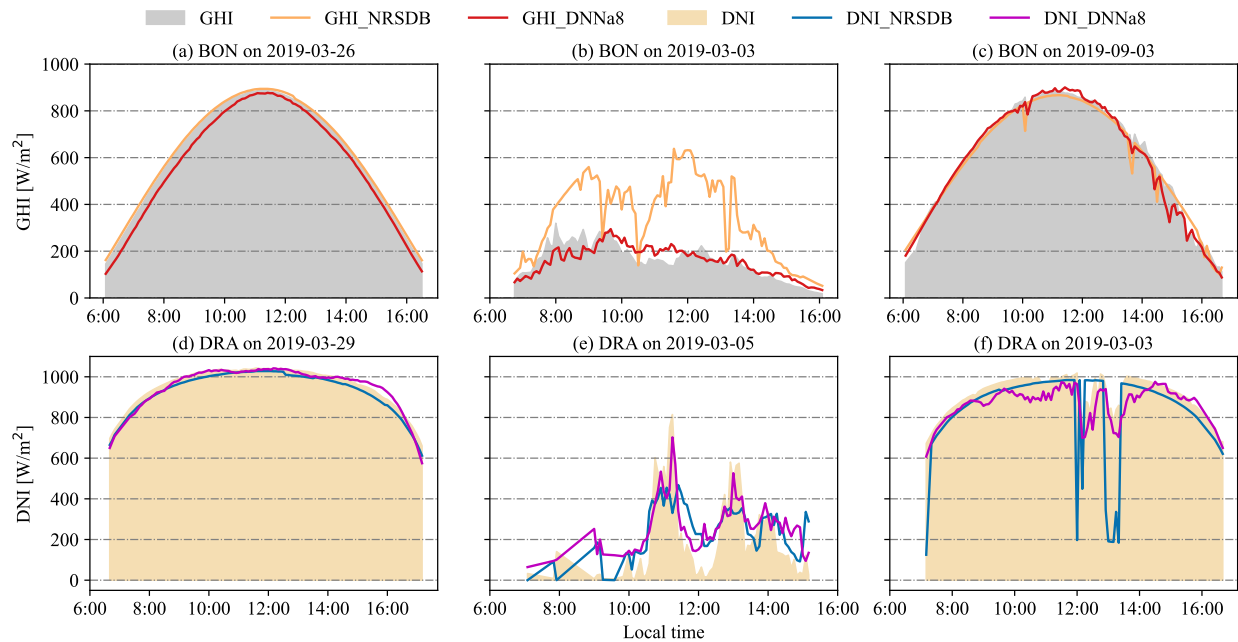


Figure 5.6: GHI and DNI estimation results on some selected days at BON and DRA. (a) and (d) are on clear days, (b) and (e) are on cloudy days, while (c) and (f) are for partially cloudy days.

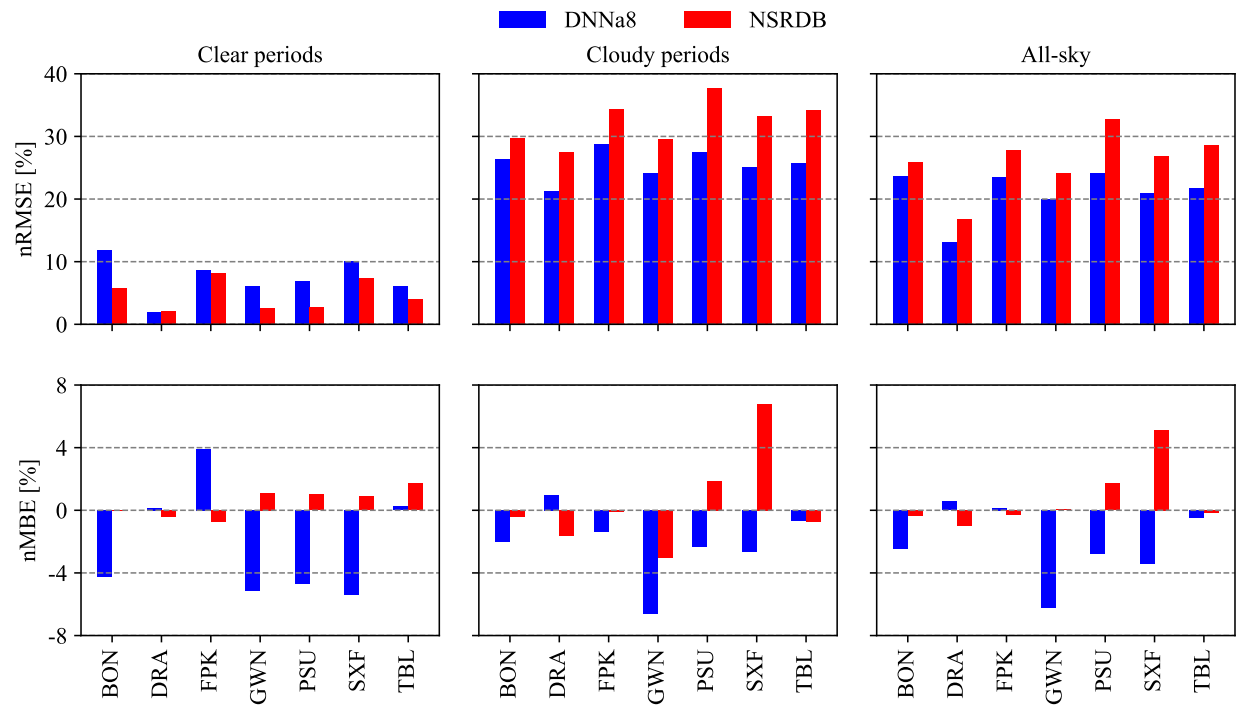


Figure 5.7: The comparison of GHI estimation using deep learning (DNNa8) and physical solar model (NSRDB) under clear, cloudy, all-sky conditions at all SURFRAD stations.

Fig. 5.7 presents the detailed comparison of GHI estimation at all SURFRAD stations using deep learning and physical model. Compared with NSRDB, DNNa8 generally produces lower RMSE in cloudy and all-sky conditions, while the RMSE value in clear periods is higher. DNNa8 turns to generates comparatively larger negative bias for both clear and cloudy periods (e.g., BON, GWN, and PSU). The site-specific comparison of DNI estimation is shown in Fig. 5.8. Generally, deep learning model outperforms the physical model in cloudy sky conditions with lower values of RMSE and MBE. Similarly, DNNa8 is more likely to yield DNI estimation with larger biases in clear periods.

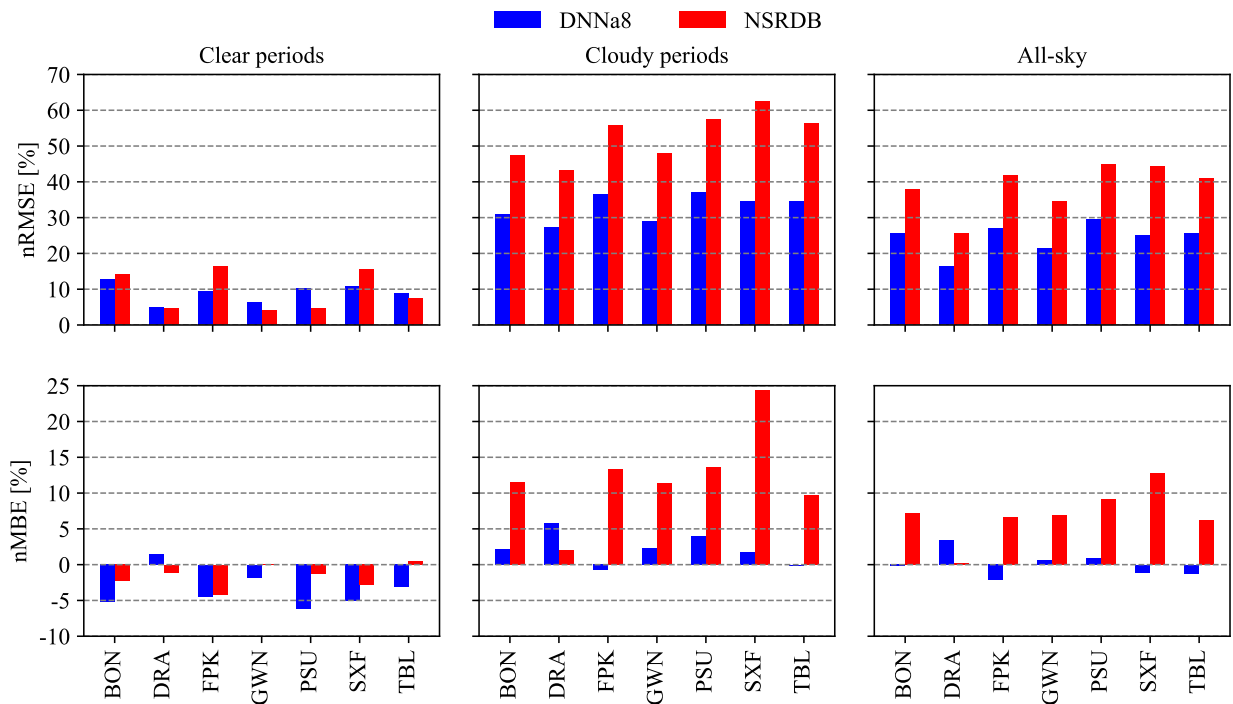


Figure 5.8: The comparison of DNI estimation using deep learning (DNNa8) and physical solar model (NSRDB) under clear, cloudy, all-sky conditions at all SURFRAD stations.

5.3.3 Error analysis

To further evaluate the results of solar irradiance estimations using deep learning based method, we herein compare the performance with physical model in NSRDB within different clear-sky index intervals based on the Ineichen-Perez model. Since the intervals of clear-sky index are determined for GHI and DNI separately, the error analysis is performed in each clear-sky index intervals for both GHI and DNI estimations. Note that the use of other clear-sky models, e.g., McClear [32] or REST2 [33] has similar results, as the aim is to evaluate the performance of GHI and DNI estimations under various conditions.

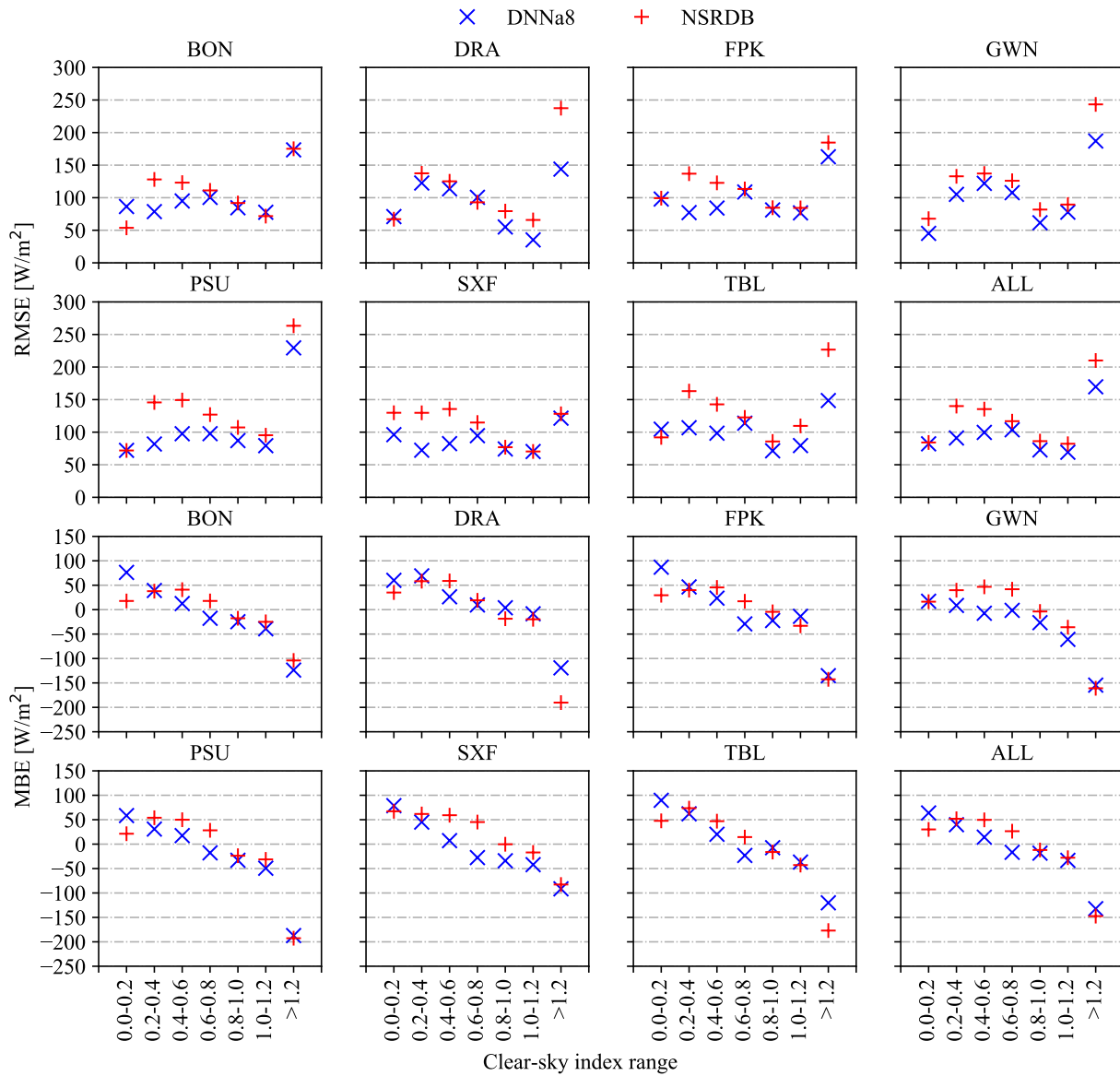


Figure 5.9: The comparison of GHI estimation using deep learning (DNNa8) and physical solar model (NSRDB) across clear-sky index intervals at all SURFRAD stations. 'ALL' means all the stations are included.

A detailed comparison of GHI estimation in different clear-sky index intervals at all SURFRAD stations is presented in Fig. 5.9. Generally, DNNa8 is more likely to produce GHI estimation with lower discrepancies (also see Fig. A5.1 for the joint and marginal distributions for GHI measurements and estimations, and Fig. A5.2 for error distributions). Both DNNa8 and NSRDB generate overestimation in the conditions of low clear-sky index and underestimation when the clear-sky index is high, especially when the clear-sky

index exceeds 1.2 as shown in Fig. 5.9. Moreover, DNNa8 and NSRDB also exhibit high divergences in GHI estimation when the clear-sky index is higher than 1.2.

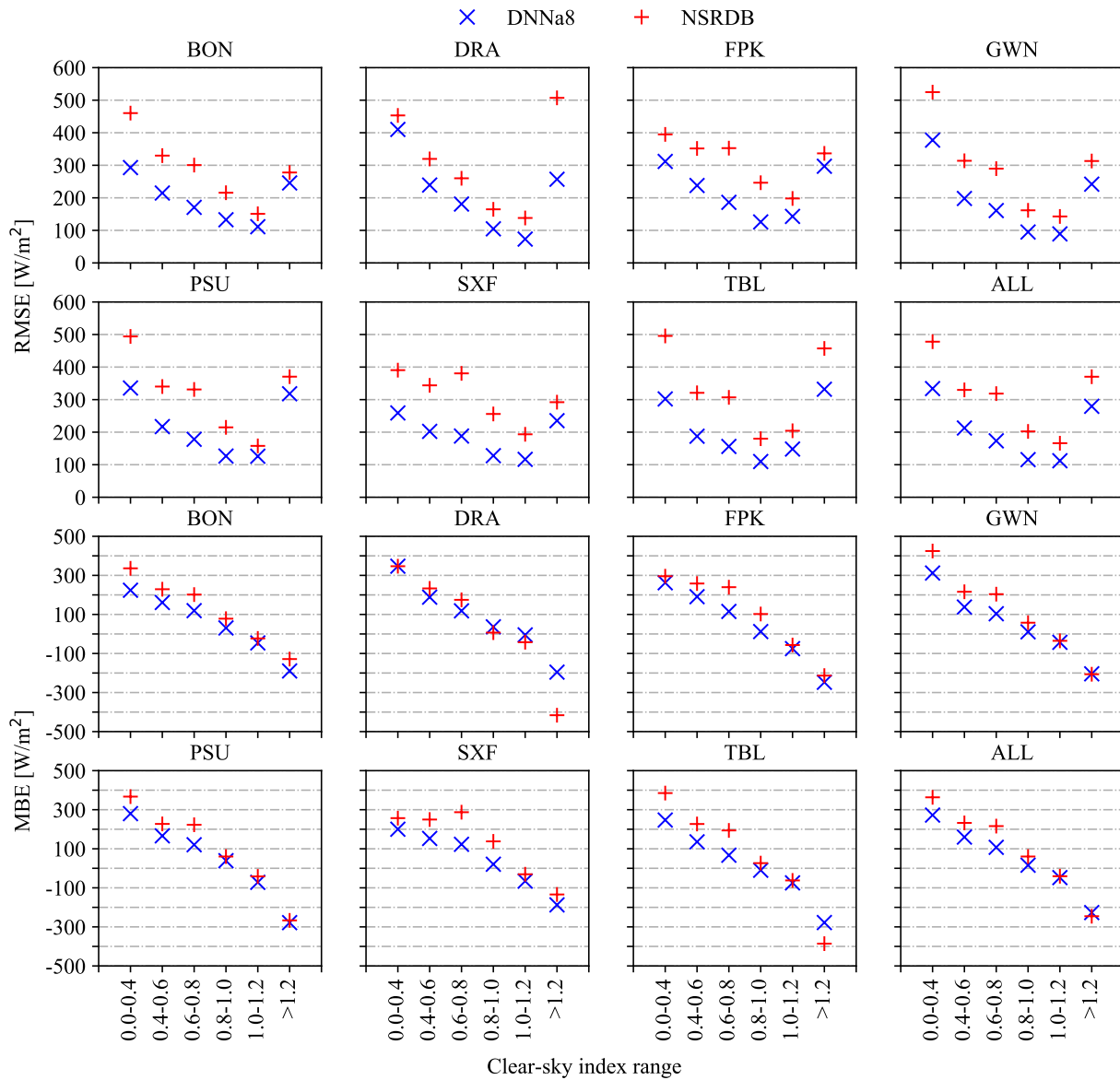


Figure 5.10: The comparison of DNI estimation using deep learning (DNNa8) and physical solar model (NSRDB) across clear-sky index intervals at all SURFRAD stations. 'ALL' means all the stations are included.

Fig. 5.10 presents the comparison of DNI estimation in different clear-sky intervals at all SURFRAD stations. The overall trend is that both deep learning and physical model yield DNI estimations with lower RMSE values when the clear-sky index increases. Meanwhile, DNI is generally overestimated when the

clear-sky index is low and underestimated for high clear-sky indexes, the bias exhibits a linear approximation and decreases from positive to negative with the increase of clear-sky index. Despite some on-site variations, for instance, high RMSE when clear-sky index exceeds 1.2 (i.e., DRA and FPK), larger divergences of DNNa8 (e.g., at GWN and PSU when clear-sky index is greater than 1.2), deep learning generally outperforms physical model (see Fig. A5.3 for the joint and marginal distributions for DNI measurements and estimations, and Fig. A5.4 for error distributions).

5.4 Discussion

Based on the results of DNN16 and DNN8, correlation analysis is effective to select the representative satellite bands to support solar irradiance modeling. Note that although the results of DNN16 and DNN08 show some site-specific variations as detailed in Tables 5.3 and 5.4, the overall picture is that divergences between DNN16 and DNN8 remain insignificant. This means the information in the sub-selected bands is still sufficient to infer the atmospheric compositions attenuating solar radiation. Therefore, it can reduce the complexity and improve the efficiency in retrieving solar irradiance using satellite data, especially for regional applications with long-time period. Similarly, based on the results of DNN8 and DNNa8, the attention layer generally shows positive impact for irradiance estimation. However, the improvement is not significant. The possible reason is that the attention mechanism is to extract information on a sub-target area rather than the whole domain, and the ground station is located on the centered pixel in relatively small images. Therefore, the attention mechanism can not outperform too much than the baseline model. Since NSRDB employs physical solar model and reanalysis products to simulate the interactions between atmospheric components and solar radiation. The improvements in both GHI and DNI estimations using deep learning and satellite images indicate that deep learning may have the potential to simplify the radiative transfer simulations for solar resource assessment.

When comparing the results in clear and cloudy periods, DNNa8 generally turns to produce larger biases for GHI estimations in both clear and cloudy sky conditions and therefore underestimates in the overall results (see Table 5.5). Nevertheless, the improvements of deep learning based model for estimating GHI in cloudy conditions are noticeable. Consequently, the overall RMSE of all-sky GHI estimation of DNNa8 is smaller than NSRDB. As for DNI estimation, DNNa8 outperforms NSRDB for all-sky conditions. Since DNI is more sensitive than GHI to the attenuating effect of atmospheric constituents, the estimation of DNI is more challenging, evidenced by the generally larger variances and biases produced by both deep learning and physical models (see Table 5.6). Deep learning shows a compromised performance for irradiance

estimation in clear sky conditions. The possible reason could be the selected satellite bands are more effective in representing the cloud properties, while the information of atmospheric aerosol and water vapor can not be extracted as accurately as the reanalysis products used in NSRDB, especially under clear sky conditions. Nevertheless, the application of deep learning could improve the overall performance of solar resource assessment inferring satellite measurements compared to the physical solar model in NSRDB. The improvements in GHI and DNI estimations might be beneficial to the solar community.

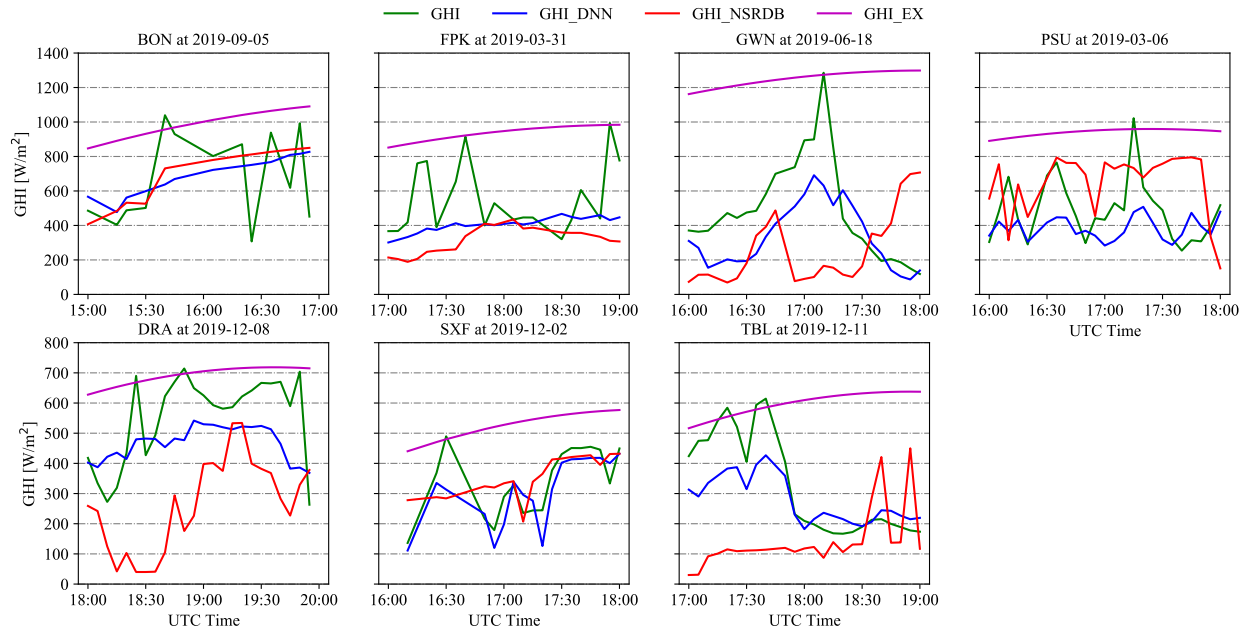


Figure 5.11: The cloud enhancement events at the SURFRAD stations. GHI is the actual measurement, GHI_DNN and GHI_NSRDB are the estimations from the deep learning model and physical solar model, respectively. GHI_EX is the extraterrestrial radiation projected on the horizontal surface.

For the high discrepancies observed in Fig. 5.9 when clear-sky index is greater than 1.2, the possible explanation could be the cloud enhancement effect [154]. Cloud enhancements can cause the GHI to instantaneously exceed the clear-sky GHI and even the solar constant [123]. As shown in Fig. 5.11, the measured GHI can be greater than the projection of extraterrestrial radiation on the horizontal surface with high fluctuations due to cloud enhancement. Therefore, the clear-sky index is expected to be greater than 1.0. However, the cloud enhancement is rather an instantaneous process, satellite sensors might not be able to capture these phenomena. Satellite-based deep learning and physical methods could not obtain accurate GHI estimation when cloud enhancement happens, which is the major contributor for the relatively larger errors (i.e., underestimation) when the clear-sky index is greater than 1.2. Meanwhile, deep learning still faces challenges in

retrieving DNI via satellite images under cloudy conditions (low clear-sky index, see Fig. 5.10), where the errors are comparatively larger. Although DNI estimation is generally with larger uncertainties, deep learning shows potential especially in extracting cloud information via satellite images. To further improve the accuracy of solar irradiance estimation, cloud enhancements on GHI should be better accounted for. While for DNI, more sophisticated methods to reveal the cloud affecting direct solar rays should be developed.

5.5 Conclusions

The 16 spectral channels of GOES-16 can be used individually or together to reveal atmospheric characteristics for various applications. In this work, multispectral GOES-16 images are used for estimating solar irradiance (i.e., GHI and DNI) by deep learning. After pre-processing, a correlation analysis is applied to select the representative bands. The satellite images of selected bands are then used as inputs for a deep learning model based on convolutional, attention, and dense layers. Clear-sky indexes are used as the labels for both GHI and DNI estimation models. The performance of the proposed methods and the effectiveness of bands selection are evaluated against the measurements and compared with irradiance estimations from NSRDB.

Deep learning models based on 16 spectral bands (DNN16) and 8 selected bands (DNN8) have comparable performance for both GHI and DNI estimations compared to the ground measurements at SURFRAD stations. This demonstrates the effectiveness of correlation analysis in selecting representative spectral satellite bands for solar irradiance estimation. It is more effective to use a subset of satellite spectral bands to reduce model complexity and computational cost, which is especially beneficial for large-scale applications.

Furthermore, the integration of attention mechanism in deep learning (DNNa8) shows improvements in both GHI and DNI estimations. When compared with NSRDB, DNNa8 generally produces GHI estimation with lower RMSE in cloudy conditions, but higher RMSE in cloudless skies. Nevertheless, the improvements in GHI estimation under cloudy conditions lead to an overall nRMSE reduction of 5.15%. Similarly, the overall nRMSE for DNI estimations is reduced from 37.40% to 23.63%, and the bias is improved from 6.25% to 0.36%. Satellite images provide more spatial information (i.e., nonlocal cloud) around the target location than a single pixel, and the attention mechanism enables the model focus on more important features. As a result, both GHI and DNI estimations show improvements, especially in cloudy conditions. This means the attention mechanism might be applicable for solar irradiance estimation over a larger area given on-site data available.

When comparing DNNa8 and NSRDB in irradiance estimations across different ranges of clear-sky

index, deep learning models still show better overall performance in both GHI and DNI estimations. That said, both GHI and DNI estimations with improved accuracy via deep learning might provide more benefits in solar irradiance modeling. It is necessary to mention that both satellite-based deep learning and physical models could not account for the cloud enhancement effects, where comparatively larger errors are observed for GHI estimation when the clear-sky index exceeds 1.2. Although deep learning performs comparatively better than physical models in extracting cloud information, more efforts are still needed for revealing the cloud properties across the vertical atmospheric layers.

In summary, correlation analysis is effective in selecting representative satellite bands to reduce the complexity and improve the efficiency in solar irradiance estimation. Although deep learning with attention mechanism provides an alternative for satellite-to-irradiance methods, there are still some limitations, such as the need of ground measurements for model development and the incapability in capturing cloud enhancement events. Notwithstanding, the combination of deep learning and remote sensing shows potential in extracting cloud information via satellite images. The high spatiotemporal resolution satellite-to-irradiance data with improved accuracy can better capture the solar variability, which is beneficial for designing solar energy projects.

5.6 Acknowledgement

This chapter, in full, is a reprint of S. Chen, C. Li, Y. Xie, and M. Li (2023). Global and direct solar irradiance estimation using deep learning and selected spectral satellite images. *Applied Energy*, 352, 121979. The abstract is accepted as an oral presentation at the *APS March Meeting*, Las Vegas, Nevada, USA, 2023. The thesis author is the first author of this manuscript.

5.7 Appendix

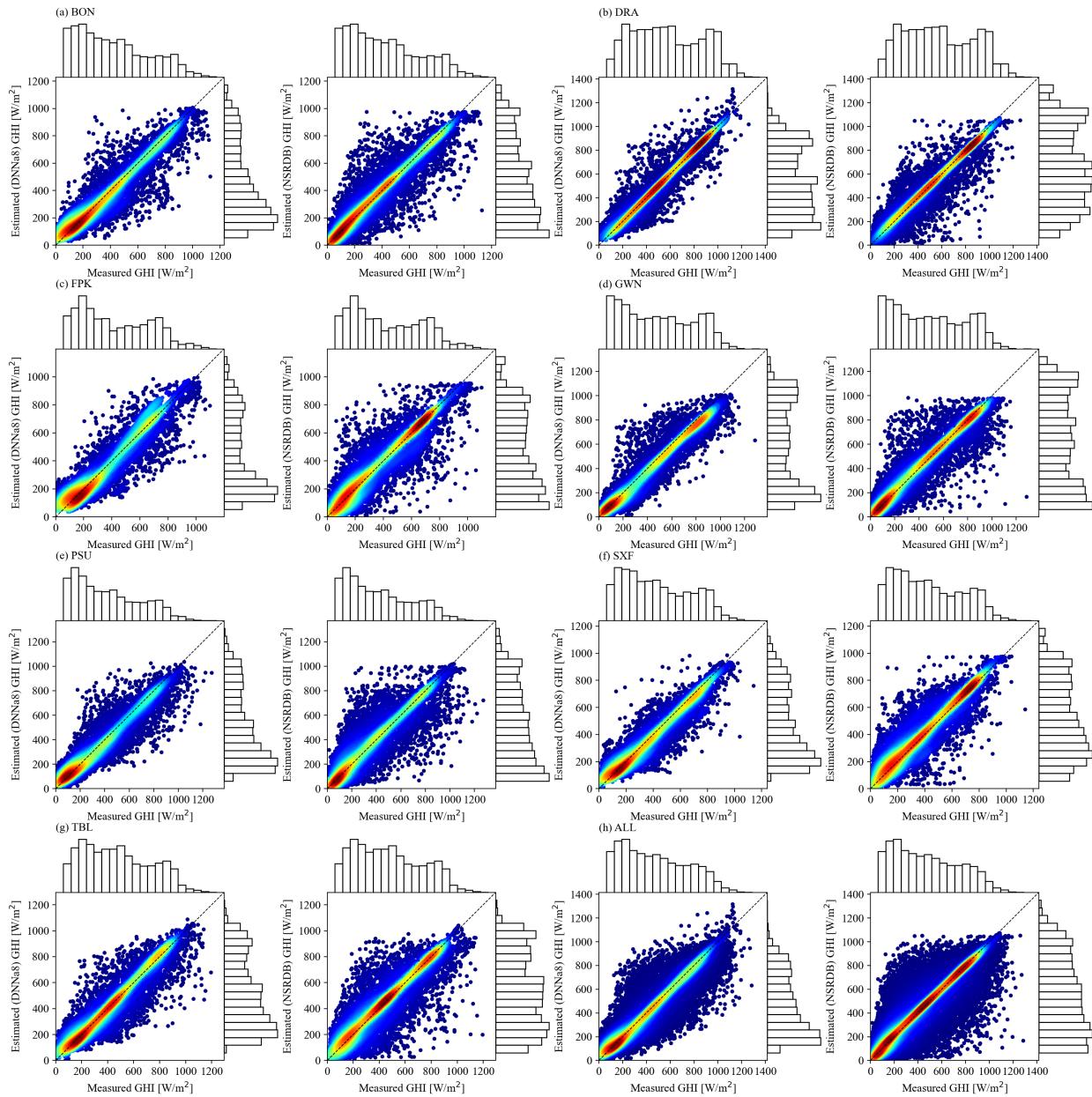


Figure A5.1: Joint and marginal distributions for GHI measurements and estimations of DNNa8 and NSRDB at all SURFRAD stations: (a) BON, (b) DRA, (c) FPK, (d) GWN, (e) PSU, (f) SXF, (g) TBL, (h) ALL. 'ALL' means all the stations are included. The colors show 2D kernel densities. GHI estimations of DNNa8 generally show better agreements with GHI observations than NSRDB.

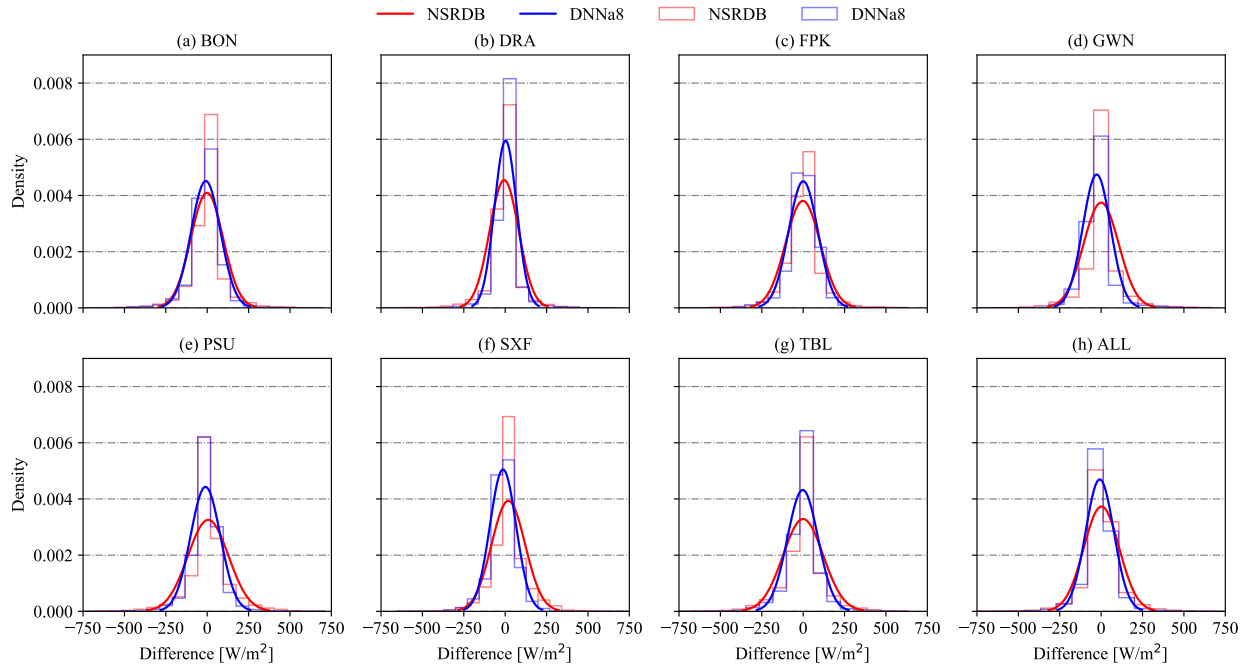


Figure A5.2: The error distributions for GHI estimations of DNNa8 and NSRDB at all the SURFRAD stations: (a) BON, (b) DRA, (c) FPK, (d) GWN, (e) PSU, (f) SXF, (g) TBL, (h) ALL. 'ALL' means all the stations are included. The density is a normalized probability density, the error is the difference between DNI estimate and measurement. A gaussian regression is performed for each distribution. The error of DNNa8 shows a narrower profile compared with NSRDB.

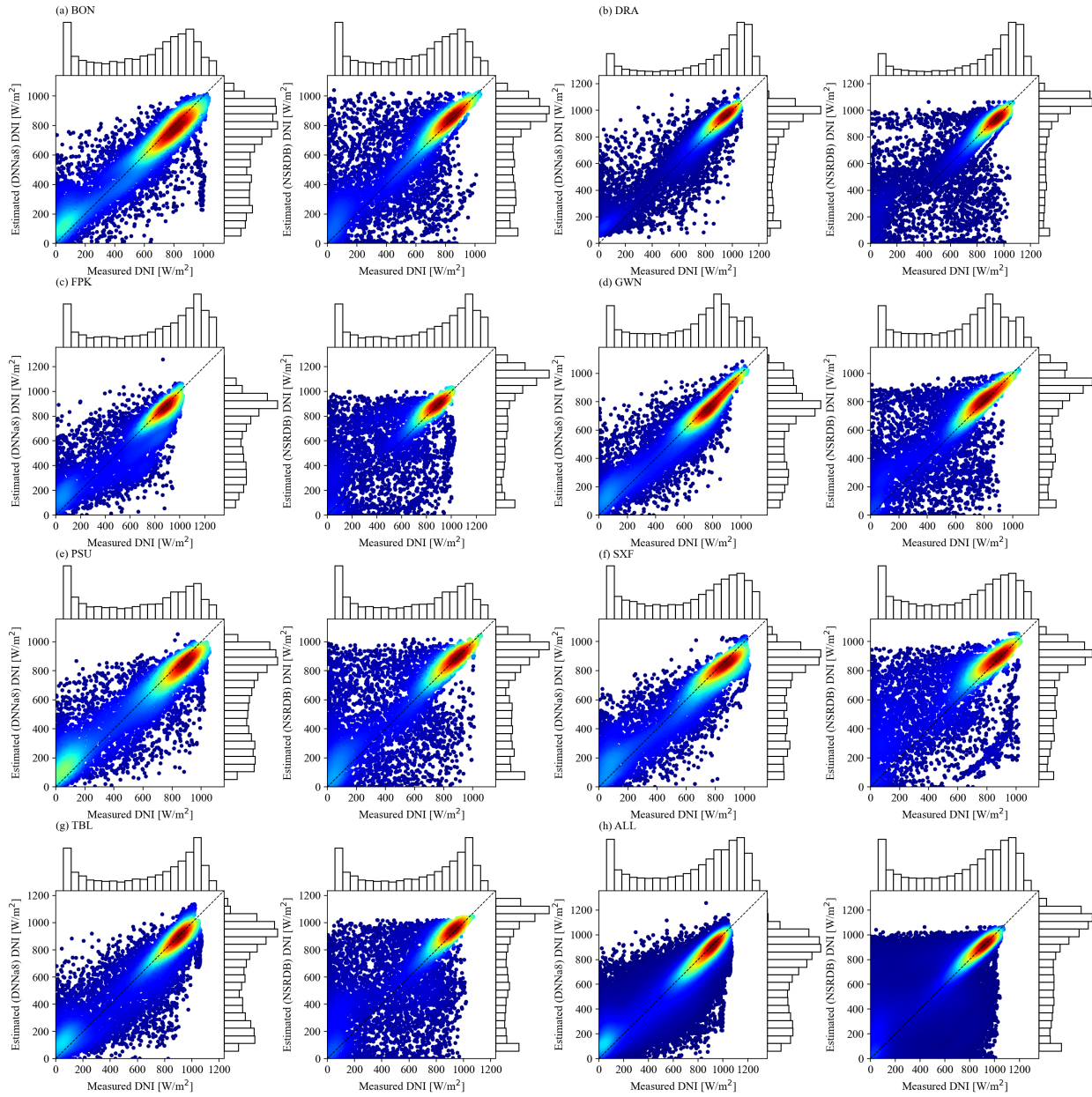


Figure A5.3: Joint and marginal distributions for DNI measurements and estimations of DNNa8 and NSRDB at all SURFRAD stations: (a) BON, (b) DRA, (c) FPK, (d) GWN, (e) PSU, (f) SXF, (g) TBL, (h) ALL. 'ALL' means all the stations are included. The colors show 2D kernel densities. DNI estimations of DNNa8 generally show better agreements with DNI observations than NSRDB.

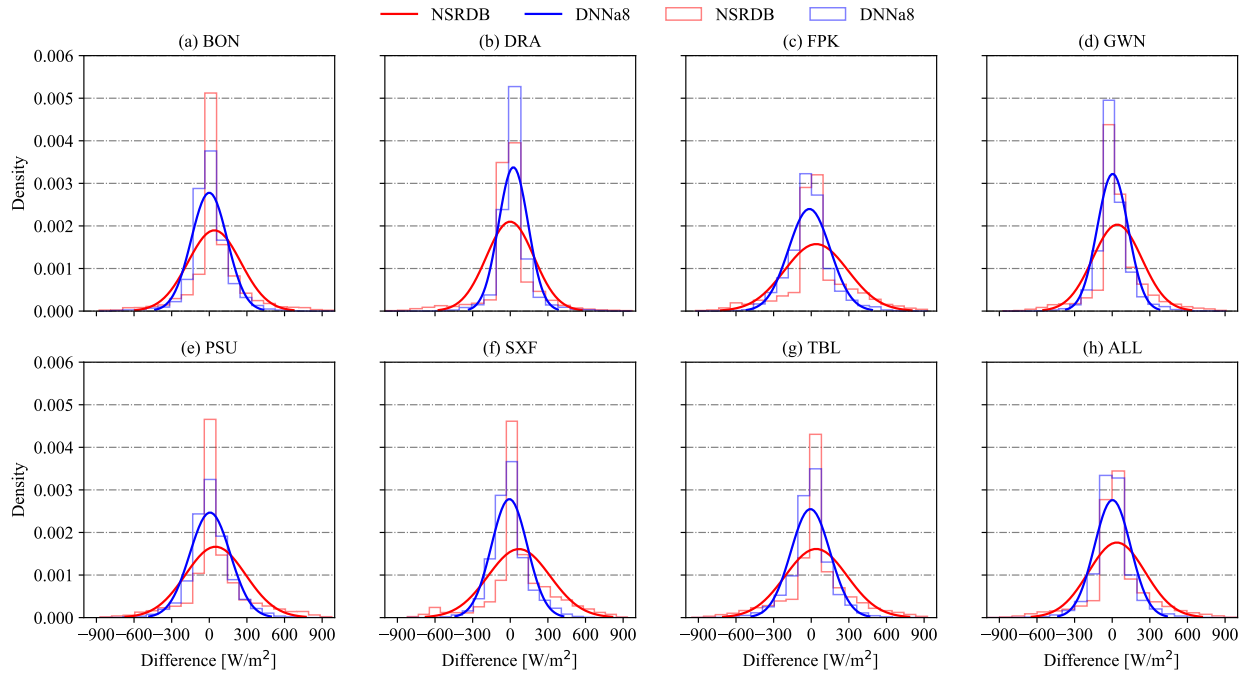


Figure A5.4: The error distributions for DNI estimations of DNNa8 and NSRDB at all the SURFRAD stations: (a) BON, (b) DRA, (c) FPK, (d) GWN, (e) PSU, (f) SXF, (g) TBL, (h) ALL. 'ALL' means all the stations are included. The density is a normalized probability density, the error is the difference between DNI estimate and measurement. A gaussian regression is performed for each distribution. The error of DNNa8 shows a narrower profile compared with NSRDB.

Chapter 6

Improved satellite-based intra-day solar forecasting with a chain of deep learning models

6.1 Introduction

Renewables are expected to account for over 90% of the global electricity expansion in the next years due to energy security concerns and climate ambitions. The total capacity of solar photovoltaic (PV) is set to surpass coal and become the world largest power source over 2022-2027 [155]. Despite the aggressive acceleration in the installed capacity, the operation and integration of solar power still face challenges because of its intermittency [11, 156]. To address the issues related with solar variability, one of the solutions could be solar forecasting [8, 14]. Indeed, Solar forecasting could be cost-effective, with the aim to support system management and scheduling to meet the changing demand and therefore mitigate the variability of solar power, by providing predictions up to a few days ahead [21]. Generally, solar forecasting refers to both solar irradiance forecasting and solar power forecasting [20]. As indicated by the names, the former is focused on irradiance quantities such as global horizontal irradiance (GHI) or direct normal irradiance (DNI), while the latter is related with the power output of PV or concentrated solar power (CSP) systems. It is paramount to have good irradiance forecasts to get solar power forecasts with high quality [117], using either a data-driven approach or a physical model chain [21, 157].

In solar forecasting, one of the salient features of solar irradiance is the two-frequency pattern (i.e., yearly and diurnal cycles). Therefore, a clear-sky model that estimates the ground-level irradiance under a

cloud-free atmosphere is usually required to remove the seasonality [36, 152]. The spatio-temporal nature, as another important feature of solar irradiance, should also be considered in solar forecasting models by integrating available spatio-temporal information [21]. In fact, solar forecasts based on spatio-temporal inputs have demonstrated to be more beneficial than forecasts based solely on local measurements [158, 159]. This performance enhancement arises from the improved representation of cloud dynamics, as clouds are the primary driver of solar variability [160]. Three main methods can be used to obtain the spatio-temporal data in solar forecasting [21], namely, sky images for intra-hour forecasting [14], satellite measurements for intra-day forecasting [55], and numerical weather prediction (NWP) data for day-ahead forecasting [21].

The utilization of remote-sensing data is one of the advanced aspects in intra-day solar forecasting [21]. Geostationary satellites, such as Geostationary Operational Environmental Satellites (GOES), Meteosat, and Himawari, collectively offer a coverage of all the area within latitudes of $\pm 60^\circ$. Modern geostationary satellites provide much finer data in both spatial and temporal resolutions with more spectral bands. The advancement in remote sensing technology has substantially contributed to the development of satellite-derived irradiance products, with the spatio-temporal resolution improved to 2-km and 5-minute [105, 127, 161]. To that end, satellite images and satellite-derived irradiance products have been extensively used in solar forecasting applications [12, 14, 21, 162].

The critical insights regarding the use of satellite data and/or satellite-derived irradiance products for intra-day solar forecasting are summarized as follows,

- Satellite data used in solar forecasting can be from one single channel [67], two visible channels [55] or multiple channels [133, 163]. Satellite data of visible channels are mainly used to derived cloud index maps [55, 67], which are used to predict future cloud information via advection and extrapolation, and then get the irradiance forecasts using the Heliosat method [55, 164]; While the usage of data from multiple spectral channels is to account for the modulation effect of clouds on solar radiation, using either a deep learning model [163] or a physical classification method [133].
- The forecasting method can be semi-empirical [55] or deep learning based [159, 163]. The semi-empirical method mainly focuses on the determination of cloud dynamics using cloud motion analysis based on optical flow [55, 164], and the clear-sky irradiance is quantified by a clear-sky model [55]; While deep learning can be applied to detect the cloud motion using images of multiple satellite channels [163] or satellite-derived irradiance over the target region [159].
- Satellite-derived irradiance products can be based on semi-empirical models [165] or physical models [166, 167]. Similar to satellite images, satellite-derived irradiance can also provide spatio-temporal

information in solar forecasting [165, 166]. The semi-empirical satellite-to-irradiance method relies on the Heliosat model that empirically determines the cloud attenuation with historical satellite measurements [165]; While the physical method applies radiative transfer models in retrieving solar irradiance from satellite-derived atmospheric properties, e.g., the National Solar Radiation Database (NSRDB) [166].

- Satellite data or satellite-derived irradiance products can be used as the single exogenous input [55, 167] or a part of the inclusive inputs [165, 168]. For example, satellite or satellite-derived data can be used as the only input to derive and predict future cloud field and thus solar irradiance [55, 167]; To further improve the forecasting performance, some other types of data such as on-site measurements [165], NWP products [165], and sky images [168] are used as additional inputs for solar forecasting.
- Solar forecasts can be deterministic [163] or probabilistic [167]. So far, studies on solar forecasting are more focused on deterministic forecasts that offer single "best-guess" values [159, 163, 165]. On the other hand, probabilistic forecasts that quantify the uncertainty in forecasting provide valuable information for solar energy projects, and therefore have attracted more attention in the field [167, 168].

Given the inherent spatio-temporal nature of solar irradiance, it is more likely that high-accuracy forecasts can be produced by incorporating spatio-temporal information, for instance, via satellite data or satellite-derived irradiance products. However, in the selection of spatio-temporal data for intra-day solar forecasting, a clear determination has not yet been made regarding whether it is better to employ raw satellite measurements or satellite-derived irradiance products. Moreover, in our recent study [161], spectral satellite images of GOES-16 and deep learning algorithms are applied to estimate both GHI and DNI with the spatio-temporal resolution of 2-km and 5-minute at the ground level. The estimation results show substantial accuracy improvements when compared with NSRDB [49], which represents the-state-of-the-art in the satellite-based estimation of solar irradiance.

Therefore, one more research question herein is that if the satellite-derived irradiance products with improved accuracy (i.e., satellite-derived irradiance by deep learning (SAT-DL)) could lead to more accurate solar forecasts. In this regard, a deep learning model chain method is proposed for improved intra-day solar forecasting using spectral satellite data. The deep learning model chain consists of two deep learning models, one is to obtain spatial GHI estimates with improved accuracy, and the other is to subsequently produce forecasts based on the improved spatial estimates. The efficacy of the deep learning model chain

is evaluated by the comparisons with an end-to-end deep learning model using spectral satellite images and a hybrid physical-deep learning model based on NSRDB. The major contributions of this work are summarized as follows:

- An innovative deep learning model chain is proposed for generating intra-day GHI forecasts using spectral satellite measurements. This approach has improved forecast performance with high robustness. Instead of utilizing all spectral satellite bands, a subset of bands is selected to improve the modeling efficiency [161].
- The deep learning model chain comprises two parts: one for improving spatial GHI estimates and the other for subsequently generating GHI forecasts based on these improved estimates. Initially developed for single-location GHI estimates [161], the deep learning model has now been expanded for regional GHI estimations.
- The deep learning model chain is benchmarked against an end-to-end deep learning model using spectral satellite data and a hybrid physical-deep learning model using spatial NSRDB estimates. The superior performance of our proposed method provides valuable insights into the selection of spatio-temporal information, including satellite data and satellite-derived irradiance products, for solar forecasting applications.

The rest of this paper is structured as follows: Section 6.2 describes the data and the methods, where data acquisition and pre-processing procedure are presented in Section 6.2.1, the utilization of SAT-DL product is detailed in Section 6.2.2, the forecasting setup is presented in Section 6.2.3, and performance evaluation methods of forecasts is presented in Section 6.2.4. The forecast results are quantitatively and qualitatively evaluated and compared in Section 6.3, and the implications are discussed in Section 6.4. Finally, Section 6.5 summarizes the key findings of this study.

6.2 Data and methods

This section describes the utilized data and methods for solar irradiance forecasting. As shown in the methodology flowchart (see Fig. 6.1), lagged spectral satellite images, and two satellite-derived irradiance products are used as three alternative inputs for intra-day solar irradiance forecasting from 15 minutes to 180 minutes ahead. The raw satellite data are from several selected spectral bands of GOES-16, while datasets of NSRDB and SAT-DL are satellite-derived irradiance products from raw satellite measurements. The main difference between NSRDB and SAT-DL is that the former applies a physical solar model (radiative

transfer model) to derive irradiance, while the latter employs a deep learning method. The labels are ground measurements (i.e., GHI) at the location centered in the domain of the satellite images, NSRDB and SAT-DL irradiance matrices. Then the inputs and corresponding labels are divided into subsets of training, validation, and testing to train and evaluate deep learning-based forecast model.

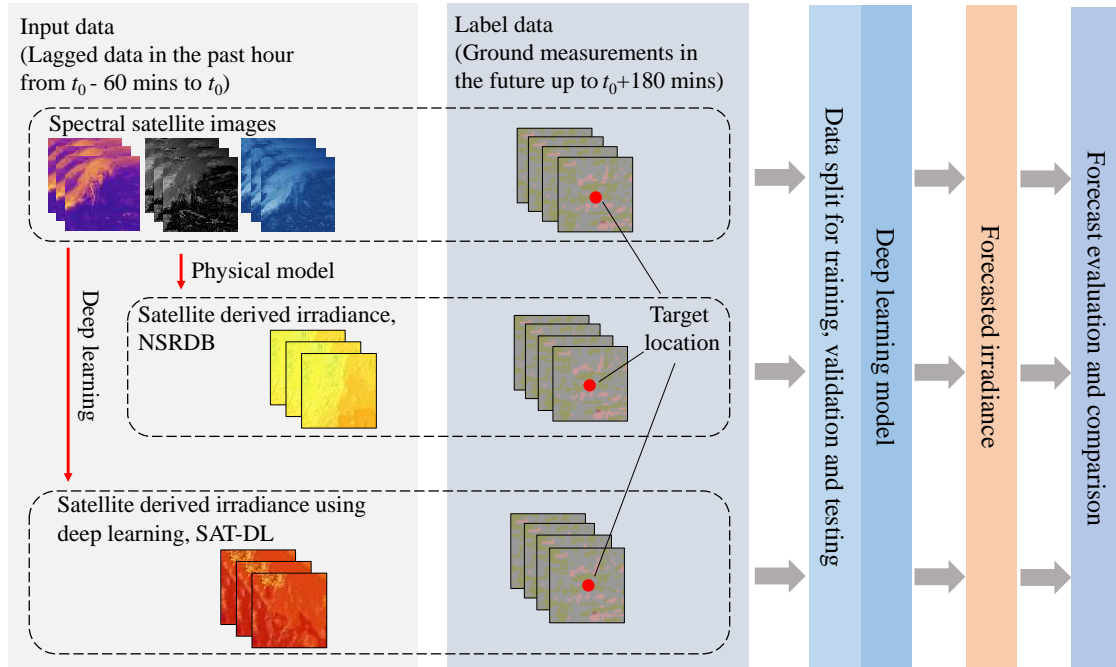


Figure 6.1: The methodology flowchart of solar irradiance forecasting employed in this work. The deep learning model chain derives irradiance from satellite data and subsequently generates forecasts. The end-to-end deep learning model only applies satellite data, and the hybrid physical-deep learning model uses physically satellite-derived NSRDB data.

The accuracy of irradiance predictions using the three alternative inputs are evaluated against ground measurements. Note that using SAT-DL irradiance estimates as inputs for another deep learning model forms a deep learning model chain, the end-to-end deep learning model using raw satellite measurements and the hybrid physical-deep learning model using NSRDB are used as benchmarks. Detailed descriptions of data pre-processing, deep learning model chain, forecasting model development and optimization are presented in the following subsections.

6.2.1 Publicly available data

Publicly available data used in this study includes ground-level irradiance measurements, spectral satellite images, and satellite-derived irradiance products. Ground-level measurements are from the Surface Radiation Budget Network (SURFRAD) stations [29]. Satellite images are from GOES-16, but only a subset of spectral bands are selected [161]. Satellite-derived irradiance products are from NSRDB [49]. A brief summary of the publicly available data used is presented in Table 6.1.

Table 6.1: A summary of the publicly available data used in this work.

	Data type	Description	Time period (year)
SURFRAD ^a	Irradiance measurements	On-site measurements of solar irradiance	2019, 2020
GOES-16 ^b	Satellite measured radiance	Radiance of eight selected spectral bands	2019, 2020
NSRDB ^c	Derived ground-level irradiance	Satellite-derived irradiance with a physical model	2020

^a Available at <https://gml.noaa.gov/grad/surfrad/>, can be downloaded by SolarData [27].

^b Available at <https://registry.opendata.aws/noaa-goes/>, can be download by GOES-2-go [169].

^c Available at <https://nsrdb.nrel.gov/>, can be downloaded by SolarData [27].

6.2.1.1 Solar irradiance measurements from SURFRAD

SURFRAD is a network of seven stations with five different climatological zones across the contiguous United States. As one of the radiation networks with the highest data quality in the world, SURFRAD has been supportive in widespread applications and research since its establishment in 1995 [29]. Data of all seven stations are used, namely, Bondville (BON), Desert Rock (DRA), Fort Peck (FPK), Goodwin Creek (GWN), Pennsylvania State University (PSU), Sioux Falls (SXF), and Table Mountain (TBL). Since SURFRAD data has been extensively utilized and described in the literature and our previous works [103, 127, 152], the details will not be reproduced here.

Raw measurements including GHI, DNI, diffuse horizontal irradiance (DHI), solar zenith angle in 2019 and 2020 at all seven stations are downloaded. Although GHI is the forecasting target, other data of DNI, DHI, and solar zenith angle are required for quality control (QC). The pre-processing of SURFRAD data includes: (i) QC to remove unreasonable data points, (ii) data aggregation, and (iii) normalization, described as follows,

- QC: Several QC procedures are considered, including the extremely rare limit test and the three-component closure test [27]. These QC steps are based on the theoretical aspects detailed by Long

and Shi [28].

- Data aggregation: After QC, the 1-minute averaged GHI measurements are aggregated to 5-minute intervals and indexed in Coordinated Universal Time (UTC). This is to be compatible with satellite data with the temporal resolution of 5-minute. Due to the high airmass effect at solar mornings and evenings, all GHI measurements for solar zenith angle of 85° or greater are discarded [103].
- Normalization: It is suggested to remove the double-seasonal pattern of solar irradiance prior to forecasting [21]. On this point, the 5-minute GHI measurements are normalized using clear-sky GHI (GHI_{cs}) estimations in NSRDB to generate clear-sky indexes ($CSI = GHI/GHI_{cs}$), which are used as labels in the forecasting model.

6.2.1.2 Spectral radiance data from GOES-16

GOES-16 is one of the GOES-R series geostationary satellites with the operation location of $75.2^\circ W$ during the investigated period of this study. The Advanced Baseline Imager (ABI) has 16 spectral bands (two visible, four near-infrared, and ten infrared channels), which monitors the Earth with much finer temporal and spatial resolutions compared with the previous generation of GOES. Among the available spectral information, only a subset of satellite bands are selected as shown in Table 6.2. This is because some bands are highly correlated [161], and using only the representative satellite bands can improve the learning efficiency by eliminating redundant features [161]. 5-minute GOES-16 images of eight selected spectral bands in 2019 and 2020 are extracted and georeferenced to the target SURFRAD stations with the size of 11×11 pixels (for 2019), and 21×21 pixels (for 2020), respectively. The pre-processing of GOES-16 data includes radiance conversion and normalization:

- Radiance conversion: This is to convert the packed-scaled value into radiance received by each band of GOES-16. The radiance for each band is obtained using the scale factor and add offset (see Table 6.2):

$$radiance = raw * scale + offset \quad (6.1)$$

where *raw* is the packed-scaled value, *scale* is the scale factor, and *offset* is the add offset.

- Normalization: To remove diurnal effects for the benefit of training, the spectral radiance data of each band is further normalized by the band range (i.e., the minimum and maximum spectral responses) and solar zenith angle. This is adopted from [160] to weight each band equally:

$$\tilde{L}_{ij|t}^b = 1 - \frac{L_{ij|t}^b - L_{min}^b}{\cos(\theta_z|t)(L_{max}^b - L_{min}^b)} \quad (6.2)$$

where $\tilde{L}_{ij}^b|_t$ is the normalized value at each pixel in band b at time t , $L_{ij}^b|_t$ is the measured radiance of that pixel, $\theta_z|_t$ is the solar zenith angle at time t , L_{\min}^b and L_{\max}^b are the minimum and maximum spectral responses of band b , respectively.

Note that the spectral bands have different spatial resolutions at the sub-satellite point as shown in Table 6.2, the bands with better resolutions are re-scaled as 2-km to ensure consistency among selected bands. As a multi-band passive imaging radiometer, the radiance received by ABI cannot theoretically be less than zero. Therefore, all negative values are discarded. The end timestamp of each scan in UTC time is used to index the image after rounding to the next nearest 5-minute interval, to be compatible with GHI measurements, and for real-time applications.

Table 6.2: The detailed information of the selected ABI spectral bands of GOES-16 [104].

Band	λ [μm]	Center λ [μm]	Resolution [km]	Type	Valid range	Scale factor	Add offset
1	0.45-0.49	0.47	1	Visible	0-1022	0.8121	-25.9366
3	0.846-0.885	0.865	1	Near-Infrared	0-1022	0.3769	-20.2899
4	1.371-1.386	1.378	2	Near-Infrared	0-2046	0.0707	-4.5224
5	1.58-1.64	1.61	1	Near-Infrared	0-1022	0.0958	-3.0596
6	2.225-2.275	2.25	2	Near-Infrared	0-1022	0.0301	-0.9610
7	3.80-4.00	3.90	2	Infrared	0-16382	0.0016	-0.0376
9	6.75-7.15	6.95	2	Infrared	0-2046	0.0225	-0.8236
11	8.30-8.70	8.50	2	Infrared	0-4094	0.0334	-1.3022

6.2.1.3 Satellite-derived irradiance from NSRDB

NSRDB is a widely accessed and publicly available satellite-derived database that provides solar irradiance over the United States and a growing number of international locations [49, 170]. Data in NSRDB includes broadband solar radiation of GHI, DHI, DNI, and their clear-sky expectations. Meanwhile, there are also many other auxiliary variables, such as solar zenith angle, cloud type, and meteorological data. NSRDB is serially complete with more than 20 years of coverage, providing data in 30-minute temporal and 4 km spatial resolutions. Starting in 2018, the temporal and spatial resolutions of NSRDB are further improved to 5-minute and 2-km, respectively [170]. Moreover, NSRDB is produced using a physical solar model, which is a two-step model to compute solar radiation from satellite data (e.g., GOES-16) and

products of a number of other associations [49]. The validation of 5-minute irradiance data of NSRDB against SURFRAD measurements shows that the new 5-minute NSRDB has higher discrepancies due to its higher temporal resolution [105]. However, it is still a remarkable milestone in solar irradiance modeling and resource assessment.

The NSRDB GHI values and their clear-sky expectations in 2020 are downloaded for 11×11 locations around each SURFRAD station. The temporal resolution is 5-minute and spatial resolution is 2-km. Clear-sky GHI estimations in NSRDB are calculated using the REST2 model [33], which has been repeatedly identified as one of the clear-sky models with high-performance [34, 36]. The pre-processing of NSRDB mainly includes normalization: Similar to the removal of double-seasonal effects of irradiance measurements, the GHI estimates are normalized by the GHI_{cs} to generate CSI, which are used as one of the alternative inputs. The region of these 121 surrounding locations can provide spatio-temporal information for solar forecasting at the target station.

6.2.2 Satellite-derived irradiance from SAT-DL

In our previous study [161], high spatio-temporal resolution spectral satellite images of GOES-16 are used to estimate ground-level GHI and DNI via deep learning. The results are verified against measurements at SURFRAD stations and show better performance in estimating both GHI and DNI compared with NSRDB. There are mainly three steps: (i) mapping spectral satellite images of representative bands with ground observations, (ii) training and optimizing the deep learning model, and (iii) obtaining irradiance estimates from new satellite images. The deep learning model used in [161] employs convolutional neural networks (CNNs) [78], the attention mechanism [140] and fully-connected dense layers.

The original deep learning model in [161] is developed for ground irradiance estimates at a single location, which is centered in the domain of satellite images with 11×11 pixels. As shown in Fig. 6.2(a), the target is one of the SURFRAD stations (e.g., TBL), and the satellite images cover the same region with the surrounding locations. The target station can be anywhere as long as there are on-site irradiance measurements available. Following the same methodology, we expand the target from one station to the 11×11 surrounding area with 121 locations. As shown in Fig. 6.2(b), selected spectral satellite images of GOES-16 (see Table 6.2) with the size of 21×21 pixels are used to obtain the GHI estimates for the whole region (11×11 pixels) via the pre-trained model. Specifically, datasets in 2019 are used to develop the pre-trained deep learning model for GHI estimation at a single SURFRAD station using spectral satellite images (11×11 pixels) and ground measurements. The pre-trained model is then applied to obtain GHI estimates in 2020 for the whole surrounding region (121 locations) by shifting an 11×11 -pixel window

over the larger satellite images (21×21 pixels) as illustrated in Fig. 6.2(b). Note that the model’s output is CSI of GHI normalized by the REST2 clear-sky model (available in NSRDB). The whole 11×11 matrices of CSI are used as inputs for GHI forecasting of the target station. Therefore, CSI outputs are not converted back to GHI estimates at this step.

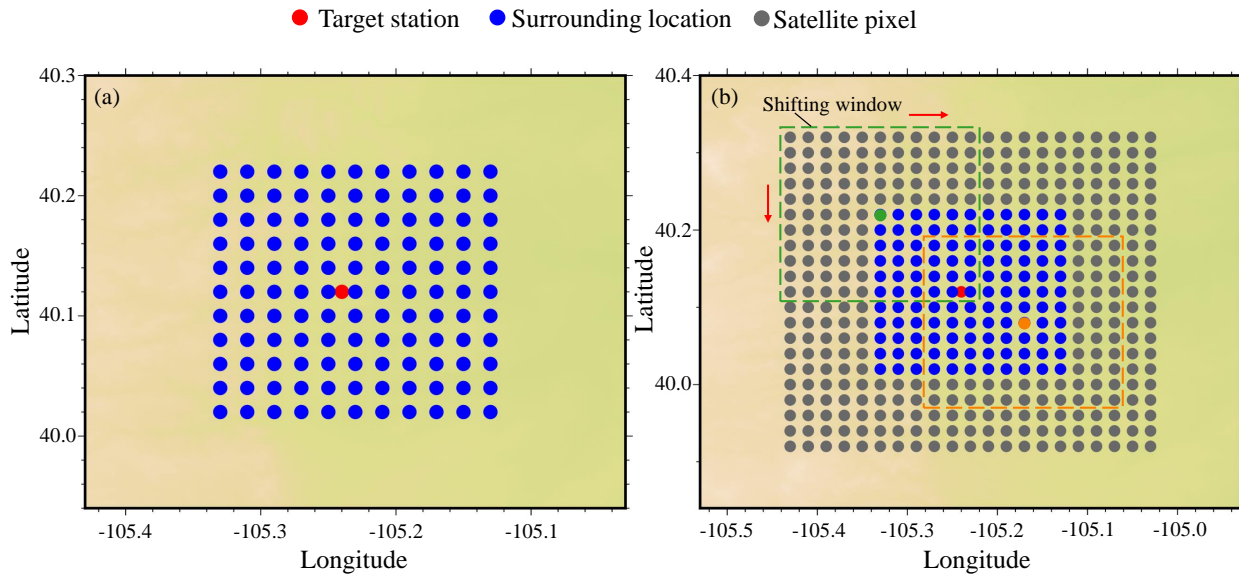


Figure 6.2: An illustration of solar irradiance forecasting for the Table Mountain (TBL) station using surrounding spatial information. (a) The target and 121 surrounding locations with satellite-derived irradiance, (b) The target with 121 surrounding locations and the domain of used spectral satellite images. A pixel-wise 11×11 shifting window is applied to get the SAT-DL for the 121 surrounding stations.

Forecasting using SAT-DL irradiance thus forms a deep learning model chain, i.e., satellite data are converted to GHI estimates by a deep learning based model [161], and the resulting GHI estimates are used subsequently to produce GHI forecasts using another deep learning model. Recall that satellite images and ground measurements in 2019 are used to train and validate the deep learning model for GHI estimates (SAT-DL), while SAT-DL GHI estimates in 2020 are used as inputs for solar irradiance forecasting.

The method to generate GHI estimates for a single location is efficient to implement. Using the pre-trained model to get GHI estimates over a large region could be more time-consuming, therefore, we do not consider larger areas around the target station. Also, the pre-trained model is developed only using ground data at the target stations, thus the accuracy might decrease with the increased distance for locations that are

too far away. Considering that the surrounding terrain and climate feature would not be significantly different for a certain location, it is reasonable to assume that GHI estimates of SAT-DL have lower discrepancies than NSRDB in the area around the SURFRAD stations. In a more general case, one can change the size of the surrounding area to investigate the effects on GHI estimates and forecasting, but this is not considered in this study.

6.2.3 Forecasting method

Deep learning is extensively used in solar forecasting and resource assessment applications using satellite images and related products. The deep learning forecasting model applied in this work applies CNNs, the attention mechanism and fully-connected dense layers based on Tensorflow [151]. Compared with the deep learning irradiance estimation model in [161], the main differences are the sources of inputs and the number of outputs. As illustrated in Fig. 6.3, three different datasets are used as inputs to generate CSI forecasts for lead times from 15 to 180 minutes. As mentioned before, the deep learning model chain can obtain more accurate spatial GHI estimates from satellite data and subsequently produce GHI forecasts using the spatial GHI estimates of SAT-DL. The end-to-end deep learning model only employs spectral satellite data as inputs, while the hybrid physical-deep learning model applies GHI estimates of NSRDB as inputs. The inputs are lagged spectral satellite images or satellite-derived GHI matrices in the past hour with the temporal resolution of 5-minute and spatial resolution of 2-km, while the outputs are 5-minute averaged CSI forecasts for the various forecast horizons. For example, the 5-minute average means that the CSI forecast at $t = 12:00$ is the averaged value over times 11:58, 11:59, 12:00, 12:01, and 12:02 [105].

Note that the input sizes of satellite-derived GHI matrices and satellite images are different, the satellite-derived GHI matrices are in the size of 11×11 surrounding locations as shown in Fig. 6.2(a), while the spectral satellite images are in the size of 21×21 pixels as illustrated in Fig. 6.2(b). This is done to perform a fair comparison among satellite images and derived GHI products, since GHI estimates of SAT-DL is based on the image size of 21×21 .

The deep learning model \mathbb{F} can produce multiple CSI forecasts (multiple-output model) with forecast horizons (Δt) up to 180 minutes (i.e., 15, 30, 45, 60, 90, 120, 150, and 180-minute), which can be formulated as,

$$\hat{I}_{t_0+15}, \hat{I}_{t_0+30}, \dots, \hat{I}_{t_0+180} = \mathbb{F}(x_{t_0}, x_{t_0-5}, \dots, x_{t_0-60}) \quad (6.3)$$

where \hat{I} denotes the CSI forecast, which can be converted back to GHI by multiplying clear-sky GHI of REST2 at time $t + \Delta t$; x represents the spatio-temporal input, i.e., $x \in \mathbb{R}^{21 \times 21 \times 8}$ for spectral satellite images, $x \in \mathbb{R}^{11 \times 11}$ for GHI estimates from NSRDB or SAT-DL.

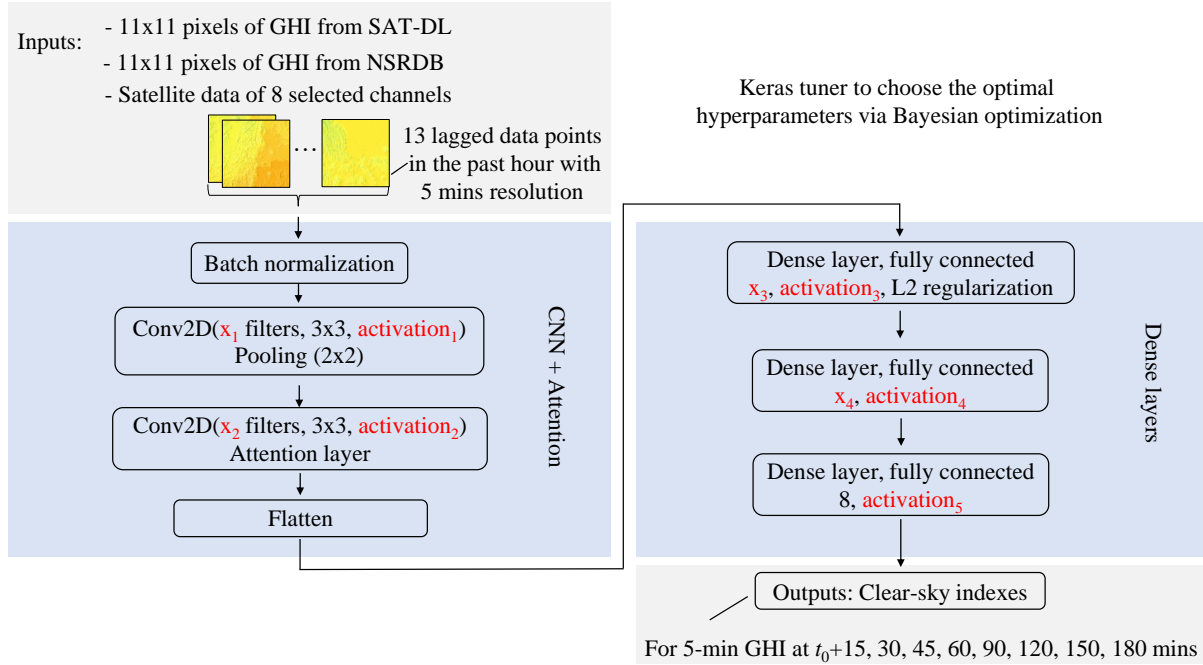


Figure 6.3: The structure of the deep learning model for CSI forecasts using spectral satellite images or satellite-derived GHI products. This is a model with multiple CSI forecasts (multiple outputs), where the structures of different inputs are similar, but the hyperparameters are optimized separately using the Keras-Tuner, as shown in Table 6.3.

Table 6.3: Hyperparameters shown in Fig. 6.3 for Bayesian optimization using the KerasTuner.

Hyperparameter	Values
Optimizer	Adam
Loss function	Huber
Learning rate	[1e-5, 1e-4, 2e-4, 5e-4, 1e-3, 2e-3, 1e-2]
x_1	range(min = 16, max = 128, step = 2)
activation ₁	[relu, gelu, selu, tanh]
x_2	range(min = 8, max = 64, step = 2)
activation ₂	[relu, gelu, selu, tanh]
x_3	range(min = 8, max = 64, step = 2)
activation ₃	[relu, gelu, selu, tanh]
x_4	range(min = 8, max = 64, step = 2)
activation ₄	[relu, gelu, selu, linear]
Early stopping	With the patience equal to 5

Although the structures of deep learning models are shared among different forecasting scenarios, the hyperparameters are different for each scenario. The forecasting models for each SURFRAD station with different inputs are trained separately, and the optimal hyperparameters are obtained using Bayesian optimization of the KerasTuner [171] as shown in Table 6.3. Since the forecasting model is developed using data from year 2020, to better represent the yearly variability, data in March, June, September, and December are utilized for testing, while the rest of the datasets in 2020 are used as training and validation subsets (in which 20% of the data is used for validation).

One may argue that the convolutional long-short-term memory (ConvLSTM) network could capture the spatio-temporal feature better and thus might lead to better forecasts. Indeed, the study of Gallo et al. [163] shows that ConvLSTM performs slightly better than CNN with lower divergences for longer forecast horizons. However, ConvLSTM requires larger images as inputs and thus consumes more computing power and time. Considering the comparable performance and less computing burden, CNNs are adopted in this work.

6.2.4 Performance evaluation of forecasts

As mentioned, the model outputs are CSI forecasts, which are converted back to irradiances by multiplying the clear-sky irradiance at the predicted time stamps. That said, the final error evaluations and visualizations are performed in terms of irradiance [W/m^2]. Among the used evaluation metrics, root mean squared error (RMSE), mean bias error (MBE), and their normalized counterparts (nRMSE, nMBE) are used to assess the overall forecasting accuracy,

$$\text{RMSE} = \sqrt{\frac{1}{N} \sum (f_i - o_i)^2} \quad (6.4)$$

$$\text{nRMSE} = \frac{\sqrt{\frac{1}{N} \sum (f_i - o_i)^2}}{\frac{1}{N} \sum o_i} \quad (6.5)$$

$$\text{MBE} = \frac{1}{N} \sum (f_i - o_i) \quad (6.6)$$

$$\text{nMBE} = \frac{\sum (f_i - o_i)}{\sum o_i} \quad (6.7)$$

where f_i and o_i are the pair of irradiance forecast and ground observation (i.e., GHI), N is the total number of compared data points.

The forecast skill is to provide a relative improvement for a model's prediction over a reference model, which can be calculated based on RMSE:

$$\text{FS} = \left(1 - \frac{\text{RMSE}_f}{\text{RMSE}_r} \right) \times 100\% \quad (6.8)$$

where FS is the forecast skill, $RMSE_f$ is based on forecasts of the evaluated model, and $RMSE_r$ is calculated using forecasts of a reference model. Smart persistence is used as the reference model here, which assumes the CSI for now would not change over the forecast horizon, as defined by:

$$CSI_{t+\Delta t} = CSI_t \quad (6.9)$$

where Δt is the forecast horizon, and the GHI forecast is obtained by multiply the clear-sky irradiance at $t + \Delta t$.

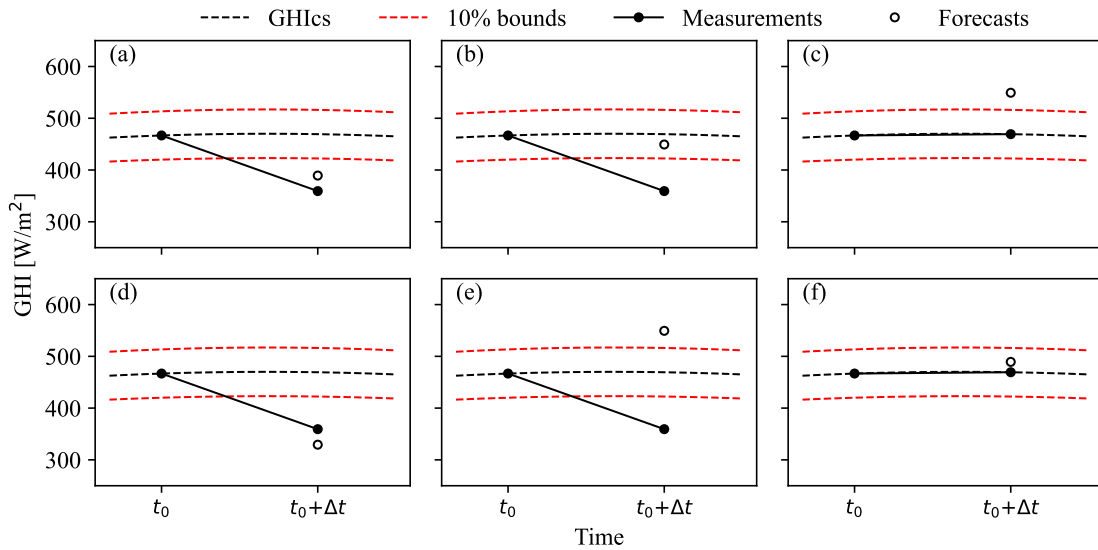


Figure 6.4: Some possible outputs of ramp forecasts. GHIcs denotes the clear-sky irradiance, 10% bounds define the upper and lower bounds on the threshold, Δt is the forecast horizon. Modified based on Fig. 2 in [156].

Solar irradiance exhibits huge variability with the rapid change of clouds in the sky. The ramp analysis is to evaluate the forecasting performance for capturing the ramp events in irradiance, which can better support the integration of solar power. A ramp event is defined by the irradiance change in the time interval of $[t, t + \Delta t]$ that exceeds a threshold (e.g., 10% of current clear-sky irradiance [156]). Some possible outputs of ramp forecasts are shown in Fig. 6.4. Following the definitions in [156], three metrics are defined in the ramp analysis, namely, ramp detection index (RDI), false ramp index (FRI), and ramp magnitude forecast index (RMI) as defined by:

$$RDI = \frac{N_{hit}}{N_{hit} + N_{miss}} \quad (6.10)$$

$$FRI = \frac{N_{FRP}}{N_{FRP} + N_{TNR}} \quad (6.11)$$

$$\text{RMI} = 1 - \sqrt{\frac{\sum_{i=1}^{N_r} (o_{t_i+\Delta t} - f_{t_i+\Delta t})^2}{\sum_{i=1}^{N_r} (o_{t_i+\Delta t} - o_{t_i})^2}} \quad (6.12)$$

where N_{hit} means the number of cases when ramps are detected (cases (a) and (d) in Fig. 6.4), N_{miss} means the number of cases when ramps are missed (cases (b) and (e) in Fig. 6.4), N_{FRP} means the number of cases when ramp is forecasted but there is no ramp (Fig. 6.4(c)), N_{TNR} means the number of cases when ramp is not forecasted and is actually not presented (Fig. 6.4(f)), N_r is the number of ramp events, o is the observation and f is the forecast. More details are available in [156].

6.3 Results

In this section, performance of GHI forecasts using the developed deep learning model is evaluated and compared with different inputs, namely, spectral satellite images (the end-to-end deep learning model), GHI estimates from NSRDB (the hybrid physical-deep learning model), and GHI estimates of SAT-DL (the deep learning model chain). Three categories of evaluation are adopted: (i) the forecasting accuracy in terms of nRMSE and nMBE is presented in Section 6.3.1, along with the comparison of forecast skill over the smart persistence reference model, (ii) the ramp analysis of irradiance forecasts including ramp detection and magnitude forecasts, are elaborated in Section 6.3.2, and (iii) the distribution-oriented approaches for verifying irradiance forecasts are detailed in Section 6.3.3.

6.3.1 Forecast evaluation in terms of statistical metrics

The results of intra-day GHI forecasts using different inputs at all SURFRAD stations are presented in Fig. 6.5 (for nRMSE) and Fig. 6.6 (for nMBE). It is shown in Fig. 6.5 that the forecasting accuracy generally decreases with the increase of forecast horizon regardless of the used inputs. When comparing between different inputs, deep learning models generally outperform the smart persistent reference model (SP) in terms of nRMSE, especially for longer forecast horizons (e.g., longer than 60 minutes). Furthermore, satellite-derived GHI products (NS and SDL) yield better forecasts than raw satellite images (SAT) in most cases, even though the region of used satellite images are much larger (see Fig. 6.2). When comparing the forecast results based on satellite-derived irradiance products, GHI estimates of SAT-DL typically produce forecasts with lower nRMSE than GHI estimates in NSRDB, as reflected by the comparison between NS and SDL in Fig. 6.5 for all SURFRAD stations.

Although satellite-derived products generally yield better GHI forecasts (in terms of nRMSE) than raw satellite images, there are some site-specific differences across the SURFRAD stations. For instance, at

PSU, the nRMSE values of GHI forecasts in all forecast horizons are larger than other stations, and SAT are more accurate than NS in most conditions. However, SDL still yields the best results at PSU. When it comes to the comparison of nMBE for irradiance forecasts (see Fig. 6.6), apart from some site-specific divergences, there are also some differences across the forecast horizon, but no obvious trends are observed. In general, satellite-product-based forecasts (NS and SDL) tend to have larger bias.

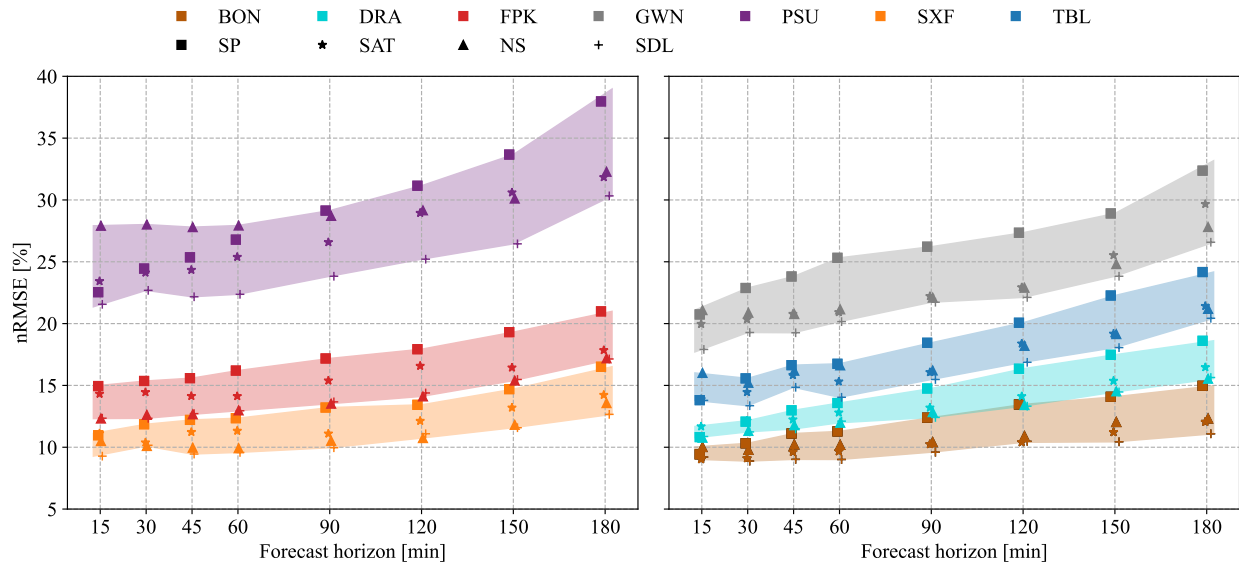


Figure 6.5: Comparison of nRMSE [%] for GHI forecasts up to 180 minutes using different methods/inputs: smart persistent (SP), spectral satellite images (SAT), NSRDB GHI estimates (NS), GHI estimates of SAT-DL (SDL), at all the SURFRAD stations. The colors are to differ the stations, and the symbols are to distinguish the methods.

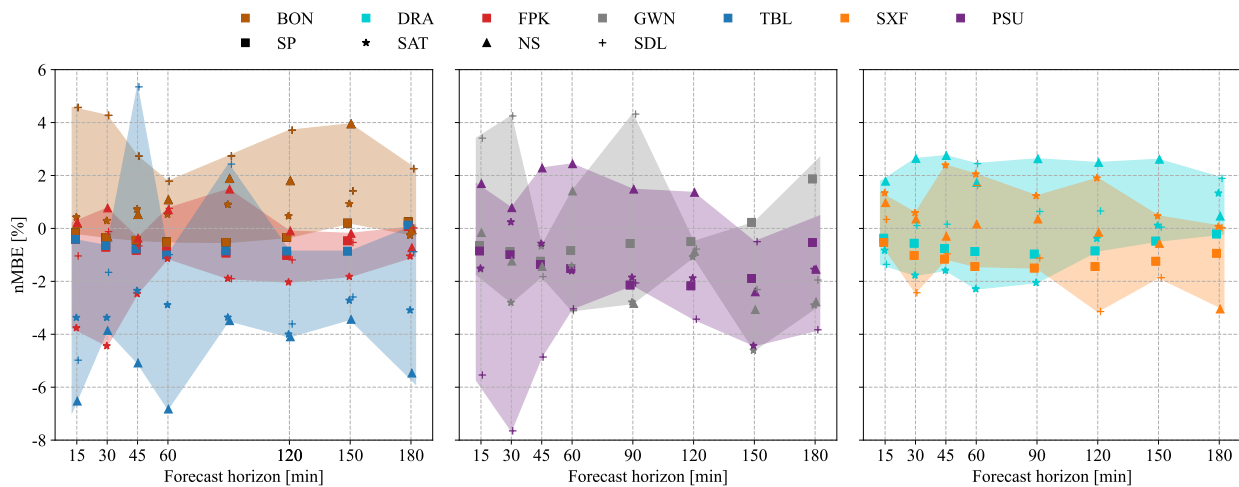


Figure 6.6: Same as Fig. 6.5, but for the comparison of nMBE [%] for GHI forecasts.

Forecast skills over the smart persistent reference model for GHI forecasts with different inputs are further compared. As presented in Fig. 6.7, the general trend is that forecast skill improves with the increase of forecast horizon no matter which input is used. The increase of forecast skill is more obvious for the shorter forecast horizons (i.e., less than 60 minutes), while in longer forecast horizons (e.g., longer than 60 minutes), fluctuations and even decreases in skill can be observed. When comparing the forecast skill of inputs used, SDL generally outperforms NS and SAT at all the SURFRAD stations. One more interesting observation is that SDL also has higher robustness than NS, evidenced by the inferior performance of NS at BON, TBL, and especially PSU (see Fig. 6.7).

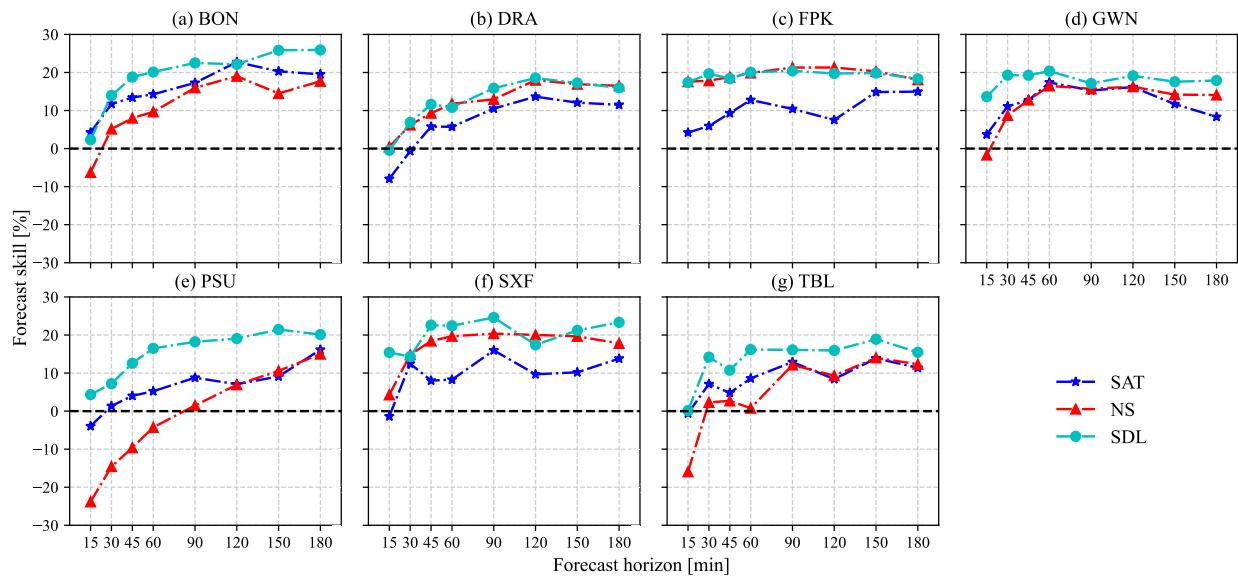


Figure 6.7: Comparison of forecast skill for GHI forecasts using different inputs across the forecast horizons up to 180 minutes at all the SURFRAD stations. Larger skill indicates a more accurate forecast.

6.3.2 Forecast evaluation in terms of ramp metrics

Since solar variability introduces great difficulties in the grid integration of solar power systems especially when sudden fluctuations present, it is also beneficial to perform the ramp analysis of irradiance forecasts to evaluate the model’s ability in predicting the variability. As defined in Section 6.2.4, three indexes are used in ramp analysis, namely, RDI to identify the successful rate of ramp detection, FRI to evaluate the false ramp events, and RMI to quantify the magnitude of ramp predictions.

Table 6.4 shows the percentage of clear and cloudy periods in 2020 at the SURDRAD stations. It is shown that DRA has the most occurrence of clear conditions, PSU has the most occurrence of cloudy conditions,

while the remaining sites show similar distributions of clear and cloudy periods. It has also been observed in many studies that DRA has a higher occurrence of clear periods, while PSU shows the most frequent cloudy skies [160, 172, 103]. Therefore, the ramp analysis is performed at DRA, PSU and SXF, which are selected as the representatives of different cloudy conditions across the SURFRAD stations as shown in Fig. 6.8.

Table 6.4: The amount of clear and cloudy periods (in percentage) in 2020 at all the SURFRAD stations. The clear and cloudy conditions are labeled based on 1-minute QC data and the Bright-Sun clear-sky detection model [112].

	BON	DRA	FPK	GWN	PSU	SXF	TBL
Clear periods [%]	27.83	49.88	22.89	27.44	14.64	28.50	29.38
Cloudy periods [%]	72.17	50.12	77.11	72.56	85.36	71.50	70.62

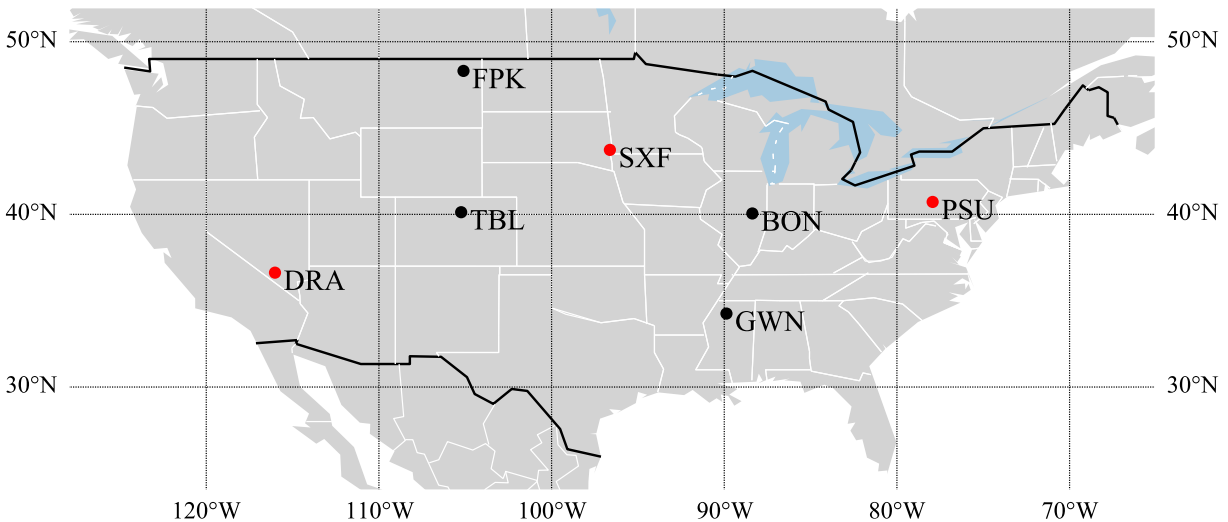


Figure 6.8: The selected representative stations of SURFRAD. DRA has the most clear periods, PSU has the most cloudy skies, and SXF is selected as it is in the geographical 'middle' of the rest stations.

As shown in Fig. 6.9, both RDI and FRI generally increase while the RMI decreases with the extended forecast horizons. When more frequent cloudy conditions present, the forecast method generally exhibits more uncertainties in forecasting ramp events. Specifically, the RDI at PSU is lower than DRA and SXF, while the FRI of PSU is comparatively larger. As for ramp magnitude forecasts, the RMI at PSU is relatively higher than DRA and SXF, especially for longer forecast horizons (except the use of NSRDB GHI as inputs, which will be discussed in Section 6.4).

When comparing the inputs used for ramp forecasts, none of them shows dominant performance over the others (see Fig. 6.9). All the inputs show similar performance for ramp detection at DRA and SXF, while SDL typically has higher RDI at PSU, especially for longer forecast horizons. For the false ramps detected, DRA does not present huge difference across the forecast horizons, while SXF shows some fluctuations but the general performance is still comparable. Conversely, at PSU, NS tends to generate relatively higher false ramp rates across all forecast horizons. Similarly, the ramp magnitude forecasts at DRA and SXF do not differ greatly, while NS could not produce equivalent results compared with the other two types of inputs at PSU.

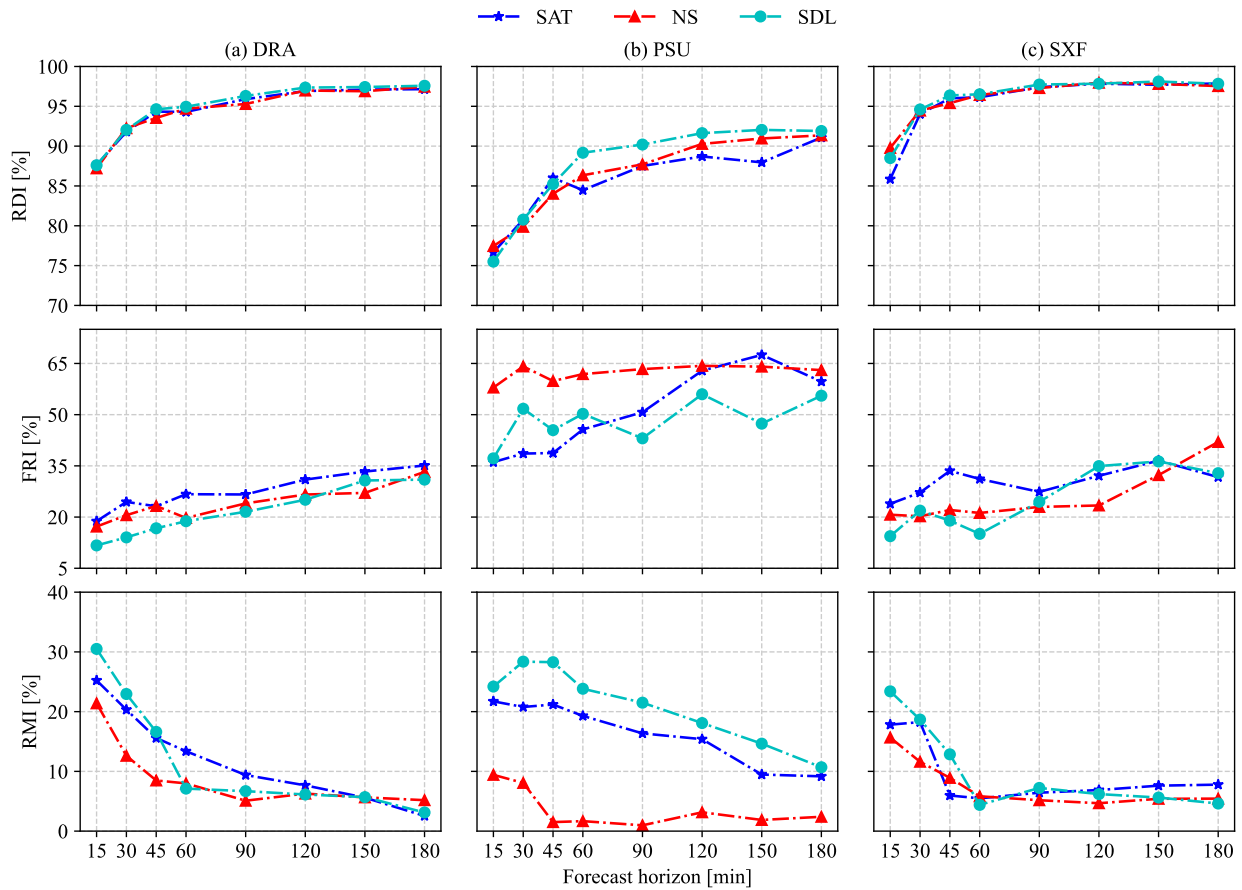


Figure 6.9: The ramp analysis for GHI forecasts across the forecast horizon up to 180 minutes. RDI, FRI and RMI at (a) BON, (b) DRA and (c) PSU. For RDI and RMI, values closer to 100% are better. For FRI, smaller is better.

6.3.3 Distribution-oriented forecast evaluation

As stated by Yang et al. [172], the evaluation based only on accuracy is not always inclusive. Therefore, other aspects of forecasting quality, for instance, distribution-oriented approaches, should be investigated. In this section, the irradiance forecasts based on three different inputs (SAT, NS and SDL) are verified against observations using different distribution-oriented approaches including joint, marginal, and conditional distributions of forecasts and measurements. Joint distribution enables the identification of obvious outliers and unnatural patterns, while the verification of marginal and conditional distributions are equivalent. More details about joint, marginal and conditional distributions can be found in [172, 173].

The joint and marginal distributions of GHI forecasts based on three different inputs (i.e., SAT, NS and SDL) against the measurements at three SURFRAD stations (i.e., DRA, PSU and SXF) over different forecast horizons are shown in Fig. 6.10. Compared with PSU, the joint distributions at DRA and SXF have higher probabilities around the identity line, no matter which inputs are used. Apart from the higher probability density under the diagonal, GHI forecasts at PSU also show sparser distributions compared with those for DRA and SXF, which indicates that larger divergences are presented (see Fig 6.5). The histograms in Fig. 6.10 represent marginal distributions (forecast is to the right, and measurement is on the top). If the forecasts had no errors, the two marginal distributions would be the same. Fig. 6.10 shows different extents of discrepancies observed for various scenarios regarding different locations and forecast horizons. When comparing the inputs used for GHI forecasts, predictions based on SDL are distributed closer to the identity line than SAT and NS, especially at PSU. Moreover, at PSU, NS tends to produce larger errors in forecasts, as evidenced by the more scattered density distributions.

Fig. 6.11 shows the conditional distribution of GHI forecasts given observations at DRA, PSU and SXF, where the forecasts are based on three different inputs (i.e., SAT, NS and SDL). The forecasts are said to be synchronized if the centroids of the distributions align with the identity line [172]. It can be seen in Fig. 6.11 that the distributions of GHI forecasts at DRA and SXF are more centered than those at PSU no matter which input is used. Generally, the forecasts are associated with positive bias in the low-irradiance range and tend to produce under-predictions for high-irradiance conditions. It is more obvious to notice the over-prediction (for low-irradiance conditions) and under-prediction (for high-irradiance conditions) at PSU. When comparing the forecasts based on different inputs, the results at DRA and SXF are similar, the centroids of GHI forecasts from SDL are slightly closer to the identity line compared with SAT and NS. However, at PSU, forecasts based on NS show more divergences than SDL, with wider forecast distributions for given measurements and the sparser centroids dispersed around the identity line.

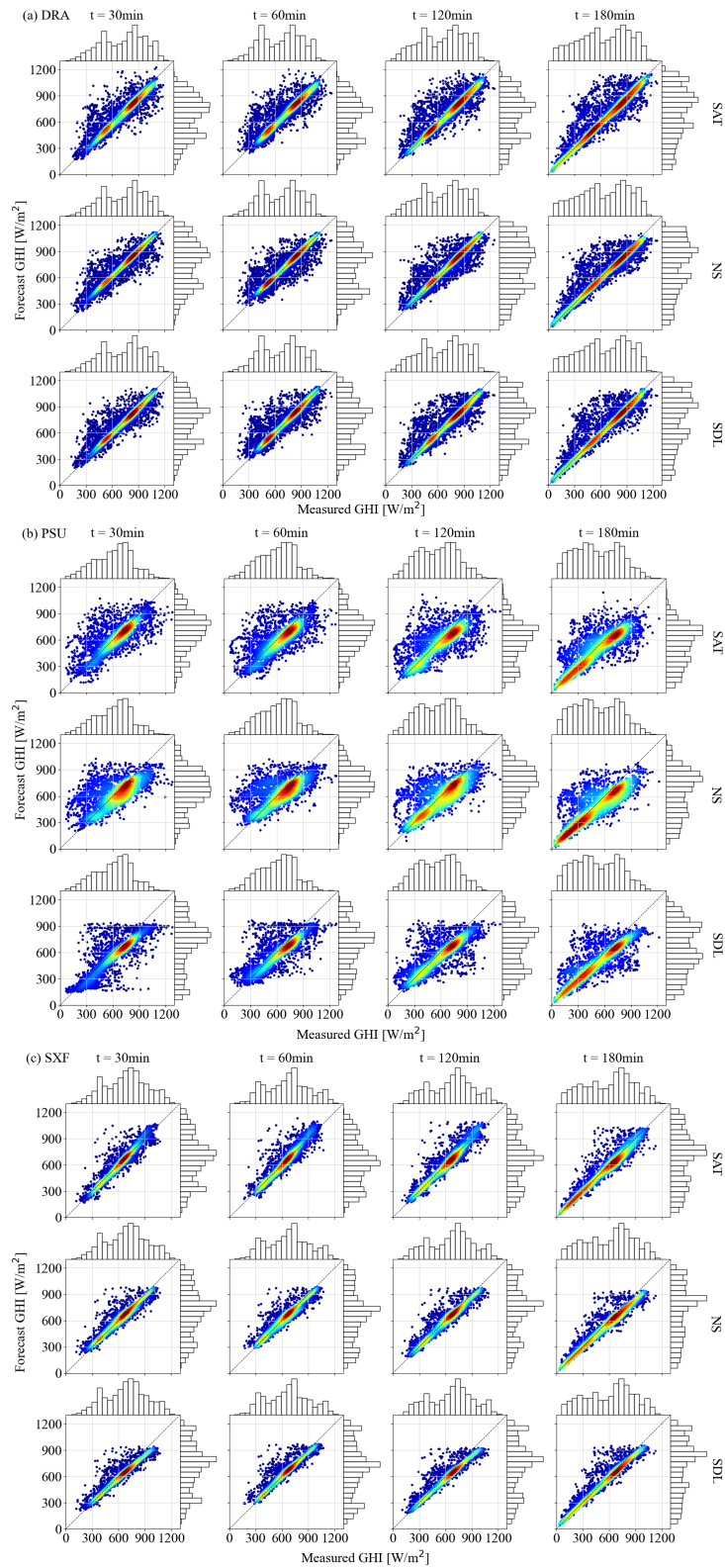


Figure 6.10: Joint and marginal distributions of GHI forecasts and measurements, at (a) DRA, (b) PSU, and (c) SXF, for forecast horizons of 30, 60, 120, and 180 minutes (only a subset of forecast horizons is selected to be representatives). GHI forecasts are based on raw satellite data (SAT), satellite-derived GHI estimates of NSRDB (NS) and SAT-DL (SDL).

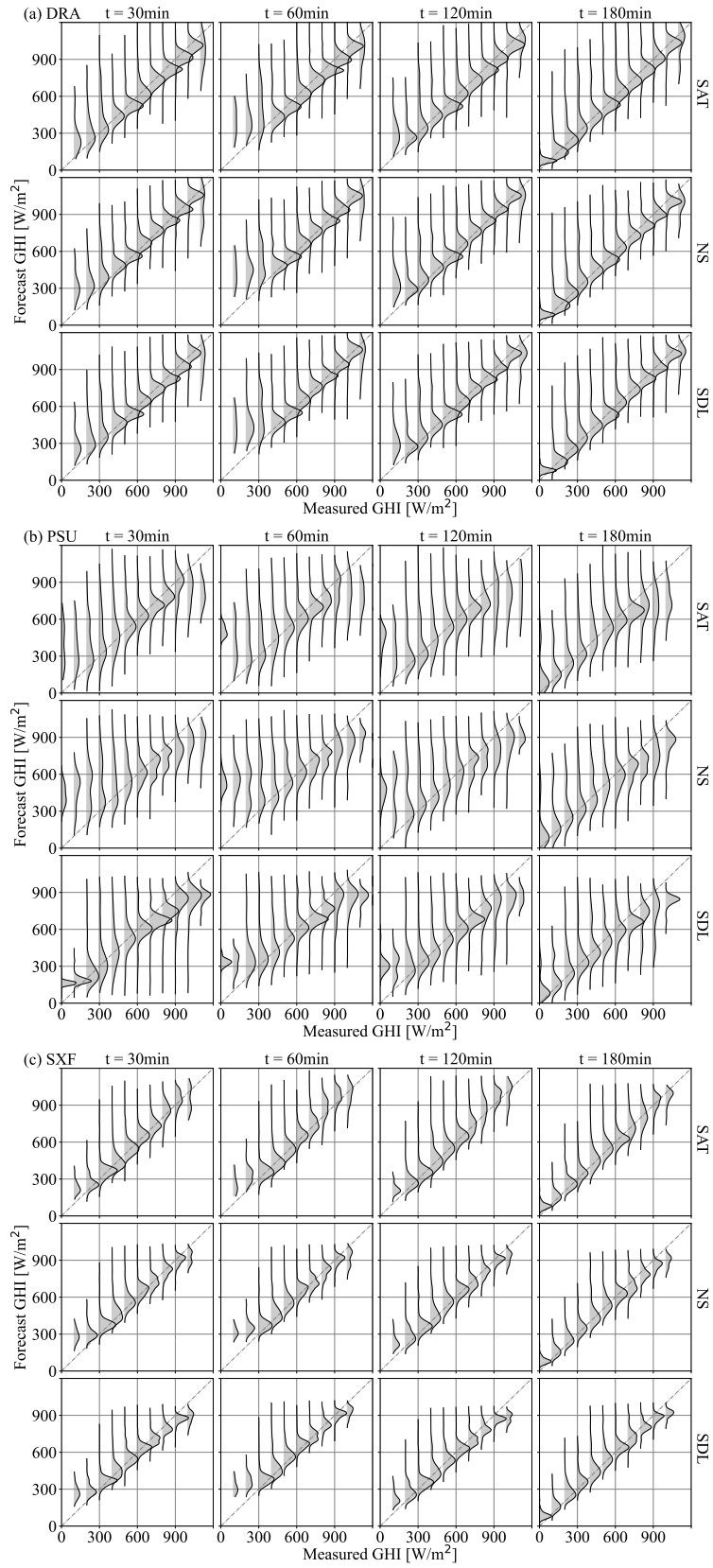


Figure 6.11: Same as Fig. 6.10, but for conditional distributions of GHI forecasts, given the measurements.

6.4 Discussion

Based on the evaluation of GHI forecasts in terms of statistical metrics (see Section 6.3.1), NS and SDL generally show lower discrepancies than SAT as shown in Fig. 6.5. However, deriving irradiance products from satellite images using either physical models or deep learning methods needs extra computation time, which should be considered in operational forecasting applications. Since GHI forecasts of SDL has comparatively lower errors than NS, the proposed deep learning model chain to map satellite data firstly to spatial irradiance and then to irradiance forecasts is effective in improving intra-day GHI forecasts. Although GHI forecasts based on NS and SDL have larger biases compared to SAT as shown in Fig. 6.6, satellite-derived irradiance products are still valuable inputs for solar irradiance forecasting, since the bias could be further corrected by post-processing methods [174].

GHI forecasts of SDL have higher forecast skill and higher robustness when compared to SAT and NS (see Fig. 6.7). According to the assumption made in Section 6.2.2 that GHI estimates of SAT-DL exhibit lower discrepancy than NSRDB in the surrounding region of a target station, one implication here is that using surrounding spatial information (i.e., GHI estimates) with lower uncertainty could improve the forecasting performance at the target station. That said, deep learning itself can be a feature extraction tool, and using the extracted features (SAT-DL GHI estimates) to another deep learning model could produce better forecasting results than the end-to-end model (directly from satellite data to irradiance forecasts) and the hybrid physical-deep learning model (based on NSRDB). Since better forecasts can be produced with improved accuracy in GHI estimates, it is beneficial to improve the satellite-derived irradiance products for solar forecasting.

In terms of ramp analysis presented in Fig. 6.9, the increased detection of ramps and false ramps means that the forecasts of ramp events for longer time horizons are relatively easier, but are also associated with a higher likelihood of false ramp forecasts. The decrease in ramp magnitude forecasts indicates that it is possible to detect ramp events for longer time horizons, but the accurate forecast of ramp magnitude is much more challenging. The compromised RDI performance at PSU indicates that the ramp forecasts for locations with frequent cloudy skies may have larger unpredictability. As for the higher RMI at PSU, the reason could be the greater attenuation of irradiance by more frequent clouds which leads to a lower irradiance magnitude. Therefore, the ramp magnitude forecasts at PSU perform better than at DRA and SXF.

When it comes to distribution-oriented evaluation, the distributions of forecasts at DRA and SXF are more closely aligned along the identity line (see Figs. 6.10 and 6.11), which means that the GHI forecasts are more calibrated at DRA and SXF than PSU. When comparing the results at each location, the distributions

of SDL forecasts are distributed more centered than SAT and NS, especially at PSU. This indicates again the proposed deep learning model chain can produce better forecasts. The conditional distributions in Fig. 6.11 reveal that GHI forecasts for more frequent cloudy skies (at PSU) are more challenging compared with moderate and low cloudy conditions (at SXF and DRA) regardless of what input is used.

The results of both ramp analysis and distribution-oriented evaluation show compromised performance when more frequent clouds are present. For instance, higher rates of false ramp detection, lower forecasts of ramp magnitude, and enlarged biases can be observed at PSU. This is related to the difficulties in cloud detection and prediction, as clouds are present in the three-dimensional atmosphere while geostationary satellites can only provide two-dimensional information. It is suggested to integrate locally-sensed data (e.g., sky images [168]) to provide additional information. Condition-based forecasting that classifies clear, partially clear, and cloudy situations for model development might be helpful to address the issues related with cloudy skies. Meanwhile, spatio-temporal satellite-derived irradiance products can also be used to track cloud movements [167]. Therefore, deriving more accurate irradiance estimates from satellite data also serves the purpose, as evidenced by the performance of the proposed deep learning model chain for GHI estimates and forecasts. However, more work is still needed in modeling cloud movements in a three-dimensional perspective, since the ability to predict the amount, optical depth, movements, and locations of clouds is indispensable in improving solar forecasting [21].

6.5 Conclusions

Satellite data and satellite-derived irradiance products have been extensively used in solar forecasting, and the inclusion of spatio-temporal information is likely to produce high-accuracy forecasts. However, the potential benefits of satellite-derived irradiance products and their improvements for solar forecasting have not been fully investigated in the literature. In this regard, this study proposes a deep learning model chain for GHI forecasts, i.e., mapping satellite data to spatial GHI estimates via deep learning, and then using the estimates as inputs to another deep learning forecasting model. Then the effectiveness of such approach in improving intra-day GHI forecasting is evaluated by comparing verification statistics with other spatio-temporal inputs, namely raw satellite images (the end-to-end deep learning model) and satellite-derived irradiance products from NSRDB (the hybrid physical-deep learning model).

Compared with spectral satellite images, satellite-derived GHI estimates generally produce better forecasts (with lower nRMSE) in most cases, and SAT-DL GHI estimates yield forecasts with comparatively lower nRMSE than NSRDB. However, the forecasts based on satellite-derived GHI estimates tend to have

larger bias. Despite the presence of larger biases, GHI estimation products are still promising inputs for solar forecasting as post-processing methods can be used for bias correction and refinement. When comparing the forecast skill, the proposed deep learning model chain generally performs better and is more robust. Given that GHI estimates of SAT-DL have higher accuracy than NSRDB in the nearby surrounding area, the improvement in GHI estimates is more likely to generate better forecasts.

The results of ramp analysis and distribution-oriented verification show that there are larger uncertainties and biases for locations with cloudier conditions. This is due to the higher unpredictability of irradiance in such cloudy conditions. When there are more clouds, the forecasts are found to have compromised performance in ramp detection. Meanwhile, GHI forecasts are also associated with larger biases for low- and high-irradiance conditions. This indicates that more efforts are needed in detecting and predicting cloud movements. Nevertheless, the deep learning model chain shows better forecasting performance than the reference models.

In summary, the deep learning model chain shows great potential for improving GHI forecasts via the derivation of more accurate spatial GHI estimates from satellite measurements. Compared with the end-to-end deep learning model based on raw satellite measurements and the hybrid physical-deep learning model based on NSRDB, the proposed method shows better performance, especially under frequent cloudy conditions. However, there are still some limitations, such as the need of ground measurements and extra computational time to obtain GHI estimates via the pre-trained deep learning model. Considering that the physical radiative transfer model in NSRDB also requires extra time to produce GHI estimates for operational forecasting, the deep learning model chain could be used as an alternative to obtain spatial GHI estimates for improved intra-day solar forecasts when adequate on-site measurements are available for model development.

6.6 Acknowledgement

This chapter, in full, is a reprint of the manuscript submitted to *Energy Conversion and Management*. S. Chen, C. Li, R. Stull, and M. Li (2023). Improved satellite-based intra-day solar forecasting with a chain of deep learning models. The thesis author is the first author of this manuscript.

Chapter 7

Conclusions and recommendations

7.1 Conclusions

Solar energy is set as one of the main power sources to meet the growing need for clean energy and to mitigate climate change. Solar PV, solar heating and cooling, and CSP are all important technologies on the pathway towards carbon neutrality. As solar radiation is the fuel for all solar energy technologies and its intermittency nature, knowledge of the quality and future reliability of the fuel is crucial for feasibility and financial variability determination in the designing phase, as well as the scheduling, maintenance, and grid integration in the operation phase of solar energy projects. To help with the integration of solar energy projects into current power systems, a few studies in this thesis have been conducted to support solar resource assessment and forecasting.

Firstly, an improved method for estimating turbidity is proposed using common meteorological measurements, namely, ambient air temperature, relative humidity, wind speed, and atmospheric pressure. The estimated turbidity is then served as the input to the Ineichen-Perez model to estimate clear-sky irradiance. Compared with the monthly climatological means, the improved turbidity estimation better captures the seasonal and annual variations, and therefore shows substantial improvements in estimating clear-sky GHI and DNI. The RMSE of clear-sky GHI is reduced from 24.02 W m^{-2} to 9.94 W m^{-2} , and the RMSE of clear-sky DNI is decreased from 76.40 W m^{-2} to 29.96 W m^{-2} . Meanwhile, the proposed method is also capable to estimate turbidity in partially cloudy days with improved accuracy, evidenced by that the corresponding estimated clear-sky irradiance has smaller deviation from measurements in the cloudless periods. Considering the improved accuracy and less complexity in implementation, the presented method brings new insights in clear-sky irradiance estimation in both clear and partially cloudy days, providing support to solar forecasting and resource assessment.

To explore the benefits of the improved turbidity estimation for estimating clear-sky irradiance, an optimized semi-empirical satellite method is applied to estimate GHI using GOES-16 imagery. Four clear-sky models including REST2, McClear, Ineichen-Perez, and improved Ineichen-Perez (Ineichen-Perez TL) are compared and evaluated in estimating GHI from satellite measurements. The results show that there is no significant different all-sky GHI estimation for the used clear-sky models regarding nRMSE (25.19%-25.53%), which is comparable with the referenced physical solar model in NSRDB. Clouds cause the largest uncertainty, where the nRMSE of GHI estimation is in the range of 31.12%-31.54%, indicating that more efforts are need in quantifying the cloud effects in semi-empirical satellite methods. When using clear-sky GHI as GHI estimates in clear periods, Ineichen-Perez TL shows the lowest nRMSE and nMBE, therefore has potential in physical methods where clear-sky irradiance is the irradiance estimation when the sky is cloudless.

Although the improved turbidity estimation method shows substantial improvements in estimating clear-sky irradiance, and has been evaluated and compared with other clear-sky models for GHI estimation using semi-empirical satellite method, one limitation is the need of on-site irradiance measurements. To address this limitation, a transferable turbidity estimation method is proposed. Instead of using on-site irradiance measurements (i.e., the local model), a transferable model is developed involving stations with sufficient information, and then applied at locations with limited data availability. Compared with the local method, the transferable model yields results with slightly higher discrepancies regarding normalized root mean squared error (nRMSE, 2.80% vs 2.75%). When compared with the default Ineichen-Perez model, the nRMSE of clear-sky GHI estimation is reduced from 4.99% to 2.44%, and the nMBE is improved from -3.37% to 0.57%. The clear-sky GHI estimation is comparable with physical models (i.e., McClear and REST2). Further comparisons are made for day-ahead clear-sky GHI forecasts using a day persistent way. Clear-sky GHI forecast from the transferable method has slightly lower discrepancies of nRMSE and nMBE than the physical models. Considering the complexity of physical models, the transferable turbidity estimation method with comparable performance demonstrates valuable potential for solar resourcing and forecasting applications.

Since clouds are the main attenuation factor of ground-level solar irradiance, modeling clear-sky irradiance is just a small part in solar forecasting and resource assessment. To fully exploit the spectral information of modern geostationary satellites and extract cloud properties, a deep learning framework based on CNNs and attention mechanism for 5-min ground-level GHI and DNI estimations is proposed as deep learning has been extensively applied in vision and image based tasks to learn the nonlinear relationships. Correlation analysis is performed to select the representative satellite bands, which can improve the model-

ing efficiency without accuracy loss when compared with the usage of all spectral bands. The results show that the proposed model produces GHI estimation with an nRMSE of 20.57% and an nMBE of -2.04%, and the DNI estimation has an nRMSE of 23.63% and the nMBE is 0.36%. Compared with NSRDB, the proposed model produces a GHI estimation with the nRMSE reduction of 5.15%. As for DNI estimation, the proposed method shows an nRMSE reduction of 13.77%. Meanwhile, the proposed deep learning models generally yield better GHI and DNI estimations under different intervals of clear-sky index than NSRDB. The combination of deep learning and remote sensing shows potential in better extracting the cloud information via multispectral satellite images, which can better support solar resource assessment, especially for cloudy conditions.

In addition, satellite data and satellite-derived irradiance products have been extensively used in solar forecasting due to the spatio-temporal nature of solar irradiance. However, the potential advantages of satellite-derived irradiance and its improvements in solar forecasting have not been thoroughly explored. Therefore, a comparative study is conducted to evaluate and compare the performance of solar forecasts based on deep learning and three different inputs, namely, spectral satellite images, satellite-derived irradiance, and satellite-derived irradiance with improved accuracy. The results show that satellite-derived irradiance products generally outperform raw spectral satellite images. The improved accuracy in satellite-derived irradiance products is more likely to produce forecasts with lower nRMSE, higher forecast skill, and better performance in ramp forecasts. It is found that solar forecasting under frequent cloudy conditions is more challenging, evidenced by the enlarged nRMSE and compromised performance in ramp analysis. Based on the results of distribution-oriented verification approaches, solar forecasts are biased under high- and low-irradiance conditions, which is more obvious when more frequent clouds are present. Nevertheless, satellite-derived irradiance with improved accuracy might lead to better forecasts, which is beneficial to a wide range of stakeholders in solar energy.

It should be noted that different machine learning methods are applied for different scenarios in this thesis. For instance, classical machine methods such as MLP are used for improved turbidity estimation, while deep learning algorithms, e.g., convolutional neural networks (CNNs) are adopted for solar resource assessment and forecasting with satellite images or satellite-derived irradiance products. This is because the data used for turbidity estimation is in an one-dimensional form and therefore the classical methods are applied, while for solar irradiance modeling with satellite images or satellite-derived products, the data is in a two-dimensional form and therefore CNNs are applied to better extract the features. Moreover, in solar forecasting, the integration of spatio-temporal information is likely to produce better results than the locally-sensed data. The spatio-temporal data is usually in a grid format, where the deep learning algorithms

such as CNNs are particularly suitable, owing to their great performance in feature extraction of grid data.

The ultimate goal in solar resource assessment and forecasting is to obtain solar irradiance estimations and forecasts with high accuracy, and currently it is still challenging in modeling the cloud physics and dynamics since clouds are the major factor in affecting solar irradiance. The accurate modeling of solar irradiance and solar power output for the integration of solar energy systems requires efforts from atmospheric sciences, weather forecasting, data science and also many other domains. Although there are still limitations, such as the inability in the detection of cloud enhancements, the need of measurements of training machine/deep learning models, the constraints on computation resources, the methods developed in this thesis for clear-sky irradiance modeling, solar resource assessment and forecasting with improved performance can help with the integration of the solar energy systems.

7.2 Recommendations

This dissertation has explored the use of remote sensing and deep learning for solar resource assessment and intra-day forecasting, there are still many aspects in which the research could be extended. Therefore, the following recommendations for future work are based on the limitations and incomplete aspects.

- *Further expansion of the improved turbidity estimation method.* Although the transferable turbidity estimation method has substantially expanded the applicability, the results are only based on SURFRAD stations with five different climate types in the contiguous United States. In the future, the method should be tested in other Continents with more climate zones. The used machine learning methods are just classical methods, more advanced methods might produce better results and therefore should be tested. Meanwhile, the used inputs are common meteorological measurements, however, they might not be available for some locations of interest.
- *Improvement of the cloud properties determination.* In the applications of semi-empirical satellite method and deep learning for ground-level solar irradiance estimation, clouds are the major cause of large uncertainties. In future work, methods to accurately quantify the cloud properties in the atmosphere and its effect on solar radiation should be developed. Specifically, since semi-empirical satellite methods usually apply satellite images of one visible spectral band, it might be worthwhile to use more bands in the visible spectral bands and even the near-infrared spectrum to determine the dynamic range and cloud index. While for deep learning based methods, the investigations on the bands combination could be worthwhile.

- *Expansion of the deep learning based solar irradiance modeling.* The deep learning models for solar irradiance estimation and forecasting are based on satellite data of GOES-16 and the ground measurements of SURFRAD stations. Theoretically, the methodology developed could also be applied using other geostationary satellites such as Fengyun-4 and Himawari-8. Therefore, in future works, models should be developed and tested using other satellites and ground stations. However, the bands of GOES, Fengyun and Himawari have different wavelengths and the available satellite measurements are also different. Therefore, it is necessary to consider the correlation analysis, the size of the satellite images, and the spatio-temporal resolutions in a different perspective.
- *Investigation on the modeling three-dimensional cloud features in the atmosphere.* Satellite data used in this thesis only provides the views of the top of the atmosphere, which are two-dimensional features. However, the interaction of solar radiation and atmosphere compositions is a three-dimensional problem. Future studies should consider how to get or couple more information of atmospheric layers, for example, sky images which provide additional information at the ground level. Actually, the combination of sky images and satellite images have already been proposed for intra-hour solar forecasting. Therefore, the investigation should be more focused on how to better extract useful features.
- *Integration of numerical weather prediction products for forecasting at long time scales.* Geostationary satellite data is only suitable for short-term solar forecasting, for example, intra-day forecasting. Future studies that aims to extend the forecast horizon should consider more suitable data or methods, for instance, the numerical weather prediction (NWP). Meanwhile, it could also be beneficial for solar forecasting to develop hybrid deep learning models with NWP, as physics-informed machine/deep learning is important in improving the interpretability. However, NWP products usually consists of a large amount of data, which imposes new challenges on data storage and computing resources. Therefore, future studies should focus on how to use NWP products and how to combine NWP and deep learning efficiently.

Bibliography

- [1] IEA, World energy outlook 2020, <https://www.iea.org/reports/world-energy-outlook-2020>, (Accessed on 17/03/2022) (2020).
- [2] IEA, World energy outlook 2021, <https://www.iea.org/reports/world-energy-outlook-2021>, (Accessed on 06/09/2023) (2021).
- [3] IEA, World energy outlook 2022, <https://www.iea.org/reports/world-energy-outlook-2022>, (Accessed on 06/09/2023) (2022).
- [4] D. S. Kumar, G. M. Yagli, M. Kashyap, D. Srinivasan, Solar irradiance resource and forecasting: a comprehensive review, *IET Renewable Power Generation* 14 (10) (2020) 1641–1656.
- [5] P. Murphy, 2020 Annual Report, Report, IEA Solar Heating & Cooling Programme (2021).
- [6] Energy Institute Statistical Review of World Energy 2022, <https://www.energyinst.org/statistical-review/>, (Accessed on 05/09/2023) (2023).
- [7] Solar resource maps and GIS data for world — Solargis, <https://solargis.com/maps-and-gis-data/download/world>, (Accessed on 17/03/2022) (2021).
- [8] J. Kleissl, Solar energy forecasting and resource assessment, Academic Press, 2013.
- [9] R. H. Inman, H. T. C. Pedro, C. F. M. Coimbra, Solar forecasting methods for renewable energy integration, *Progress in energy and combustion science* 39 (6) (2013) 535–576.
- [10] Y. Chu, M. Li, C. F. M. Coimbra, Sun-tracking imaging system for intra-hour DNI forecasts, *Renewable Energy* 96 (2016) 792–799.
- [11] M. Li, Y. Chu, H. T. C. Pedro, C. F. M. Coimbra, Quantitative evaluation of the impact of cloud transmittance and cloud velocity on the accuracy of short-term DNI forecasts, *Renewable Energy* 86 (2016) 1362–1371.
- [12] G. M. Yagli, D. Yang, O. Gandhi, D. Srinivasan, Can we justify producing univariate machine-learning forecasts with satellite-derived solar irradiance?, *Applied Energy* 259 (2020) 114122.
- [13] T. J. Schmit, S. S. Lindstrom, J. J. Gerth, M. M. Gunshor, Applications of the 16 spectral bands on the Advanced Baseline Imager (ABI), *Journal of Operational Meteorology* 6 (4) (2018) 33–46.
- [14] Y. Chu, M. Li, C. F. M. Coimbra, D. Feng, H. Wang, Intra-Hour Irradiance Forecasting Techniques for Solar Power Integration: A Review, *iScience* (2021) 103136.
- [15] N. Javaid, G. Hafeez, S. Iqbal, N. Alrajeh, M. S. Alabed, M. Guizani, Energy efficient integration of renewable energy sources in the smart grid for demand side management, *ieee access* 6 (2018) 77077–77096.
- [16] L. Wen, K. Zhou, S. Yang, X. Lu, Optimal load dispatch of community microgrid with deep learning based solar power and load forecasting, *Energy* 171 (2019) 1053–1065.

- [17] A. Z. Arsal, M. Hannan, A. Q. Al-Shetwi, M. Mansur, K. Muttaqi, Z. Dong, F. Blaabjerg, Hydrogen energy storage integrated hybrid renewable energy systems: A review analysis for future research directions, *International Journal of Hydrogen Energy*.
- [18] P. Denholm, Greening the Grid: The Role of Storage and Demand Response, <https://www.nrel.gov/docs/fy15osti/63041.pdf>, (Accessed on 17/03/2022) (2015).
- [19] T. Hong, P. Pinson, Y. Wang, R. Weron, D. Yang, H. Zareipour, Energy forecasting: A review and outlook, *IEEE Open Access Journal of Power and Energy* 7 (2020) 376–388.
- [20] D. Yang, W. Wang, X. Xia, A concise overview on solar resource assessment and forecasting, *Advances in Atmospheric Sciences* (2022) 1–13.
- [21] D. Yang, W. Wang, C. A. Gueymard, T. Hong, J. Kleissl, J. Huang, M. J. Perez, R. Perez, J. M. Bright, X. Xia, et al., A review of solar forecasting, its dependence on atmospheric sciences and implications for grid integration: Towards carbon neutrality, *Renewable and Sustainable Energy Reviews* 161 (2022) 112348.
- [22] C. B. Martinez-Anido, A. R. Florita, B.-M. Hodge, The impact of improved solar forecasts on bulk power system operations in ISO-NE.
- [23] V. Sharma, A. Cortes, U. Cali, Use of forecasting in energy storage applications: A review, *IEEE Access*.
- [24] D. Neves, M. C. Brito, C. A. Silva, Impact of solar and wind forecast uncertainties on demand response of isolated micro-grids, *Renewable energy* 87 (2016) 1003–1015.
- [25] J. A. Duffie, W. A. Beckman, *Solar Engineering of Thermal Processes*, 4th Edition (2013).
- [26] K.-N. Liou, *An introduction to atmospheric radiation*, Elsevier, 2002.
- [27] D. Yang, SolarData: An R package for easy access of publicly available solar datasets, *Solar Energy* 171 (2018) A3–A12.
- [28] C. N. Long, Y. Shi, An automated quality assessment and control algorithm for surface radiation measurements, *The Open Atmospheric Science Journal* 2 (1).
- [29] J. A. Augustine, J. J. DeLuisi, C. N. Long, SURFRAD—A national surface radiation budget network for atmospheric research, *Bulletin of the American Meteorological Society* 81 (10) (2000) 2341–2358.
- [30] F. Linke, Transmission coefficient and turbidity factor, *J Beitrage Phys Fr Atom* 10 (2) (1922) 91–103.
- [31] P. Ineichen, R. Perez, A new air mass independent formulation for the Linke turbidity coefficient, *Solar Energy* 73 (3) (2002) 151–157.
- [32] M. Lefèvre, A. Oumbe, P. Blanc, B. Espinar, B. Gschwind, Z. Qu, L. Wald, M. Schroedter-Homscheidt, C. Hoyer-Klick, A. Arola, et al., McClear: a new model estimating downwelling solar radiation at ground level in clear-sky conditions, *Atmospheric Measurement Techniques* 6 (9) (2013) 2403–2418.
- [33] C. A. Gueymard, REST2: High-performance solar radiation model for cloudless-sky irradiance, illuminance, and photosynthetically active radiation—validation with a benchmark dataset, *Solar Energy* 82 (3) (2008) 272–285.
- [34] X. Sun, J. M. Bright, C. A. Gueymard, B. Acord, P. Wang, N. A. Engerer, Worldwide performance assessment of 75 global clear-sky irradiance models using principal component analysis, *Renewable and Sustainable Energy Reviews* 111 (2019) 550–570.
- [35] F. Antonanzas-Torres, R. Urraca, J. Polo, O. Perpiñán-Lamigueiro, R. Escobar, Clear sky solar irradiance models: A review of seventy models, *Renewable and Sustainable Energy Reviews* 107 (2019) 374–387.
- [36] D. Yang, Choice of clear-sky model in solar forecasting, *Journal of Renewable and Sustainable Energy* 12 (2) (2020) 026101.
- [37] R. Perez, P. Ineichen, K. Moore, M. Kmiecik, C. Chain, R. George, F. Vignola, A new operational model for satellite-derived

- irradiances: description and validation, *Solar Energy* 73 (5) (2002) 307–317.
- [38] R. W. Mueller, K.-F. Dagestad, P. Ineichen, M. Schroedter-Homscheidt, S. Cros, D. Dumortier, R. Kuhlemann, J. A. Olseth, G. Piernavieja, C. Reise, L. Wald, D. Heinemann, Rethinking satellite-based solar irradiance modelling: The SOLIS clear-sky module, *Remote sensing of Environment* 91 (2) (2004) 160–174.
- [39] W. F. Holmgren, C. W. Hansen, M. A. Mikofski, pvlib python: A python package for modeling solar energy systems, *Journal of Open Source Software* 3 (29) (2018) 884.
- [40] J. Remund, L. Wald, M. Lefèvre, T. Ranchin, J. Page, Worldwide Linke turbidity information, in: *ISES Solar World Congress 2003*, Vol. 400, International Solar Energy Society (ISES), 2003, pp. 13–p.
- [41] J. Polo, L. F. Zarzalejo, L. Martin, A. A. Navarro, R. Marchante, Estimation of daily Linke turbidity factor by using global irradiance measurements at solar noon, *Solar Energy* 83 (8) (2009) 1177–1185.
- [42] C. L. Moldovan, R. Păltănea, I. Visa, Improvement of clear sky models for direct solar irradiance considering turbidity factor variable during the day, *Renewable Energy* 161 (2020) 559–569.
- [43] B. Mayer, A. Kylling, The libRadtran software package for radiative transfer calculations-description and examples of use, *Atmospheric Chemistry and Physics* 5 (7) (2005) 1855–1877.
- [44] M. Schroedter-Homscheidt, F. Azam, J. Betcke, C. Hoyer-Klick, M. Lefèvre, L. Wald, E. Wey, L. Saboret, User’s Guide to the CAMS Radiation Service (CRS): Status December 2020, Copernicus Atmosphere Monitoring Service.
- [45] R. Gelaro, W. McCarty, M. J. Suárez, R. Todling, A. Molod, L. Takacs, C. A. Randles, A. Darmenov, M. G. Bosilovich, R. Reichle, et al., The modern-era retrospective analysis for research and applications, version 2 (merra-2), *Journal of climate* 30 (14) (2017) 5419–5454.
- [46] T. S. Pagano, R. M. Durham, Moderate resolution imaging spectroradiometer (modis), in: *Sensor Systems for the Early Earth Observing System Platforms*, Vol. 1939, SPIE, 1993, pp. 2–17.
- [47] L. Ayompe, A. Duffy, An assessment of the energy generation potential of photovoltaic systems in Cameroon using satellite-derived solar radiation datasets, *Sustainable Energy Technologies and Assessments* 7 (2014) 257–264.
- [48] A. Hammer, D. Heinemann, C. Hoyer, R. Kuhlemann, E. Lorenz, R. Müller, H. G. Beyer, Solar energy assessment using remote sensing technologies, *Remote Sensing of Environment* 86 (3) (2003) 423–432.
- [49] M. Sengupta, Y. Xie, A. Lopez, A. Habte, G. Maclaurin, J. Shelby, The National Solar Radiation Database (NSRDB), *Renewable and Sustainable Energy Reviews* 89 (2018) 51–60.
- [50] Z. Qu, A. Oumbe, P. Blanc, B. Espinar, G. Gesell, B. Gschwind, L. Klüser, M. Lefèvre, L. Saboret, M. Schroedter-Homscheidt, Fast radiative transfer parameterisation for assessing the surface solar irradiance: The Heliosat-4 method, *Meteorologische Zeitschrift* 26 (1) (2017) 33–57.
- [51] P. M P Garniwa, R. A A Ramadhan, H.-J. Lee, Application of Semi-Empirical Models Based on Satellite Images for Estimating Solar Irradiance in Korea, *Applied Sciences* 11 (8) (2021) 3445.
- [52] A. Laguarda, G. Giacosa, R. Alonso-Suárez, G. Abal, Performance of the site-adapted CAMS database and locally adjusted cloud index models for estimating global solar horizontal irradiation over the Pampa Húmeda, *Solar Energy* 199 (2020) 295–307.
- [53] D. Fu, M. Liu, D. Yang, H. Che, X. Xia, Influences of atmospheric reanalysis on the accuracy of clear-sky irradiance estimates: Comparing MERRA-2 and CAMS, *Atmospheric Environment* 277 (2022) 119080.
- [54] X. Zhong, J. Kleissl, Clear sky irradiances using REST2 and MODIS, *Solar Energy* 116 (2015) 144–164.
- [55] V. Kallio-Myers, A. Riihelä, P. Lahtinen, A. Lindfors, Global horizontal irradiance forecast for Finland based on geostation-

- ary weather satellite data, *Solar Energy* 198 (2020) 68–80.
- [56] Z. Qu, B. Gschwind, M. Lefèvre, L. Wald, Improving HelioClim-3 estimates of surface solar irradiance using the McClear clear-sky model and recent advances in atmosphere composition, *Atmospheric Measurement Techniques* 7 (11) (2014) 3927–3933.
- [57] H. G. Beyer, C. Costanzo, D. Heinemann, Modifications of the Heliosat procedure for irradiance estimates from satellite images, *Solar Energy* 56 (3) (1996) 207–212.
- [58] C. Rigollier, M. Lefèvre, L. Wald, The method Heliosat-2 for deriving shortwave solar radiation from satellite images, *Solar energy* 77 (2) (2004) 159–169.
- [59] D. Cano, J.-M. Monget, M. Albuissou, H. Guillard, N. Regas, L. Wald, A method for the determination of the global solar radiation from meteorological satellite data, *Solar energy* 37 (1) (1986) 31–39.
- [60] D. Jia, J. Hua, L. Wang, Y. Guo, H. Guo, P. Wu, M. Liu, L. Yang, Estimations of Global Horizontal Irradiance and Direct Normal Irradiance by Using Fengyun-4A Satellite Data in Northern China, *Remote Sensing* 13 (4) (2021) 790.
- [61] Solcast, Inputs and algorithms [online], Available: [:https://solcast.com/historical-and-tmy/inputs-and-algorithms/](https://solcast.com/historical-and-tmy/inputs-and-algorithms/), (Accessed on 17/03/2022) (2021).
- [62] R. Mueller, T. Behrendt, A. Hammer, A. Kemper, A new algorithm for the satellite-based retrieval of solar surface irradiance in spectral bands, *Remote Sensing* 4 (3) (2012) 622–647.
- [63] H. Long, Z. Zhang, Y. Su, Analysis of daily solar power prediction with data-driven approaches, *Applied Energy* 126 (2014) 29–37.
- [64] Y. Jiang, H. Long, Z. Zhang, Z. Song, Day-ahead prediction of bihourly solar radiance with a markov switch approach, *IEEE Transactions on Sustainable Energy* 8 (4) (2017) 1536–1547.
- [65] C. Huang, Z. Zhao, L. Wang, Z. Zhang, X. Luo, Point and interval forecasting of solar irradiance with an active gaussian process, *IET Renewable Power Generation* 14 (6) (2020) 1020–1030.
- [66] C. Arbizu-Barrena, J. A. Ruiz-Arias, F. J. Rodríguez-Benítez, D. Pozo-Vázquez, J. Tovar-Pescador, Short-term solar radiation forecasting by advecting and diffusing MSG cloud index, *Solar Energy* 155 (2017) 1092–1103.
- [67] T. M. Harty, W. F. Holmgren, A. T. Lorenzo, M. Morzfeld, Intra-hour cloud index forecasting with data assimilation, *Solar Energy* 185 (2019) 270–282.
- [68] P. Wang, R. van Westrhenen, J. F. Meirink, S. van der Veen, W. Knap, Surface solar radiation forecasts by advecting cloud physical properties derived from meteosat second generation observations, *Solar Energy* 177 (2019) 47–58.
- [69] C. W. Chow, S. Belongie, J. Kleissl, Cloud motion and stability estimation for intra-hour solar forecasting, *Solar Energy* 115 (2015) 645–655.
- [70] D. Aicardi, P. Musé, R. Alonso-Suárez, A comparison of satellite cloud motion vectors techniques to forecast intra-day hourly solar global horizontal irradiation, *Solar Energy* 233 (2022) 46–60.
- [71] C. D. Kuglin, The phase correlation image alignment method, in: Proc. Int. Conference Cybernetics Society, 1975, pp. 163–165.
- [72] S. Cros, N. Sébastien, O. Liandrat, N. Schmutz, Cloud pattern prediction from geostationary meteorological satellite images for solar energy forecasting, in: Remote Sensing of Clouds and the Atmosphere XIX; and Optics in Atmospheric Propagation and Adaptive Systems XVII, Vol. 9242, International Society for Optics and Photonics, 2014, p. 924202.
- [73] J. Du, Q. Min, P. Zhang, J. Guo, J. Yang, B. Yin, Short-term solar irradiance forecasts using sky images and radiative transfer model, *Energies* 11 (5) (2018) 1107.

- [74] Y. Xie, M. Sengupta, A fast all-sky radiation model for solar applications with narrowband irradiances on tilted surfaces (farms-nit): Part i. the clear-sky model, *Solar Energy* 174 (2018) 691–702.
- [75] Y. Xie, M. Sengupta, C. Wang, A fast all-sky radiation model for solar applications with narrowband irradiances on tilted surfaces (farms-nit): Part ii. the cloudy-sky model, *Solar Energy* 188 (2019) 799–812.
- [76] C. M. Bishop, Pattern recognition, *Machine Learning* 128 (9).
- [77] G. Biau, E. Scornet, A random forest guided tour, *Test* 25 (2) (2016) 197–227.
- [78] I. Goodfellow, Y. Bengio, A. Courville, *Deep learning*, MIT press, 2016.
- [79] Y. Chu, M. Li, H. T. C. Pedro, C. F. M. Coimbra, Real-time prediction intervals for intra-hour DNI forecasts, *Renewable Energy* 83 (2015) 234–244.
- [80] D. P. Larson, M. Li, C. F. M. Coimbra, SCOPE: Spectral cloud optical property estimation using real-time GOES-R longwave imagery, *Journal of Renewable and Sustainable Energy* 12 (2) (2020) 026501.
- [81] M. Chaâbane, M. Masmoudi, K. Medhioub, Determination of Linke turbidity factor from solar radiation measurement in northern Tunisia, *Renewable Energy* 29 (13) (2004) 2065–2076.
- [82] X. Sun, J. M. Bright, C. A. Gueymard, X. Bai, B. Acord, P. Wang, Worldwide performance assessment of 95 direct and diffuse clear-sky irradiance models using principal component analysis, *Renewable and Sustainable Energy Reviews* 135 (2021) 110087.
- [83] P. Ineichen, A broadband simplified version of the Solis clear sky model, *Solar Energy* 82 (8) (2008) 758–762.
- [84] P. Ineichen, Conversion function between the Linke turbidity and the atmospheric water vapor and aerosol content, *Solar Energy* 82 (11) (2008) 1095–1097.
- [85] L. Narain, S. N. Garg, Estimation of Linke turbidity factors for different regions of india, *International Journal of Environment and Waste Management* 12 (1) (2013) 52–64.
- [86] T. Hove, E. Manyumbu, Estimates of the Linke turbidity factor over Zimbabwe using ground-measured clear-sky global solar radiation and sunshine records based on a modified ESRA clear-sky model approach, *Renewable Energy* 52 (2013) 190–196.
- [87] C. Rigollier, O. Bauer, L. Wald, On the clear sky model of the ESRA—European Solar Radiation Atlas—with respect to the Heliosat method, *Solar energy* 68 (1) (2000) 33–48.
- [88] R. H. Inman, J. G. Edson, C. F. M. Coimbra, Impact of local broadband turbidity estimation on forecasting of clear sky direct normal irradiance, *Solar Energy* 117 (2015) 125–138.
- [89] O. Behar, D. Sbarbaro, A. Marzo, L. Moran, A simplified methodology to estimate solar irradiance and atmospheric turbidity from ambient temperature and relative humidity, *Renewable and Sustainable Energy Reviews* 116 (2019) 109310.
- [90] C. A. Gueymard, J. M. Bright, D. Lingfors, A. Habte, M. Sengupta, A posteriori clear-sky identification methods in solar irradiance time series: Review and preliminary validation using sky imagers, *Renewable and Sustainable Energy Reviews* 109 (2019) 412–427.
- [91] C. N. Long, T. P. Ackerman, Identification of clear skies from broadband pyranometer measurements and calculation of downwelling shortwave cloud effects, *Journal of Geophysical Research: Atmospheres* 105 (D12) (2000) 15609–15626.
- [92] C. N. Long, K. L. Gaustad, The shortwave (SW) clear-sky detection and fitting algorithm: Algorithm operational details and explanations, Pacific Northwest National Laboratory, 2004.
- [93] C. N. Long, D. D. Turner, A method for continuous estimation of clear-sky downwelling longwave radiative flux developed using ARM surface measurements, *Journal of Geophysical Research: Atmospheres* 113 (D18).

- [94] L. D. Riihimaki, K. L. Gaustad, C. N. Long, Radiative Flux Analysis (RADFLUXANAL) Value-Added Product: Retrieval of Clear-Sky Broadband Radiative Fluxes and Other Derived Values, Tech. rep., ARM Data Center, Oak Ridge National Laboratory (ORNL), Oak Ridge, TN (United States) (2019).
- [95] C. A. Gueymard, Analysis of monthly average atmospheric precipitable water and turbidity in Canada and northern United States, *Solar Energy* 53 (1) (1994) 57–71.
- [96] C. A. Gueymard, Assessment of the accuracy and computing speed of simplified saturation vapor equations using a new reference dataset, *Journal of Applied Meteorology and Climatology* 32 (7) (1993) 1294–1300.
- [97] F. Pedregosa, G. Varoquaux, A. Gramfort, V. Michel, B. Thirion, O. Grisel, M. Blondel, P. Prettenhofer, R. Weiss, V. Dubourg, et al., Scikit-learn: Machine learning in python, the *Journal of Machine Learning Research* 12 (2011) 2825–2830.
- [98] M. Ali, PyCaret: An open source, low-code machine learning library in python, PyCaret version 2.
- [99] IEA, Solar PV [online], Available: <https://www.iea.org/reports/solar-pv>, (Accessed on 17/03/2022) (2020).
- [100] Y. Chu, H. T. Pedro, C. F. M. Coimbra, Hybrid intra-hour DNI forecasts with sky image processing enhanced by stochastic learning, *Solar Energy* 98 (2013) 592–603.
- [101] C. Rigollier, L. Wald, Selecting a clear-sky model to accurately map solar radiation from satellite images, in: EARSel Symposium 1999 “remote sensing in the 21st Century: economic and environmental applications”, Balkema, 1999, pp. 131–137.
- [102] C. Rigollier, L. Wald, The HelioClim Project: from satellite images to solar radiation maps, in: Proceedings of the ISES Solar World Congress, Citeseer, 1999.
- [103] S. Chen, M. Li, Improved turbidity estimation from local meteorological data for solar resourcing and forecasting applications, *Renewable Energy* 189 (2022) 259–272.
- [104] GOES R SERIES PRODUCT DEFINITION AND USERS’ GUIDE (PUG) VOLUME 3: LEVEL 1B PRODUCTS, Available at: <https://www.goes-r.gov/users/docs/PUG-L1b-vol3.pdf> (2019).
- [105] D. Yang, Validation of the 5-min irradiance from the National Solar Radiation Database (NSRDB), *Journal of Renewable and Sustainable Energy* 13 (1) (2021) 016101.
- [106] P. Broxton, X. Zeng, N. Dawson, Daily 4 km gridded SWE and snow depth from assimilated in-situ and modeled data over the conterminous US, version 1, NASA National Snow and Ice Data Center Distributed Active Archive Center, Boulder, CO.
- [107] X. Zeng, P. Broxton, N. Dawson, Snowpack change from 1982 to 2016 over conterminous United States, *Geophysical Research Letters* 45 (23) (2018) 12–940.
- [108] T. Albarelo, I. Marie-Joseph, A. Primerose, F. Seyler, L. Wald, L. Linguet, Optimizing the Heliosat-II method for surface solar irradiation estimation with GOES images, *Canadian Journal of Remote Sensing* 41 (2) (2015) 86–100.
- [109] A. T. Lorenzo, M. Morzfeld, W. F. Holmgren, A. D. Cronin, Optimal interpolation of satellite and ground data for irradiance nowcasting at city scales, *Solar Energy* 144 (2017) 466–474.
- [110] D. Mouhamet, A. Tommy, A. Primerose, L. Laurent, Improving the Heliosat-2 method for surface solar irradiation estimation under cloudy sky areas, *Solar Energy* 169 (2018) 565–576.
- [111] S. Williamson, S. Businger, D. Matthews, Development of a solar irradiance dataset for Oahu, Hawai’i, *Renewable Energy* 128 (2018) 432–443.
- [112] J. M. Bright, X. Sun, C. A. Gueymard, B. Acord, P. Wang, N. A. Engerer, Bright-Sun: A globally applicable 1-min irradiance clear-sky detection model, *Renewable and Sustainable Energy Reviews* 121 (2020) 109706.

- [113] M. Lefèvre, M. Albuisson, L. Wald, Description of the software Heliosat-2 for the conversion of images acquired by Meteosat satellites in the visible band into maps of solar radiation available at ground level.
- [114] E. Scolari, F. Sossan, M. Haure-Touzé, M. Paolone, Local estimation of the global horizontal irradiance using an all-sky camera, *Solar Energy* 173 (2018) 1225–1235.
- [115] A. F. Zambrano, L. F. Giraldo, Solar irradiance forecasting models without on-site training measurements, *Renewable Energy* 152 (2020) 557–566.
- [116] C. A. Gueymard, D. Yang, Worldwide validation of cams and merra-2 reanalysis aerosol optical depth products using 15 years of aeronet observations, *Atmospheric Environment* 225 (2020) 117216.
- [117] M. Sengupta, A. Habte, S. Wilbert, C. Gueymard, J. Remund, Best practices handbook for the collection and use of solar resource data for solar energy applications, Tech. rep., National Renewable Energy Lab.(NREL), Golden, CO (United States) (2021).
- [118] Y. Eissa, S. N. Beegum, I. Gherboudj, N. Chaouch, J. Al Sudairi, R. K. Jones, N. Al Dobayan, H. Ghedira, Prediction of the day-ahead clear-sky downwelling surface solar irradiances using the REST2 model and WRF-CHIMERE simulations over the Arabian Peninsula, *Solar Energy* 162 (2018) 36–44.
- [119] IEA, World Energy Outlook 2021 [online], Available at: <https://www.iea.org/reports/world-energy-outlook-2021>, (Accessed on 04/08/2022) (2021).
- [120] IEA, Renewables 2021 [online], Available at: <https://www.iea.org/reports/renewables-2021>, (Accessed on 04/08/2022) (December 2021).
- [121] IEA, Solar PV [online], Available at: <https://www.iea.org/reports/solar-pv>, (Accessed on 04/08/2022) (November 2021).
- [122] IEA, Concentrated Solar Power (CSP) [online], Available at: <https://www.iea.org/reports/concentrated-solar-power-csp>, (Accessed on 04/08/2022) (November 2021).
- [123] R. H. Inman, Y. Chu, C. F. M. Coimbra, Cloud enhancement of global horizontal irradiance in California and Hawaii, *Solar Energy* 130 (2016) 128–138.
- [124] G. Salazar, C. Gueymard, J. B. Galdino, O. de Castro Vilela, N. Fraidenraich, Solar irradiance time series derived from high-quality measurements, satellite-based models, and reanalyses at a near-equatorial site in Brazil, *Renewable and Sustainable Energy Reviews* 117 (2020) 109478.
- [125] B. Babar, L. T. Luppino, T. Boström, S. N. Anfinsen, Random forest regression for improved mapping of solar irradiance at high latitudes, *Solar Energy* 198 (2020) 81–92.
- [126] G. Huang, Z. Li, X. Li, S. Liang, K. Yang, D. Wang, Y. Zhang, Estimating surface solar irradiance from satellites: Past, present, and future perspectives, *Remote Sensing of Environment* 233 (2019) 111371.
- [127] S. Chen, Z. Liang, S. Guo, M. Li, Estimation of high-resolution solar irradiance data using optimized semi-empirical satellite method and GOES-16 imagery, *Solar Energy* 241 (2022) 404–415.
- [128] J. Polo, S. Wilbert, J. A. Ruiz-Arias, R. Meyer, C. Gueymard, M. Suri, L. Martin, T. Mieslinger, P. Blanc, I. Grant, et al., Preliminary survey on site-adaptation techniques for satellite-derived and reanalysis solar radiation datasets, *Solar Energy* 132 (2016) 25–37.
- [129] M. A. Hassan, A. Khalil, S. Kaseb, M. A. Kassem, Exploring the potential of tree-based ensemble methods in solar radiation modeling, *Applied Energy* 203 (2017) 897–916.
- [130] L. Cornejo-Bueno, C. Casanova-Mateo, J. Sanz-Justo, S. Salcedo-Sanz, Machine learning regressors for solar radiation

- estimation from satellite data, *Solar Energy* 183 (2019) 768–775.
- [131] F. Liu, X. Wang, F. Sun, H. Wang, Correct and remap solar radiation and photovoltaic power in china based on machine learning models, *Applied Energy* 312 (2022) 118775.
- [132] H. Jiang, N. Lu, J. Qin, W. Tang, L. Yao, A deep learning algorithm to estimate hourly global solar radiation from geostationary satellite data, *Renewable and Sustainable Energy Reviews* 114 (2019) 109327.
- [133] A. Nespoli, A. Niccolai, E. Ogliari, G. Perego, E. Collino, D. Ronzio, Machine learning techniques for solar irradiation nowcasting: Cloud type classification forecast through satellite data and imagery, *Applied Energy* 305 (2022) 117834.
- [134] G. Notton, C. Voyant, A. Fouilloy, J. L. Duchaud, M. L. Nivet, Some applications of ANN to solar radiation estimation and forecasting for energy applications, *Applied Sciences* 9 (1) (2019) 209.
- [135] N. Lu, J. Qin, K. Yang, J. Sun, A simple and efficient algorithm to estimate daily global solar radiation from geostationary satellite data, *Energy* 36 (5) (2011) 3179–3188.
- [136] P. Verma, S. Patil, A machine learning approach and methodology for solar radiation assessment using multispectral satellite images, *Annals of Data Science* (2021) 1–26.
- [137] J. Chen, W. Zhu, Q. Yu, Estimating half-hourly solar radiation over the Continental United States using GOES-16 data with iterative random forest, *Renewable Energy* 178 (2021) 916–929.
- [138] J. Chen, W. Zhu, Q. Yu, High-spatiotemporal-resolution estimation of solar energy component in the united states using a new satellite-based model, *Journal of Environmental Management* 302 (2022) 114077.
- [139] P. A. Rocha, V. O. Santos, Global horizontal and direct normal solar irradiance modeling by the machine learning methods XGBoost and deep neural networks with CNN-LSTM layers: a case study using the goes-16 satellite imagery, *International Journal of Energy and Environmental Engineering* (2022) 1–16.
- [140] A. Vaswani, N. Shazeer, N. Parmar, J. Uszkoreit, L. Jones, A. N. Gomez, Ł. Kaiser, I. Polosukhin, Attention is all you need, *Advances in neural information processing systems* 30.
- [141] M. Sengupta, Y. Xie, A. Habte, G. Buster, G. Maclaurin, P. Edwards, H. Sky, M. Bannister, E. Rosenlieb, The national solar radiation database (nsrdb) final report: Fiscal years 2019-2021, Tech. rep., National Renewable Energy Lab.(NREL), Golden, CO (United States) (2022).
- [142] G. Chandrashekar, F. Sahin, A survey on feature selection methods, *Computers & Electrical Engineering* 40 (1) (2014) 16–28.
- [143] S.-y. Jiang, L.-x. Wang, Efficient feature selection based on correlation measure between continuous and discrete features, *Information Processing Letters* 116 (2) (2016) 203–215.
- [144] M. A. Hall, *Correlation-based Feature Selection for Machine Learning*, Ph.D. thesis, Citeseer (1999).
- [145] L. Yu, H. Liu, Feature selection for high-dimensional data: A fast correlation-based filter solution, in: *Proceedings of the 20th international conference on machine learning (ICML-03)*, 2003, pp. 856–863.
- [146] P. Kumari, D. Toshniwal, Deep learning models for solar irradiance forecasting: A comprehensive review, *Journal of Cleaner Production* 318 (2021) 128566.
- [147] C. Feng, J. Zhang, Solarnet: A sky image-based deep convolutional neural network for intra-hour solar forecasting, *Solar Energy* 204 (2020) 71–78.
- [148] M. Ajith, M. Martínez-Ramón, Deep learning based solar radiation micro forecast by fusion of infrared cloud images and radiation data, *Applied Energy* 294 (2021) 117014.
- [149] J. Zhang, J. Wu, H. Wang, Y. Wang, Y. Li, Cloud detection method using CNN based on cascaded feature attention and

- channel attention, *IEEE Transactions on Geoscience and Remote Sensing* 60 (2021) 1–17.
- [150] Z. Niu, G. Zhong, H. Yu, A review on the attention mechanism of deep learning, *Neurocomputing* 452 (2021) 48–62.
- [151] M. Abadi, A. Agarwal, P. Barham, E. Brevdo, Z. Chen, C. Citro, G. S. Corrado, A. Davis, J. Dean, M. Devin, et al., *Tensorflow: Large-scale machine learning on heterogeneous distributed systems*, arXiv preprint arXiv:1603.04467.
- [152] S. Chen, Z. Liang, P. Dong, S. Guo, M. Li, A transferable turbidity estimation method for estimating clear-sky solar irradiance, *Renewable Energy* 206 (2023) 635–644.
- [153] X. Glorot, Y. Bengio, Understanding the difficulty of training deep feedforward neural networks, in: *Proceedings of the thirteenth international conference on artificial intelligence and statistics, JMLR Workshop and Conference Proceedings*, 2010, pp. 249–256.
- [154] R. Tapakis, A. Charalambides, Enhanced values of global irradiance due to the presence of clouds in Eastern Mediterranean, *Renewable energy* 62 (2014) 459–467.
- [155] IEA, *Renewables 2022* [online], Available at: <https://www.iea.org/reports/renewables-2022>, (Accessed on 14/06/2023) (December 2022).
- [156] Y. Chu, H. T. C. Pedro, M. Li, C. F. M. Coimbra, Real-time forecasting of solar irradiance ramps with smart image processing, *Solar Energy* 114 (2015) 91–104.
- [157] W. Wang, D. Yang, N. Huang, C. Lyu, G. Zhang, X. Han, Irradiance-to-power conversion based on physical model chain: An application on the optimal configuration of multi-energy microgrid in cold climate, *Renewable and Sustainable Energy Reviews* 161 (2022) 112356.
- [158] D. W. Van der Meer, J. Widén, J. Munkhammar, Review on probabilistic forecasting of photovoltaic power production and electricity consumption, *Renewable and Sustainable Energy Reviews* 81 (2018) 1484–1512.
- [159] E. Pérez, J. Pérez, J. Segarra-Tamarit, H. Beltran, A deep learning model for intra-day forecasting of solar irradiance using satellite-based estimations in the vicinity of a pv power plant, *Solar Energy* 218 (2021) 652–660.
- [160] L. M. Matsunobu, H. T. C. Pedro, C. F. M. Coimbra, Cloud detection using convolutional neural networks on remote sensing images, *Solar Energy* 230 (2021) 1020–1032.
- [161] S. Chen, C. Li, Y. Xie, M. Li, Global and direct solar irradiance estimation using deep learning and selected spectral satellite images, *Applied Energy* 352 (2023) 121979.
- [162] Z. Si, M. Yang, Y. Yu, T. Ding, Photovoltaic power forecast based on satellite images considering effects of solar position, *Applied Energy* 302 (2021) 117514.
- [163] R. Gallo, M. Castangia, A. Macii, E. Macii, E. Patti, A. Aliberti, Solar radiation forecasting with deep learning techniques integrating geostationary satellite images, *Engineering Applications of Artificial Intelligence* 116 (2022) 105493.
- [164] F. J. Rodríguez-Benítez, M. López-Cuesta, C. Arbizu-Barrena, M. M. Fernández-León, M. Á. Pamos-Ureña, J. Tovar-Pescador, F. J. Santos-Alamillos, D. Pozo-Vázquez, Assessment of new solar radiation nowcasting methods based on sky-camera and satellite imagery, *Applied Energy* 292 (2021) 116838.
- [165] L. M. Aguiar, B. Pereira, P. Lauret, F. Díaz, M. David, Combining solar irradiance measurements, satellite-derived data and a numerical weather prediction model to improve intra-day solar forecasting, *Renewable Energy* 97 (2016) 599–610.
- [166] Y. Liu, H. Qin, Z. Zhang, S. Pei, C. Wang, X. Yu, Z. Jiang, J. Zhou, Ensemble spatiotemporal forecasting of solar irradiation using variational Bayesian convolutional gate recurrent unit network, *Applied Energy* 253 (2019) 113596.
- [167] G. M. Yagli, D. Yang, D. Srinivasan, Ensemble solar forecasting and post-processing using dropout neural network and information from neighboring satellite pixels, *Renewable and Sustainable Energy Reviews* 155 (2022) 111909.

- [168] Q. Paletta, G. Arbod, J. Lasenby, Omnivision forecasting: Combining satellite and sky images for improved deterministic and probabilistic intra-hour solar energy predictions, *Applied Energy* 336 (2023) 120818.
- [169] B. K. Blaylock, GOES-2-go: Download and display GOES-East and GOES-West data (Version 2022.07.15) [Computer software], <https://github.com/blaylockbk/goes2go> (2023).
- [170] G. Buster, M. Bannister, A. Habte, D. Hettinger, G. Maclaurin, M. Rossol, M. Sengupta, Y. Xie, Physics-guided machine learning for improved accuracy of the National Solar Radiation Database, *Solar Energy* 232 (2022) 483–492.
- [171] T. O’Malley, E. Bursztein, J. Long, F. Chollet, H. Jin, L. Invernizzi, et al., Kerastuner, <https://github.com/keras-team/keras-tuner> (2019).
- [172] D. Yang, W. Wang, J. M. Bright, C. Voyant, G. Notton, G. Zhang, C. Lyu, Verifying operational intra-day solar forecasts from ECMWF and NOAA, *Solar Energy* 236 (2022) 743–755.
- [173] D. Yang, S. Alessandrini, J. Antonanzas, F. Antonanzas-Torres, V. Badescu, H. G. Beyer, R. Blaga, J. Boland, J. M. Bright, C. F. M. Coimbra, et al., Verification of deterministic solar forecasts, *Solar Energy* 210 (2020) 20–37.
- [174] D. Yang, D. van der Meer, Post-processing in solar forecasting: Ten overarching thinking tools, *Renewable and Sustainable Energy Reviews* 140 (2021) 110735.